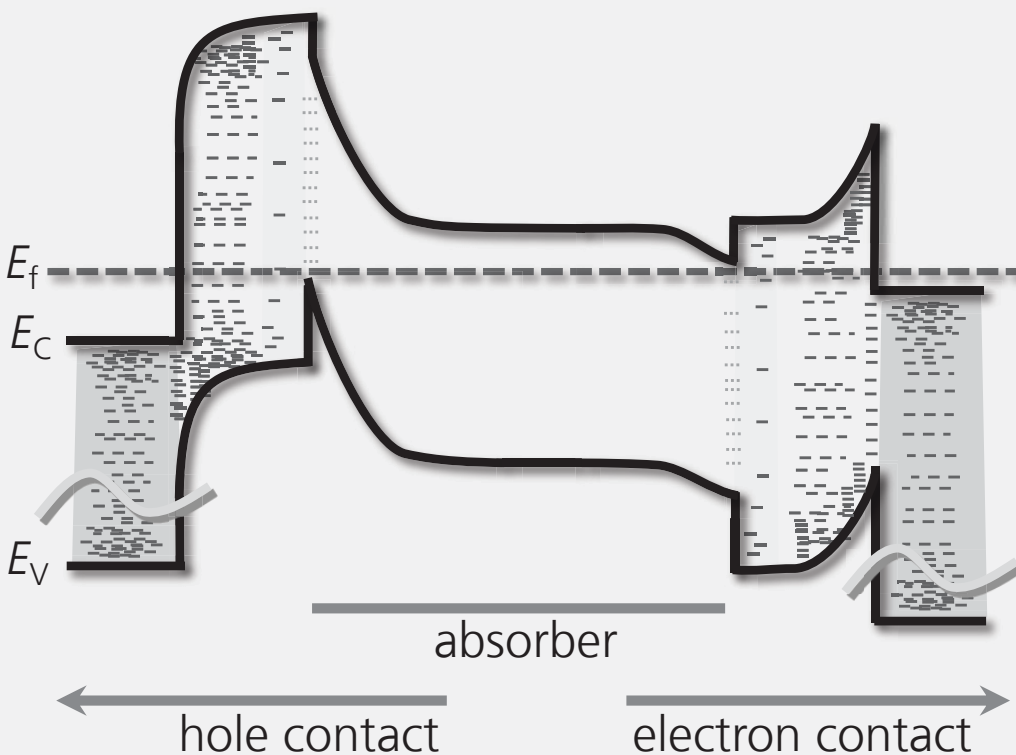


Martin Bivour

SILICON HETEROJUNCTION SOLAR CELLS: ANALYSIS AND BASIC UNDERSTANDING



Fraunhofer Institute for Solar Energy Systems ISE

SOLARE ENERGIE- UND SYSTEMFORSCHUNG /
SOLAR ENERGY AND SYSTEMS RESEARCH

Silicon Heterojunction Solar Cells: Analysis and Basic Understanding

Martin Bivour

FRAUNHOFER VERLAG

Contact:

Fraunhofer Institute for Solar Energy Systems ISE
Heidenhofstrasse 2
79110 Freiburg
Phone +49 761/4588-5150
Fax +49 761/4588-9342
E-Mail info@ise.fraunhofer.de
URL www.ise.fraunhofer.de

Bibliographic information published by Die Deutsche Bibliothek

Die Deutsche Bibliothek lists this publication in the Deutsche Nationalbibliografie;
detailed bibliographic data is available in the Internet at [<http://dnb.d-nb.de>](http://dnb.d-nb.de).

D 25

Zugl.: Freiburg/Brsg., Univ., Diss., 2016

Book Series: »Solare Energie- und Systemforschung / Solar Energy and Systems Research«

Printing and Bindery:

Mediendienstleistungen des
Fraunhofer-Informationszentrum Raum und Bau IRB, Stuttgart

Printed on acid-free and chlorine-free bleached paper.

All rights reserved; no part of this publication may be translated, reproduced, stored in a retrieval system, or transmitted in any form or by any means, electronic, mechanical, photocopying, recording or otherwise, without the written permission of the publisher.

Many of the designations used by manufacturers and sellers to distinguish their products are claimed as trademarks. The quotation of those designations in whatever way does not imply the conclusion that the use of those designations is legal without the consent of the owner of the trademark.

© by Fraunhofer Verlag, 2017, ISBN 978-3-8396-1166-1

Regional Planning and Building Construction IRB
P.O. Box 80 04 69, D-70504 Stuttgart
Nobelstrasse 12, D-70569 Stuttgart
Phone +49 (0) 7 11/9 70-25 00
Fax +49 (0) 7 11/9 70-25 07
E-Mail: verlag@fraunhofer.de
URL www.verlag.fraunhofer.de

SILICON HETEROJUNCTION SOLAR CELLS ANALYSIS AND BASIC UNDERSTANDING

Dissertation zur Erlangung des Doktorgrades
der Technischen Fakultät
der Albert-Ludwigs Universität Freiburg im Breisgau

vorgelegt von
MSc. Martin Bivour

Dezember 2015
Freiburg im Breisgau

Angefertigt am Fraunhofer-Institut für Solare Energiesysteme
Freiburg im Breisgau

To
My ladies, my son ;-)

and in loving
memory of my parents

Dekan:
Prof. Dr. Georg Lausen

Erstgutachter:
Prof. Dr. Eicke R. Weber

Zweitgutachter:
Prof. Dr. Leonhard Reindl

Vorsitzender der Prüfungskommission:
Prof. Zacharias

Beisitzer:
Prof. Wöllenstein

Tag der Disputation: 12.04.2016

Institut für Mikrosystemtechnik
Technische Fakultät der Albert-Ludwigs-Universität Freiburg

Table of Contents

Abstract	v
Zusammenfassung	ix
1 Introduction	- 1 -
1.1 Motivation	- 1 -
1.2 Research objectives	- 3 -
1.3 Outline.....	- 4 -
2 Fundamentals of Solar Cell Device Physics	- 5 -
2.1 Semiconductor equations	- 5 -
2.2 Recombination processes.....	- 8 -
2.3 Fundamental considerations on the excess carrier extraction.....	- 13 -
2.4 Diode equation and J - V parameters.....	- 16 -
2.5 Alternatives to homojunctions – basic concepts and history.....	- 20 -
2.5.1 Amorphous Silicon / Crystalline Silicon Heterojunction	- 30 -
2.6 Chapter Summary.....	- 37 -
3 Technology, Characterization and Simulation	- 39 -
3.1 Technology: Preparation of solar cells and QSSPC and Suns- V_{oc} samples	- 39 -
3.1.1 Process flow	- 39 -
3.1.2 Deposition tool.....	- 42 -
3.2 Characterization.....	- 42 -
3.2.1 Interpretation of fill factor losses	- 44 -
3.3 Numerical device simulations	- 45 -

4	Relevant Design Parameters for Carrier Selective Contacts: A Simulation Study	- 47 -
4.1	Contact recombination: Homojunction vs. heterojunction	- 47 -
4.1.1	Motivation	- 48 -
4.1.2	Simulation Details	- 48 -
4.1.3	Simulation results: Heterojunction vs. homojunction	- 51 -
4.1.4	Conclusion	- 54 -
4.2	Basic aspects for carrier selective contacts	- 55 -
4.2.1	Motivation: Non-ideal voltage extraction	- 55 -
4.2.2	p/n-Homojunction	- 60 -
4.2.3	MS contact: An induced p/n homojunction	- 62 -
4.2.4	MIS like contact: a-Si:H buffer	- 65 -
4.2.5	Classical SHJ: a-Si:H doping and TCO work function	- 66 -
4.2.6	Role of electric field	- 79 -
4.2.7	Important bulk parameters for semiconductor buffer layers	- 83 -
4.2.8	Selectivity from an asymmetric surface recombination velocity	- 86 -
4.2.1	Selectivity from an asymmetric mobilities and hetero-barriers	- 88 -
4.3	Chapter Summary	- 90 -
5	Limit of the Internal Voltage at MPP and Open-Circuit Conditions:	
	Chemical and Field-Effect Passivation of the Absorber	- 93 -
5.1	Motivation	- 93 -
5.2	Simulation: Influence of interface defects and absorber	- 96 -
5.2.1	Input parameters and qualitative influence of variables	- 97 -
5.2.2	Simulation Results	- 99 -
5.3	Experimental: Influence of a-Si:H(i) thickness and Corona charge	- 112 -
5.3.1	Motivation	- 112 -
5.3.2	Device fabrication – Suitable Dielectric Capping Layer	- 114 -
5.3.3	Experimental Results	- 115 -
5.3.4	Conclusion	- 122 -
5.4	Chapter Summary	- 123 -

6 Carrier Extraction from the Absorber:

Realization and Evaluation of Different Carrier Selective Contact Schemes.....	- 125 -
6.1 a-Si:H doping variation as a showcase for a non-ideal voltage extraction.....	- 125 -
6.1.1 Motivation.....	- 126 -
6.1.2 Illumination-level dependence of open-circuit voltage	- 127 -
6.1.3 Correlation with the fill-factor.....	- 131 -
6.1.4 Temperature dependence of cell parameters.....	- 139 -
6.1.5 Further investigations and remarks.....	- 142 -
6.1.6 Conclusion	- 146 -
6.2 Interfacial ITO doping variation: An attempt to modify the parasitic Schottky contact-	147 -
6.2.1 Probing the tunability of the effective work function.....	- 148 -
6.2.2 SHJ cells with modified hole and electron Schottky contact.....	- 151 -
6.2.3 Possible origins of the fill factor limitation.....	- 154 -
6.2.4 Conclusion	- 159 -
6.3 Replacing the TCO by a metal: An approach to improve the Schottky contact ?	- 160 -
6.3.1 Motivation.....	- 160 -
6.3.2 Probing the effective work function	- 162 -
6.3.3 Limited applicability of metal films as contact layers	- 167 -
6.3.4 High efficiency hybrid rear emitter cells: ITO vs. metal films	- 168 -
6.3.5 Conclusion	- 170 -
6.4 Contact materials adopted from organic electronics	- 171 -
6.4.1 Motivation.....	- 171 -
6.4.2 Assessing the suitability of different contact materials.....	- 172 -
6.4.3 SIS like cells and modification of the parasitic Schottky contact	- 175 -
6.4.4 Conclusion	- 182 -
6.5 Chapter Summary.....	- 185 -

7 Lateral Carrier Transport at the Front: Mitigating the Associated Losses	- 189 -
7.1 Motivation	- 189 -
7.2 Simulation: Front vs. rear emitter.....	- 191 -
7.2.1 Simulation details	- 191 -
7.2.2 Collection of absorber's minority carriers at the rear emitter	- 193 -
7.2.3 Improved 2D carrier collection for the rear emitter design	- 197 -
7.2.4 Further aspects	- 204 -
7.3 Solar cell results: Front vs. rear emitter	- 211 -
7.3.1 Experimental details.....	- 211 -
7.3.2 Results.....	- 211 -
7.4 Chapter Summary.....	- 216 -
8 Summary and Outlook	- 217 -
8.1 Summary.....	- 217 -
8.2 Outlook	- 221 -
9 References	- 223 -
10 Publications	- 247 -
11 Acknowledgements	- 253 -

Abstract

Crystalline silicon (c-Si) wafer-based solar cells with homojunctions dominate the photovoltaic market. These cells feature hole or electron selective contacts formed by p-type or n-type doping of the c-Si absorber surface via diffusion or alloying. In this thesis silicon heterojunction (SHJ) solar cells which share many similarities with induced junction solar cells (e.g. Metal-Insulator-Semiconductor) are investigated. In contrast to diffused homojunction cells they rely on thin films that are deposited onto the crystalline silicon absorber. Unlike homojunction devices, recombination losses at the c-Si surface and the metalized regions can be greatly suppressed enabling record open-circuit voltages close to the intrinsic limit of the c-Si absorber. So far, layer stacks of intrinsic and doped amorphous silicon (a-Si:H) capped with a transparent conductive oxide (TCO) are used to form the hole and electron selective contact. The parasitic absorption in these films is the cause for a design trade-off between optical and electrical losses. Hence, the efficiency of such cells is typically limited by the short-circuit current and the fill-factor.

One main focus of this work is to analyze the cell performance mainly at **maximum power point conditions** which is closely linked to the fill-factor limitations of such cells. The fill-factor limitation results from transport related losses and the moderate surface passivation at maximum-power point condition as discussed in this work. The **transport and recombination related fill-factor losses** are the key challenges that are tackled in this thesis, experimentally and by device simulation. For this purpose solar cells and test structures were fabricated and characterized using plasma enhanced chemical vapor deposition (PECVD), sputtering, thermal evaporation and e.g. illumination level dependent open-circuit voltage, surface photo-voltage measurements, respectively.

To facilitate the basic understanding, the fundamental requirements on a contact scheme in terms of a highly **selective hole or electron extraction from the absorber** are discussed on the basis of **numerical device simulations**. It is pointed out that, unlike for standard homojunction cells, the characteristics of such novel contact schemes might be limited rather by a non-ideal excess carrier extraction from the absorber than by surface passivation and ohmic losses. It is shown that such a non-ideal carrier extraction is linked to the fact that the contact region is operating in high-injection conditions, a result from, e.g. insufficient doping and / or unsuited work functions. The importance of analyzing the contact characteristic regarding distinctive

features which reveal if the carrier extraction is ideal, i.e. obeys the standard p/n-junction theory as described by the diode model is pointed out.

The interplay between the optical and **ohmic transport losses** caused by the lateral carrier transport in the **TCO electrode** at the front side were studied in detail. A simple yet successful approach, consisting of positioning the emitter at the rear of the cell, was investigated for the first time. This cell design makes use of the lateral conductivity of the silicon absorber reducing ohmic losses due to lateral carrier transport in the TCO electrode. This **rear emitter cell design** has been widely adopted by the community and seems to become a standard design for SHJ cells. An efficiency of 20.8% was achieved using such a cell design.

The **non-ohmic transport** losses caused by the TCO / doped a-Si:H Schottky contact were studied by analyzing the interaction between the a-Si:H doping and the work function of the TCO (or metal). It is shown that a minimum doping of the a-Si:H is mandatory to **form the junction with the c-Si absorber** and ensure an efficient **tunneling transport into the TCO**. Furthermore, it is shown that for the case that the ITO is replaced by a metal film, the transport-related fill-factor loss can be reduced and be as low as 1%_{abs}. A simple characterization approach allowing to identify and quantify such non-ohmic losses was established. It is based on the measurement of the open-circuit voltages as a function of illumination density.

The **fill-factor limitation due to non-perfect surface passivation** was investigated experimentally and by device simulation. It is shown that it constitutes a significant fill-factor loss which amounts to about 6%_{abs}. The latter is linked to the fact that, unlike for open-circuit conditions, for maximum-power point conditions surface passivation is insufficient to allow operation near the intrinsic limit of the absorber. Accordingly, the requirements for the surface passivation with respect to a very high fill-factor and efficiency are much higher as compared to a very high open-circuit voltage. A novel experimental approach is used to distinguish between chemical and field-effect passivation of the c-Si absorber by a-Si:H. It reveals that surface passivation is mainly limited by the hole contact, which is pointing towards a higher capture cross section of electrons at the a-Si:H / c-Si interface.

Furthermore, investigations regarding **novel thin films adopted from organic electronics** were conducted. While none of the investigated materials was suited to form an effective electron selective contact, the high **work function metal oxides** tungsten and molybdenum oxide reveal to be interesting candidates for the hole selective contact. A significant **efficiency improvement (~1%_{abs})** compared to cells featuring the p-type a-Si:H could be obtained. The replacement of the

p-type a-Si:H leads to an improved current (about 1 mA/cm^2) as the parasitic absorption in the metal oxides is lower. These metal oxide films were also used as an additional contact layer, sandwiched between the p-type a-Si:H and the TCO. A significantly **fill-factor gain (about 1.5 %)** is observed in this case as hole extraction from the a-Si:H into the TCO is improved, presumably by an **improved work function matching**. Furthermore, as the metal oxides are deposited by soft deposition (thermal evaporation), such films also provide some protection of the a-Si:H / c-Si interface from the sputter damage caused by the subsequent TCO sputter deposition.

The investigation performed in this thesis led to a better understanding of the fundamental loss mechanisms in heterojunction solar cells. With this improved understanding it was possible to increase the efficiency of heterojunction solar cells up to 22.8% at Fraunhofer ISE, to introduce suitable characterization approaches and new contact materials which are promising candidates for a new generation of carrier-selective contacts for silicon wafer based solar cells.

Zusammenfassung

Die Arbeit befasst sich mit grundlegenden Untersuchungen von Silizium Solarzellen deren ladungsträgerselektiven Kontakte nicht wie herkömmlich durch die oberflächennahe Diffusion oder Legierung des c-Si Wafers (Homojunction), sondern ähnlich wie bei MIS (Metal-Insulator-Semiconductor) Solarzellen durch aufbringen einer Schicht mit hoher/geringer Austrittsarbeit (Hetero- oder Inducedjunction) ausgebildet werden. Anders als bei den Standard-Solarzellen werden hier die löcher- oder elektronenselektiven Kontakte durch dünne Schichten, die bei geringen Temperaturen auf den Absorber abgeschieden werden, ausgebildet. Insbesondere die Verwendung von amorphen Silizium (a-Si:H) ermöglicht die Rekombinationsverluste an der c-Si Grenzfläche und den metallisierten Bereichen stark zu unterdrücken und führt zu sehr hohen Leerlaufspannungen, nahe am intrinsischen Limit des c-Si Absorber. Die Effizienz solcher Zellen wird typischerweise durch den Kurzschlussstrom und den Füllfaktor beschränkt.

Ein Schwerpunkt dieser Arbeit war es, die **Verluste** vor allem unter **Maximum Power Point** (MPP) Bedingungen, die eng mit dem **Füllfaktor** (FF) der Zelle verbunden sind, zu analysieren. Die Füllfaktorbeschränkungen durch **transport- und rekombinationsbedingte Verluste** waren dabei die wichtigsten Herausforderungen, die in dieser Arbeit experimentell und mittels Simulation untersucht wurden. Die **Evaluierung neuartiger Materialien**, als Alternative zu den dotierten a-Si:H Schichten, stellte eine weitere wichtige Fragestellung diese Arbeit dar. Zu diesem Zweck wurden Solarzellen und Teststrukturen, unter Verwendung von plasmaunterstützter chemischer Gasphasenabscheidung (a-Si:H), Sputtern (ITO) und thermischer Verdampfung (Metalloxide) hergestellt. Entsprechende Charakterisierungsverfahren und innovative Zellkonzepte wurden etabliert.

Es wurden umfangreiche Simulationsstudien durchgeführt, wobei anders als bei bisherigen Untersuchungen zwischen den internen und externen Zellparametern unterschieden wurde. Dies ermöglichte ein ganzheitliches Verständnis und eine detaillierte Verlustanalyse, welche offenbarte, dass für die untersuchten Systeme neben den „klassischen“ Verlusten, die in der Standardtheorie zum p / n-Übergang berücksichtigt werden, „**nicht-klassische**“ **Verluste** einen signifikanten Einfluss auf die externen Zellparameter haben können. Letzteres zeigte sich etwa für Kontaktsysteme mit nicht ausreichend hoher Dotierung oder ungeeigneten Austrittsarbeiten. Hier konnte das Kontaktsystem die interne Zellspannung nicht vollständig abgreifen, so dass die externe Spannung unterhalb der internen Spannung lag. Dies führte nicht nur zu Verlusten bzgl.

FF und Leerlaufspannung (V_{oc}), sondern auch zu charakteristischen Eigenschaften der externen Zellparametern. So wurde etwa die Analyse der **Bestrahlungsstärkenabhängigkeit des V_{oc}** ($Suns-V_{oc}$) in dieser Arbeit als eine wirksame Methode für die Identifizierung derartiger „nicht-klassische“ Verluste etabliert. Dies stellt eine einfache und aussagekräftige Methode dar, die bereits im frühen Entwicklungsstadium eine Bewertung der Kontaktsysteme ermöglichte.

Die Limitierung der internen Spannung (implizierte Spannung, iV) durch die **Rekombinationsverluste an der c-Si Grenzfläche** wurde durch einen neuartigen Ansatz untersucht. Durch Coronaaufladung des a-Si:H(i) / c-Si Systems konnten die chemische und die Feldeffekt Passivierung getrennt voneinander untersucht werden. Es wurde gezeigt, dass sich eine exzellente Oberflächenpassivierung eher in einem hohen impliziten Füllfaktor (iFF) als in einer hohen implizierten Spannung bei Leerlaufbedingungen (iV_{oc}) widerspiegelt. Während der iV_{oc} oft bereits relativ nahe am intrinsischen Limit des c-Si Absorber lag, lieferte für den iV_{MPP} und damit den iFF , die Rekombination an der c-Si Grenzfläche noch immer den dominanten Beitrag. Dies stellt einen **signifikanten FF Verlust** im Vergleich zu dem intrinsischen Limit von etwa 89 % dar, der sich bei den Zellen in einem pseudo Füllfaktor (pFF) zeigte der kaum 83 % überschritt. Folglich können deutlich höhere Füllfaktoren und Effizienzen erreicht werden, wenn es gelingt die Rekombinationsverluste an der a-Si :H / c-Si Grenzfläche zu verringern .

Bezüglich des Abgreifens der internen Spannung wurden verschiedene Kontaktsysteme untersucht. Für eine grundlegende Analyse wurde eine Dotiervariation des a-Si:H(p) Emitters durchgeführt. Bei unzureichender Dotierung zeigte sich, dass die Kontakteigenschaften vom **parasitären ITO / a-Si:H(p) Schottky** Kontakt dominiert wurde. Ohne Dotierung ergab sich ein Spannungsverlust von etwa 300 meV im Kontakt, der externe V_{oc} lag damit bei nur etwa 400 mV. Bei **ausreichend hoher Dotierung** entsprach der externe V_{oc} dem iV_{oc} , beide lagen dann bei etwa 730 mV. Es konnte gezeigt werden, dass ein Spannungsverlust im Kontakt zu Idealitätsfaktoren der $Suns-V_{oc}$ Kennlinie führt, die geringer sind als mit der Standardtheorie zum p/n-Übergang zu erklären ist. Eine klare Korrelation zwischen diesen **Idealitätsfaktoren** und entsprechenden FF und V_{oc} Verlusten konnte gezeigt werden. Ein weiterer Indikator für nicht ideales Abgreifen der internen Spannung durch das Kontaktsystem war die **Temperaturabhängigkeit der FF** und V_{oc} . So zeigte sich für den FF , dass dieser nicht wie typischerweise durch die Temperaturabhängigkeit der Rekombinationsverluste und damit den pFF dominiert wurde, da die Transport behafteten FF Verluste keine deutliche Temperaturabhängigkeit zeigten. Die Existenz von nicht-ohmschen Transportverlusten führte hier jedoch zu einer deutlichen Abnahme der Transport behafteten FF

Verluste, welche die Zunahme der Rekombinationsbehafteten FF Verluste mit der Temperatur kompensierten.

Neben dem etablierten dotierten amorphen Silizium wurden weitere Kontaktmaterialien wie **Metalle**, TCOs und Materialien aus der organischen Elektronik untersucht. Es zeigte sich, dass reine Metalle nicht zur **Ausbildung selektiver Kontakte** geeignet sind. Neben einem ausgeprägten **Fermi level pinning** zeigte sich die Degradation des c-Si Absorbers durch eine a-Si:H Passivierschicht bereits bei moderaten Annealing Temperaturen, eine schlechte Haftung und schlechte optische Eigenschaften im Hinblick auf die Rückseiten Reflexion. Es konnte jedoch gezeigt werden, dass Silber prinzipiell verwendet werden kann, um die ITO Elektrode auf der Rückseite eines a-Si:H (p) Emitters zu ersetzen. So konnte für **Hybrid SHJ Zellen**, ein Zelledesign das im Rahmen dieser Arbeit eingeführt wurde, ein Wirkungsgrad von 22,8% ($V_{oc} = 705$ mV, $J_{sc} = 39.9$ mA / cm², $FF = 81.2\%$) erreicht werden.

Eine Dotiervariation von **ITO** zeigte, dass die **Austrittsarbeit** an der ITO / a-Si:H(i) Grenzfläche in der gewünschten Weise verändert werden kann. Dies motivierte einen weiteren Versuch den parasitären ITO / a-Si:H(p) und ITO / a-Si:H(n) durch eine entsprechende Anpassung der Austrittsarbeit des ITO zu verbessern. Auf Zellniveau zeigte sich jedoch ein ähnlicher Einfluss der ITO Dotierung für den Löcher- und den Elektronenkontakt. Dies deutete darauf hin, dass neben der Austrittsarbeit andere Einflussgrößen für den ITO / a-Si:H Heterokontakt zu berücksichtigen sind.

Hinsichtlich alternativer Kontaktmaterialien, die in der organischen Elektronik bereits Anwendung finden (Cäsiumcarbonat, Lithiumfluorid, PEDOT:PSS, Titandioxid, ITO, Molybdänoxid und Wolframoxid) konnte bisher kein Material gefunden werden, dass zur Ausbildung eines elektronenselektiven Kontakts geeignet war. Allerdings wurden vielversprechende Ergebnisse für den Löcherkontakt auf Teststrukturen mit PEDOT:PSS, Molybdänoxid (MoO_x) und Wolframoxid (WO_x) erzielt. Die Messung der Oberflächenphotospannung zeigte die hohe Austrittsarbeit der Schichten und den ausgeprägten p / n-Homoübergang, der für diese Systeme in dem Absorber induziert wird. Genauere Untersuchungen auf Zellniveau für die **Metalloxide** zeigten deren allgemeine Anwendbarkeit. Entweder zum Ausbilden eines direkten Löcherkontaktes, wenn das a-Si:H(p) ersetzt wurde oder für den Standard Silizium Heteroübergang zur Verbesserung des ITO / a-Si:H(p) oder AZO / a-Si:H(p) Kontaktes, wenn das Metalloxid als Zwischenschicht verwendet wurde. Mit MoO_x als direkten Löcherkontakt konnte die Effizienz der planaren Solarzellen vor dem Tempern deutlich verbessert werden im Vergleich

zur Referenz ($\sim 18,7\%$ vs. $\sim 17,6\%$). Für WO_x als zusätzliche Kontaktschicht konnte eine signifikante Verringerung der transportbedingten FF Verluste im Vergleich zur Referenz erzielt werden. Dies zeigte sich in einem deutlichen FF Anstieg ($\sim 81,1\%$ vs. $\sim 79,6\%$). Schließlich wurde für WO_x , welches direkt auf c-Si abgeschieden wurde (kein a-Si:H), eine Effizienz vergleichbar zu der Referenz beobachtet ($\sim 17,6\%$ vs. $\sim 17,5\%$). Diese einfache Struktur könnte ein attraktives Konzept zum Ersetzen des Al-BSF der Standard Homozellen darstellen. Mit diesen Ergebnissen konnte gezeigt werden, dass Kontaktmaterialien aus dem Bereich der organischen Elektronik interessante Kandidaten für zukünftige Silizium Solarzellen sind.

Schließlich wurden auch die Verluste, die durch den **lateralen Transport an der Vorderseite** von Standard SHJ Zellen entstehen, untersucht. Ein einfacher, aber erfolgreicher Ansatz zur Vereinfachung dieses Optimierungsproblems basierend auf der Ausnutzung der Querleitfähigkeit des Absorbers wurde etabliert. Dies wird durch das Umlegen des p/n-Übergang von der Vorderseite auf die Rückseite erreicht und führt zu geringen Anforderungen an die TCO Querleitfähigkeit und das Design der Grیدهlektrode. Dieses "**Rear Emitter**" Design wurde bereits von verschiedenen Firmen und Instituten übernommen und hat sich als vorteilhaft in Bezug auf die Effizienz erwiesen. Es ist daher wahrscheinlich, dass sich dies zum Standard Zelldesign entwickelt.

1 Introduction

1.1 Motivation

Around 90% of all photovoltaic (PV) modules are based on crystalline silicon. Like for other mass-production (electronic) devices, cost reduction is a main driver for research and development. The cost reduction is not directly related to the cost of the device itself but to the cost of PV-generated electricity. In this sense, increasing the solar cell efficiency by applying advanced cell architectures is one route for crystalline silicon wafer based PV to achieve significant cost reduction. This applies especially to the case when high-quality mono crystalline silicon (c-Si) wafers are used as absorber material. For this absorber material silicon heterojunction (SHJ) solar cells are a promising high-efficiency cell design for which the higher production and material cost could translate into lower costs per Watt peak ($\text{€}/W_p$) on module level [1], [2].

The unique feature of SHJ cells is that hole and electron selective contacts (emitter and back/front surface field) can be formed without significantly increasing the overall minority carrier recombination of the solar cell. This is the decisive difference compared to the homojunction cells currently dominating the market. For the latter the realization of hole and electron collecting regions comes at the expense of increased intrinsic and extrinsic recombination in the bulk and at the surface of the doped c-Si regions and even more important at the metal/semiconductor contacts. This leads to two basic advantages of SHJ cells over the classical homojunction cells. Firstly, the low minority carrier recombination allows for very high voltages at both open-circuit and maximum power point conditions. Hence, if well designed such devices are characterized by a much higher efficiency potential enabled by a higher open-circuit voltage (V_{oc}) and fill factor (FF). The absence of recombination at the metal/semiconductor contacts is the most important feature which enables such low recombination losses. The latter also leads to the second advantage over homojunction cells, the possibility to apply a simple one-dimensional junction design. Hence, structuring and alignment steps as e.g. in PRC (partial rear contact) cells are not needed during cell production and geometrical constraints, caused by the need to optimize regions for either low recombination or efficient carrier extraction / transport, are not dictating the optimum device design.

While for homojunction cells much knowledge was gathered in the last decades, SHJ cells are still rather novel. The classical SHJ combines the advantages of the wafer-based solar cells (high-

quality crystalline absorber) and the silicon thin-film solar cells (silicon thin-films and transparent conductive oxides for selective contacts). Both solar cell approaches on their own can benefit from extensive research and development in laboratories and industry over the last decades and even more knowledge was gathered for other electronic devices where silicon thin-films are involved including transistors and (light emitting) diodes.

To date the formation of the hole and electron selective contacts in SHJ cells is mainly realized by amorphous silicon (a-Si:H). This material has already proven to be a very promising candidate as demonstrated by the very high efficiencies reached by various companies and research institutes [3]. For the champion cells from Panasonic and Kaneka outstanding efficiencies of 24.7 % [4] and 24.2 % [5] for large-area devices on Cz wafers using screen printing and Cu plating have been reported, respectively. Especially for open-circuit conditions the junction recombination can be very efficiently suppressed by these a-Si:H / c-Si SHJs so that device recombination is mainly due to intrinsic recombination of the high-quality crystalline silicon absorber. This allows for very high open-circuit voltages (V_{oc}) of 750 mV [4] which are only about 10 mV below the upper limit that is determined by the high-quality crystalline silicon absorber [6]. This clearly demonstrates that a-Si:H / c-Si SHJ cells can show a nearly ideal device performance for the operation at open-circuit conditions. However, in terms of solar cell efficiency the **losses at maximum power point are decisive**. Consequently, besides an improved light management (higher J_{sc}), a further reduction and understanding of the losses at maximum power point conditions (higher fill factors) is essential to improve the device performance even further and to evaluate the potential of **alternative contact materials** such as metal oxides for future device structures.

For such rather novel SHJ like approaches, metal oxides and other contact materials adopted from organic electronics might be interesting candidates to replace the silicon thin films typically applied as contact layers. Such materials might allow for a wider variation of the heterojunction properties enabling superior junction properties in terms of **transparency** (higher J_{sc}), **defect density** (higher V_{oc}) and **doping efficiency** and more **suited work functions** (higher FF). Improving the **temperature stability** of the junctions, to allow for higher temperatures for back-end processing (TCO, metallization, module integration), is another driver for reserve on such rather novel contact schemes. Regarding the latter, especially novel or rediscovered approaches based on ultrathin dielectric passivation layers and doped poly silicon like contact schemes have already proven to be interesting candidates [7], [8].

1.2 Research objectives

The objective of this thesis is to improve the understanding of the operation principles of silicon wafer based heterojunction solar cells. The main focus is set on understanding and improving the device limiting fill factor issues linked to recombination and ohmic and non-ohmic transport losses. Another objective, which is closely linked to this, is dealing with the identification and evaluation of rather novel contact materials for c-Si based solar cells. These problems are tackled experimentally and by numerical device simulations.

The main points can be summarized as follows:

- Provide a simple but meaningful methodology to evaluate different contact schemes regarding their ability to form a carrier selective contact (emitter/BSF). The key point is to analyze whether V_{oc} and FF are limited by “classical” losses such as surface passivation and ohmic losses or if a non-ideal carrier extraction is limiting the solar cell characteristics. Rather than reaching high efficiencies, the focus is on building a deeper understanding of non-classical losses since this constitutes the basis for an efficient engineering of such contact schemes.
- Gain a detailed understanding of the FF losses limiting the “classical” silicon heterojunction cells. Distinguish between losses caused by ohmic and non-ohmic carrier transport and carrier recombination. Find and investigate approaches to reduce these losses.
- Screen different “non-classical” contact schemes formed by low-temperature processing regarding their potential for future applications.
- Utilize the gained understanding to improve cell performance and integrate novel contact materials in solar cells.

1.3 Outline

This manuscript is divided in the following chapters:

Chapter 2 reviews the main theory needed for the discussion in the following sections, namely c-Si surface passivation, carrier extraction and the fundamental parameters of the current-voltage characteristic.

Chapter 3 addresses the sample preparation and the metrology used throughout this thesis.

Chapter 4 is based on device simulations. First, the need to balance recombination, ohmic and shading losses at the front side of a solar is motivated. Distinctive differences between heterojunction and homojunction solar cells are pointed out. Then, the basic requirements for a carrier-selective contact scheme are motivated. The actual contact properties which are needed to ensure an efficient extraction of excess carriers and voltage from the absorber are identified. It is found that it is important to distinguish two limiting cases: .

- i) Providing a high excess carriers density within the absorber by an efficient surface passivation of the absorber, which defines the extractable voltage.
- ii) Enabling a lossless extraction of this excess carrier and voltage from the absorber.

Chapter 5 addresses the c-Si surface passivation by a carrier-selective contact scheme. The main objective is the analysis of the injection-level dependence of the c-Si surface passivation by a-Si:H. It defines the excess carrier density within the absorber and hence the upper limit of the extractable voltage. An integral assessment of the V_{oc} and FF limitation by minority carrier recombination is performed as this defines the upper efficiency limit that would be reached if voltage extraction by the contacts is ideal (for simplicity, voltage “extraction” is used in the following to describe the ability of the contact to maintain the majority carrier Fermi-level).

Chapter 6 tackles the question of the excess carrier extraction from the absorber. To this end, different contact materials are evaluated. Doped amorphous silicon, metals and rather novel materials adopted from organic electronics are investigated using test structures, and if promising, applied to solar cells. New approaches are introduced which allow to distinguish whether surface passivation or excess carrier extraction is the limiting case.

Chapter 7 deals with the ohmic losses at the front side. The trade-off between an efficient lateral carrier transport enabled by both, a reasonable pitch of the metal grid electrode and the TCO conductivity and the corresponding optical losses caused by grid shading and free carrier absorption in the TCO are analyzed. A simple yet successful approach to facilitate this optimization problem is presented.

Chapter 8 summarizes the main finding of this thesis and gives an outlook for future work.

2 Fundamentals of Solar Cell Device Physics

This chapter reviews the main theory needed for the discussion in the following sections, namely the basic operation principles of a solar cell, the recombination of excess carriers and the fundamental parameters of the current-voltage characteristic¹. Most discussions are based on the approach from the textbook from Würfel [9] according to which “The structure of a solar cell is much better represented by a semiconducting absorber in which the conversion of solar heat into chemical energy takes place and by two semi-permeable membranes which at one terminal transmit electrons and block holes and at the second terminal transmit holes and block electrons”. This approach is quite distinct from most standard textbooks. Furthermore, an historical review of alternatives to the classical homojunctions are presented and important physical aspects are pointed out.

2.1 Semiconductor equations

Current equations for hole and electrons in one direction

Two forces are acting on electrons and holes and causing a current flow. A diffusion-driven current is caused by an inhomogeneous carrier density, i.e. a gradient of the chemical potential. A drift-driven component due to an electric field, i.e. a gradient of the electrical potential (φ). Both forces result in a net force which is the gradient of the electrochemical potential. As the electrochemical potential is also expressed by the quasi-Fermi level (QFL) of holes ($E_{f,p}$) and electrons ($E_{f,n}$) the contribution of this forces to the hole (J_n) and electron (J_p) current can be expressed by [9]

¹ This section is partly adapted from the standard literature. For a more detailed insight the reader is referred to the textbooks from Würfel [9], Green [10], Swanson et al. [11], Goetzberger et al. [12] and the website from Honsberg and Bowden PV Education [13]. A textbook covering more heterojunction specific aspects is the one from Fahrenbruch et al. [14]. For more aspects regarding the fundamentals of silicon based heterojunction solar cells it is referred to book from van Sark et al. [15]. Other PhD theses related to the field of silicon heterojunction solar cells such as Ref [16], [17], [18], [19], [20], [21], [22], [23], [24], [25] are also recommended. A broader view on the basics of semiconductor device physics is given in the book from Sze [26].

$$J_p = -qD_p \frac{dp}{dx} - q\mu_p p \frac{d\phi}{dx} = \mu_p p \frac{dE_{f,p}}{dx} \tag{2.1}$$

$$J_n = +qD_n \frac{dn}{dx} - q\mu_n n \frac{d\phi}{dx} = \mu_n n \frac{dE_{f,n}}{dx} \tag{2.2}$$

where p and n are the hole and electron densities, respectively. μ_p and μ_n denote the respective mobility and D_p and D_n the diffusion constant. In consequence a hole and electron current is caused by the gradient of their respective QFL. This is depicted in Figure 2.1 for different conditions with the help of a band diagram.

The total current of charge carriers is determined by the sum of this hole and electron currents and replacing the mobility and carrier density in the last term in equations (2.1) and (2.2) by the respective conductivity of holes and electrons (σ) leads to [9]

$$J_{total} = J_p + J_n = \frac{\sigma_p}{q} \frac{dE_{f,p}}{dx} + \frac{\sigma_n}{q} \frac{dE_{f,n}}{dx} \tag{2.3}$$

The last term shows the important relation between the hole and electron conductivity and the gradient of the respective QFL driving the current.

With respect to the engineering of a solar cell, different device regions must be designed in such

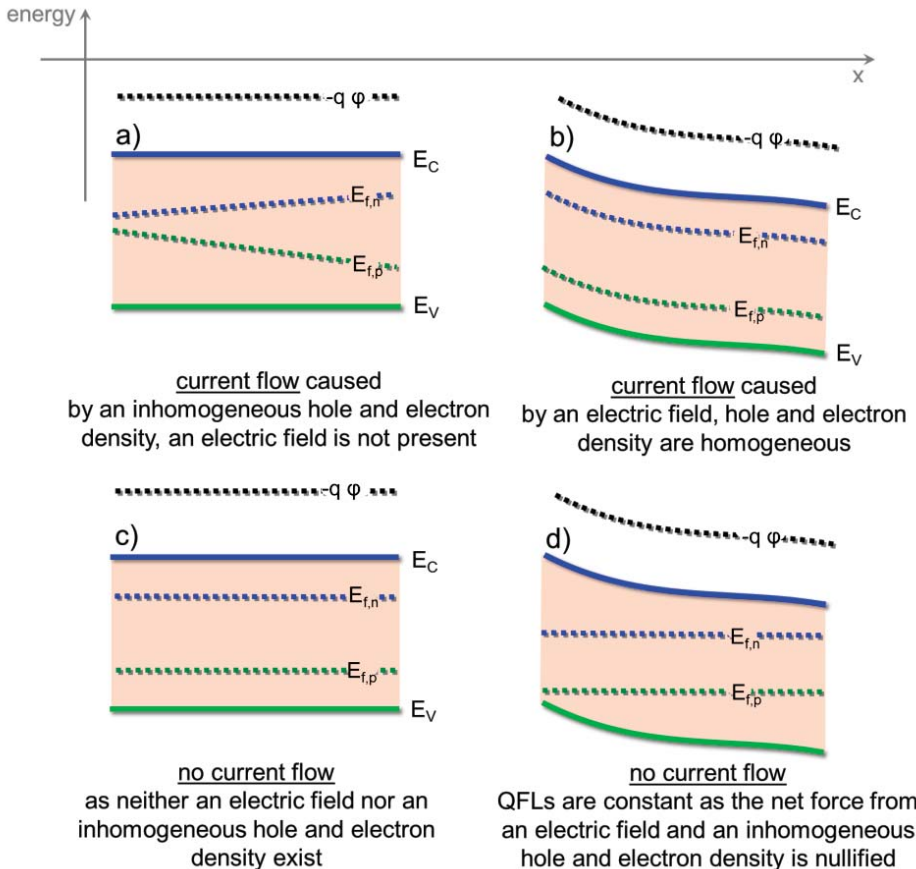


Figure 2.1: Different conditions regarding a current flow in a semiconductor. The solid blue and green lines corresponds to the conduction and valence band energies, respectively. An inhomogeneous carrier density causing a diffusion current (a, d) is represented by a changing distance between the hole and electron QFL and the valence and conduction band energy, respectively. An electric field causing a drift current (b, d) is represented by a gradient of the electrical potential (black).

a way that that total current in one direction is dominated either by the hole or the electron current. Equation (2.3) reveals that for the hole selective contact, this can be achieved if the electron conductivity (σ_n) is reduced to a minimum while the hole conductivity (σ_p) should remain sufficiently high such that a negligible gradient of E_{fp} is needed to drive the hole current. The importance of such an asymmetry in the hole and electron currents will be discussed in detail in section 4.2.

Poisson's equation

The electric field (E), i.e. the gradient of the electrical potential which is driving the drift current results from the charge density (Q) in the semiconductor

$$dE = \frac{d\phi}{dx} = -\frac{Q}{\varepsilon_r \varepsilon_0} = -\frac{q}{\varepsilon_r \varepsilon_0} (p - n + N_D^+ - N_A^- + N_{tr}^+ - N_{tr}^-). \quad (2.4)$$

With ε_r and ε_0 the permittivity of the respective material and the vacuum, respectively. The charge density Q is defined by the mobile charges of the free holes (p) and free electrons (n). Fixed charges are represented by ionized dopant atoms and the charged defects states. The ionized donors (N_D^+) are positive and ionized acceptors (N_A^-) are negative. The contribution of defect levels to the net charge is described by N_{tr}^+ and N_{tr}^- .

One important quantity related to the electric field is the depletion layer width or screening length (L_s) of a junction. L_s describes how far an electric field penetrates into the semiconductor and can be expressed by

$$L_s = 2 \cdot \sqrt{\frac{\varepsilon_r \varepsilon_0 k T}{2 q^2 |Q|}} \cdot \sqrt{\frac{q |V_{bi}|}{k T}} \quad (2.5)$$

The first square root corresponds to the Debye length of the respective material. The second one describes the magnitude of the electrical potential difference which has to be screened in the material. V_{bi} is the built-in potential of a junction which for the classical p/n-junction is defined by electrical potential difference which in turn results from the charges of the ionized doping atoms on either side of the junction. For a metal / semiconductor like junction V_{bi} is the result of the work function difference between the materials in contact.

Continuity equation

The fact that a local increase or reduction of charge carriers is caused by the generation and recombination of carriers and a charge carrier flow is expressed by:

$$\frac{dp}{dt} = G_p - R_p - \frac{1}{q} \frac{dJ_p}{dx} \quad (2.6)$$

$$\frac{dn}{dt} = G_n - R_n - \frac{1}{q} \frac{dJ_n}{dx} \quad (2.7)$$

With the generation rate G and the recombination rate R . While the photo-generation of excess carriers is not treated here the annihilation of excess carriers by recombination and the corresponding change of carrier density will be addressed below.

2.2 Recombination processes²

For crystalline silicon the annihilation of excess carriers occurs via three recombination paths in parallel. Two of them are intrinsic processes, namely (i) radiative band-to-band recombination and (ii) Auger recombination while (iii) defect or impurity recombination through states within the bandgap either in the bulk or at the surface of silicon is presenting an extrinsic recombination path. Preventing this extrinsic recombination path is one of the major challenge for the engineering of solar cell.

The different recombination processes are typically characterized by their average carrier lifetime (τ), which is the average residence time of an excess carrier in the valence or conduction band before it is annihilated by recombination. This lifetime is defined as the ratio of excess charge carrier density (Δn) and the net recombination rate (R)

$$\tau = \frac{\Delta n}{R} \quad (2.8)$$

with $\Delta p = \Delta n$, i.e. an equal excess carrier density of holes and electrons.

The experimentally determined lifetime is influenced by all processes as they occur simultaneously. This lifetime is referred to as average effective lifetime (τ_{eff}). As the recombination rates of the individual paths (R_i) are additive τ_{eff} can be expressed as sum of the reciprocal of each individual lifetime τ_i

$$\frac{1}{\tau_{eff}} = \sum_i \frac{1}{\tau_i} \quad (2.9)$$

² For an excellent and recent overview on the recombination processes in the bulk and at the surface of crystalline silicon it is referred to [27]. For the recombination in amorphous silicon to Ref [20].

Radiative band-to-band recombination

The radiative recombination event is presenting the inverse process of the photon absorption. During band-to-band recombination the energy of the electron-hole pair is passed to one photon. As one electron and one hole need to be involved, the recombination rate (R_{rad}) is proportional to the density of the free holes times free electrons.

$$R_{\text{rad}} = B (p n - p_0 n_0) = B (p n - n_i^2) \quad (2.10)$$

With B the coefficient of radiative recombination and $p \cdot n = (p_0 + \Delta n) \cdot (n_0 + \Delta n)$, where p_0 and n_0 are the hole and electron density in thermal equilibrium, respectively. n_i is the intrinsic carrier density. It can be seen that the key driver for recombination is the deviation between the actual carrier density and equilibrium carrier density that is expressed by the term in the parenthesis.

The corresponding lifetime is

$$\tau_{\text{rad}} = \frac{1}{B (p_0 + n_0) + B \Delta n} \quad (2.11)$$

Depending on the injection conditions, one of the summands in the denominator is dominating the lifetime. For low injection conditions when the excess carrier density is well below the equilibrium carrier density which is typically defined by the concentration of the density ionized dopant atoms ($\Delta n \ll p_0 + n_0 \approx N_{\text{dop}}$), the first summand dominates. τ_{rad} is reduced with higher doping. For high injection conditions on the other hand for which the excess carrier density exceeds the equilibrium carrier density ($\Delta n \gg p_0 + n_0 \approx N_{\text{dop}}$), τ_{rad} depends only on Δn . However, irrespective of the injection conditions, for crystalline silicon τ_{rad} is rather large not limiting the overall recombination. This is explained by the quantity of B which is small as compared to e.g. direct band gap materials. For crystalline silicon, being an indirect band gap material, a phonon needs to be involved as well which makes this recombination process less likely compared to the two discussed in the following.

Band-to-band Auger recombination

For crystalline silicon Auger recombination is the more relevant intrinsic recombination path. It requires the interaction of three particles. The recombination rate for two holes and one electron is R_{hhe} . For two electrons and one hole is R_{eeh} . Unlike for radiative recombination, the energy of the electron-hole pair is passed to either a hole or an electron and not to a photon. The need for a third particle makes Auger recombination more likely at higher carrier densities, e.g. in highly doped material or for high injection conditions.

The net Auger recombination rate (R_{Auger}) is the sum of both processes which are proportional to the carrier densities involved

$$R_{Auger} = R_{hhe} + R_{eeh} = C_p (p^2 n - n_i^2 p_0) + C_n (p n^2 - n_i^2 n_0) \quad (2.12)$$

With C_n and C_p being the respective Auger coefficients. The Auger lifetimes for low injection for a n-type silicon can be approximated by

$$\tau_{Auger,li} = \frac{1}{C_n N_{dop}^2} \quad (2.13)$$

for high injection conditions with

$$\tau_{Auger,hi} = \frac{1}{(C_p + C_n) \Delta n^2} = \frac{1}{C_a \Delta n^2} \quad (2.14)$$

It follows that for low injection τ_{Auger} strongly depends on the doping and for high injection on the excess carrier density.

For a recent parametrization of the combined influence of radiative and Auger recombination it is referred to Ref [28].

Defect recombination in the bulk

Defect recombination is caused by defects states within the bandgap owing to impurities, but lattice defects can also be involved. A model was first presented by Shockley, Read [29] and Hall [30] (SRH recombination statistics) which is sufficient for most cases. The net recombination rate for a single defect reads

$$R_{SRH} = \frac{pn - n_i^2}{\tau_{p0}(p + p_{1,SRH}) + \tau_{n0}(n + n_{1,SRH})} \quad (2.15)$$

with the characteristic capture times or lifetimes for holes and electrons

$$\tau_{p0} = \frac{1}{v_{th} \sigma_{p,SRH} N_{tr}} \quad \text{and} \quad \tau_{n0} = \frac{1}{v_{th} \sigma_{n,SRH} N_{tr}} \quad (2.16)$$

which are defined by the density of traps (N_{tr}), the respective capture cross sections (σ_{SRH}) and the thermal velocity (v_{th}).

$$p_{1,SRH} = N_V \exp\left(\frac{E_V - E_{tr}}{k_B T}\right) \quad \text{and} \quad n_{1,SRH} = N_C \exp\left(\frac{E_{tr} - E_C}{k_B T}\right) \quad (2.17)$$

are quantities taking the occupation of the trap level into account. The numerator in the exponent relates the energy level of the trap (E_{tr}) to the valence band energy (E_V) and conduction band

energy (E_C). N_V and N_C are the density of states in the valence and conduction band, respectively. The corresponding SRH lifetime is

$$\tau_{SRH} = \frac{\tau_{n0}(p_0 + p_{1,SRH} + \Delta n) + \tau_{p0}(n_0 + n_{1,SRH} + \Delta n)}{p_0 + n_0 + \Delta n} \quad (2.18)$$

The influence of the different parameters in the equations (2.15) to (2.17) on τ_{SRH} are discussed in details in section 5 and 7.

According to equation (2.9) the effective bulk recombination lifetime can be expressed by

$$\frac{1}{\tau_{eff,bulk}} = \frac{1}{\tau_{rad}} + \frac{1}{\tau_{Auger}} + \frac{1}{\tau_{SRH}} = \frac{1}{\tau_{intr}} + \frac{1}{\tau_{SRH}} \quad (2.19)$$

For the results presented in this thesis, the influence of τ_{SRH} can be neglected since high quality float zone silicon was used as substrate material. Hence, the contribution of the absorber to the bulk recombination is limited to the intrinsic recombination processes. However, the measured effective lifetime is influence by the bulk and surface recombination according to

$$\frac{1}{\tau_{eff}} = \frac{1}{\tau_{eff,bulk}} + \frac{1}{\tau_{eff,surface}} \approx \frac{1}{\tau_{intr,bulk}} + \frac{1}{\tau_{defect,surface}} \quad (2.20)$$

Unlike for the bulk, defect recombination at the surface can not be neglected. It follows that the measured effective lifetime for the investigations performed in this thesis is defined by the interplay between the intrinsic recombination in the c-Si bulk and the defect recombination at or near the surfaces of the c-Si wafer.

Defect recombination at the surface

At the surface of the c-Si wafer the crystal lattice is interrupted and neighboring c-Si atoms do not exist. Such a surface or more precisely the interface formed with the adjacent thin film can host a large density of surface states which are continuously distributed over the band gap. The annihilation of excess carriers by recombination is very efficient under such conditions. Accordingly, the surface of the wafer can act as a sink for the excess carriers causing a hole and electron current to flow into this device region. This diffusion current is driven by the reduction of the hole and electron density at the surface via recombination. Basically, the recombination at the surface can be treated similar to bulk. As the total recombination rate is the sum over the contribution from each energy interval the surface recombination rate (R_s) reads [31]

$$R_S = v_{th} (p_s n_s - n_i^2) \int_{E_V}^{E_C} \frac{D_{it}(E) dE}{\frac{(p_s + p_{1,SRH}(E))}{\sigma_{n,SRH}(E)} + \frac{(n_s + n_{1,SRH}(E))}{\sigma_{p,SRH}(E)}} \quad (2.21)$$

With p_s and n_s the hole and electron density at the surface, respectively. Here, the bulk recombination rate (R) having the unit $\text{cm}^{-3} \text{s}^{-1}$ is replaced by a surface recombination rate (R_S) having a unit per area, i.e. $\text{cm}^{-2} \text{s}^{-1}$. Furthermore, the bulk defect density (N_{tr}) is replaced by energy dependent interface defect density (D_{it}) and the capture cross section becomes energy dependence as well.

The influence of the different parameters is discussed in detail in section 5 and 7 but two fundamental strategies exist to minimize R_S . (i) Minimizing the density of defects, i.e. minimizing the density of recombination sites. This is referred to as chemical passivation as it is achieved by the saturation of the silicon dangling bonds with atoms of a passivating thin film. (ii) Minimizing either the hole or the electron density at the surface. In this case the absence of one charge carrier species is limiting the recombination event of the electron-hole pair. This is referred to as field-effect passivation and results from a diffused or induced junction.

Unlike for the bulk the ratio of the excess carrier density at the surface (Δn_s) and R_S is not expressed by a surface lifetime but by the surface recombination velocity (S)

$$S(p_s, n_s) = \int_{E_V}^{E_C} \frac{R_S(E, p_s, n_s)}{\Delta n_s} dE \quad (2.22)$$

To take the modification of the hole and electron density at the surface with respect to the bulk by the diffused or induced junction into account an effective surface recombination velocity (S_{eff}) is introduced. This quantity describes the recombination at a virtual surface at the edge of the depletion region rather than directly at the surface

$$S_{eff}(p_s, n_s) = \int_{E_V}^{E_C} \frac{R_S(E, p_s, n_s)}{\Delta n_{bulk}} dE \quad (2.23)$$

With Δn_{bulk} the excess carrier density in the bulk.

The recombination at the interface formed between a dielectric passivation layer and the c-Si surface is studied extensively in literature, e.g. [32], [33], [27]. The recombination at the interface between a semiconductor (a-Si:H) and c-Si is studied in [19], [21], [34].

The measured effective lifetime for the investigations presented in this thesis is defined by

$$\frac{1}{\tau_{eff}} = \frac{1}{\tau_{intr,bulk}} + \frac{2 S_{eff}}{W} \tag{2.24}$$

where defect recombination at the surface is expressed by the last summand. W it the thickness of the c-Si wafer. The interplay between the intrinsic recombination in the c-Si bulk and the defect recombination at or near the surfaces of the c-Si wafer is investigated in detail in section 5.

2.3 Fundamental considerations on the excess carrier extraction

The thermodynamic losses caused during photovoltaic energy conversion [35], [9], [36] can be illustrated with the help of a band diagram as shown in Figure 2.2a. From the left to the right, a part of the photon’s energy is lost due to cooling down of the photogenerated electron-hole pairs close to the band edges. The mean energy after this thermalization is further reduced by the generation of entropy. The latter is related to the rate of excess carrier generation, recombination and extraction which defines the density the remaining excess carriers [35], [9], [36]. The free energy of the system is than defined by the splitting of the hole and electron quasi Fermi-level (QFL, $E_{f,p}$ and $E_{f,n}$), i.e. the implied voltage (iV) which follows from

$$E_{f,n} - E_{f,p} = iV/q = \frac{k_B T}{q} \ln \left(\frac{(p_0 + \Delta p)(n_0 + \Delta n)}{n_i^2} \right) = \frac{k_B T}{q} \ln \left(\frac{p n}{n_i^2} \right) \tag{2.25}$$

with $\Delta n = \Delta p$. This quasi Fermi level splitting describes how far the excess hole (Δp) and electron (Δn) density deviates from the equilibrium hole (p_0) and electron (n_0) density owing to the interplay between carrier generation, recombination and extraction. Hence, the splitting of the

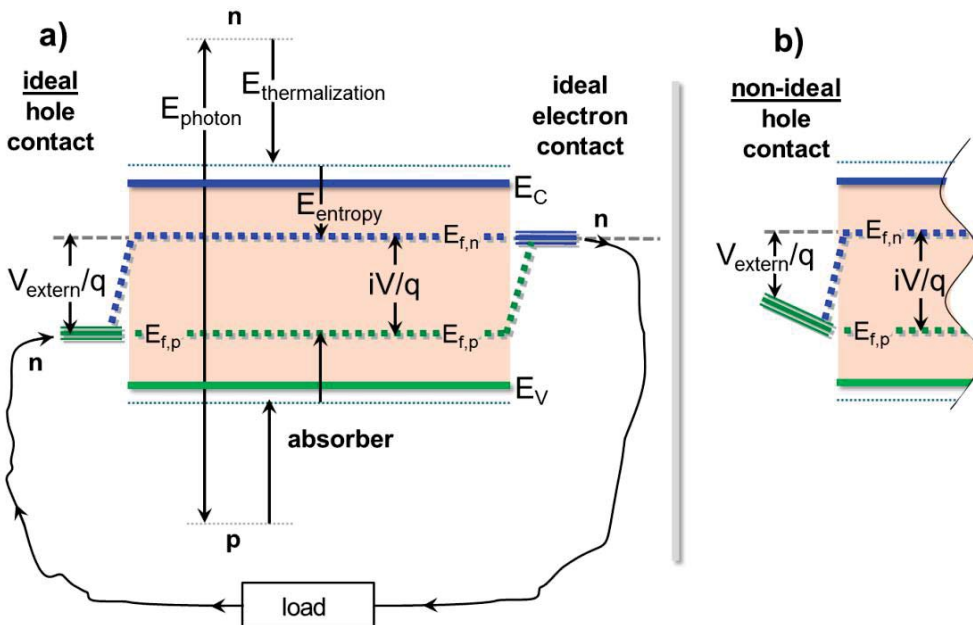


Figure 2.2: a) Graphical representation of thermodynamic losses during photovoltaic energy conversion. Ideal voltage and QFL extraction from the absorber by the hole and electron selective contacts are assumed. b) As an results of a non-ideal voltage extraction at the hole selective contact, the external voltage is below the implied voltage.

Fermi-levels is the main objective of a solar cell.

In principle, losses caused by thermalization can be partly overcome by an appropriate solar cell design (multiple band gaps, hot carrier devices) but are intrinsic losses for a given system. The splitting of the QFL on the other hand, i.e. the excess hole and electron density can be influenced to a large extent. Increasing the density of photo-generated excess carriers, lowering their annihilation by recombination and reducing their flow into the external circuit increases the excess carrier density and thus the QFL splitting. For open-circuit (OC) conditions, when no excess carriers are extracted from the device, the corresponding implied voltage (iV_{oc}) is defined only by the excess carrier density resulting from the balance of carrier generation and recombination. As the carrier generation is more or less constant for a given system, minimizing the recombination losses is of major importance to maximize the excess carrier density and hence the voltage. However, no power is generated at open-circuit conditions as no carriers exit the device, i.e. as no external current flows. For the maximum power point (MPP) conditions, when the product of the external current density (J_{MPP}) and the external voltage (V_{MPP}) has its maximum. The voltage is lower as compared to open-circuit conditions since carriers are extracted from the absorber. For short-circuit conditions the excess carriers are extracted instantaneously from the absorber as they can travel from the electron contact to the hole contact via the external circuit without encountering any resistance. For this conditions no excess carrier remain inside the device. Accordingly, no splitting of the QFLs occurs and no voltage is generated.

For the considerations above (Figure 2.2a), hole and electron contacts have been assumed which ensure the lossless extraction of the hole QFL of the absorber at the hole contact and the electron QFL at the electron contact. This means the implied voltage built up in the absorber can be fully extracted at the external terminals. This is not the case for Figure 2.2b where a significant gradient in the hole Fermi-level in the contact region is indicating a voltage loss in the contact region. It can be seen that the external voltage drops below the implied voltage for such conditions. The ability of a contact to maintain the hole QFL at the hole contact and the electron QFL at the electron contact is defined by hole and electron conductivity in the respective contact region [9]. For the carrier species for which the contact is intended to be selective, the local conductivity must be sufficiently high during operation to guarantee that a negligible gradient in the QFL is needed to drive the respective current into the external electrodes. On the other hand, the local conductivity of the carrier species that shall be blocked must be as small as possible to prevent current to flow of the “wrong” carrier species in the same direction. According to

equation (2.3), this guarantees that the total current at the hole (electron) contact is dominated by the hole (electron) current while the electron (hole) current is negligible. In other words, a strong asymmetry of the local hole and electron conductivity during operation must be ensured. For the experimentally relevant systems, the conductivity is almost exclusively tuned by the carrier density. A sufficient high doping or an induced junction ensure that already during equilibrium a pronounced asymmetry exist. The doping and the induced junction of a hole (electron) contact must be chosen in such a way that the much higher hole (electron) density is also maintained during operation when additional excess electrons (holes) are generated or injected in the contact region.

It should be noted that the claim for the local asymmetry in hole and electron conductivity is similar to one of the basic assumptions that must be fulfilled for the validity of the classical p/n-junction theory [37] and the derived diode equation (discussed below). A basic requirement is that low-injection conditions in the contact region are maintained during operation. This means that the generated or injected minority carrier density must remain small compared to the majority carrier density. If this is expressed in terms of conductivities, for a hole (electron) selective contact it reads – the electron (hole) conductivity must remain small compared to the hole (electron) conductivity.

However, besides maintaining the Fermi-level in the respective contact region, a contact must also enable a high splitting of the QFL in the absorber to ensure that the extractable voltage is on a high level. In this sense, the contact must be optically transparent to enable the generation of excess carriers in the absorber and recombination of the excess carriers must be reduced to a minimum.

However, the way in which a preferred conductivity of either holes or electrons is experimentally realized (e.g. doping, induced junctions) typically comes at the cost of increased recombination losses. Hence, the major challenge with respect to contact engineering is to find a contact system which enables the preferred conductivity of holes and electrons in specific device regions without adding significant recombination losses. For such an idealized contact system the recombination losses of the absorber would limit the efficiency.

In section 4.2 the important aspect of a contact schemes which enable a low recombination, i.e. and efficient surface passivation and more important the selective excess carrier extraction are investigated in detail by numerical device simulations. Section 5 and 6 tackle the surface passivation and the selective excess carrier extraction experimentally, respectively.

It should be noted that besides in the textbook from Würfel [9] the issues of a non-ideal voltage extraction from the absorber is discussed in two PhD thesis from Fraunhofer ISE. Fischer [38] (p. 161) described the problem of a gradient in the hole QFLs for hole contact of homojunction (PERC) cells mathematically. Pysch [22] investigated the hole contact of heterojunction cells. In a recent publication from Würfel *et al.* [39] the issues discussed in a textbook from Würfel [9] are investigated by numerical device simulation providing good overview of this problem.

2.4 Diode equation and J - V parameters

The double-diode model

For well working devices the illuminated current-voltage (J - V_{light}) characteristic can be approximated by the dark forward current-voltage (J - V_{dark}) characteristics of the p/n diode from Shockley [40] and Sha *et al.* [41] which is shifted by a voltage independent photo-generated minority carrier current (J_{ph}) [42], [43]. This is illustrated in Figure 2.3a and expressed by

$$J(V) = J_{0,1} \left[\exp \left(\frac{q(V - J(V)R_s)}{n_1 k_B T} \right) \right] + J_{0,2} \left[\exp \left(\frac{q(V - J(V)R_s)}{n_2 k_B T} \right) \right] + \frac{V - J(V)R_s}{R_p} - J_{\text{ph}}. \quad (2.26)$$

The corresponding equivalent circuit is shown in Figure 2.3b. The dark characteristic of the p/n-junction is described by the first three summands in the equation above. The voltage independent photo-generated excess carrier current (J_{ph}) is given by the last summand. The rectifying behavior of the junction and the exponential dependence of the current on the applied terminal voltage for forward biasing are determined by the first two summands. The third summand takes current losses by an ohmic shunt resistance (R_p) into account. The reduction of the terminal voltage by an ohmic series resistance (R_s) is considered by the second summand in the numerator of the first three summands.

According to the general explanation of a p/n-junction, for the case that a positive voltage is applied. Majority carriers from the p-type material (holes) will flow in the n-type material and vice versa. Once the other part of the junction is reached these carriers are minority carriers which eventually recombine. This is the cause for the recombination driven forward current over the junction which increases exponentially with the voltage. For the solar cell this current is representing a parasitic current (red in Figure 2.3a) as it is competing with the voltage independent current of the photo-generated excess carriers (blue in Figure 2.3a). The superposition of both yields the actual J - V_{light} characteristic. Equation (2.26) reveals that a low recombination current calls for minimizing the recombination current prefactors (J_0) while the

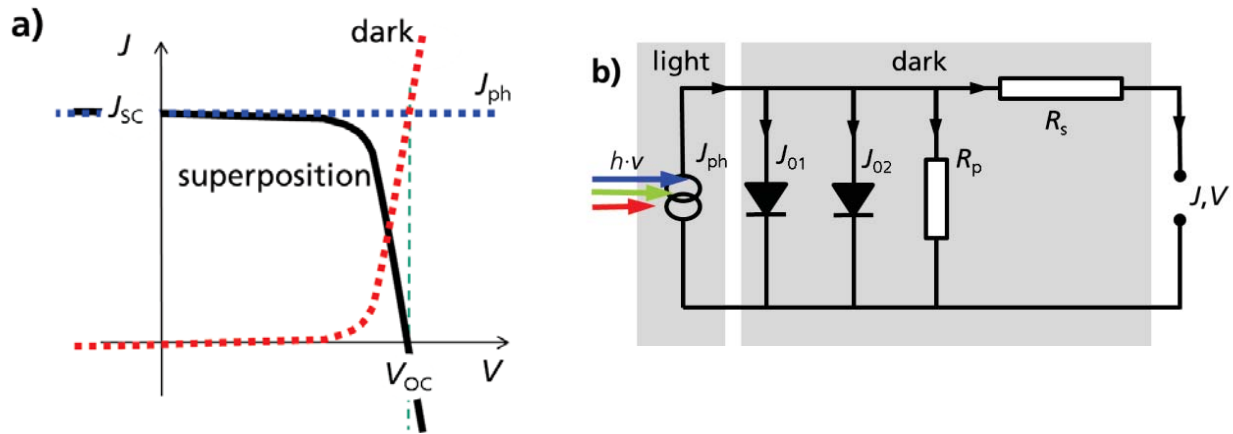


Figure 2.3: a) Schematic of illuminated solar cell J - V curve (black) that results from the superposition of voltage independent J_{ph} (blue) and dark J - V characteristic (red). b) Equivalent circuit. The current source delivers the photo-current which is partly bypassed and lost by different recombination mechanisms described by the diodes and the current lost by the parallel resistance. A voltage drop occurs at the series resistance and the remaining current and voltage are available as output power.

ideality factors (n) [44] influence the slope of the exponential increase of the parasitic current. Two different J_0 and n values are considered to take two different recombination path into account. They are chosen in such a way that the first summand describes the regime of higher voltages where the recombination current is in the range of J_{ph} . This characterizes the recombination dominating the open-circuit conditions. The second summand describes the recombination current for lower voltages where the recombination current is moderate. $J_{0,2}$ is representing the dominant recombination near MPP conditions. It should be noted that recombination currents lump together the recombination occurring in the bulk of the junction region and at its surface. Similar to the definition used for S_{eff} in equation (2.23), the recombination currents can be expressed by a currents into a virtual surface at the edge of the depletion region rather than directly at the surface. It reads

$$J_{rec} = J_0 \left[\exp\left(\frac{q iV}{k_B T} - 1\right) \right] = J_0 \frac{p n - n_i^2}{n_i^2} = J_0 \frac{(p_0 + \Delta n)(n_0 + \Delta n)}{n_i^2} \approx J_0 \frac{p n}{n_i^2} \quad (2.27)$$

where iV is the QFL splitting at the edge of the depletion region, i.e. the implied junction voltage. The latter is linked to the product of the local hole and electron density which in turn follows from the local equilibrium hole and electron density which is defined by the diffused or induced junction (p_0, n_0) and the excess carrier density. A basic assumption for the applicability of the diode model is that this junction voltage matches the terminal voltage in equation (2.26). For an excellent overview on the strategies to minimize J_0 and hence the recombination currents taking

the peculiarities of both homojunction and heterojunctions into account is referred to Ref [16] and for more recent consideration to Ref [45].

Finally, it should be noted again that one requirement for the validity of equation (2.26) is that low-injection condition in the contact region are maintained during operation. In other words, that the implied junction voltage from equation (2.27) is maintained in the junction region such that the terminal or external voltage matches the implied junction voltage (Figure 2.2a). If this is the case the cell characteristic is defined solely by the “classical” recombination and ohmic transport losses as described by the diode model. However, an important aspect of this work are “non-classical” recombination and transport losses. As will be shown, for such conditions the external voltage can drop below the implied junction voltage (Figure 2.2b) and equation (2.26) fails to describe the J - V characteristic properly.

A simple approach for the identification of such effects is to check for characteristic features of the cell characteristics which reveal that the cell does not obey the standard p/n-junction theory and the diode equation. To this end, the illumination level and temperature dependence of the cell characteristic are investigated in section 6.

Parameters of the J - V_{light} characteristic

Three fundamental parameters and working condition are used to analyze the J - V_{light} characteristic (Figure 2.4). For the short-circuit (SC) condition no power ($P = VJ$) is generated as the external voltage is zero. Almost all carriers can exit the device, thus the lowest excess carrier density within the device is observed. The short-circuit current (J_{sc}) equals the generation current (J_{ph}) from the whole device reduced by the recombination current at zero voltage as can be derived from equation (2.26). The J_{sc} is the current of the photo-generated minority carriers

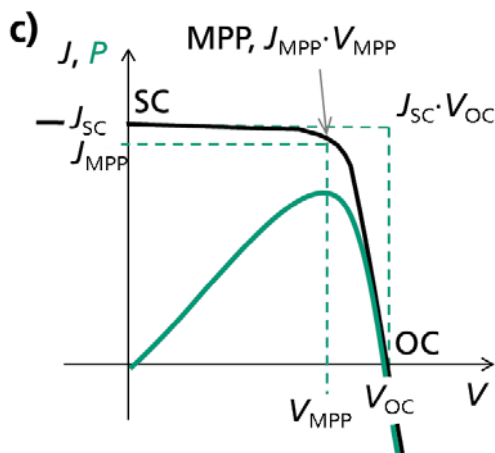


Figure 2.4: Illuminated J - V (black) and P - V (green) characteristics and the relevant working conditions.

which managed to survive the journey from their place of generation to the separating junction. For forward biasing the recombination currents increase which means that J_{ph} is reduced by the latter (Figure 2.3a). Hence, the external current of the solar cell is reduced. For a low external voltage the parasitic current via R_p is typically dominating over the recombination currents. The most efficient working condition is obtained for the maximum power point (MPP) where the product of external voltage (V_{MPP}) and current (J_{MPP}) has its maximum (green line in Figure 2.4). For further forward biasing open-circuit (OC) conditions are reached when the recombination currents eventually match J_{ph} (Figure 2.3a). No external power is generated for this condition as no carriers exit the device ($J = 0$). The highest carrier density within the device is observed and all generated carriers must recombine in the device. Equation (2.26) reveals the MPP and OC conditions are shifted to higher external voltages the lower the recombination currents are. Consequently, low J_0 's are mandatory to ensure a high V_{MPP} and V_{oc} .

The ratio of power at MPP (P_{MPP}) and the input power from illumination (P_{in}) defines the efficiency (η) for the conversion of radiative in electrical power by the solar cell

$$\eta = \frac{P_{MPP}}{P_{in}} = \frac{J_{MPP} V_{MPP}}{P_{in}} = \frac{J_{SC} V_{OC} FF}{P_{in}} \quad (2.28)$$

where FF is the fill-factor. It is defined by the ratio of maximum power output of the device and the product of J_{sc} and V_{oc}

$$FF = \frac{P_{MPP}}{V_{OC} J_{SC}} = \frac{V_{MPP} J_{MPP}}{V_{OC} J_{SC}} \quad (2.29)$$

It describes the "squareness" of the J - V curve and is a measure for the transport and recombination related losses. In this work, rather than maximizing the efficiency, minimizing and understanding this transport and recombination related losses is of major concern. Accordingly, the FF plays an important role in this thesis.

2.5 Alternatives to homojunctions – basic concepts and history³

A brief overview of the existing alternatives to homojunctions is presented in the following. These approaches share the basic characteristic that the p/n-junction or the high/low-junction are not formed by doping of the absorber but rather by a junction which is induced into the absorber. This is achieved by a suitable layer or layer stack which is deposited or grown on top of the c-Si surface. For example, for the hole selective contact of an n-type c-Si absorber the surface becomes inverted if a film with a high work function is placed on top of the absorber. This results in a highly hole populated c-Si region similar to the case for a p-type doping close to the absorber surface. The absence of the highly doped c-Si regions and the possibility to provide a passivation of the c-Si surface provides the decisive advantage in terms of minority carrier recombination while maintaining the rectifying properties of the classical p/n-junction and high/low-junction. In other words the metallurgical heterojunction induces a homojunction within the c-Si absorber and passivates the surface of the absorber while allowing for an efficient transport of carriers into the electrode. This is the reason why the J - V characteristic of properly designed induced junction devices can be described by equation (2.26) which is, strictly speaking, derived for a homojunction formed by the doping of the absorber surface. A good overview on such induced junction devices is given in Ref [46]. A large group of devices can be assigned to this class of solar cells ranging from metal-semiconductor (MS) and metal-insulator-semiconductor (MIS) to semiconductor-insulator-semiconductor (SIS) like approaches.

Discovery of the heterojunction

The application of heterojunctions for electronic devices was proposed in the 1950s by Shockley [47] in order to overcome the given limitations for homojunctions. In contrast to homojunction devices where engineering of the material and junction properties is limited to the doping type and profile as well as the device geometry, heterojunction device engineering quickly proved to have unprecedented degrees of freedom.

The heterojunction approach applied to solar cells is somewhat inspired by the heterojunction transistor first proposed by Shockley in 1951 [47] and in 1954 discussed in detail by Kroemer [48]. The latter received the Nobel prize in 2000 for “developing semiconductor heterostructures

³ A good overview on the fundamentals and the history of silicon based heterojunction solar cells with contacts made of a-Si:H is given in the book from van Sark *et al.* [15]. The review paper from De Wolf *et al.* [3] is also recommended to the reader.

used in high-speed and opto-electronics”. The advantage of a heterojunction over a homojunction for a transistor was summarized by Kroemer as;

“In order to obtain a low ratio of electron to hole current (which means a high selectivity of the contact, in this case to holes), it is necessary in a semiconductor with constant band gap to dope the p-side of the junction much more heavily than the n-side. There are practical limits, however, as to the magnitude of doping possible, and there are situations where a high doping of the emitter is undesirable for other reasons. In all cases, an improvement could be obtained if the injection deficit (which means the opposite of selectivity) could be decreased by other means instead of, or in addition to, the high doping.” [48]

“The underlying central principle is the use of energy gap variations beside electric fields to control the forces acting on electrons and holes separately and independently of each other. The resulting greater design freedom permits a re-optimization of doping levels and geometriesBy a judicious combination of energy gap variations and electric fields it then becomes possible, within wide limits, to control the forces acting on electrons and holes, separately and independently of each other, a design freedom not achievable in homostructures.” [49]

In Figure 2.5a the band diagram of such a wide-gap emitter is shown. It can be seen that the higher E_g of the p-type emitter adds an additional barrier for the electrons from the n-type base without changing the doping of the emitter region and without influencing the hole current from the emitter in the base. In this case the additional barrier in the conduction band results from a

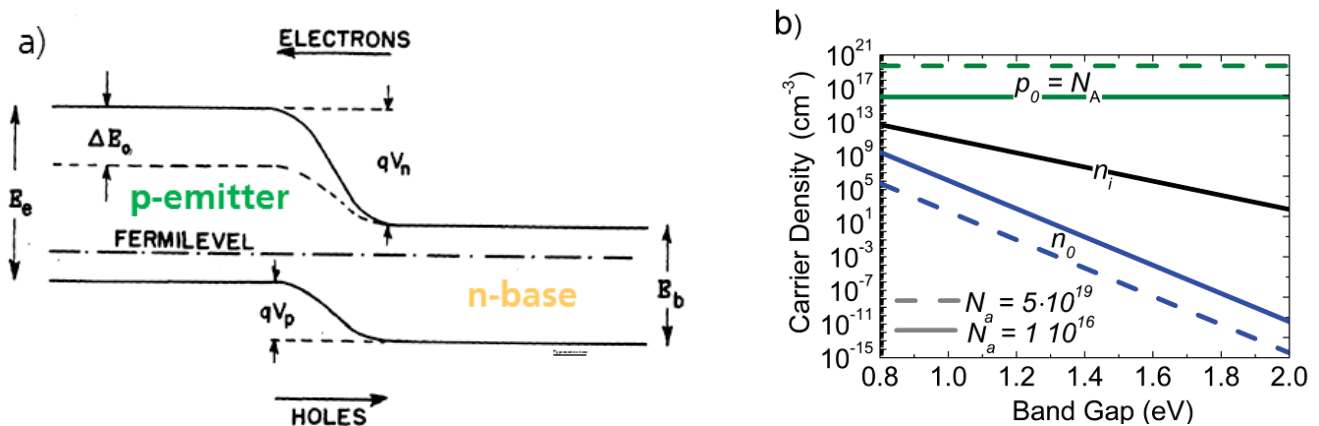


Figure 2.5: a) Band diagram of wide-gap p-type emitter adapted from [48]. The higher band gap, more precisely the lower electron affinity, adds an additional barrier for the electron flow into the emitter. A non-abrupt heterojunction, obtained by a graded electron affinity is assumed here. This is in contrast to the sharp conduction band offset that results from an abrupt hetero structure. b) Dependence of intrinsic carrier density and the equilibrium hole and electron density on the electrical band gap for two different p-type doping levels.

graded electron affinity which is increasing towards the base. Another significant advantage of the wide gap layer that is not apparent from this graph is that its intrinsic carrier density is lower compared to a material with a lower band gap. The drop of n_i with increasing band gap (E_g) reads

$$n_i = \sqrt{N_V N_C} \exp\left(\frac{-E_g}{2 k_B T}\right) \quad (2.30)$$

According to $n_i^2 = p_0 n_0$ and $n_0 = n_i^2 / p_0 = n_i^2 / N_A$ the electron density and hence electron conductivity is decreased in the p-type emitter. This also means that the asymmetry of the hole and electron conductivity in the hole contact region is more pronounced. It results in a lower electron (or recombination) current according to

$$J_0 = \frac{q n_i^2}{p_0} S_0 = q n_0 S_0 \quad (2.31)$$

which improves selectivity of the contact to holes in addition the heterobarrier. It means that besides increasing the hole density by doping (or an induced junction) increasing the band gap offers another degree of freedom to lower the parasitic electron current. The modification of the asymmetry of the hole and electron density, i.e. the reduction of the electron density by the increase of E_g and p-type doping is shown in Figure 2.5b.

It should be noted that unlike the current III-V heterojunction device (transistors, LEDs, solar cells) for silicon heterojunction solar cells the junction is not formed between two high quality crystalline materials. While the silicon absorber can be a quality crystalline material, this is typically not the case for the contacting thin films. These are either amorphous or contain a certain crystalline fraction. The abundance of defects in such materials leads to doping efficiencies, mobilities, lifetimes and diffusion length which are much lower compared to a crystalline material. Hence, another distinction to III-V devices is that the reduction of recombination at the metallurgic interface is not based on lattice matching but on an amorphous buffer layer for which hydrogen and oxygen atoms are involved in the chemical passivation of the interface. In addition, compared to the III-V systems fewer degrees of freedom exist to tune the material and the heterojunction properties.

SIPOS and poly-silicon emitters:

The most prominent (but not the first) transfer of a heterojunction from a silicon based heterojunction bipolar transistors (HBT) [51] (1979, Sony) to a silicon based solar cell was done in 1984 by Yablonovitch *et al.* which nicely showed the very low recombination and high V_{oc} potential of such a contact scheme [50].

“... a narrow band-gap active layer (the absorber) is sandwiched between two wide band-gap layers of opposite doping It is usually assumed that the wide band-gap heterocontact layers must be single crystal and lattice matched to the active layer to assure high performance. While this has been very successful for the III-V class of semiconductors, it is not actually a necessary condition. The wide band-gap layers need only be of sufficient electronic quality to support the quasi-Fermi level separation in the high quality narrow-gap active layer. Due to its larger band gap, the heterocontact material may be disordered and of poor quality and still be able to support the voltage generated in the active layer (i.e. maintain a constant majority carrier Fermi-level in the wide band gap layer). That is the key point. The other main point is that the interface states at the heterocontacts must be passivated.”

A very high V_{oc} of 720 mV was obtained thanks to a passivating and carrier selective n-doped SIPOS (semi-insulating polycrystalline silicon [poly-Si]) emitter for the structure shown in Figure 2.6a while the aspect of an efficient current extraction (FF) and parasitic absorption remained unknown.

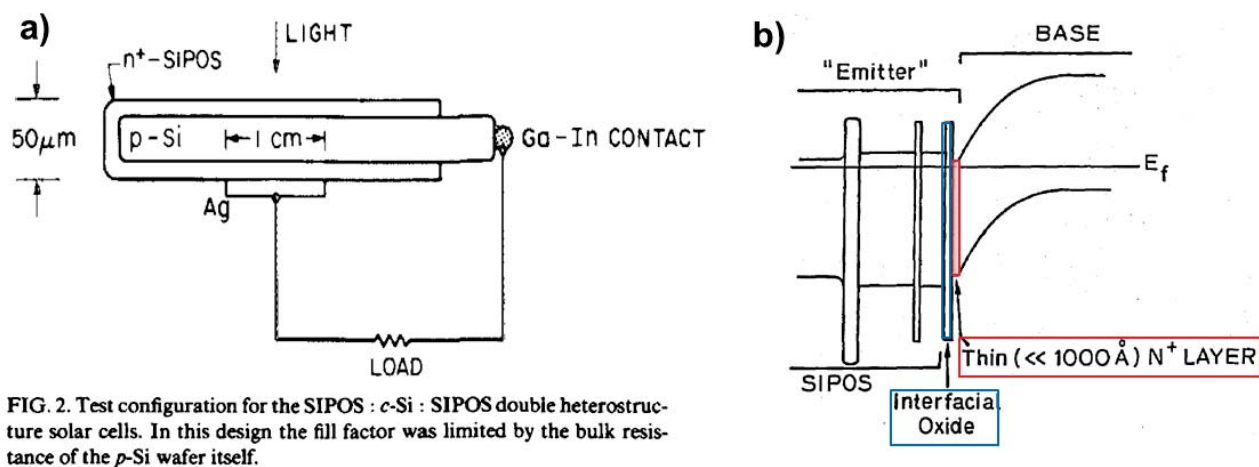


FIG. 2. Test configuration for the SIPOS : c-Si : SIPOS double heterostructure solar cells. In this design the fill factor was limited by the bulk resistance of the p-Si wafer itself.

Figure 2.6: a) SIPOS “test structure” and caption reproduced from [50]. b) Band diagram of SIPOS emitter from [16]. The oxide at the SIPOS / c-Si interface and the n⁺ region that results from out diffusion of donor impurities from the SIPOS are highlighted in blue and red, respectively.

However, it should be noted that, as well as for a poly-Si, depending on the thermal budget applied during processing the out diffusion of doping impurities into the absorber might lead to the formation of a lightly doped and shallow homojunction [16] as sketched in Figure 2.6b. In this case the SIPOS serves the purpose of a doping source that remains an active part of the device, i.e. is not removed. It is featuring the unique property of providing a c-Si surface doping that is sufficient high to form a junction but low enough to prevent the detrimental effects associated with commonly applied doping schemes, e.g. increased Auger recombination, band gap narrowing and a less efficient passivation of highly doped surfaces. The interfacial oxides provides excellent passivation of this lowly doped (or undoped) electrically transparent diffused (or induced) emitter. At the same time, thanks to its high band gap and low n_i , SIPOS is eliminating the recombination at the metal / SIPOS interface. For the case without out-diffusion the structure corresponds to an SIS like structure featuring an induced junction. For the case with out-diffusion it might be described as an buried homojunction [14] or an MINP structure (more below) where the oxide and the high band gap SIPOS are passivating the shallow homojunction underneath.

Recent results from Fraunhofer ISE [52] and ISFH [53], [8] connect to the pioneering work of poly silicon based contacts [54], [55], [56], [57]. The TOPCon (tunneling oxide passivated contact) scheme developed by Feldmann et al. at ISE [45] could demonstrate that carrier transport and efficiency can be excellent for such contact schemes. It should be noted that the investigations performed in this thesis contributed significantly to the TOPCon development which is evidenced by the publication list in the appendix.

Conductor-insulator-semiconductor stacks

Adapted from the working principle of the metal-oxide-semiconductor field effect transistor (MOS-FET) induced junctions bases on the conductor-insulator-semiconductor approach (CIS) [46] like the MIS [58], [59] and SIS [60] structure were applied to silicon solar cells. Back in 1974 Green *et al.* [58] and Shewchun *et al.* [59] showed that for a “pinned” MIS devices a minority carrier (of the absorber) selective Schottky contact [61] can be formed by the application of a metal featuring a suitable work function. Basically, for the hole selective contact a material is need which enables a high work function close to the valence band of the absorber to induce a highly hole populated (p^{++}) surface region. For the electron selective contact a material is need which enables a low work function close to the valence band of the absorber to induce a highly electron populated (n^{++}) surface region. Hence, for these devices the function of the doped c-Si

region, i.e. the modification of the conductivity in the contact region, is fulfilled by the gate material. This can be either a metal, a metal like and degenerately doped semiconductor (e.g. TCO) or a highly doped semiconductor (e.g. poly-Si) featuring suitable work function. In 1980 Shewchun *et. al.* [60] showed that MIS and SIS are basically one and the same type of device. It was shown that a substantial inversion of the c-Si surface and thus a high concentration of the absorbers minority carriers remained for non-equilibrium conditions, i.e. for a forward bias. For such a device, the J - V characteristic is similar to that of a p/n-junction formed by the opposed doping of the absorber, i.e. a homojunction. A schematic of an MIS cell is presented in Figure 2.7a. The benefits of MIS cells were outlined by Godfrey *et al.* in 1979 [62];

“It has been shown that a class of metal- thin-insulator (< 30 Å)-semiconductor (MIS) contact has electronic properties identical to an “abrupt one-sided” p-n junction diode. New experimental support for this mode of operation has recently been described. This class of MIS cell has advantages over actual p-n junction diodes as used in solar cells in three areas:

- (a) lower-temperature processing giving longer lifetimes in completed devices;*
- (b) collecting junction located right at the surface;*
- (c) elimination of heavy doping effects obtained with diffused junctions.*

It has been suggested that these advantages could lead to more efficient cells than diffused cells.”

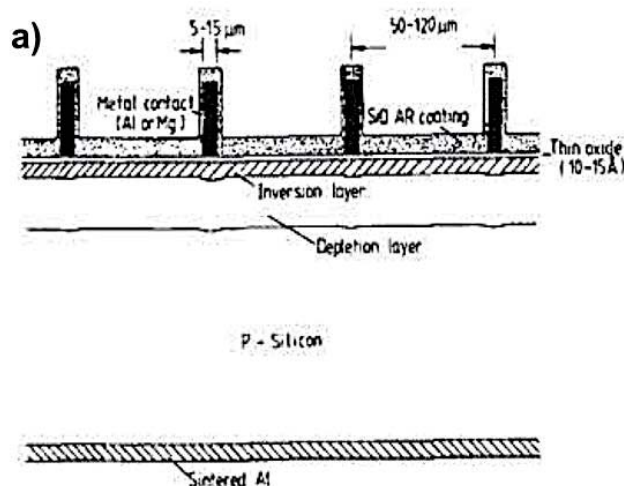


FIG. 1. Schematic diagram of the MIS solar-cell structure as used in this work. The SiO layer not only acts as an AR coating but also induces an inversion layer in the regions between the top grating lines.

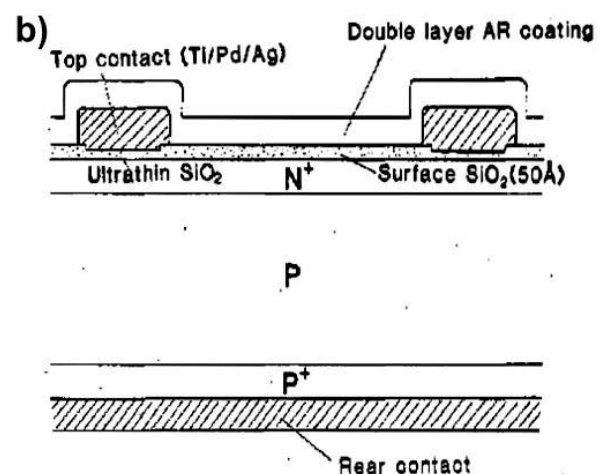


Fig. 1. Cross section of the high-voltage high-efficiency cells described in the text. Major features are the use of thin oxides to passivate the top surface of the cell, a double-layer antireflection coating, and plated metallization.

Figure 2.7: a) MIS cell and captions reproduced from [62]. b) MINP cell and captions reproduced from [63]

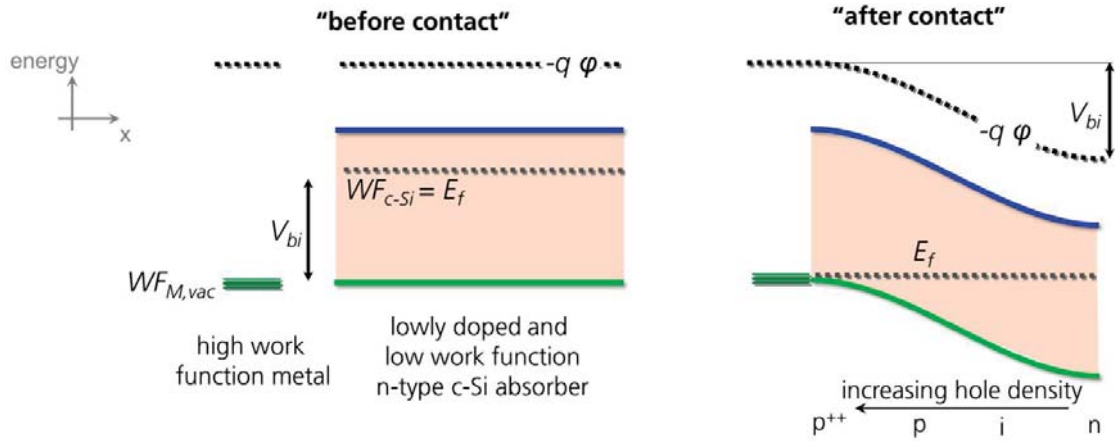


Figure 2.8: Band diagram before and after contact formation between a high work function metal and a n-type c-Si absorber. The Schottky limit is assumed here where Fermi-level pinning is neglected. The work function difference between both materials defines the induced band bending. The screening length in the metal is negligible due to its very high free carrier density. Hence, most of the band bending is screened in the lowly doped c-Si where an inverted and highly hole populated device region is formed.

The ultra-thin tunneling oxide sandwiched between the gate material and the absorber is a vital part of the devices as it provides chemical passivation of the inverted or accumulated c-Si surface. However, to enable an efficient tunneling transport its thickness should not exceed 20 Å [64]. Another important aspect of such tunneling dielectrics is that they reduce the parasitic Fermi-level pinning compared to the bare c-Si surface [65]. The latter is a basic requirement to prevent that actual work function is pinned, typically to near mid-gap. Hence, one of the major concerns of induced junction devices is not only to find contact materials with suitable work functions but also to ensure that Fermi-level pinning is reduced to a minimum. This is analogous to the problem of the modification of the Schottky barrier height by surface effects which is well known from other induced junction devices [66], [67]. To describe the effective work function difference which defines the induced band bending (ϕ_{c-Si}) and the built-in potential of the induced junction (V_{bi} , see also Figure 2.8), the standard formula for the Schottky barrier height is slightly modified. The electron affinity of the c-Si absorber is replaced by the work function of the absorber (WF_{c-Si}) which leads to

$$V_{bi} \approx \phi_{c-Si} \approx WF_{M,eff} - WF_{c-Si} = S (WF_{M,vac} - E_{CNL}) + E_{CNL} - WF_{c-Si}. \quad (2.32)$$

$WF_{M,vac}$ is the bulk or vacuum work function of the contact material (e.g. metal) which is pinned to a material specific surface energy which is typically close to mid-gap (the charge neutrality level, E_{CNL}). S is a the slope parameter which describes to which extent $WF_{M,vac}$ is pinned to E_{CNL}

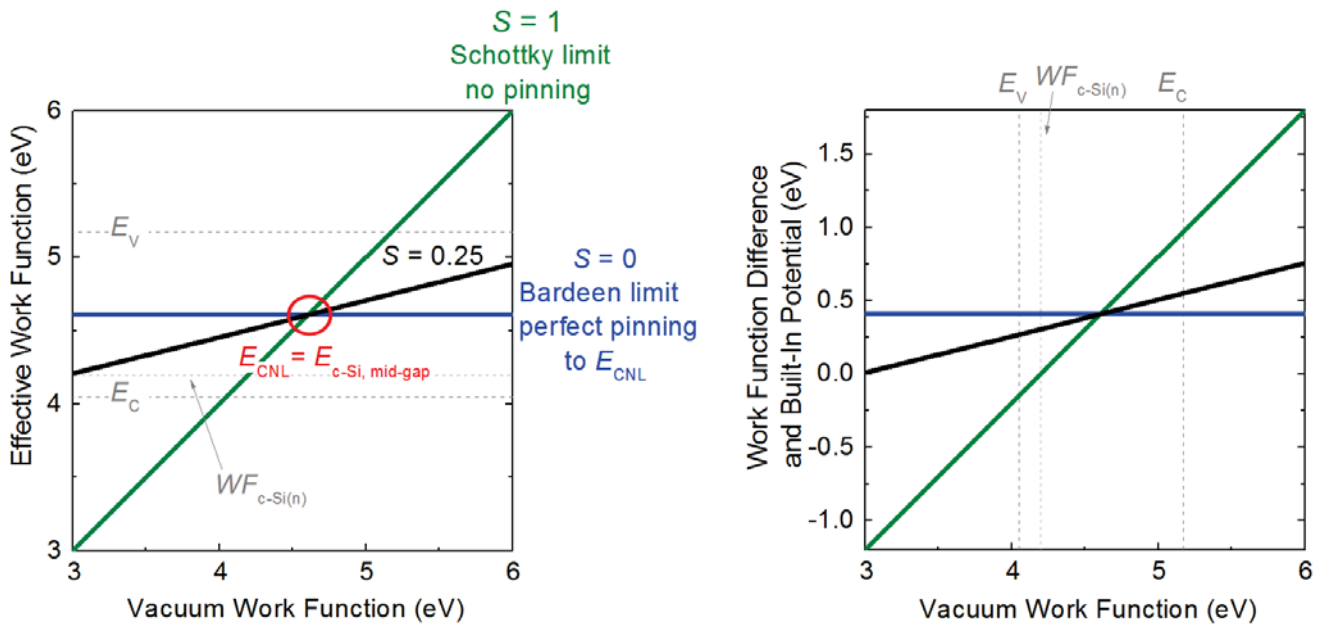


Figure 2.9: Left, dependence of effective work function at the interface on the vacuum work function of the contact material for the three cases discussed in the text. Right, the corresponding built-in potentials and work function difference. Latter obtained by subtracting the effective work function in the left graph by the work function of the c-Si (4.2eV) according to equation (2.32).

(see Figure 2.9). $S = 1$ describes the Schottky limit of no pinning where $WF_{M,eff}$ matches $WF_{M,vac}$. $S = 0$ corresponds to the Bardeen limit of pinning to E_{CNL} . $S = 0.25$ is an experimentally obtained value discussed in section 6. In terms of work function engineering this means that not only $WF_{M,vac}$ must be close to the valence / conduction band of the absorber. S must be close to unity as well. In principle, if the latter is not fulfilled E_{CNL} must be close to $WF_{M,vac}$ to yield a high effective work function difference. However, E_{CNL} can hardly be tuned experimentally. This illustrates that work function engineering goes beyond choosing an appropriate contact material, i.e. $WF_{M,vac}$ and that the surface properties and interactions have to be taken into account as well [66], [67]. For example, as mentioned before adding a thin electric layer is known to increase S which relaxes the demands on $WF_{M,vac}$ and hence the choice of the applicable contact materials.

Further requirements on the contact layer / stack are a high transparency for the relevant spectrum and a sufficient vertical and lateral conductivity. For the MIS cell shown in Figure 2.7a, the metal electrode is only locally applied but the high sheet resistance of the induced junction requires a very dense spacing of the grid electrode. The lateral transport can be improved to some extent if dielectrics featuring a suitable fixed charge are applied which induce a junction also in-between the local metal grid electrode.

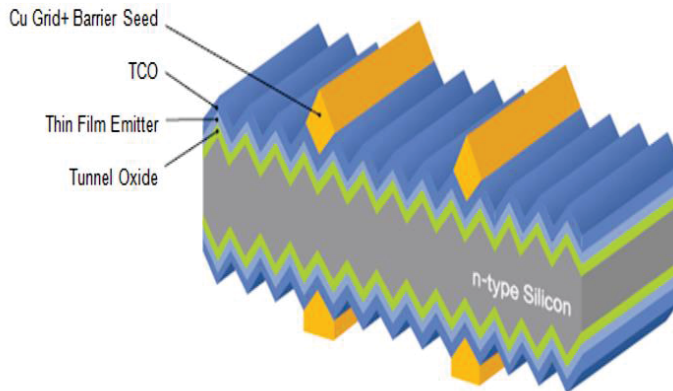


Figure 1: Schematic Diagram of a Triex[®] Solar Cell.

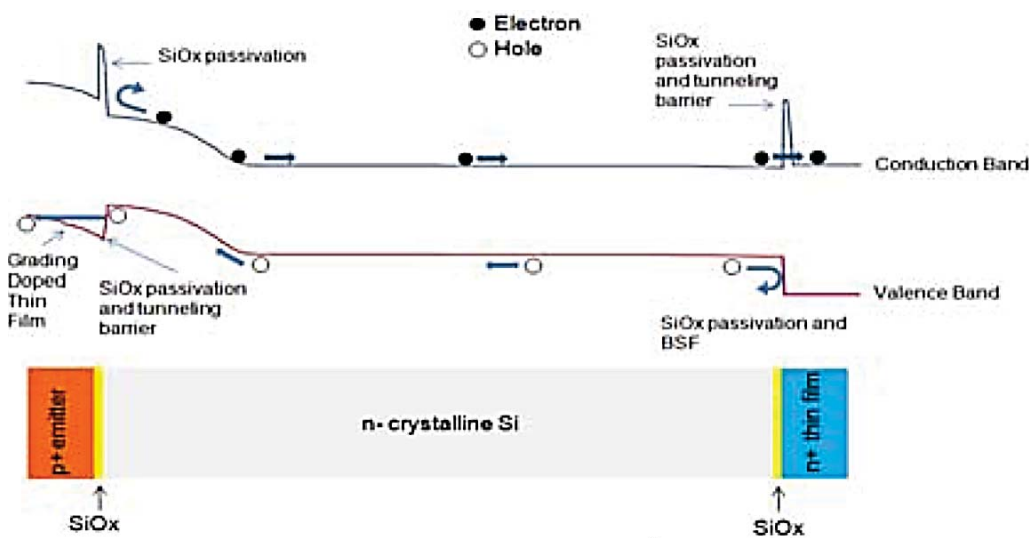


Figure 2: Band Diagram of a Triex[®] Solar Cell.

Figure 2.10: Top, cell design from SILEVO showing the tunneling oxide in-between the c-Si absorber and the “thin film emitter”. Bottom, band diagram showing the SiOx passivation layer and the graded doping of the thin film. Reproduced from [68]

Encouraging results from the company SILEVO were presented recently [68]. While not fully disclosed, it is claimed that an MIS approach for the cells is used. Comparing the SILEVO cell (Figure 2.10) to the so-called HIT-cell (Figure 2.11 and Figure 2.12b), for the SILEVO cell the passivating buffer layer is made of silicon dioxide and it is featuring a silicon-based thin film with a graded doping. The latter is undoped and hence less defective near the SiOx / c-Si interface but highly doped close to the TCO electrode. The high doping induces the junction into the c-Si and ensures an efficient tunneling transport into the TCO. For the amorphous silicon based heterojunction solar cells (Figure 2.12b) an additional SiOx is not needed/applied and a two layer stack of amorphous silicon are used. An undoped and less defective amorphous silicon film near the c-Si serves as the buffer layer. On top a highly doped film is deposited to form the junction with the c-Si and the TCO.

MIS or SIS contacts can also be applied to homojunction solar cells where the actual c-Si junction is already formed by diffusion. The main purpose is to provide passivation of the metal /semiconductor regions while maintaining an efficient carrier extraction from the doped c-Si region. Such contacts are featuring a tunneling oxide and might be assigned as passivating Schottky contacts. A MIS approach is used e.g. for the metal-insulator-np junction (MINP) cell [69],[63] which is sketched in Figure 2.7b. However, combining a good interface passivation of the highly doped c-Si and a sufficient carrier transport is far from easy and calls for a high degree of control over the thickness and quality of the tunneling dielectric. It was shown recently in Ref. [70] that the onset of surface passivation falls together with a significant increase of the contact resistivity for a thermally grown SiO₂ and ALD Al₂O₃ thickness of about 22 Å and 16 Å, respectively. These values are in good agreement with the result from Shewchun *et al.* [60] who could show that for MIS or SIS cells on undoped c-Si surfaces the thickness of the dielectric should be below 20 Å to avoid tunneling-limited operation, i.e. allow for an efficient carrier extraction from the c-Si absorber.

A rather recent approach is the application of the organic/inorganic hetero structure including c-Si as the absorber material. Efficiencies above 12 % have been reached for lab-type devices so far (e.g. [71],[72], [73]). The application of a III-V material / silicon hetero structure might be another appealing approach. The applicability of gallium phosphide as emitter for single junction solar cells is discussed on the basis of numerical device simulations in Ref. [74].

Unfortunately, approaches which relay on schemes adapted from microelectronics (MOS-FET, HBT, etc.) could not prove their suitability for industrial production yet. Hopefully the applicability of such approaches for the next generation silicon solar cells and their relevance to the PV industry will be demonstrated in the near future.

2.5.1 Amorphous Silicon / Crystalline Silicon Heterojunction

A heterojunction approach which could already proof a very high efficiency on industrial scale is the structure formed between amorphous silicon (a-Si:H, $E_g \sim 1.7$ eV) and c-Si absorber ($E_g \sim 1.1$ eV). It was successfully applied to solar cells by Sanyo (now Panasonic) in 1992 [76] and is known as the HIT (heterojunction with intrinsic thin layer) solar cell which is sketched in Figure 2.11. However, pioneering work started back in 1974 by Fuhs *et al.* [77]. Whilst the approaches discussed above could benefit considerably from the experience gained from transistors and optoelectronic devices, this SHJ approach is strongly related to silicon based thin film solar cells from which the carrier selective contacts (doped and undoped SiTFs) and the TCO electrode are adapted. For such devices a hetero structure between a-Si:H / alloyed a-Si:H, a-Si:H / μ c-Si:H and a-Si:H / poly-Si was presented e.g. by Hamakawa *et al.* in 1983. Different absorber materials were discussed in this publication as well. It is worth mentioning that the early wafer based a-Si:H / c-Si SHJ cells from Sanyo were produced on both mc-Si and c-Si absorber material [78]. The V_{oc} of the early a-Si:H / c-Si cells from Sanyo was only about 600 mV, yet an efficiency of 18.1 % has been achieved for monocrystalline absorbers.

Taguchi *et al.* [79] motivated this silicon based heterojunction approach by;

“The most prominent features of the HIT solar cell can be summarized as follows.

1. *Simple structure: A high efficiency can be obtained with no complicated structural techniques, such as partly heavy doping or a partial oxidation method.*
2. *Simple low temperature process: Due to the simple structure, the process is very simple and cost effective. In addition, the process temperature is so low (<200°C) that degradation of the minority carrier lifetime for the substrate is negligible even for low-quality Si materials.*
3. *Simultaneous realization of surface passivation and p-n junction: With the insertion of a very thin intrinsic a-Si layer at the a-Si/c-Si heterojunction, surface recombination is*

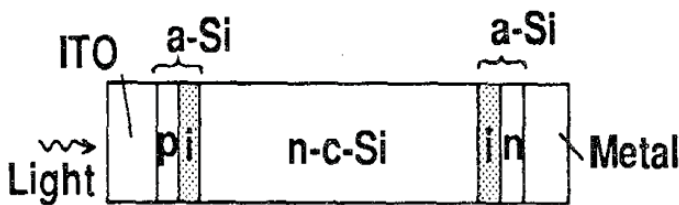


Figure 9. HIT structure on both sides of the cell.

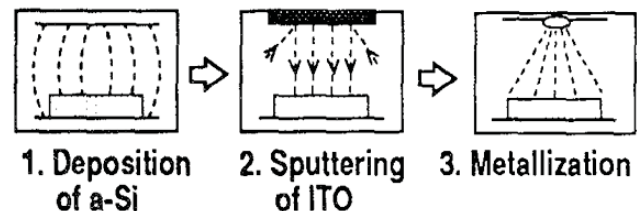


Figure 6. Process sequence of HIT solar cells.

Figure 2.11: Sony HIT cell (left) and process flow (right) reproduced from [75]. The process flow is simplified as, e.g. texturing of the wafer and cleaning of the wafer prior a-Si:H deposition and formation of the grid electrode have been omitted.

drastically suppressed. Therefore, during the junction fabrication process, good surface passivation on the c-Si surface is also realized.

4. The BSF structure can be realized with the same process: The HIT structure is also suitable for fabricating the Back Surface Field (BSF) structure. The same process with a different impurity can be used to obtain the BSF structure and good surface passivation.

5. Stability: The Staebler-Wronski effect, which is seen in a-Si based solar cells, is not seen in the HIT Cell. This is probably due to the fact that the a-Si layers are very thin and contribute little to the power generation. Besides the degradation of the carrier lifetime caused by the metastable defect related to the boron-oxygen complex does not apply to the HIT cell which uses phosphorous doped CZ Si.

6. Improved high-temperature performance: One disadvantage of c-Si solar cells for practical use is their poor high-temperature performance compared with a-Si solar cells. The HIT cell, which has both a-Si and c-Si, shows an improved high-temperature performance. ... The HIT cell has better temperature dependence than the conventional p-n diffused cell. ...The HIT cell showed 8.8% higher output power under this condition”.

Impressive improvements have been achieved in the last two decades. In 2013 Panasonic and Kaneka have presented champion cells from their R&D lines featuring excellent efficiencies of 24.7 % [80] and 24.2 % [5] on large area, respectively. The cell parameters from the Panasonic HIT cell and the homojunction champion cell from the UNSW and SunPower are shown in Table 2-1, the respective device design is sketched in Figure 2.12. A comparable and very high

Table 2-1: Cell parameters of very-high efficiency silicon solar cells.

device	grid electrode	structuring / alignment	area (cm ²)	V _{oc} (mV)	J _{sc} (mA/cm ²)	FF (%)	η (%)
Panasonic / HIT [80]	screen printing	w/o	101.8	750	39.5	83.2	24.7
UNSW / PERL [81]	photolithography, PVD + plating	photolithography	4	706	42.7	82.8	25.0
SunPower / Gen 3 [82]	applied schemes unknown + plating	applied schemes unknown	155.1	721	40.5	82.9	24.2

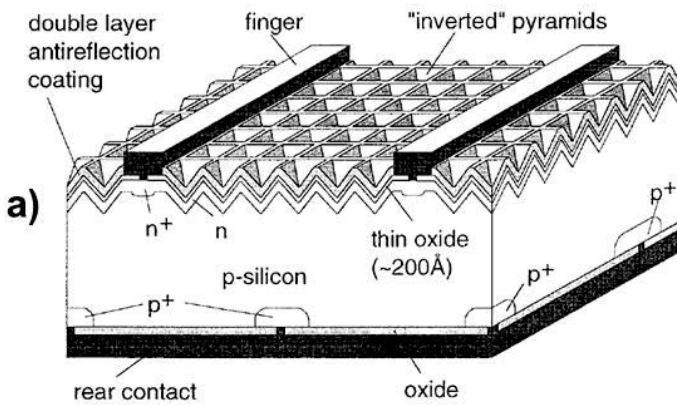


Figure 1. PERL (passivated emitter, rear locally-diffused) cell structure

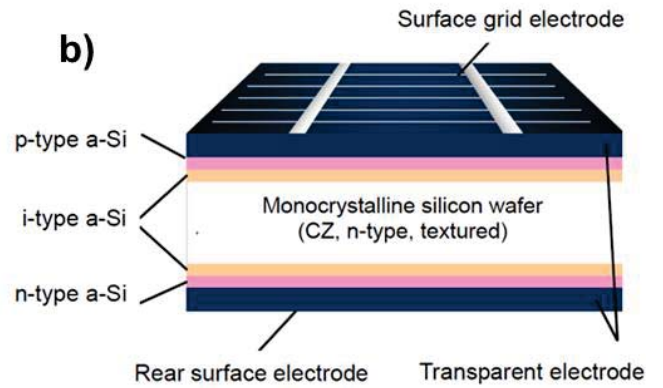


Fig. 2. Structure of a HIT solar cell.

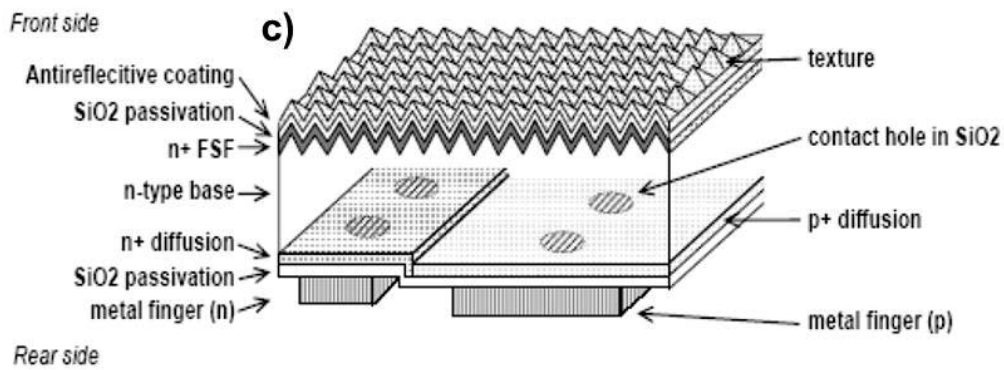


Figure 1: Schematic diagram of SunPower's A-300 solar cell (not to scale).

Figure 2.12: Representation of very-high efficiency silicon wafer bases solar cell designs. a) UNSW p-type PERL cell reproduced from [83]. b) Panasonic n-type HIT cell [80]. c) n-type SunPower A300 cell [84]. It can be seen, that obtaining high efficiency's for homojunction cells comes at the cost of a complex cell design.

efficiency above 24% was achieved. The homojunction champion cell is featuring a designated illumination area (4 cm^2) efficiency of 25.0 % [85], [81] for 1 sun standard test conditions (STC) and a thick FZ c-Si absorber. The designated area represents the illuminated cell area which is smaller than the total device area due to masking of the cell during measurements. More important some active parts of the device, i.e. the bus bar, lie outside the illuminated area which means that their negative influence on the efficiency is not considered for the efficiency given in Table 2-1. Whilst this is a common approach for concentrator cells, it is rather uncommon for standard cells. This makes a comparison with the intrinsically lower but more relevant total area efficiency very difficult. Moreover, it is a small area lab-type cell for which very complicated process steps were used. It comprised photolithography for the multiple structuring and alignment steps, heavily and lowly doped c-Si regions, tiny feature sizes, double layer anti reflection coating, PVD and plating for the metal electrodes. Thus, it becomes clear that a very

complex cell design and process flow are required to obtain such high efficiencies for a homojunction device.

Keeping this in mind it is quite impressive that the total area efficiency of the 101.8 cm² Panasonic cell featuring a CZ wafer and screen-printed electrodes lacks behind the designated area efficiency from the homojunction champion cell from *UNSW* by only 0.3 %_{abs}. The 24.7 % are representing the highest efficiency for a c-Si solar cell on large area which is based mainly on the very high V_{oc} and FF . Another important advantage in terms of performance is the lower temperature coefficient enabling a higher yield for the operation at higher temperatures. It can be seen in Figure 2.12 that the SHJ consist of an (i) intrinsic a-Si:H buffer layer. This film provides the chemical passivation of the absorber. It is capped by (ii) doped a-Si:H which defines the selectivity of the contact to either the holes or electrons. This SiTF stack is capped by the TCO that serves as an optical layer and for the lateral carrier transport towards the local metal grid electrode. The rear is featuring either a 1D metal electrode or a 2D grid electrode. The latter allows light to enter also from the rear (bifacial design) which can increase the output power in the field [79]. The deposition of the two semiconductor films, TCO layer and the metal electrodes on each side of the wafer does not require any structuring and alignment step. Thus, a 2D carrier transport is caused only by the local grid electrode whereas for the PERL and *SunPower* cell the carrier flow is much more complex. A 3D transport is caused by the local diffusions and openings of the dielectrics. The transfer of the very high efficiencies from the lap-type PERL cells to industrial like devices was not successful in past. However, *SunPower* managed to take this hurdle. Their champion cell is characterized by an excellent total area efficiencies of 24.2 % on large area [82] but very high efficiencies are reached in production, too [86]. On the other hand already several companies and institutes managed to produce large area SHJ cells with efficiencies well above 20 % in their R&D lines [3]. This clearly states the high efficiency potential of SHJ devices fabricated by industrial like approaches. Yet, the economic aspects of such devices including the yield in high volume production, etc. remain to be shown to fully evaluate its potential for the PV industry.

Band diagram and basic function of each layer

Figure 2.13 shows a sketched equilibrium band diagram of the standard SHJ depicted in Figure 2.12b. A band diagram with individual layers before contact formation is given Figure 2.14. It can be seen that the c-Si absorber is sandwiched between three thin films on each side, two a-Si:H films and one TCO. Similar films are applied to the front and rear with the only significant difference that a p-type a-Si:H film (green) is used at the side facing the sun (front) and a n-type a-Si:H film (red) is used at the rear.

The passivating buffer layer is found on both sides and consists of an nominal undoped a-Si:H with a thickness of 5 to 10 nm. Its very low defect density and sufficiently high hydrogen content enable the chemical passivation of the c-Si surface [20]. An atomically sharp a-Si:H(i) / c-Si interface [87] and a clean c-Si surface [88] are further prerequisites for an excellent passivation. Another very important aspect is the high band gap of the buffer layer. As will be discussed in section 4.2, it allows to decouple the c-Si passivation from the abundance of defects in the doped a-Si:H, TCO and metal films which are placed onto the buffer layer. While the a-Si:H(i) thickness needs to be high enough to provide the passivation [89] it must be thin enough to allow for an

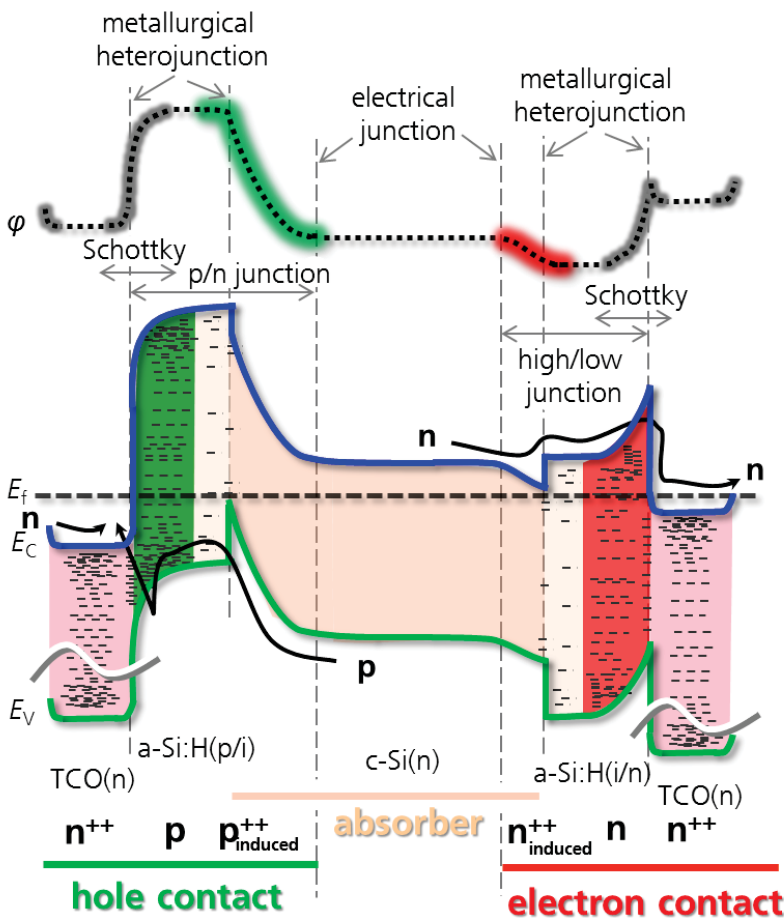


Figure 2.13: Schematic of a SHJ equilibrium band diagram for the cell depicted in Figure 2.12b.

The dotted lines in the upper part correspond to the local electrical potential. The grayish regions are indicating the parasitic band bending which is induced into the doped a-Si:H forming a Schottky like contact. In greenish and reddish the regions where holes and electrons are induced in the a-Si(i) buffer and the c-Si absorber, respectively.

In the lower part, the local conduction and valence band energy are displayed. The red and green areas denote the n-doped and p-doped regions, respectively. The dashed vertical lines are in indicating the position of the electrical junction and the metallurgical heterojunctions. The electrical junctions indicated here are the induced homojunctions inside of the a-Si absorber. The metallurgical heterojunctions are formed between the undoped a-Si:H and c-Si and the TCO and doped a-Si:H.

efficient carrier transport from the absorber in the adjacent films [75]. Another limitation for the upper limit of the thickness is imposed by need to prevent the significant parasitic absorption of photons [75] which should be rather absorbed in the c-Si to contribute to the photo-current.

The function of the doped a-Si:H is twofold. At one hand its work function must be high / low enough to induced the junction into the c-Si (green and red shaded dotted lines in Figure 2.13). This is similar to the MIS or SIS induced junction devices motivated before but here the work function is tuned by the doping of a-Si:H. As indicated in Figure 2.14, p-type doping leads to an increase of the work function as the Fermi-level is pushed towards the valence band energy (~ 5.6 eV). For n-type doping the Fermi-level is pushed towards the conduction band (~ 3.9 eV) of a-Si:H. It is important to note that the abundance of defects lowers the doping efficiency significantly below the level of c-Si and that this applies in particular for p-type doping [81]. Accordingly, the Fermi-level and work function of doped a-Si:H remain well below the respective majority carrier band (either E_C or E_V). So the free carrier density is comparatively low and far from degenerate.

Another approach which allows for tuning the work function (to a lower extend) is the alloying of a-Si:H [90], [91]. This was successfully demonstrated for the first time for SHJ devices in the course of this work [92] but is not further discussed here.

The second function of the doped a-Si:H is to ensure an efficient charge carrier transport into the TCO. The common TCOs can be described as a highly doped high band gap n-type

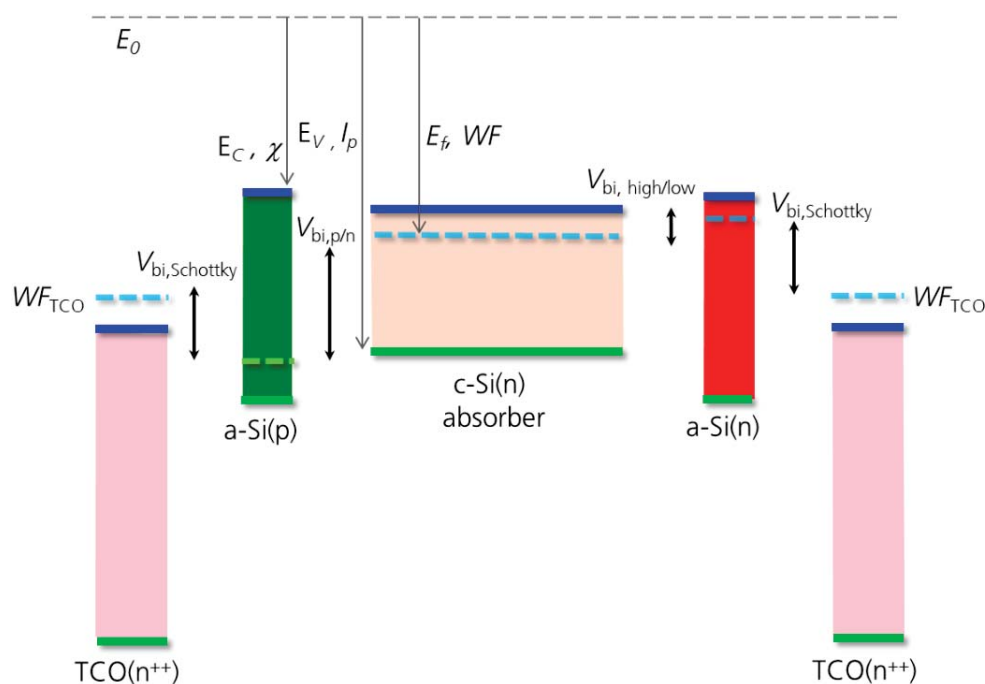


Figure 2.14: Schematic band diagram of individual layer of the SHJ cell from Figure 2.13 before contact formation. E_0 is the vacuum level. χ and I_p are the electron affinity and the ionization potential, respectively. The work function difference between the individual layers which defines the built-in potential of the induced junctions in Figure 2.13 is apparent. Furthermore, the offsets in the receptive bands which yield the abrupt heterobarriers can be seen.

semiconductor. Its work function is around 4.8 eV [93] which means its far away from both the conduction band energy ($\sim 3.9\text{eV}$) and the valence band energy of the a-Si:H ($\sim 3.9\text{eV}$) as indicated in Figure 2.14. Hence, a work function difference between the TCO and the doped a-Si:H exists. This induces a parasitic band bending (grey shaded dotted lines in Figure 2.13). As the free electron density in the TCO is typically much higher compared to the doped a-Si most of the band bending must be screened in the doped a-Si:H. This leads to the formation of a parasitic junction which is opposed to the one which is induced in the c-Si. Thanks to the metal-like nature of the TCO this TCO / doped a-Si:H contact can be approximated by an Schottky contact. The interplay between the induced c-Si junction and the parasitic Schottky is discussed in detail in section 4.2. In short, if the opposing Schottky contact is less pronounced, only the carrier extraction from the doped a-Si:H is hampered. For such conditions the J - V characteristic is influenced only by a non-ohmic series resistance. On the other hand, for a very prominent Schottky contact not only the doped a-Si:H in the vicinity of the TCO becomes depleted. The whole a-Si:H and the c-Si junction underneath become depleted. For such conditions voltage and excess carrier extraction from the absorber by the p/n- or high/low-junction is adversely affected. Low-injections conditions in the contact region are not maintained and the asymmetry of hole and electron conductivity is insufficient. For such conditions the standard p/n-junction theory and equation (2.26) fail to describe the J - V characteristic. To overcome such limitations the screening length within the a-Si:H must be sufficiently small, which was shown by the present author in Ref [94]. According to equation (2.5) this calls for a sufficient high doping and a small work function mismatch. If ensured, only a part of the a-Si:H becomes depleted and due to the narrow Schottky barrier tunneling into the TCO becomes an efficient transport path [95]. Besides the spatially distributed induced junctions, abrupt hetero barriers are also present at the TCO / a-Si contact. While for the electron contact the conduction band offset is not an issue. The valence band offset between the n-type TCO and the p-type a-Si:H is presenting a barrier which has to be overcome. However, this seems not to be an intrinsic limitation as proven by the high FF reached experimentally. According to simulations [96] band-to-band tunneling can be an efficient transport path at such junctions.

With respect to the TCO, ideally a high work function TCO at the hole contact and a low work function TCO at the electron contact would be applied to minimize the influence of the Schottky barrier. However, the function of the TCO goes well beyond providing an efficient carrier extraction from the doped a-Si:H. Simultaneously it must feature a high lateral conductivity, good contact to the metal electrode, negligible parasitic absorption and an appropriate refractive index

for light-coupling into the device the front and internal reflection at the rear. This leads to a design trade-off. For example, a high conductivity should be enabled by a high mobility rather than by a high free carrier density to avoid parasitic free carrier absorption which lowers the photo-current in the absorber [97], [98]. Hence, optimization of the TCOs is focused rather on the electrical and optical bulk properties than on the interface properties, i.e. the Schottky contact formed with the doped a-Si:H.

2.6 Chapter Summary

The basic solar cell theory and important aspect of induced junction silicon solar cells were reviewed. It was pointed out that the operation principle of the amorphous silicon / crystalline silicon heterojunction (SHJ) solar cell shares many similarities with the MIS and SIS devices. Common to all of them is that the junction which enables the selective hole and electron extraction from the absorber is formed by an induced homojunction rather than by a homojunction which is formed by doping of the absorber. The standard p/n-junction theory can be applied to all of them as long the contact regions are operating in low-injection conditions. While this is easily fulfilled for the highly doped c-Si region of the classical homojunction carrier selectivity comes at the cost intrinsically higher recombination losses, a more complex device design and hence a lower intrinsic efficiency potential for such cells. Basically, the opposite is case for induced junctions cells. While recombination can be greatly suppressed by the low defective high band gap buffer layer the applied thin films might suffer from limited doping and unsuited work function. Hence, maintaining low-injection conditions and a pronounced asymmetry of the hole and electron conductivity in the contact region during operation might be a loss mechanisms one should be aware of when dealing with such devices.

While in the next section the basic technology and metrology is outlined, more fundamental considerations on important aspect of a carrier selective contact are found in section 4.

3 Technology, Characterization and Simulation

In this chapter, the basic technology used for the fabrication of the test samples and solar cells is presented. In addition, the metrology and important aspects regarding the conducted device simulation are outlined.⁴

3.1 Technology: Preparation of solar cells and QSSPC and Suns- V_{oc} samples

In the course of this thesis a baseline process for SHJ cells was developed that allows for a efficiency of 20.8% on textured wafers. This includes the front-end processing (mainly wafer cleaning), the a-Si:H films from a new cluster tool, the back-end processing (metallization and definition of active cell area) and the characterization which were developed together with diplomat students and technicians.

3.1.1 Process flow

Firstly, the process flow for the cells is illustrated. Secondly, the process flow for test structures (lifetime/QSSPC and Suns- V_{oc} samples) which require fewer process steps is described. The process sequence typically used for solar cell and sample processing is shown in Figure 3.1 (left), the structure of the finished samples on the right side.

Solar cells

The first step was the cleaning of 4 inch FZ wafers or the quarters of an 4 inch FZ wafer by an RCA cleaning sequence [101]. Before the deposition of each a-Si:H layer (two undoped, one p- and one n-doped) the samples were dipped in diluted HF (~1%) for 2 minutes and rinsed in deionized water to remove the native/chemical oxide. It should be noted that the HF-dip and rinsing in water performed before deposition of a-Si:H on the second side of the wafer was also needed to remove particles which adhered on the surface. These particles originated from the sample holder (quartz plate) which was in contact with this side of the sample wafer during a-Si:H deposition on the first side of the sample. Before ITO sputtering another HF-Dip was performed and a shadow mask was used for the ITO deposition. The corresponding ITO windows

⁴ For more detailed insight regarding sample preparation and characterization it is referred to a related PhD thesis from the institute [45] which gives an excellent and very recent overview. Another PhD thesis from the institute covering similar, but more a-Si:H related aspects is found in [22]. Concerning the fundamentals of numerical device simulations with AFORS-HET it is referred to [99]. Detailed information on the simulations performed with Sentaurus Device and the used input parameters can be found in [100].

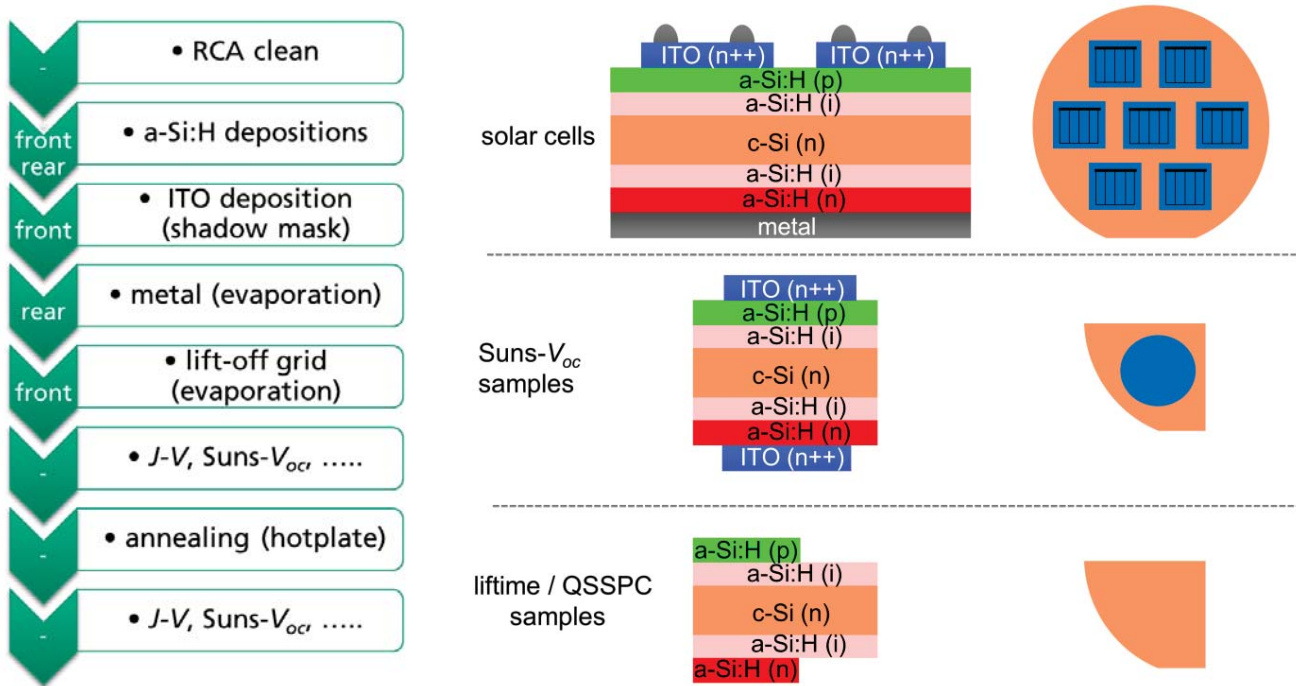


Figure 3.1. Left, process flow for solar cell processing and characterization. Right, sketched cross section and top view of different experimentally investigated samples.

(Figure 3.1, right) define the active cell area. For the solar cells, the shadow mask was designed to be compatible with the back-end processing developed for homojunction cells via photolithography. Accordingly, seven small area cells ($2.2 \cdot 2.2 \text{ cm}^2$) are formed on one 4 inch wafer. For the solar cells, ITO was typically deposited only at the front and a stack of thermally evaporated Ti/Pd/Ag was used to finish the rear. While this rear side is characterized by poor rear side reflection, omitting the TCO at the rear has some advantages. (i) It saves one ITO deposition step and thereby avoids sputter damage at the rear side. (ii) Ti ensures good electrical and mechanical contact to both the p- and n-doped silicon thin films. The front metal electrode was defined by photolithography and a subsequent lift-off step of a Ti/Pd/Ag stack. Both, thermal and e-gun evaporation have been used for deposition of the metal stack. Damage of the junction at the front by the e-gun process was not observed which is most likely explained by the presence of the photo-resist and/or the TCO which shield the a-Si:H / c-Si interface.

The process flow above is used if the p/n junction is placed at the front. For solar cells having the p/n junction at the rear the definition of the active cell area and hence the cell process are more complex. Before RCA cleaning and the a-Si:H depositions a passivating and insulating stack of a thermally grown oxide (SiO_x) and PEVCD silicon nitride (SiN_x) activated by an FGA anneal is applied to the rear. Then, $2 \cdot 2 \text{ cm}^2$ windows are opened by photolithography and wet chemical

etching. Following the process sequence described above, the seven cells are separated in $2.5 \cdot 2.5 \text{ cm}^2$ pieces by a chip saw. Another additional process step was needed in the very beginning for such “rear emitter” cells. To allow for the alignment of the front side metallization into the 2.2 cm^2 opening of the $\text{SiO}_x/\text{SiN}_x$ at the rear, a laser was used to create corresponding features at the wafer front side (alignment symbols).

It should also be mentioned that non-textured, shiny etched wafers were used for most investigations. Hence, combined with the poor rear side reflection, especially the moderate J_{sc} limited the efficiency of the solar cells to about 18%.

Lifetime/QSSPC and Suns- V_{oc} samples

Depending on the specific research question, fewer process steps as for the solar cells are sufficient. For testing the c-Si passivation by a-Si:H, a TCO deposition and metallization are not needed. Such lifetime/QSSPC samples (Figure 3.1, right) were used for example for the optimization of the a-Si:H buffer layer. If only the ability of the contact to extract a voltage from the absorber was of concern the samples were characterized after TCO deposition on both sides, i.e. without metallization. These Suns- V_{oc} samples were used extensively for example for investigating the Schottky contact between the doped a-Si:H and the TCO and to evaluate novel contact materials. It should be noted that these Suns- V_{oc} samples can be used as lifetime/QSSPC samples as well. For both, quarters of a 4 inch wafer have been used as indicated in Figure 3.1, right.

Post deposition annealing

After an initial characterization, the samples were typically annealed on a hotplate in ambient air and were characterized again. It is important to note that the process temperatures during ITO deposition and back-end processing (metallization) were below about 110°C and that therefore the a-Si:H and ITO films were hardly annealed unintentionally. As the typically applied annealing temperature of 180°C is well above this temperature, the different material and junction properties strongly respond to such an annealing. This is very helpful in gaining a fundamental understanding of the important factors which determine the final junction properties. Such information cannot be gained from cells where higher temperatures during TCO deposition or for curing of the paste (metallization) are applied. For the latter case, the different effects influencing the final cell characteristic by annealing might be superimposed and are hard to separate.

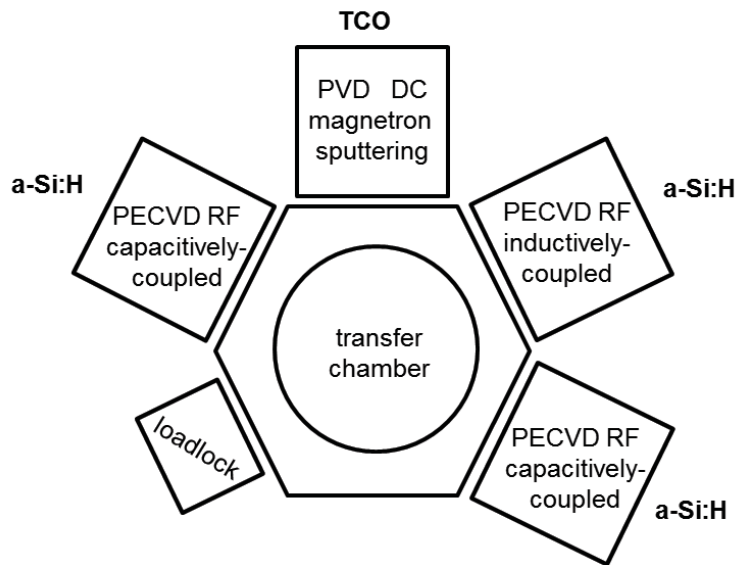


Figure 3.2. Schematics of cluster tool used for a-Si:H and ITO deposition.

3.1.2 Deposition tool

For the deposition of a-Si:H and ITO a new four chamber single wafer cluster from Oxfords Instruments was used (Figure 3.1). The majority of the a-Si:H depositions were done in the two capacitively-coupled parallel plate reactors powered by a 13.65 MHz generator and the processes were developed by the author of this thesis. ITO deposition was done by magnetron sputtering and the basic process conditions were provided by Oxford instruments. For more detailed information about the cluster tool it is referred to Ref. [22] and for the process conditions to Ref. [102].

3.2 Characterization

J-V

The typical solar cell characterization consists of measuring the J - V characteristic at STC conditions (1 sun / 1000 W/m², 25°C, AM1.5) with an in-house setup. For more detailed investigations of the J - V characteristic sometimes the temperature dependence (15°C-70°C) and illumination dependence (0-1 sun) were analyzed with the LOANA-system (pv-tools). The latter setup was also used for (temperature dependent) quantum efficiency and reflectance measurements and for obtaining the (temperature dependent) J_{sc} - V_{oc} characteristic.

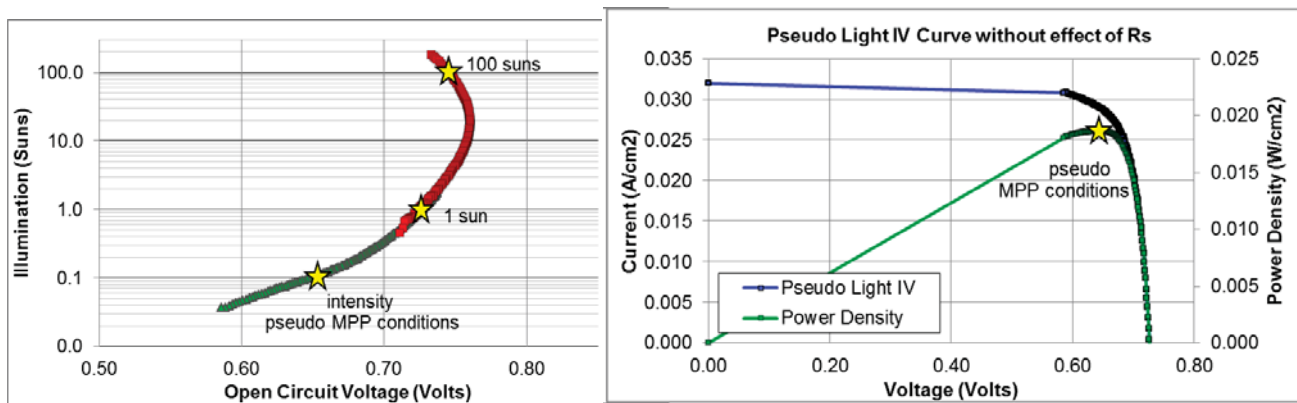


Figure 3.3 Screenshot from Suns-Voc analysis sheet. Left, results for standard illuminations up to slightly above 1 suns (green) and for higher illumination intensities (red). The yellow stars mark the relevant working conditions which were analyzed. Right, the pseudo current-voltage and power density-voltage characteristic obtained from the standard measurements (green in left graph).

Suns- V_{oc}

Measuring the J - V characteristic was typically supplemented by measuring the illumination level dependence of the open-circuit voltage with the Suns- V_{oc} setup [103] from Sinton Instruments at about 25°C. In short, by increasing the illumination intensity (flash lamp) the excess carrier generation in the sample is increased and the corresponding splitting of the hole and electron quasi Fermi-level at external terminals is probed (more details in e.g. Ref. [45]). It should be noted that the Suns- V_{oc} setup and the analysis sheet were slightly modified to allow for measurements with illumination intensity well above 1 sun. Hence, with two individual measurements the illumination level dependence of the external V_{oc} can be measured for the standard range from about 0.03 up to 3 suns and for higher illumination intensities of up to about 200 suns as shown Figure 3.3. Typically, the slope⁵ of the Suns- V_{oc} curve is analyzed at specific points (usefulness discussed in Sec. 6.1.). As a standard, a pseudo current-voltage and power density-voltage characteristic yields the open-circuit voltage at 1 sun conditions (V_{oc}) and the pseudo fill-factor (pFF).

Suns- iV_{oc}

While the former approaches allow analyzing the external open-circuit voltage of solar cells and Suns- V_{oc} samples, the characterization of the lifetime/QSSPC samples and the Suns- V_{oc} samples regarding their illumination level dependence of the effective photo-conductance gives profound

⁵ An excellent overview on the local ideality is given in the PhD theses of McIntosh [44]

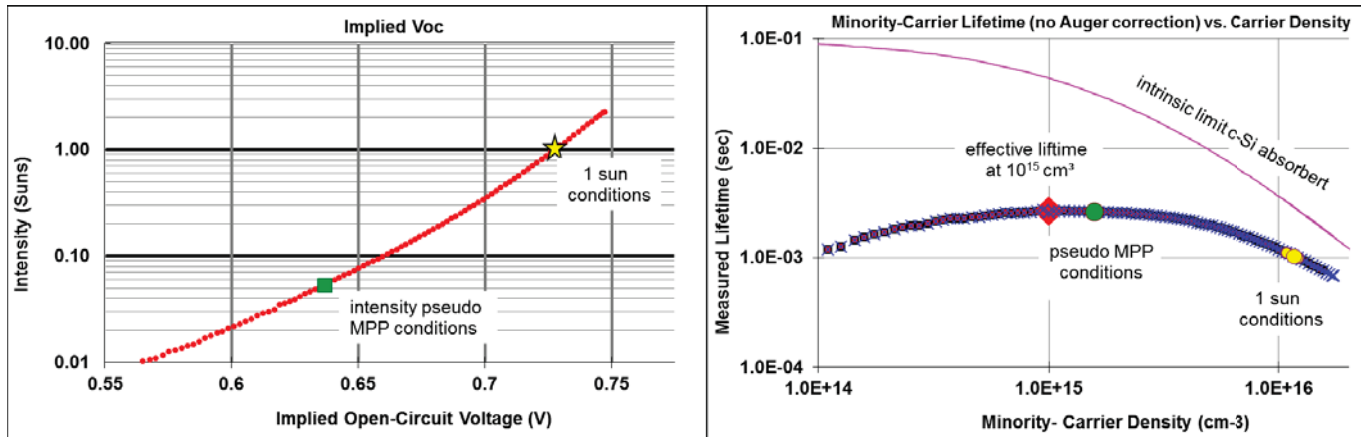


Figure 3.4. Screenshot from WCT-120 analysis sheet. Left, illumination level dependence of implied open-circuit voltage. Right, the dependence of the effective excess carrier lifetime on the effective excess carrier density.

insight regarding the surface passivation. With the WCT-120 setup from Sinton Instruments [104] the excess carrier density which results from the interplay of generation (flash lamp) and recombination is probed without making contact to the sample (more details e.g. in Ref [45]). This excess carrier density corresponds to an average splitting of the quasi Fermi-levels inside the sample, i.e. an implied voltage. The analysis of the illumination level dependence of this implied open-circuit voltage is in line with the analysis of the external voltage from the Suns- V_{oc} setup. It includes the generation of a pseudo current-voltage and power density-voltage characteristic which yield an implied open-circuit voltage at 1 sun conditions (iV_{oc}) and an implied fill-factor (iFF). The local slope of the Suns- iV_{oc} curve at specific points is determined as well. To allow for such an analysis, the analysis sheet was adapted for the quantitative evaluation of the influence of recombination on the implied MPP conditions (generation of pseudo $J-V$ curve) and to determine the local slope at specific points.

3.2.1 Interpretation of fill factor losses

For a holistic interpretation of the FF losses observed in the $J-V_{light}$ characteristic the contribution of different factors need to be separated. The latter can be done relatively easy by choosing adequate characterization techniques as indicated in Figure 3.5 and discussed in more detail in section 5.1. The upper FF limit is defined by the one sun V_{oc} and the respective ideality factor and is called FF_0 (green bar). It follows from Green's empirical expression [105] which is given in equation (5.1). The iFF (blue bar) accounts for the fact that, unlike the FF_0 the dominating recombination mechanism may change at MPP with respect to OC conditions. This is sometimes referred to as non-ideal recombination effects. In the double-diode model this is expressed by the presence of the second diode. The iFF is determined from the Suns- iV_{oc} characteristic obtained from injection level dependent photo conductance (QSSPC) or photo

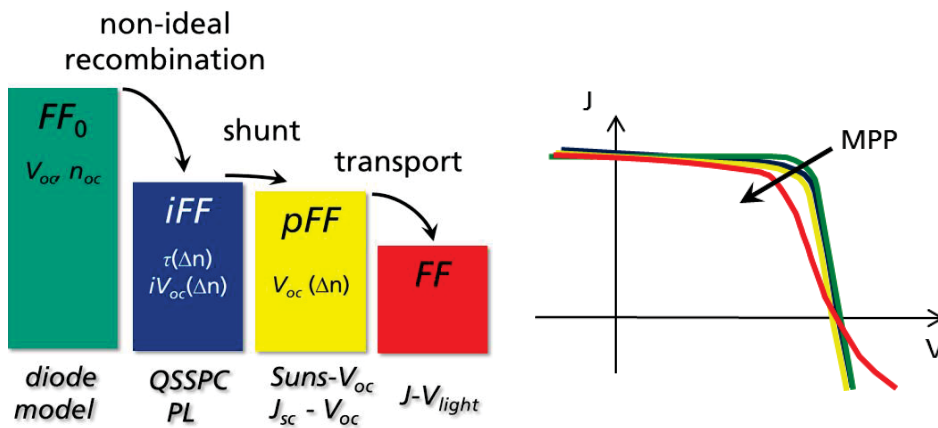


Figure 3.5: Left, contribution of different loss mechanisms defining the FF from the $J-V_{light}$ characteristic. The different techniques to obtain the respective FF is given below the bars. Right, sketch of respective $J-V$ characteristic indicating the FF loss.

luminescence (PL) measurements [106], [107] and defines the upper FF limited of the investigated structure. For the pseudo pFF the voltage is actually measured rather than calculated from the excess carrier density within the wafer like it is done for the iFF . Hence, a non-ideal voltage extraction and more common a shunt resistance modify the pFF with respect to the iFF . As the measurements before are current-less, they are free of transport related losses and basically quantified the recombination related FF losses. Hence, the comparison of the pFF and the FF from the $J-V_{light}$ characteristic allows the identification of ohmic and non-ohmic transport related FF losses.

3.3 Numerical device simulations

AFORS-HET

For insight regarding AFORS-HET the reader is referred to the textbook chapter from Stangl *et al* [99], [108] and the PhD thesis from Leenderts [21] and Varache [23]. The input parameters can be found in the master thesis of Markus Reusch [109], a master student supervised by the author.

Sentaurus

Regarding the simulations with Sentaurus, general information can be found in the PhD thesis from Rüdiger [110]. The input parameters used here can be found in the diploma thesis from Sebastian Schroer [100], a diploma student supervised by the author.

4 Relevant Design Parameters for Carrier Selective Contacts: A Simulation Study

In order to achieve a more fundamental understanding of carrier selective contacts, in this chapter important aspects for the engineering of material and junction properties are investigated in detail.

In the first section, the fundamental challenge of balancing the power losses at the front side of solar cells is analyzed by spreadsheet calculations based on the diode model. The limiting losses caused by excess carrier recombination, the lateral carrier transport and the grid shading are compared for homojunction and heterojunction cells. It is highlighted that for heterojunction cells the absence of an increased recombination in the metalized region results in a less complex design trade-off which enables not only a higher V_{oc} but also a more efficient lateral transport.

The second part is beyond the knowledge that can be gained from the analytical expressions of the diode model. Numerical device simulations are used to analyze the very basic requirements on a carrier selective contact scheme regarding voltage and excess carrier extraction from the absorber. It is highlighted that for the experimentally relevant cases the major requirement regarding contact engineering is to maintain low-injection conditions in the contact region during operation, i.e. to maintain the asymmetry of the hole and electron conductivity. Moreover, the relevant material parameters which allow the TCO / a-Si:H / c-Si contact system to maintain low-injection conditions are investigated in great detail. The second part of this simulation chapter is also intended to motivate the approaches used in the in the following experimental sections for the validation of different contact schemes.

The second subsection is partly adapted from the author's publication [111].

4.1 Contact recombination: Homojunction vs. heterojunction

A unique feature of SHJ cells, the absence of minority carrier recombination at the metal/semiconductor interface. In the following its implications on the optimum design of the front side grid electrode, are discussed on the basis of a simulation study. A comparison of SHJ and homojunction cells is presented to reveal the distinctive difference regarding the balancing of the recombination and transport losses, which is needed to maximize the efficiency.

4.1.1 Motivation

As outlined in section 2 and further below in section 4.2 the high band gap a-Si:H of the silicon heterojunction allows to decouple the minority carrier recombination at the c-Si surface from the abundance of surface states at the electrode's interface ($S_0 = 10^7 \text{ cm}^2/\text{Vs}$). This is an important advantage of SHJ cells over the homojunction cells for which the electrode is in direct contact with the absorber. Such a metal/semiconductor contact is characterized by significant minority carrier recombination which leads to the fact that device optimization is dictated by balancing minimum minority carrier recombination at the metallized and non-passivated regions (high V_{MPP} and V_{oc}) while maintaining an efficient majority carrier transport (low sheet and contact resistance). SHJ on the other hand are not subjected to such design constraints as recombination in the metallized and non-metallized regions is similar and also typically much lower.

For a quantitative interpretation of the aforementioned facts the results of a comparative analytical simulation study based on the two-diode model (equation (2.26)) is performed. For the sake of clarity, it should be pointed out that high-injection effects in the contact region or a non-ideal voltage extraction are not of importance for the investigations here. Such effects will be investigated in subsequent sections.

4.1.2 Simulation Details

The Excel-based tool *Gridmaster* [112] was used for the comparison of four different cell designs which are sketched in Figure 4.1. Figure 4.1 a) shows the standard SHJ and b) the standard homojunction design with a homogenous c-Si doping at the front. In Figure 4.1 c) and d) homojunction cells for which the complexity of the front was increased to reduce the recombination in the metallized device regions, are shown. Figure 4.1 c) depicts the classical selective emitter structure where a highly doped c-Si region below the metallized regions is introduced. For Figure 4.1 d) the metallized regions are passivated by a fictive contact scheme, similar to a MINP [69], [113], [114] structure or a local heterojunction which are placed on top of a doped c-Si region.

The influence of the rear surface is greatly simplified. The same 1D rear side was assumed for all devices and as constant input parameter the recombination within the absorber and at the rear are described by a rather low recombination current pre-factor ($J_{0,b}$) of 10 fA/cm^2 . It should be noted that the low $J_{0,b}$ and the absence of the 2/3 D transport paths at the rear are representing a very optimistic scenario for the partial rear contacts of the homojunction devices

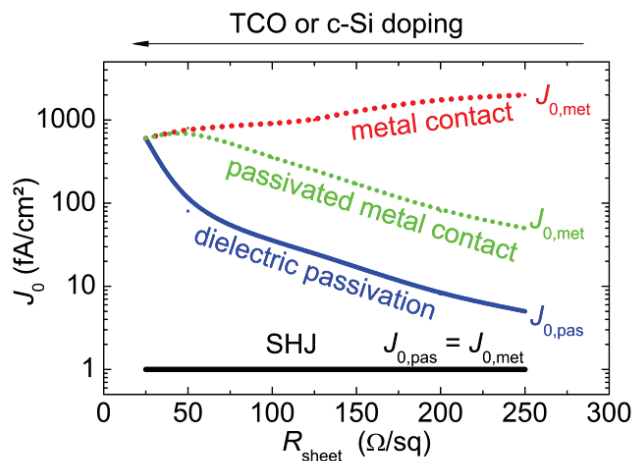
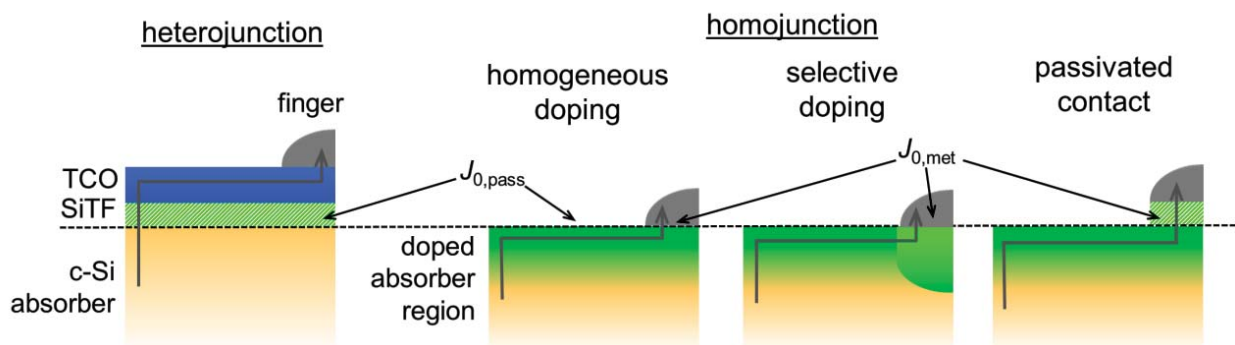


Figure 4.1: Left, qualitative behavior for J_0 as a function of R_{sheet} for the metalized area ($J_{0,\text{met}}$, red), the area passivated by a dielectric ($J_{0,\text{pas}}$, blue) or the SHJ ($J_{0,\text{pas}}$, black). In green, $J_{0,\text{met}}$ for the case where the metalized area is passivated by a fictive contact scheme which lowers minority carrier recombination but does not limit the vertical majority transport.

Bottom, sketched symmetry elements of considered cell structures.



in terms of minority carrier recombination and the FF loss caused by the lateral transport at the rear. The influence of non-ideal recombination effects ($J_{0,2}$) reflected by the two diode model and a shunt resistance (R_p) have not been considered. Therefore, pFF equals FF_0 . The variable input parameter is the sheet resistance (R_{sheet}) which is linked to the J_0 of the front side (bulk and surface recombination of doped c-Si region) as depicted in Figure 4.1. The data for the homojunction cells (blue and red) are inspired by Ref [115]. For the homojunction cells the J_0 contribution of the front surface region which is passivated by the dielectric layers is quantified by $J_{0,\text{pas}}$ (blue) whereas the recombination at the unpassivated and metallized device region is expressed by $J_{0,\text{met}}$ (red). For the passivated contact a much lower $J_{0,\text{met}}$ (green) was assumed which was chosen to be ten times $J_{0,\text{pas}}$. It is assumed that the vertical majority carrier transport (contact resistance) is not affected. For SHJ cells (black) an additional contribution from $J_{0,\text{met}}$ to the overall device recombination can be neglected which means $J_{0,\text{pas}} = J_{0,\text{met}}$. For the homojunction cells quite optimistic values for $J_{0,\text{pas}}$ were assumed which shall represent the high-quality surface passivation currently reached for lab-type cell processing of the doped c-Si regions and the dielectric passivation schemes. For the SHJ cells three scenarios have been assumed. Perfect c-Si passivation, quantified by the J_0 of 1 fA/cm² shown in Figure 4.1 in black. This J_0 result in a V_{oc} of 743 mV. Additionally, a J_0 of 5 and 30 fA/cm² were assumed to

demonstrate the influence of heterojunction schemes with less perfect performance in terms of c-Si passivation. These J_0 values correspond to a V_{oc} of 735 and 710 mV, respectively. It should be noted that V_{oc} s above 730 mV have been reported for large area a-Si:H based SHJ cells [80], [5], [3].

Concerning the metallization scheme, 60 μm wide Cu plated fingers, three bus bars and a device area of $15.6\text{ cm} \times 15.6\text{ cm} = 243\text{ cm}^2$ have been assumed. For a realistic description of the homojunction cells the width of the metal / semiconductor interface, i.e. the Ni seed layer, is smaller and was assumed to be 30 μm for all devices. For the selective emitter (d in Figure 4.1) a constant R_{sheet} of 25 Ω/sq below the seed layer characterized by the corresponding $J_{0,met}$ from Figure 4.1 was assumed. As a simplification, neither for the TCO nor the doped c-Si an increase of the contact resistivity with increasing R_{sheet} (and lower doping) was considered. A moderate and constant contact resistivity (ρ_c) of 1 $\text{m}\Omega\text{ cm}^2$ was assumed. Further simplifications refer to J_{sc} . For both, the SHJ and homojunction cells, a decrease of the J_{sc} with decreasing R_{sheet} was neglected. For the homojunction cells such J_{sc} losses are caused by a reduced blue response [116], [117] and increasing FCA within the highly doped c-Si regions [118]. Such losses are significant for an R_{sheet} below about 100 Ω/sq . For a medium and low-mobility TCO a reduction of FCA will be observed as well when reducing R_{sheet} [119]. However, we assumed that a high-mobility TCO is at the front. Excellent optical properties can be combined with an R_{sheet} as low as 40 Ω/sq for such materials [120], [98]. While the optical losses caused by the TCO electrode can be significantly reduced for a high μ -TCO, parasitic absorption in the a-Si:H contributes to an intrinsically lower J_{sc} as compared to the transparent front side of homojunctions. This J_{sc} loss is at least 1 mA/cm^2 [119] but is neglected here, hence overestimating the J_{sc} of SHJ cells.

With all input parameters at hand, *Gridmaster* optimizes the front metal grid electrode (“H-pattern”) for the four cells designs from Figure 4.1 by using one global two-diode model with a lumped series resistance [112]. *Gridmaster* calculates the optimum amount of grid fingers by balancing the optical and electrical losses to obtain the maximum efficiency. An example of a SHJ cell is shown in Figure 4.2 for three different R_{sheet} . For a too low amount of fingers and a large pitch (left from dashed vertical lines) the efficiency will be limited by series resistance related losses caused mainly by the inefficient lateral majority carrier transport or the contact resistance as the contact area decreases. For homojunction cells, this is partly compensated by reduced recombination at the metal/semiconductor area. For too many fingers and a narrow pitch (right

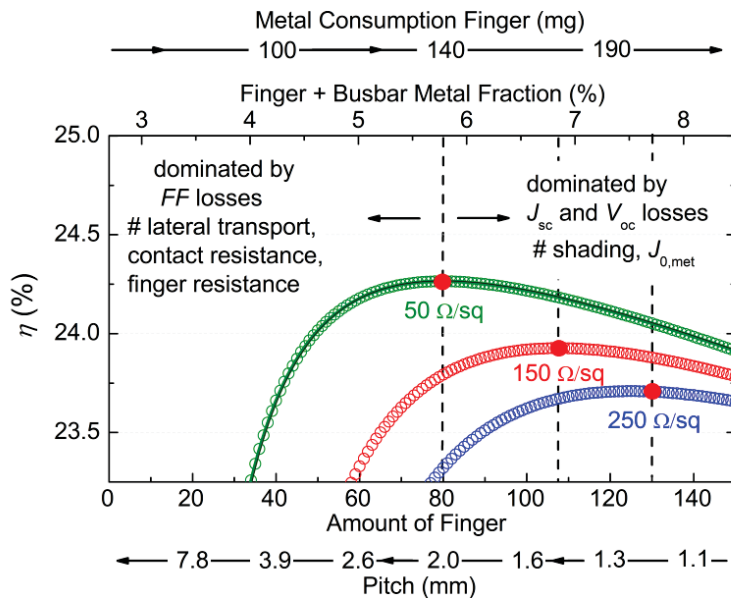


Figure 4.2: The cell efficiency as a function of the amount of grid fingers and the corresponding metalized area fraction at the front for a SHJ cell ($J_{0,pas} = 5 \text{ fA/cm}^2$) for a R_{sheet} of 50, 150 and 250 Ω/sq . The efficiency peaks for 80, 107 and 125 fingers, which corresponds to pitch of 1970, 1460 and 1250 μm , respectively.

from dashed vertical lines) the increased metalized fraction will increase shading losses and for homojunction cells also the recombination losses.

4.1.3 Simulation results: Heterojunction vs. homojunction

Figure 4.3 (a) - (h) collect some results of the three SHJ cells (black, grey, light grey) and the three homojunction cells (red, blue, green) as a function of R_{sheet} .

Generally, with the increase in R_{sheet} the lateral transport within the solar cell becomes less efficient. This has to be compensated by a reduced pitch of the grid electrode (Figure 4.3h) which is linked to an increasing amount of fingers. This increases the shading losses and for all cells a reduction of the J_{sc} (c) is observed. This J_{sc} reduction is stronger for the cells featuring a lower recombination at the metal/semiconductor region and an increase in V_{oc} (a) is observed for the homojunction cells while the V_{oc} is not affected for the SHJ cells. This behavior will be discussed in more detail the following.

In terms of the overall device recombination, the global J_0 of the solar cells reads [112]

$$\begin{aligned}
 J_{0,global} &= J_{0,b} + J_{0,pas} (1 - F_{met}) + J_{0,met} \cdot F_{met} \\
 J_{0,global} &= J_{0,b} + J_{0,pas} (1 - F_{met}) + J_{0,met}^*
 \end{aligned} \tag{4.1}$$

and $J_{0,global}$ is shown in (f). The last term in the upper equation quantifies the contribution from the metal/semiconductor device region and is denoted as $J_{0,met}^*$. As the fraction of the metal/semiconductor area (F_{met}) increases with R_{sheet} (numbers in h) the contribution of $J_{0,met}^*$ to $J_{0,global}$ increases depending on the specific $J_{0,met}$ (Figure 4.1). Hence, for the homogeneous emitter (red) and to lesser extend for the selective emitter (blue) the contribution of the metallized cell

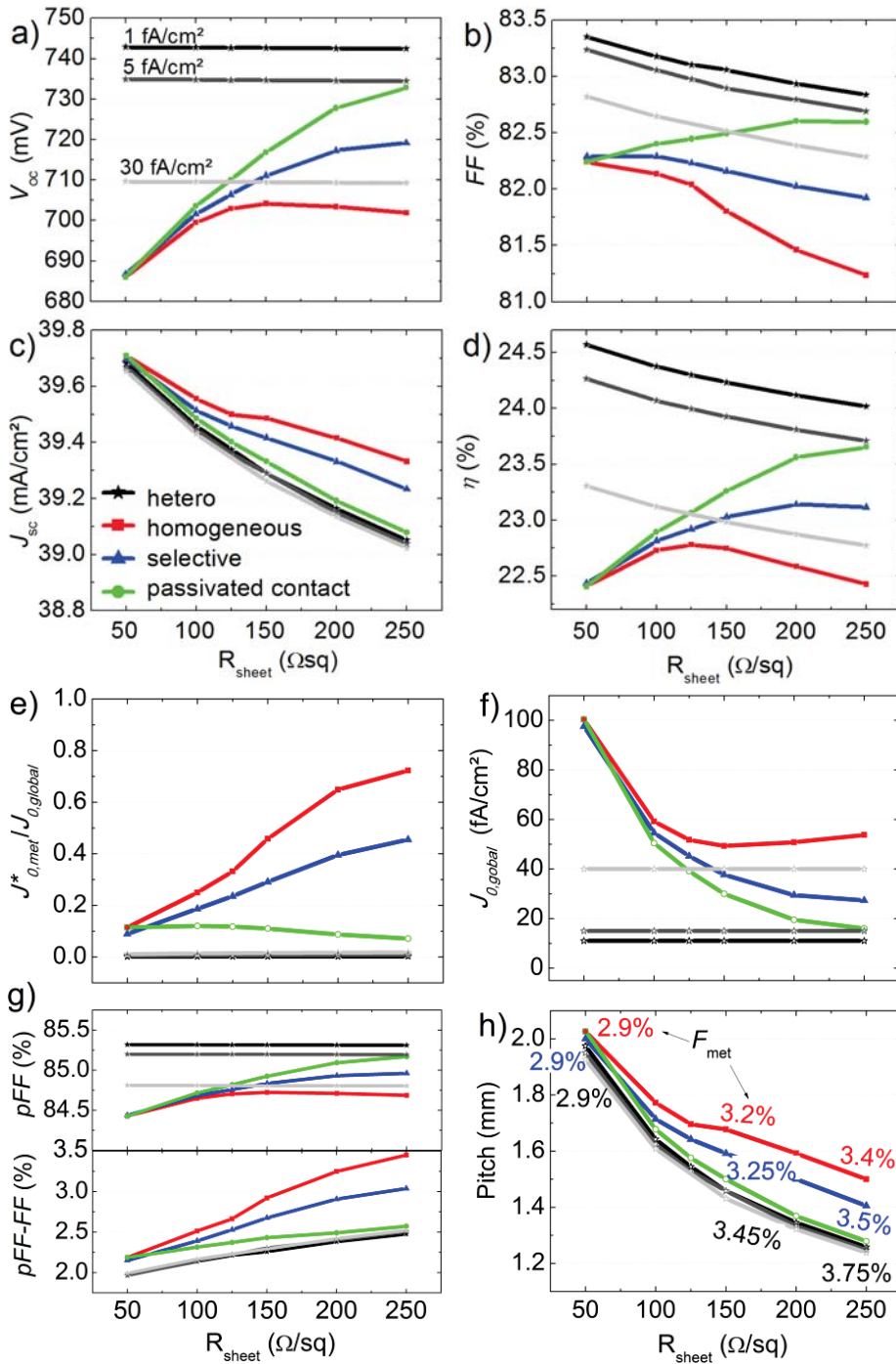


Figure 4.3: Results from the Gridmaster simulations. More details in the text.

area to $J_{0,global}$ ($J^*_{0,met} / J_{0,global}$ in e) is significant and becomes more pronounced for increasing R_{sheet} . For the SHJ cells this is not the case as $J_{0,met} = J_{0,pas}$ (Figure 4.1). For the local passivated contact (green) the contribution of $J^*_{0,met}$ to $J_{0,global}$ (e) is even slightly reduced with increasing R_{sheet} and the recombination in the non-contacted regions ($J_{0,pas}$) remains dominating the overall recombination. Here, the contribution from the increasing metallization fraction (h) is overcompensated by the reduction of $J_{0,met}$ (Figure 4.1).

$J_{0,global}$ is reflected in the V_{oc} (a) of the solar cells. For the SHJ cells no dependence of the V_{oc} on R_{sheet} is observed as $J_{0,pas} = J_{0,met}$. V_{oc} is constant and amounts to 743, 735, 710 mV. For the homojunction cells on the other hand a strong correlation between V_{oc} and R_{sheet} is observed. For a high V_{oc} , a very high R_{sheet} is mandatory to benefit from a low $J_{0,pas}$ and either a selective emitter (blue) or a passivated contact (green) are needed to limit the contribution from the metal/semiconductor device region $J_{0,met}^*$ (e). A similar $J_{0,pas}$ of 5 fA/cm² was assumed for the homojunction cells with a R_{sheet} of 250 Ω/sq (Figure 4.1) and for one of the SHJ cells (grey in Figure 4.3). Comparing the V_{oc} of the homojunction cells with the one of this SHJ cell ($J_0 = 5$ fA/cm²) for an R_{sheet} of 250 Ω/sq, only with the passivated contact the V_{oc} of the SHJ is reached. For the selective and homogeneous doping the influence of $J_{0,met}^*$ is significant and causes a V_{oc} reduction of 16 mV and 32 mV despite the excellent passivation in-between the grid fingers.

Graph (g) reveals that a structure with a lower $J_{0,met}$ has a positive influence on the series resistance related FF loss ($pFF-FF$) which is dominated by the lateral majority carrier transport. That the increasing FF loss with increasing R_{sheet} is less pronounced for all SHJ cells, irrespective of the surface passivation quality, is an intrinsic advantage over the homojunction cells. It is explained by the fact that for the optimization of the grid electrode a higher metallization fraction and thus a smaller pitch can be tolerated (h). Thus, the optimization of the amount of fingers can be focused solely on balancing the optical losses and the electrical losses caused by the lateral transport while the contribution from $J_{0,met}^*$ can be neglected for this optimization problem.

In terms of FF (b), for the homojunction cells the more pronounced FF loss (g) is partly offset by an increasing pFF (g) which is caused by the increase of the V_{oc} (a) and hence the FF_0 ($pFF = FF_0$). For the passivated contact the gain in pFF is higher than the FF loss from the less efficient lateral transport which results in an increase of the FF with R_{sheet} (b). For the SHJ cells the FF dependence on R_{sheet} is determined only by FF loss caused by the lateral transport ($pFF - FF$) as the V_{oc} and thus pFF are not affected by R_{sheet} .

Concerning the device efficiency (c) especially for a low R_{sheet} the SHJ devices are clearly outperforming the homojunction devices. For the latter a high R_{sheet} (low $J_{0,pas}$) and a sophisticated cell design (selective emitter) are mandatory to reach very high efficiencies. It is important to note that for the SHJ, which is featuring a moderate level of surface passivation ($J_{0,pas}$ of 30 fA/cm²), the efficiency for a R_{sheet} of 100 Ω/sq is still above the one of the more complex selective emitter cell. The efficiency of the fictive passivated contact approach is not discussed as

especially its influence on the transport related FF losses [113], [121] is subjected to large uncertainties and its integration in the standard cell process might be challenging as well.

4.1.4 Conclusion

The low $J_{0,pas}$ of SHJ cells and the facts that $J_{0,pas}$ is not a function of F_{met} , not coupled to R_{sheet} and matches $J_{0,met}$ allows the unique combination of a very low device recombination (high V_{oc} and FF_0) and an efficient lateral carrier collection (low $pFF-FF$). This applies in particular if a high mobility TCO is used at the front which allows for R_{sheet} as low as $40 \Omega/sq$ without generating significant optical losses. Additionally, such a highly conductive TCO allows for a very high pitch which reduces the shading by the grid electrode. The application of such low R_{sheet} is not reasonable for homojunction devices as the extrinsic and intrinsic recombination in the bulk and at the surface of such highly doped c-Si regions results in a very high $J_{0,pas}$. While a lower c-Si doping improves $J_{0,pas}$, it has a negative influence on $J_{0,met}$ and the lateral carrier transport (increased R_{sheet} and ρ_c). Hence, for homojunction cells an improved minority carrier recombination (lower $J_{0,global}$) always comes at the cost of the majority carrier transport and the need for sophisticated device designs like highly doped regions only below the metal and tiny contact fractions. Such features might be hard to implement in an industrial cell process which makes the success of homojunction cells with very high efficiencies unlikely [122]. This is not a problem for the SHJ based cells and related concepts. Irrespective of c-Si passivation quality ($J_{0,pas}$), such design constraints are not observed as the metalized region do not add recombination losses ($J_{0,pas} = J_{0,met}$). This allows the unique combination of an efficient lateral transport (low $pFF-FF$) and a very low recombination (high V_{oc} and FF_0).

4.2 Basic aspects for carrier selective contacts

The photovoltaic conversion efficiency is defined by the competition between two processes: Harvesting the photo-generated free holes and electrons at the respective spatially separated external device terminals and the charge annihilation via recombination within the device before reaching the external terminals. In this section the basic electrical layer and interface properties responsible for this interplay are discussed on the basis of numerical device simulation (*AFORS-HET*).

As a unique feature, much attention is paid to the difference between the implied and external voltage. This allows to identify whether the contact is limited by its ability to enable a high excess carrier density within the absorber or to selectively extract this excess holes or electrons. After a short motivation, the homojunction and the two metal-semiconductor like contacts are compared and the role of the electric field is discussed. Afterwards, the a-Si:H based silicon heterojunction is investigated. It is pointed out that voltage and excess carrier extraction is strongly defined by the interplay between the parasitic Schottky contact and doped a-Si:H / c-Si junction underneath. This is followed by considerations on a semiconductor buffer layer and two rather hypothetical contacts for which electrons and holes can move in opposite directions.

4.2.1 Motivation: Non-ideal voltage extraction.

A graphical motivation of the basic objective of this chapter is given in Figure 4.4. As outlined in section 2, two basic requirements have to be fulfilled for a high external voltage. (i) A high density of excess holes and electrons within the absorber that defines the upper limit of the extractable voltage (implied voltage). (ii) An ideal extraction of this voltage so that the external voltage matches the implied voltage. The ideal case is shown for structure a) in Figure 4.4. The implied voltage is close to the band gap and the external voltage matches the implied voltage. For b) the external voltage matches the implied voltage but the implied voltage is low, caused by a high recombination at the surface (or in the bulk) of the absorber, a low generation rate or a significant amount of carriers are extracted. For structure c) the external voltage is not limited by the ability of the contact to passivate the absorber surface (high iV) but the contacts fails to selectively extract the absorber's excess holes. The external voltage is limited by a voltages loss in the contact region, i.e. a gradient of the majority carrier quasi-Fermi level in the hole contact. The basic prerequisite to avoid such conditions is to enable a sufficiently high hole conductivity during operation and to block the electrons. The conductivity of electrons must be negligible as outlined in section 2. Experimentally, the local conductivity is almost exclusively modified by the

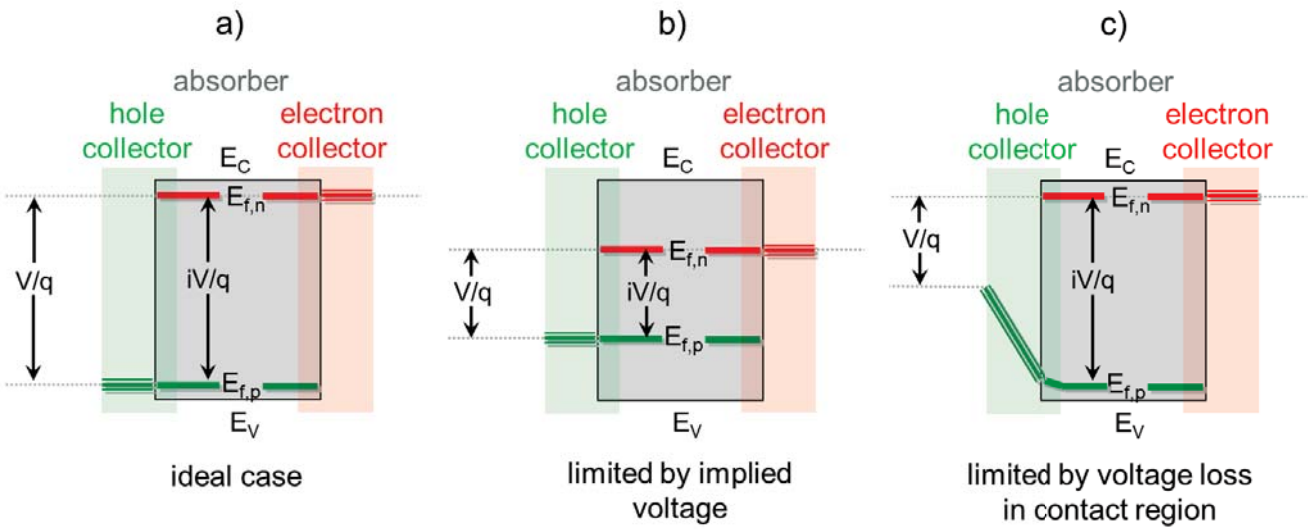


Figure 4.4. Schematic for possible limitation of external voltage in a solar cell. a) Reference system where the implied voltage is close to the band gap and the external voltage matches the implied voltage. b) The external voltage matches the implied voltage but the implied voltage is low, e.g. caused by a high recombination at the surface or in the bulk of the absorber or by a low generation rate. c) The contacts allow for excellent c-Si passivation and thus a high implied voltage but the external voltage is limited by a gradient of the majority carrier quasi-Fermi level in the hole contact region.

carrier density. By doping or an induced junction. It follows that during operation the local majority carrier density (n_{maj}) must remain well above the local minority carrier density (n_{min}), i.e. $n_{maj} \gg n_{min}$. Here n_{min} is the combination of generated and the injected minority carriers. Claiming for $n_{maj} \gg n_{min}$ is synonymous to the claiming for low-injection conditions during operation in the contact region.

To highlight the importance of low-injection conditions, in Figure 4.5 the simulated $J-V_{light}$ curves of two distinctive cells are shown. The black curve represents a cell for which $n_{maj} \gg n_{min}$ is fulfilled in the contact region, in case of the red one this is not fulfilled. Clearly, a non-ideal characteristic is observed for the latter. The green line is the characteristics where the external voltage is replaced by the implied voltage, the $J-iV_{light}$ curve. The same $J-iV_{light}$ curve is obtained for both contacts as the ability of the contacts to passivate the wafer is similar. It can be seen that for the case that voltage extraction is ideal (black) the $J-V_{light}$ the $J-iV_{light}$ curve coincide. For the red curve the non-ideal voltage extraction is dominant for working conditions where the excess carrier density within the device is high. Which means for maximum power point and open circuit conditions. Accordingly, FF and V_{oc} are reduced whereas J_{sc} is hardly effected.

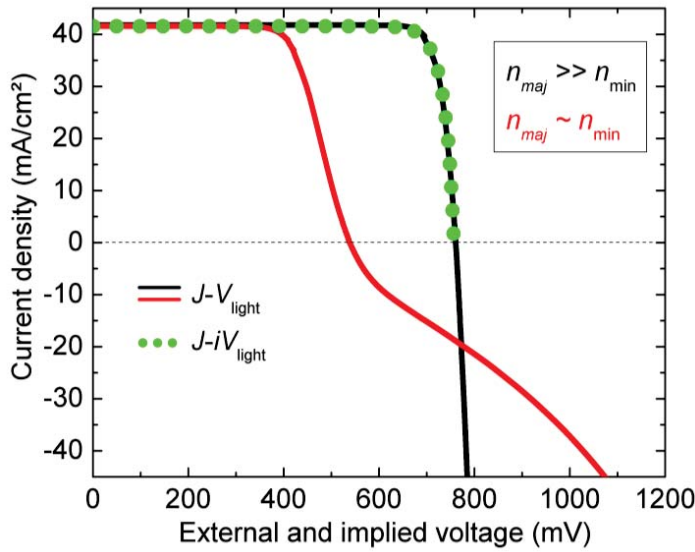


Figure 4.5. J - V_{light} characteristics for low-injection (black) and high-injection (red) in the contact region. The green curve is the J - iV_{light} characteristics which is identical for both cases.

As a design rule, the built-in potential (or diffusions voltage) of a junction must always exceed implied voltage to avoid such a non-ideal voltage extraction. For a junction formed by doping this is expressed by [9]

$$V_{\text{bi}} \approx \varphi_{\text{c-Si}} = k_B T / q \ln \left(\frac{N_A \cdot N_D}{n_i^2} \right) \geq iV = E_{f,n} - E_{f,p} / q \quad (4.2)$$

For an induced junction this can be expressed by the work difference between both contact materials

$$V_{\text{bi}} \approx \varphi_{\text{c-Si}} = |WF_{\text{electrode}} - WF_{\text{absorber}}| \geq iV = E_{f,n} - E_{f,p} / q \quad (4.3)$$

The equations above show that the requirements on doping and the work function increase with increasing QFL splitting and implied voltage, i.e. increasing excess carrier density.

The fact that the way in which the junction is formed is intrinsically linked to an electrical potential difference for both cases is responsible for the circumstance that the built-in potential equals the respective c-Si band bending. However, while this suggests that the electric field is the relevant force driving holes and electrons in different directions. The electric field has to be regarded as an “*accompanying phenomenon of a structure ... and not an essential property of a solar cell*” [9]. Rather, the gradient of electrochemical potential, i.e. the gradient of the respective Fermi-level is the important force (equation (2.3)).

In terms of a low minority carrier recombination and hence a high implied voltage a high V_{bi} is also needed. This is explained by the facts that a low minority carrier density, which limits the recombination for low injection conditions, follows from a high majority carrier density (and

thus a high V_{bi}) via $n_{min} = n_i^2 / n_{maj}$. Adding a factor that lumps together the recombination activity of the contact, i.e. the surface recombination velocity, we end up with the well known recombination current pre-factor

$$J_0 = \frac{q n_i^2}{n_{0,maj}} S_0 = q n_{0,min} S_0 \tag{4.4}$$

This quantity must be minimized as it is presenting the parasitic current caused by minority carrier recombination which is opposed to the current of the majority carriers. The superposition of both currents is expressed by the diode model (equation (2.26)).

Basically, the total current into the external electrode for the hole contact, which is the sum of the hole (majority) and electron (minority) carrier current must be dominated by the hole current ($J_{total} \approx J_p \gg J_n$) and the voltage drop needed to drive the hole current must be minimal. For the electron contact $J_{total} \approx J_p \ll J_n$ must be fulfilled as it is motivated in Figure 4.6. An intuitive explanations on the possibilities to lower the parasitic current of the “wrong”, the minority carrier species in the contact region is given in Ref [16] and requires minimizing the product of the density and velocity term in the equations below (charge not a variable)

$$J_p = \text{charge}_p \cdot \text{carrier density}_p \cdot \text{transport velocity}_p \tag{4.5}$$

$$J_n = \text{charge}_n \cdot \text{carrier density}_n \cdot \text{transport velocity}_n \tag{4.6}$$

As motivated above, the charge carrier density terms for the “wrong” current can be reduced by doping or an induced junction. The transport velocity term can in principle be reduced by lowering the mobility of the wrong carrier species. Another approach would be to reduce the transition rate of the “wrong” carrier species in the contact region. The transition can, among

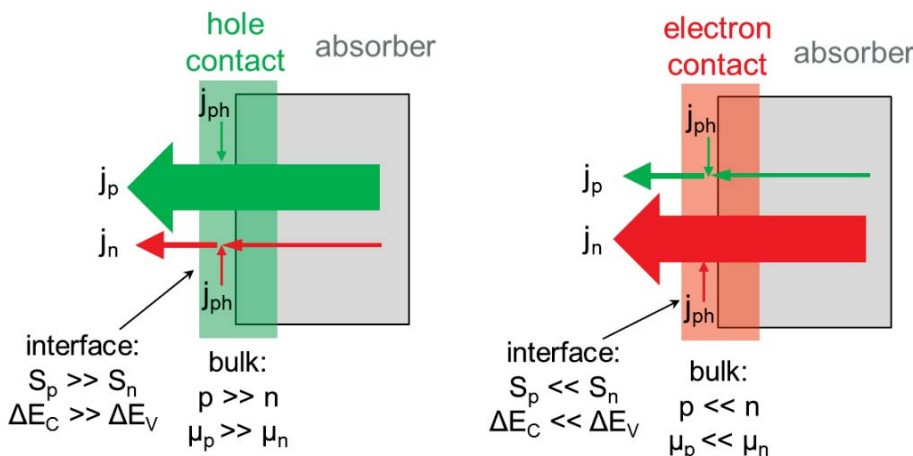


Figure 4.6. Schematic of possible limiting cases for the electron and hole current into the external electrode for a hole selective contact (left) and an electron selective contact (right).

other factoring be influenced by asymmetric hetero-barriers, recombination rates or tunneling probabilities. Common to all asymmetries is that they must avoid the transport of the “wrong” species without hampering the transport of the other one for which the contact is intended to be selective for. Rather hypothetical contacts based on the transition rate limited case of asymmetric hetero-barriers, and asymmetric recombination rates as well as the influence of an asymmetric mobility are discussed in the end of this chapter.

For a good overview on the aspects of the selective carrier extraction, besides the textbook from Würel et. al [9], the recent publication from Würfel et. al [39] is suggested to the reader. In the latter it was nicely shown that

“.. the difference in conductivities of electrons and holes on the way to “their” contact is the decisive condition for selective transport and that this condition has to be maintained even under illumination. This means that the electrons move—on their way toward the electron contact—through regions with a large electron conductivity, while the current of the holes in that direction is suppressed by a very small hole conductivity, although the force they are subjected to, the gradient of their electrochemical potential, may be much larger than that of the electrons. The opposite happens for holes and electrons on the way toward the hole contact.”

Approach

For the results presented here the focus is set on the trends and their explanations rather than on quantitative results. Some of the contact systems are greatly simplified and are rather fictive. Nevertheless, they give valuable insight into the basic design constrains for a carrier selective contact. For the sake of clarity, the investigations focus on the hole contact but the same findings apply to the electron contact. The electron contact assumed here is idealized and does not limit the device performance. The same holds for the c-Si absorber. An intrinsic c-Si absorber was assumed while defect recombination was neglected. Apart from the hole contact, ideal optical properties were assumed. Hence, for an ideal contact an efficiency close to the intrinsic limit of the c-Si absorber (~29 %) is reached. To facilitate comprehension of the different simulation studies, a sketch in the beginning of each subsection motivates the simulated structure and the variables.

4.2.2 p/n-Homojunction

Influence of doping and chemical surface passivation

Figure 4.7 shows a structure in which the hole contact is defined by a 5 nm thin c-Si layer for which the p-doping was varied from undoped to near degeneracy as shown in the table in Figure 4.7. The corresponding work function (WF) of the p-layer and the work function difference (ΔWF) to the intrinsic c-Si absorber are also indicated. Any doping related variations of the c-Si material properties of the 5 nm layer, e.g. Auger bulk recombination or other heavy doping effects have not been considered. The simulated structure most closely corresponds to a homojunction formed with an idealized very thin epitaxially grown c-Si layer and a perfect metallurgical c-Si(p) / c-Si(i) interface. It should be noted that mainly due to its very low thickness and high mobility the p-region is highly (electrical) transparent for the injected minority carriers [123], [124], [16] which makes the structure very sensitive to the surface recombination at the electrode. S_0 describes the chemical c-Si surface passivation by the contact and is varied from very low to the thermal velocity, i.e. 1 to 10^7 cm/s. The latter reflects the case

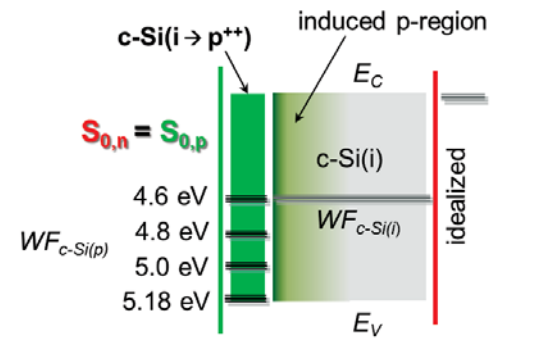
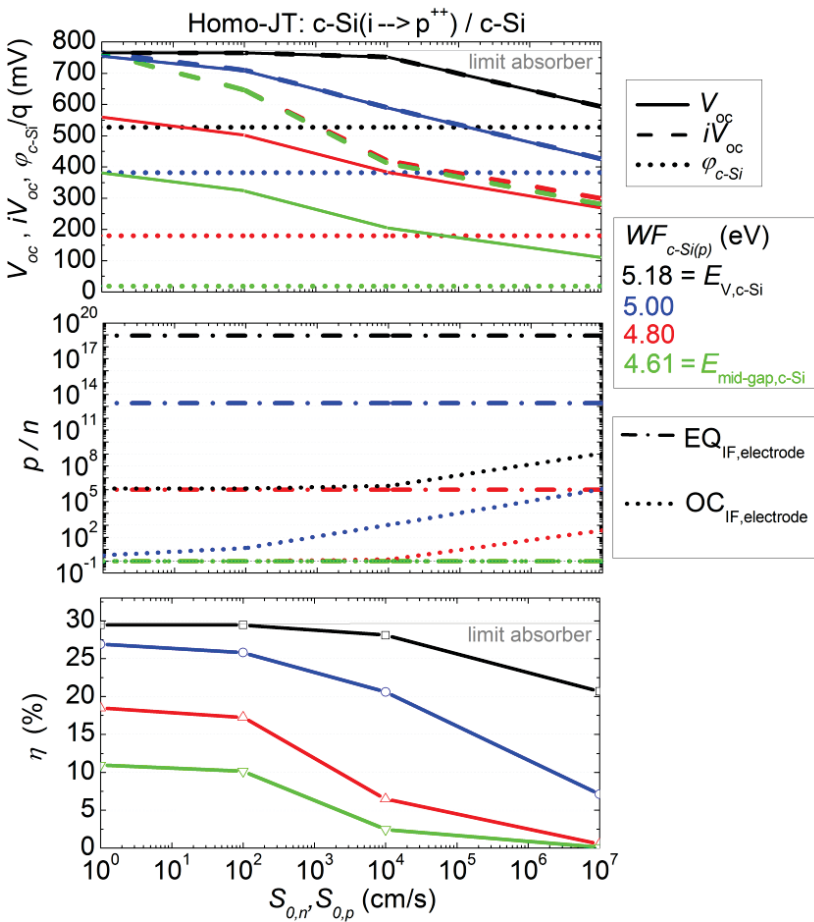


Figure 4.7. Above, sketch of simulated homo-junction like devices indicating the variation of the p-layer's doping and work-function. Left, results of the simulations as a function of S_0 at the interface to the electrode. Below, change of p-layer WF and ΔWF with p-doping.

$N_A = p_0$ (cm^{-3})	WF (eV)	ΔWF (eV)
3×10^{19}	5.18 = $E_{C,c-Si}$	0.56 = $E_{g,c-Si} / 2$
3×10^{16}	5.0	0.39
1×10^{13}	4.8	0.19
0	4.61 = $WF_{c-Si(i)}$	0.00

of an unpassivated metal / semiconductor interface. The computed results are plotted vs. S_0 . From the top to the bottom graph in Figure 4.7, this includes the external and implied voltage at 1sun open-circuit (OC) conditions and the equilibrium c-Si band bending in the dark. The ratio of the hole and electron density directly at the interface between the electrode and the c-Si(p) for OC conditions and for the equilibrium (EQ) and in the dark. Finally, the efficiency obtained from the $J-V_{light}$ curves. The different colors denote the different acceptor doping levels of the c-Si(p) film.

Starting with the EQ conditions, the results in green in Figure 4.7 reveals that for an undoped c-Si film, i.e. when contact is made between an intrinsic c-Si thin film and the intrinsic absorber flat-band conditions are observed. The induced band bending (φ_{c-Si}) is zero (upper graph, dotted lines) and the p/n ratio at the interface (middle graph, dashed-dotted lines) is unity. The latter shows that the p/n ratio at the interface is not modified with respect to the absorber. For increasing doping φ_{c-Si} is increased according to equation (4.2) which results in significant increase of the hole density and $p/n \gg 1$ (dashed-dotted lines). It is important to note that φ_{c-Si} matches $\Delta WF = WF_{c-Si(p)} - WF_{c-Si(i)}$. While this correlation is typically not indicated for a homojunction formed by doping it clarifies that the built-in voltage of a homojunction formed by doping can be quantified in a similar way it is done for an induced homojunction (equation (4.3)). Shown by the sketch of the simulated structure, for the highest doping $WF_{c-Si(p)}$ matches the valence band energy of the c-Si absorber. For this case φ_{c-Si} and ΔWF corresponds to $E_g/2$ which is 0.56 eV for the c-Si absorber.

In terms of c-Si passivation, for OC conditions it can be seen that regardless of the doping, $S_0 = 1$ cm/s is sufficient to ensure a very high density of excess carriers within the absorber, i.e. an iV_{oc} (dashed lines) which is limited by the intrinsic limit of the absorber (~ 760 mV). For moderate chemical passivation and increasing S_0 increasing the doping is beneficial for surface passivation and hence the iV_{oc} . This is explained by the reduced electron density at the interface (equation (4.4)). It is typically referred to as field-effect passivation and lowers the demands on the chemical passivation (S_0). In terms of external voltage it can be seen that voltage extraction is ideal only for sufficiently high doping. The external V_{oc} matches the iV_{oc} only for the case that $p/n \gg 1$ is maintained for OC conditions (dotted lines). If p/n is approaching unity a voltage loss in the contact region reduces the external voltage well below the implied voltage. In other words, the contact fails to selectively extract the excess holes from the absorber. It can be seen that for a given doping p/n is reduced the better the chemical passivation. This is again explained by the

fact that for higher excess carrier densities maintaining low-injection becomes more challenging. Accordingly, for insufficient doping the voltage loss becomes even higher the lower S_0 is.

Such a voltage loss is not only observed for OC conditions but also for MPP conditions (not shown here but discussed below). The iV_{MPP} and the V_{MPP} show the same behavior like the iV_{oc} and the V_{oc} . Accordingly, a voltage loss in the contact region at MPP also leads to a reduced FF . The efficiency reveals that a sufficient high doping and surface passivation are essential ingredients. For the highest doping and $S_0 < 1000$ cm/s an high efficiency close to the intrinsic limit (29.1%) is obtained.

The major advantage of homojunctions is that $p/n \gg 1$ is easily fulfilled due to its high net doping. However, for the commonly applied techniques doping is higher than actually needed. This results in heavy doping effects. A rather intrinsic limitation is the unpassivated metal / semiconductor interface. It follows, that voltage extraction is typically ideal but the higher recombination limits the implied voltage and hence the efficiency.

4.2.3 MS contact: An induced p/n homojunction

Influence of electrode's work function and chemical surface passivation

The structure investigated here corresponds to a metal-semiconductor contact. The work function of the transparent metal like electrode ($WF_{\text{electrode}}$) and S_0 at the c-Si surface underneath are variable. $WF_{\text{electrode}}$ was chosen to match the values of the p-doped c-Si film from the previous section.

Figure 4.8 reveals that the behavior of the induced homojunction matches that of the homojunction formed by doping from above (Figure 4.7). It follows, that in principle there is no difference if the highly hole populated device region close to the external electrode is realized by p-doping or by a high WF electrode.

While the MS structure is a very simple one, finding a material with a proper WF is one of the major challenges for this structure. An intrinsic limitation is set by the absence of passivation at the metal / semiconductor interface which is covering the whole surface. In this sense, in the next subsection section a buffer layer is added to this structure.

Yet, before moving to the next subsection, we take a more holistic view comparing the hole and electron contact. Additionally, a basis for an experimental approach used in section 6 is provided. The investigated structures are sketched in Figure 4.9. One with a hole contact of a 1 Ω cm n-type absorber (green) and one with an electron contact of a 1 Ω cm p-type absorber (red). Three

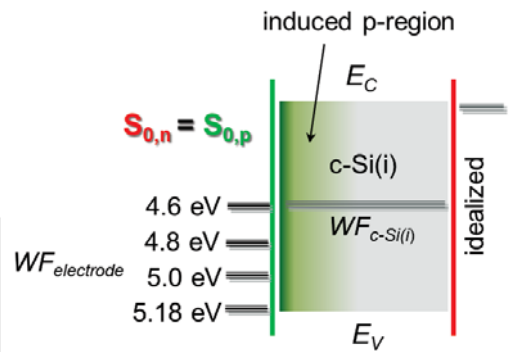
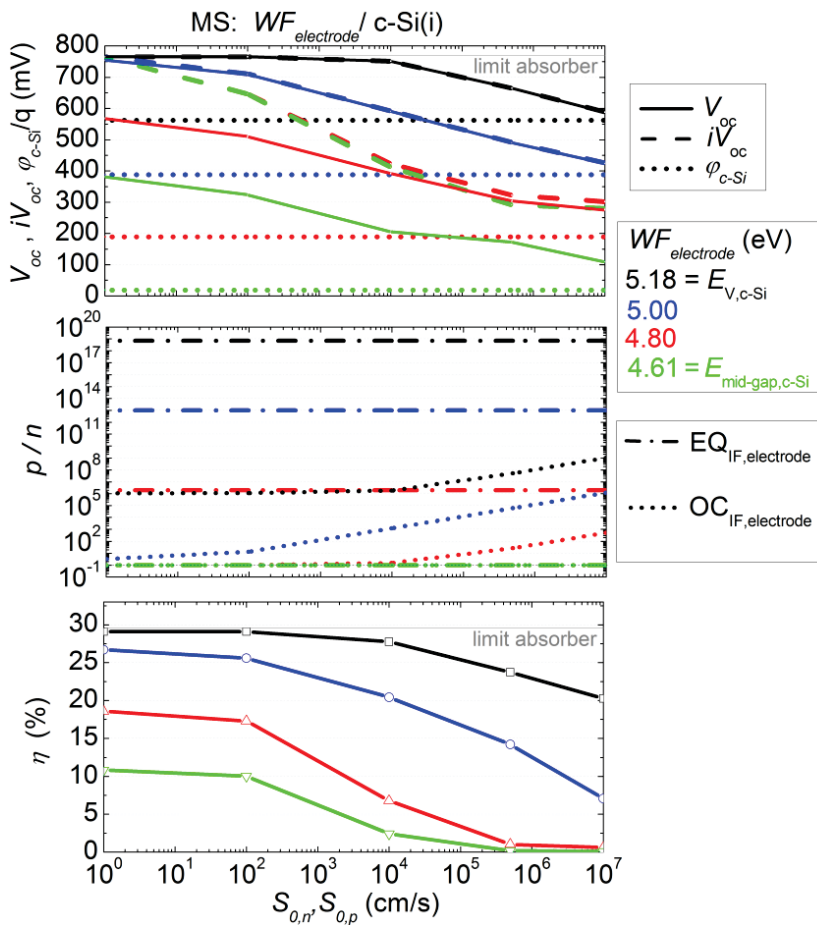


Figure 4.8. Right, sketch of simulated MS like devices indicating the variation of the work function of the electrode. Left, results of the simulations as a function of S_0 at the interface to the electrode.

different levels of surface passivation (S_0) were assumed. The work function for both contacts is changed from the conduction band to the valence band of the c-Si absorber. For the hole contact $\Delta WF = WF_{\text{electrode}} - WF_{\text{c-Si}(n)}$ defines the built-in potential and $p/n \gg 1$ must be fulfilled. For the electron contact $\Delta WF = WF_{\text{c-Si}(p)} - WF_{\text{electrode}}$ and $n/p \gg 1$ must be fulfilled.

The results in Figure 4.9a are mirrored around the mid-gap energy of the c-absorber (4.61 eV). For a hole contact the work function must be close to the valence band energy of the absorber. For the electron contact it must be close to the conduction band energy of the absorber to maximize ΔWF and to obtain a highly inverted surface. The slope of $\phi_{\text{c-Si}}$ is unity as $\phi_{\text{c-Si}} \approx \Delta WF$. ΔWF is about 900 meV for both contacts if matching the valence / conduction band of the absorber. For such conditions the induced hole and electron densities are in the range of that obtained for the standard p/n-junctions formed by doping. At mid-gap the p/n ratio is close to unity for both, the hole and electron densities corresponds to about the intrinsic carrier density and ΔWF is about 350meV.

Regarding surface passivation and the iV_{oc} and iV_{MPP} , for moderate and poor chemical passivation, the increased of $\phi_{\text{c-Si}}$ leads to improved field effect passivation. With respect to the

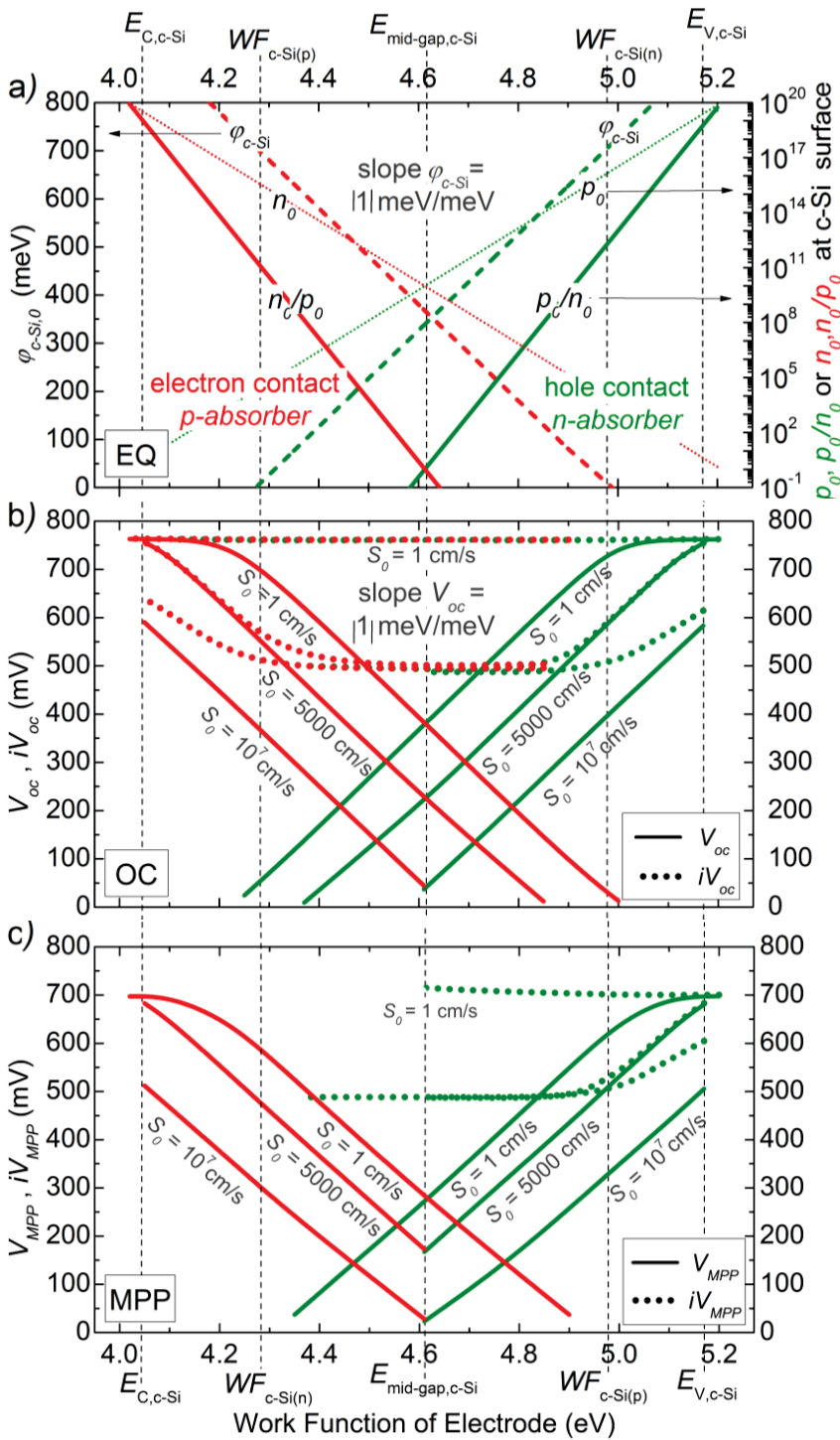
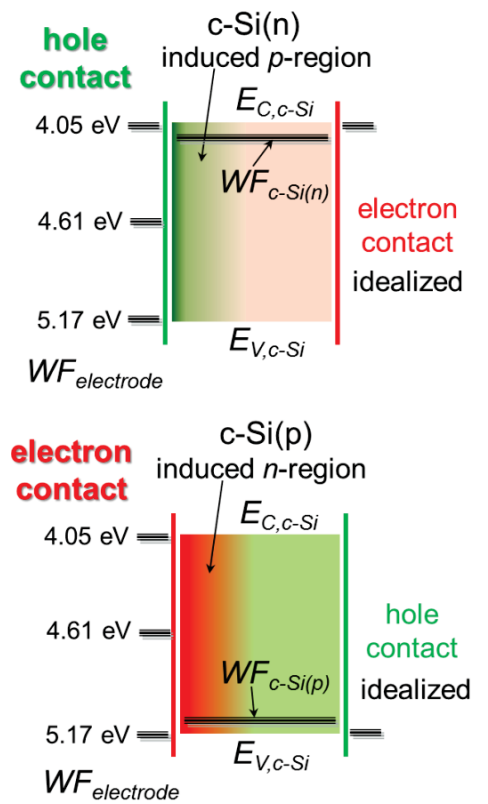


Figure 4.9: Left, results showing the influence of the electrode or contact layer work function on the properties of an induced hole contact of an n-type absorber (green) and the induced electron contact of a p-type absorber (red). Three levels of chemical c-Si passivation were assumed (S_0). Below, sketch of simulated MS devices indicating the variation of the electrode's work function.



external voltage, a sufficient high/low WF is needed to extract this implied voltage. It can also be seen that for improved chemical passivation and higher implied voltage a higher/lower WF is needed to ensure an ideal voltage extraction. Another important feature is that the slope of the external voltage is also unity, up to a level where the external voltage saturates since the implied voltage becomes limited by the intrinsic c-Si bulk recombination. However, for real devices the influence of Fermi-level pinning or adjacent junctions other than the induced p/n-junction (see

Figure 4.16) will cause a different behavior. Both aspects are addressed in section 6.3 and 6.1, respectively.

4.2.4 MIS like contact: a-Si:H buffer

Decoupling the chemical surface passivation from the defects of the electrode

The structure simulated here corresponds to the MS structure from Figure 4.8 but features an additional 5 nm thick undoped a-Si:H buffer with a band gap of 1.7 eV in-between the metal like electrode and the c-Si absorber (Figure 4.10). It should be noted that in a classical MIS structures dielectric buffer layers (e.g. SiO₂) with a thickness of 1-2 nm are typically applied. However, as *AFORS-HET* does not support tunneling as transport mechanism we had to restrict the investigations to a semiconductor buffer.

For the simulated structure, S_0 refers to the recombination at the interface between the metal like electrode and the buffer. c-Si surface defects are neglected which is equivalent to a perfect chemical passivation of the absorber by the buffer. To account for the fact that the hole contact region is extended by the undoped a-Si:H buffer the p/n ratio for EQ and OC is shown in Figure 4.10 for the c-Si interface (bottom graph) and as before directly at the electrode (middle graph).

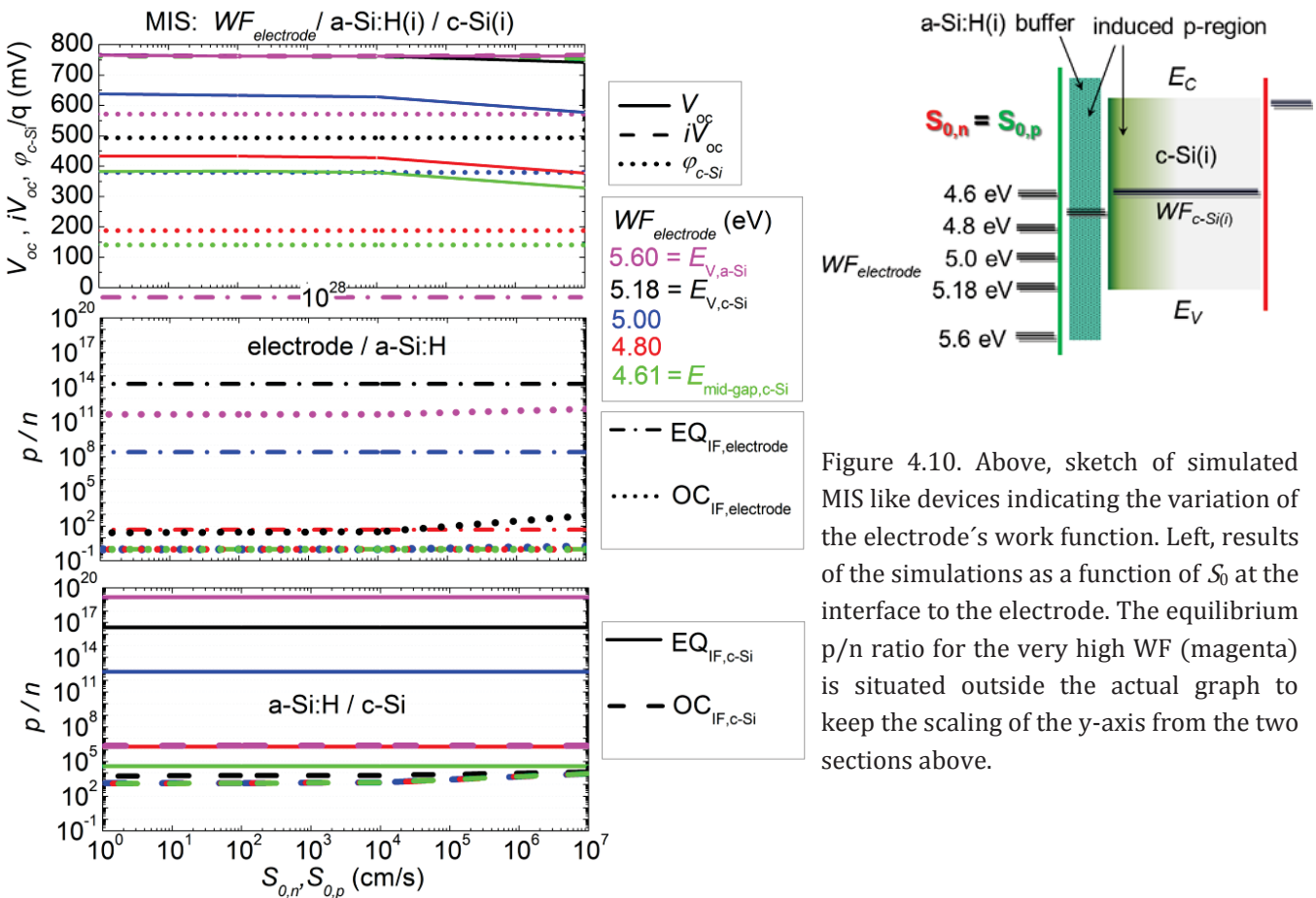


Figure 4.10. Above, sketch of simulated MIS like devices indicating the variation of the electrode’s work function. Left, results of the simulations as a function of S_0 at the interface to the electrode. The equilibrium p/n ratio for the very high WF (magenta) is situated outside the actual graph to keep the scaling of the y-axis from the two sections above.

The latter is also representative for the p/n ratio in the bulk of the buffer.

Compared to the MS device from Figure 4.8 two major differences arise when introducing a buffer. The most important is that the c-Si passivation and thus the iV_{oc} are decoupled from S_0 at the interface between the electrode and the buffer. Irrespective of S_0 and $WF_{\text{electrode}}$ the iV_{oc} is limited by the intrinsic recombination of the absorber and is close to 760 mV. In other words the abundance of defects at the electrode / buffer interface that is characterized by a high S_0 , is not “seen” by the minor carriers (more further below). In terms of the external voltage, again a $WF_{\text{electrode}}$ close to the valence band of the absorber is needed to ensure an ideal voltage extraction. Comparing the p/n ratio at the c-Si surface (bottom) and at the interface of the electrode (middle) it can be seen that the occurrence of high-injection conditions for which p/n is close to unity is limited to the interface region (and the a-Si:H part of the junction). Unlike for the MS structure the p/n ratio at the c-Si interface remains well above unity.

The second aspects is that some band bending is also induced into the buffer. The latter is reflected in the slightly lower c-Si band bending (490 vs. 560 meV) but becomes more obvious from the lower hole density at the c-Si surface as compared to the values of the MS structure in Figure 4.8. To compensate for the fact that a high hole density has to be induced in the undoped buffer as well and to obtain a similar inversion of the c-Si surface, $WF_{\text{electrode}}$ has to be increased to values well above the valence band energy of the c-Si absorber. For the results in magenta the WF matches the valence band of the a-Si:H buffer. Further discussion based on simulations reading the buffer can be found in section 4.2.5, 4.2.7 and 6.3.2.

4.2.5 Classical SHJ: a-Si:H doping and TCO work function

Now we turn to the standard SHJ. Compared the MIS like structure from above p-doping of an additional a-Si:H layer is applied to tune the p/n ration in the contact region. Basically, the need for this additional p-doped a-Si:H layer in the conventional SHJ structure is explained by the unsuited work function of the TCO electrode. It will be shown how that a parasitic junction is induced by the TCO which needs to be compensated for by the doped a-Si:H. First the influence of such an unsuited TCO work function on the band diagram is discussed in detail for the relevant working conditions. Then the interplay between the a-Si:H(p) and the work function and its influence on the external as well as internal cell parameter is demonstrated. Finally, the influence of the a-Si:H(p) thickness and screening length is discussed.

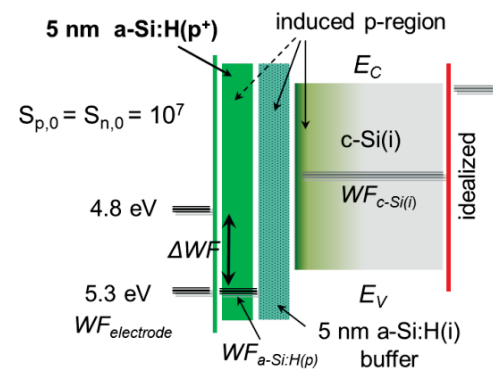
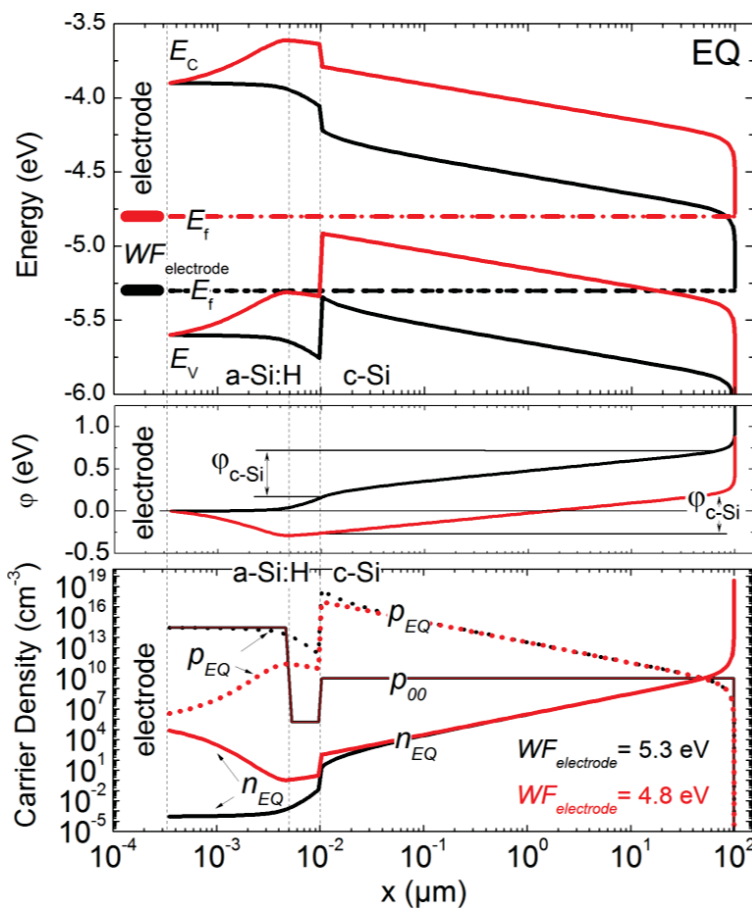


Figure 4.11. Above, sketch of simulated devices indicating the variation of the a-Si:H(p) doping the electrode work function.

Left, internal cell parameters for equilibrium conditions for an p-doped a-Si:H with a WF of 5.3 eV and a $WF_{\text{electrode}}$ of either 5.3 eV (black) or 4.8 eV (red).

Band diagrams

The influence of $WF_{\text{electrode}}$ on the overall contact properties shall be motivated in the following in detail. To this end, the structure from Figure 4.11 is investigated. The a-Si:H p-type doping is kept constant and $WF_{\text{electrode}}$ is chosen to either result in flat-band (5.3 eV, black) or depletion conditions (4.8 eV, red) at the electrode / a-Si:H(p) contact. The focus is on the band diagram, the local electric field and the local currents and carrier densities and how this properties change for the relevant working conditions.

First it should be demonstrated how the equilibrium hole density of the individual layers before contact formation (p_{00}) is changed during contact formation. And how this results in the equilibrium hole density (p_0) of the actual SHJ structure. In the lower graph of Figure 4.11 p_{00} (thin solid lines) is shown. In the p-doped a-Si:H p_{00} has the highest value, it is much lower in the undoped a-Si:H buffer and the undoped absorber. While in the undoped films it amounts to the respective intrinsic carrier density of $\sim 5 \cdot 10^5$ and 10^{10} cm^{-3} it is $\sim 9 \cdot 10^{15} \text{ cm}^{-3}$ in the a-Si:H(p). It should be noted that the latter is 3-4 orders of magnitude lower compared to a highly doped crystalline silicon regions of the homojunctions. After contact formation between this layers the

p_0 indicates the local hole density. The increase of p_0 in the undoped a-Si:H and the c-Si reveals the induced p/n-junction and the formation of the highly hole populated region. For the flat-band case where $WF_{\text{electrode}}$ matches the work function of the a-Si:H(p) (black) the equilibrium hole density at the a-Si:H / c-Si interface and at the interface to the electrode amounts to $5 \cdot 10^{18}$ and $1 \cdot 10^{15} \text{ cm}^{-3}$, respectively. For the much lower and unsuited work function of the TCO electrode (red) this values are only $3 \cdot 10^{17}$ and $4 \cdot 10^6 \text{ cm}^{-3}$, respectively. The latter shows that the p-doped a-Si:H close to the electrode becomes virtually intrinsic ($p_0 \approx n_0$). Hence, a high density is in the contact region is not ensured here. This becomes also apparent from the band diagram where the Fermi-level near the electrode is situated rather close to mid-gap then close to the valence band. With respect to the induced junctions for the flat-band case, $\Delta WF = WF_{\text{a-Si:H(p)}} - WF_{\text{c-Si(i)}} \approx 5.3 - 4.6 = 0.7 \text{ eV}$ which defines the total electrical potential difference which is responsible for the band bending seen in the band diagram. It is shared by the a-Si:H(p) ($\sim 0.05 \text{ eV}$) the a-Si:H(i) ($\sim 0.12 \text{ eV}$) and the c-Si ($\sim 0.54 \text{ eV}$).

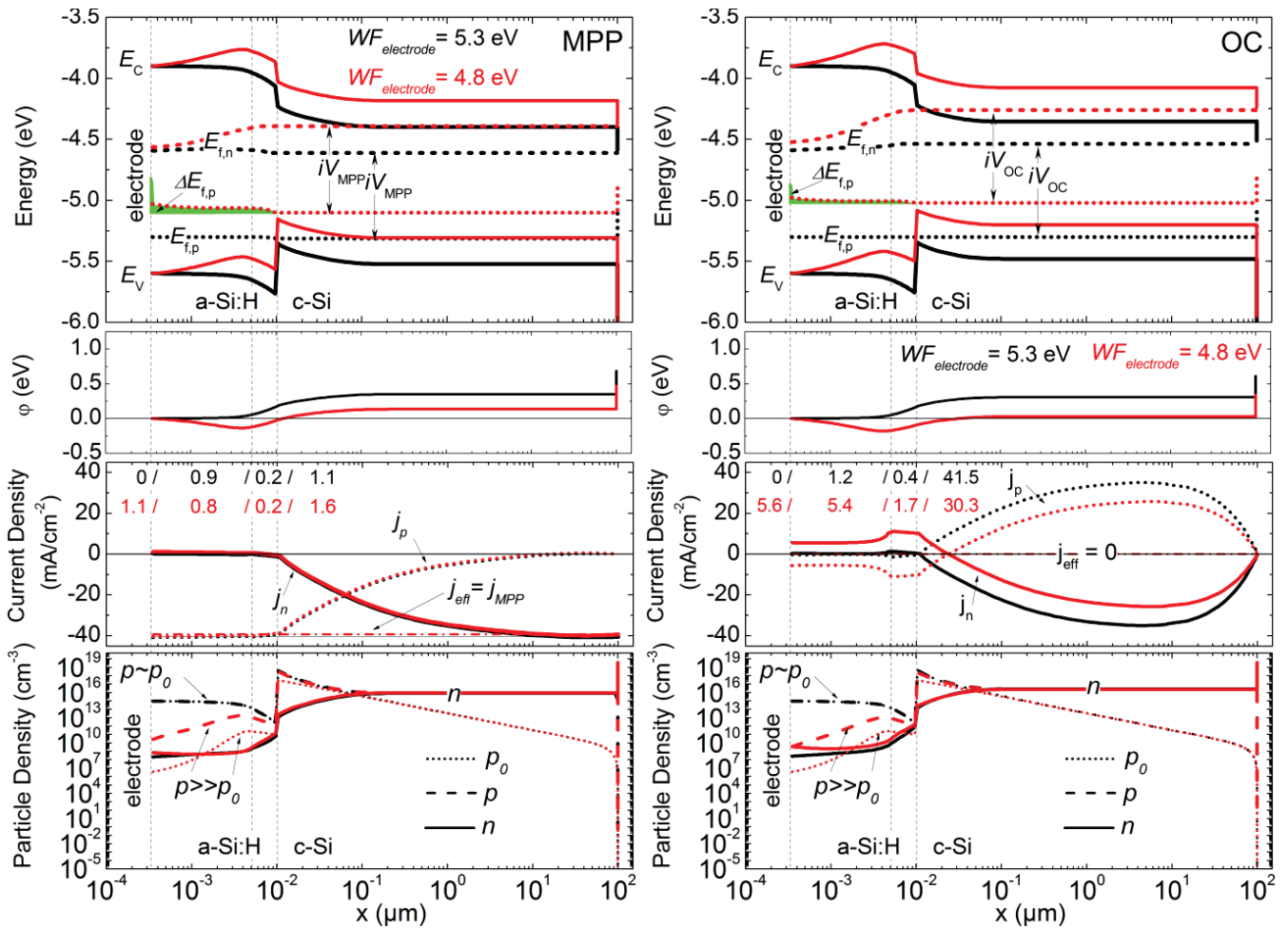


Figure 4.12. Internal cell parameters for maximum power point (left) and open circuit conditions (right) for a p-doped a-Si:H with a WF of 5.3 eV and a $WF_{\text{electrode}}$ of either 5.3 eV (black) or 4.8 eV (red). The numbers in the current density graphs correspond to the local recombination current densities as explained in the text.

The work function difference for the case where the parasitic junction forms is only $\Delta WF = WF_{electrode} - WF_{a-Si:H(p)} \approx 5.3 - 4.8 = 0.5$ eV. An opposed band bending in the a-Si:H(p) is observed, the Schottky barrier. The parasitic junction stretched through the a-Si:H into the c-Si, which means that the c-Si band bending is also reduced. For this case the electrical potential difference and band bending are shared as follows, a-Si:H(p) (~ -0.29 eV), a-Si:H(i) (~ 0.18 eV) and the c-Si (~ 0.5 eV).

For the unsuited TCO work function, upon operation a very low excess carrier density is sufficient to push the hole contact in high-injection conditions. This is shown for MPP and OC conditions in Figure 4.12. For both cases the hole density (dashed red lines) exceeds the equilibrium hole density ($p \gg p_0$) and p/n at the interface to the electrode is close to unity. The non-ideal voltage extraction and the gradient in the hole QFL are highlighted in green. Such conditions are not observed for the flat-band case. The hole density is much higher, hardly changed with respect to equilibrium and well above the electron density. A gradient in the hole QFL is not observed and the external voltage matched the implied voltage for all working conditions. The local currents are also shown in Figure 4.12. The numbers in the current density graphs quantify the recombination current density in different device region. From left to right, at the electrode's interface, within the doped and undoped a-Si:H and in the c-Si. For OC conditions device recombination is clearly limited by the absorber for flat-band conditions (black) as indicate by the fact the most of the generation current recombines in the absorber (41.5 mA/cm^2). This is not the case for the unsuited work function, only 30.3 mA/cm^2 recombine in the absorber and a significant fraction in the a-Si:H and at the interface to the electrode⁶. For MPP conditions the recombination is much lower as current exits the device (J_{MPP}). Now the generation current is nullified by both the J_{MPP} and the global recombination current. Again, at the interface of the electrode the recombination current is higher compared to flat-band conditions.

J-V and *Suns-V_{oc}* characteristics

The non-ideal voltage extraction leads to some peculiarities of *J-V* and *Suns-V_{oc}* characteristics which can be exploited to identify losses arising from a poor carrier selectivity. The left graph in Figure 4.13 shows the *J-V_{light}* curves (solid lines) and *J-V_{dark}* curves shifted by the J_{sc} (dashed lines) from the two cells above (black, red) and another one with $WF_{electrode} = 5.0$ eV (grey). The *J-V_{light}* curves for which the current is plotted vs. the implied voltage are shown as well (*J-iV_{light}*, green

⁶ For amore detail recombination loss analysis it is referred to the results published in Ref. [94] by the author.

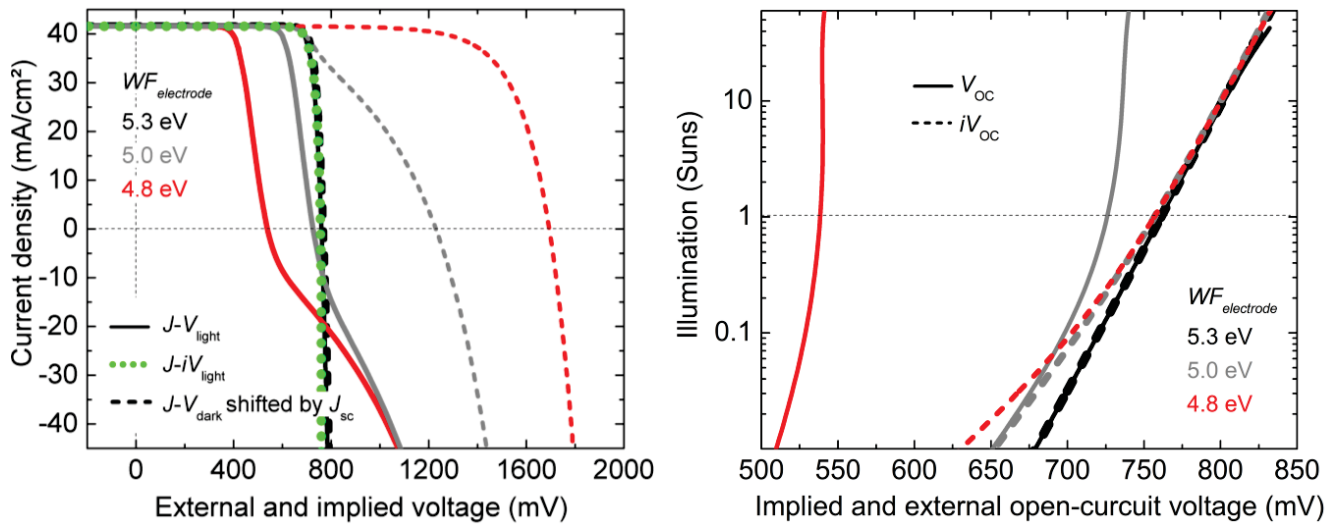


Figure 4.13. Left, $J-V_{light}$, $J-iV_{light}$ and the $J-V_{dark}$ characteristics for three different $WF_{electrode}$. The $J-V_{dark}$ is shifted by the J_{sc} . Right, $Suns-V_{oc}$ and $Suns-iV_{oc}$ characteristics.

dotted lines) and are identical for all variations. The cell featuring flat-band conditions (black) shows the characteristics of a properly operating device. The $J-V_{light}$ and $J-V_{dark}$ characteristics overlap which means the shifting approximation, i.e. the superposition principle is valid. Furthermore, the external and the implied voltage are identical for all working conditions (green line matches the black). This conditions are not fulfilled for the unsuited work functions. The $J-V_{light}$ characteristic shows an s-shaped behavior which is reflecting the influence of the opposing Schottky contact. The superposition principle fails and the external voltage is below the internal voltage as none of the $J-V_{light}$ curves matches the $J-iV_{light}$ curve.

Another import particularity of such contacts is the illumination level dependence of the implied and external J voltage at OC conditions. The $Suns-iV_{oc}$ and $Suns-V_{oc}$ of the three cells are shown in in the right graph in Figure 4.13. It can be seen that the deviation between both curves, which is the voltage loss in the contact region, becomes more pronounced with increasing illumination intensity. This follows from the fact that maintaining low-injection conditions and an ideal voltage extraction becomes more challenging with increasing illumination intensities and excess carrier density. Accordingly, the $Suns-V_{oc}$ curves deviates from the $Suns-iV_{oc}$ curve depending on the ability to maintain an ideal voltage extraction. Another observation is that for high illumination intensities and high excess carrier densities the iV_{oc} 's are rather similar. This is explained by the fact that the overall recombination becomes dominated by the contribution from the intrinsic c-Si bulk recombination rather than the recombination by the contacts at its surface. Consequently, for above 1 sun the same $Suns-iV_{oc}$ curves are observed.

As will also be shown in the experimental section, one striking feature of such Suns- V_{oc} curves is that the voltage loss in the contact region manifests itself in a slope of the Suns- V_{oc} curve which deviates from the one of an device which performs ideal in terms of voltage extraction. Furthermore, the application of illumination intensities well above 1 sun conditions makes the investigation more sensitive to the voltage loss in the contact region. This allows an easy evaluation of different contact schemes reading an ideal voltage extraction.

Interplay of a-Si:H doping and TCO work function:

Now, in addition to $WF_{electrode}$ the influence of the a-Si:H doping is taken into account. Both parameters are changed in such a way that they cause flat-band, depletion and accumulation conditions. The external and implied cell parameters are studied for MPP and OC conditions in detail as it is also of great concern to point out that a good carrier selectivity at OC does not imply a well-working device. More precisely, it shall be pointed out that the requirements on the carrier selectivity at MPP are more stringent as compared to OC.

Three different doping levels have been chosen for the p-doped layer as shown in (Figure 4.14). The idealized case where $WF_{a-Si:H(p)}$ matches the valence band energy (5.6 eV), this layer is degenerately doped and shows rather metal like behavior. And the more realistic case where the Fermi level is 0.3 or 0.42 eV below the valence band and $WF_{a-Si:H(p)}$ amounts to 5.3 and 5.18 eV, respectively. We also considered the case where the p-doped layer is omitted and the contact properties are defined by the metal like electrode (MIS like structure from section 4.2.4). $WF_{electrode}$ is changed from a very high value of 5.6 eV which matches the valence band energy of a-Si:H to a very low value of 4.8 eV which is near mid-gap of a-Si:H.

Figure 4.14 shows how the electrode's work function and the p-doping of the a-Si:H layer interact. The different a-Si:H doping levels are distinguished by the color, the case in which the doped layer is omitted is shown in green. Basically, Figure 4.14c reveals that in terms of efficiency (solid lines) a high doping of the a-Si:H is needed and $WF_{electrode}$ has to be well above the valence band energy of the absorber (5.18 eV). The high $WF_{electrode}$ is needed to prevent the depletion of the contact and a high doping helps to restrict this depletion to a small fraction of the p-doped layer where it has only a small influence on the overall SHJ properties. The implied efficiency (dashed lines) on the other hand, which is reflecting the upper efficiency limit imposed by the c-Si surface passivation by the contact and the intrinsic c-Si bulk recombination is hardly effected by $WF_{electrode}$ and the a-Si:H doping. Basically, the implied efficiency would be the one obtained if low-injection conditions could be preserved in the contact region.

For a detailed investigations first the EQ conditions are investigated, more precisely the hole density in the contact region in Figure 4.14b. The p/n ratio at the interface to the electrode (dash-dotted lines) is defined solely by $WF_{electrode}$ and increases with $WF_{electrode}$. At the c-Si surface (solid lines) the p/n ratio is additionally influenced by the doping and WF of the a-Si:H(p) in-between. The lower the a-Si:H(p) doping is the stronger is the influence of $WF_{electrode}$. This is because for decreasing net doping the a-Si:H(p) layer loses its ability to shield the parasitic built-in potential which results from the difference between $WF_{electrode}$ and $WF_{a-Si:H(p)}$. For a low doping this parasitic band bending penetrates further into the contact and also modifies the carrier density at c-Si surface. The vertical dotted lines indicate where $WF_{electrode} = WF_{a-Si:H(p)}$ which corresponds to the flat-band conditions for a given a-Si:H doping, i.e. where $WF_{electrode}$ does not modify the contact. The p/n ratio at the c-Si surface (solid lines) reveals that for $WF_{electrode} < WF_{a-Si:H(p)}$ the contact region below the electrode gets depleted from holes. For $WF_{electrode} > WF_{a-Si:H(p)}$ the hole density is further increased, i.e. holes are accumulated in the contact region. For an extremely high net doping (black lines) the equilibrium carrier density in the a-Si:H and c-Si part of the SHJ are virtually unaffected by $WF_{electrode}$ as the induced band bending is restricted to the a-Si:H(p) in close proximity to the electrode and does not penetrate further into the contact. The screening length of the doped layer is the relevant parameter which determines the electrostatic shielding and the interaction between the the electrode and the a-Si:H / c-Si part of the SHJ underneath⁷. However, it can be seen that for a sufficiently high $WF_{electrode}$, more precisely for $WF_{electrode} > WF_{a-Si:H(p)}$, the doped layer is superfluous (green lines). This follows from the fact the work function of the electrode can provide a highly hole populated and inverted contact region alone (MIS like device).

In general, the local modification of the carrier density in the a-Si:H and at the c-Si surface by $WF_{electrode}$ result from the induced band bending and the built-in potential, respectively. The equilibrium band bending induced into the absorber (φ_{c-Si}) is shown by the dotted lines in Figure 4.14a. For flat-band conditions at the electrode / doped a-Si:H interface (vertical lines), the upper bound of φ_{c-Si} is defined by the work function difference between the doped a-Si:H and c-Si

⁷ A more detailed discussion on the importance of the screening length is given in the PhD thesis of Varache [23] and the correspond paper [125].

Unlike the simulations presented in this chapter the simulations in Ref [94] from the present autor and the work from Varache include tunneling transport which gives better quantitative results but lead to the same qualitative interpretation.

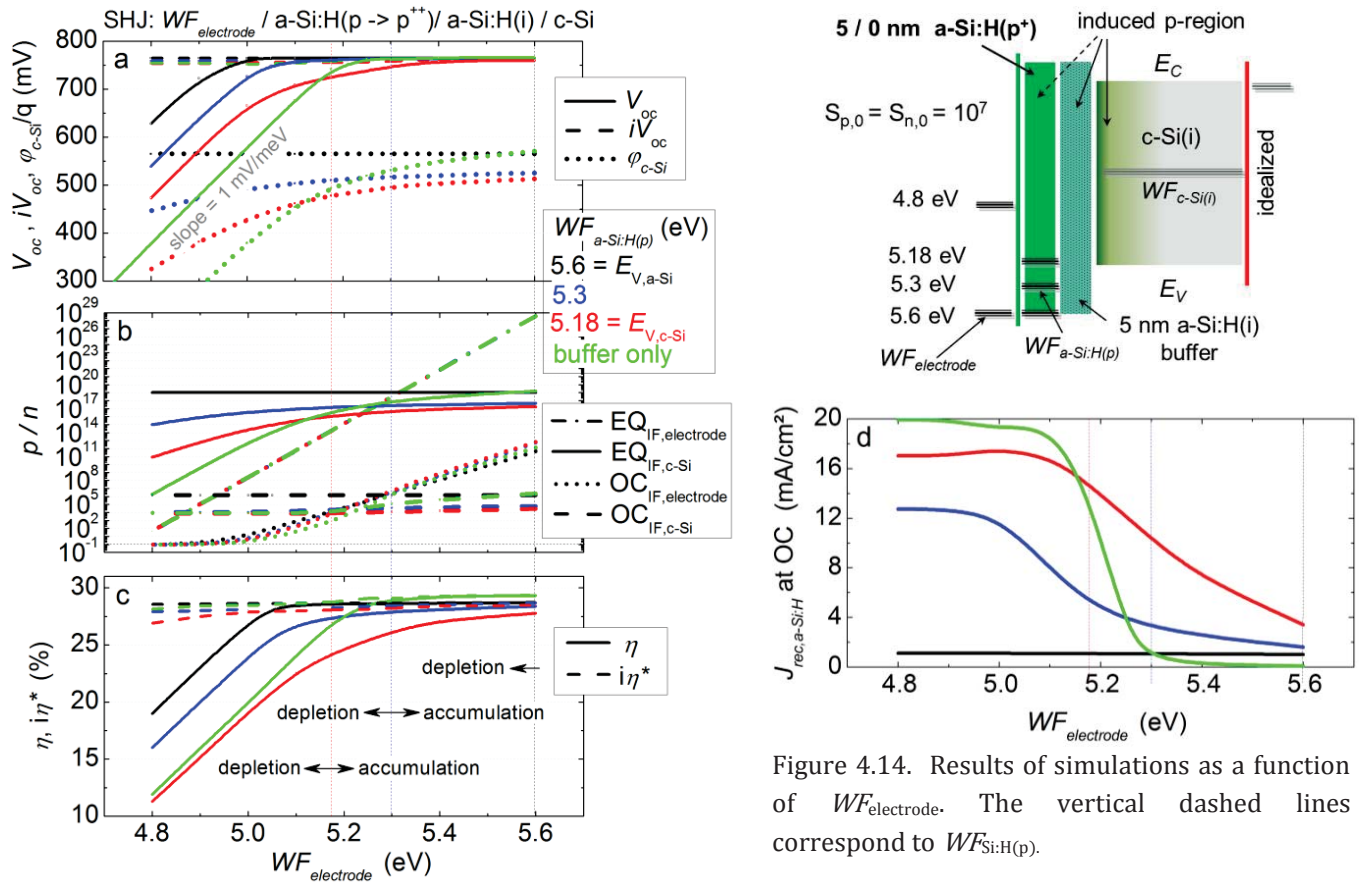


Figure 4.14. Results of simulations as a function of $WF_{electrode}$. The vertical dashed lines correspond to $WF_{Si:H(p)}$.

absorber, i.e. $\Delta WF = WF_{a-Si:H(p)} - WF_{c-Si(i)}$. If the p-layer is omitted (green) $\Delta WF = WF_{electrode} - WF_{c-Si(i)}$ defines the upper bound for the induced band bending. However, as motivated before some band bending is lost in the buffer or if lowly doped, in the p-layer itself. Hence, ϕ_{c-Si} is always below ΔWF if a buffer is present. For the intrinsic c-Si absorber the maximum ϕ_{c-Si} is about $E_{g,c-Si} / 2 = 0.56$ eV which follows from $\Delta WF = E_{v,c-Si} - WF_{c-Si(i)} = 5.18 - 4.62 = 0.56$ eV. The band bending lost in the buffer is best quantified for the MIS structure. Here, $WF_{electrode}$ has to be well above 5.18 eV and hence well below the valence band of the c-Si absorber to approach this upper limit. Furthermore, only for the unrealistic high p-doping where $WF_{a-Si:H(p)} = 5.6$ eV the standard configuration featuring a doped a-Si:H layer yield's such a high band bending. This highlights that the presence of the buffer comes at the expense of a higher WF of the electrode and/or p-layer which has to be well below the valence band energy of the c-Si absorber.

Figure 4.14b shows that under open-circuit conditions the p/n ratio at the interface to the electrode (dotted lines) and the c-Si absorber (dashed lines) is reduced as compared to EQ conditions. Especially in the a-Si:H part of the SHJ the p/n ratio is approaching unity for a low doping and a low $WF_{electrode}$ as it is indicated by the p/n ratio at the interface to the electrode. That

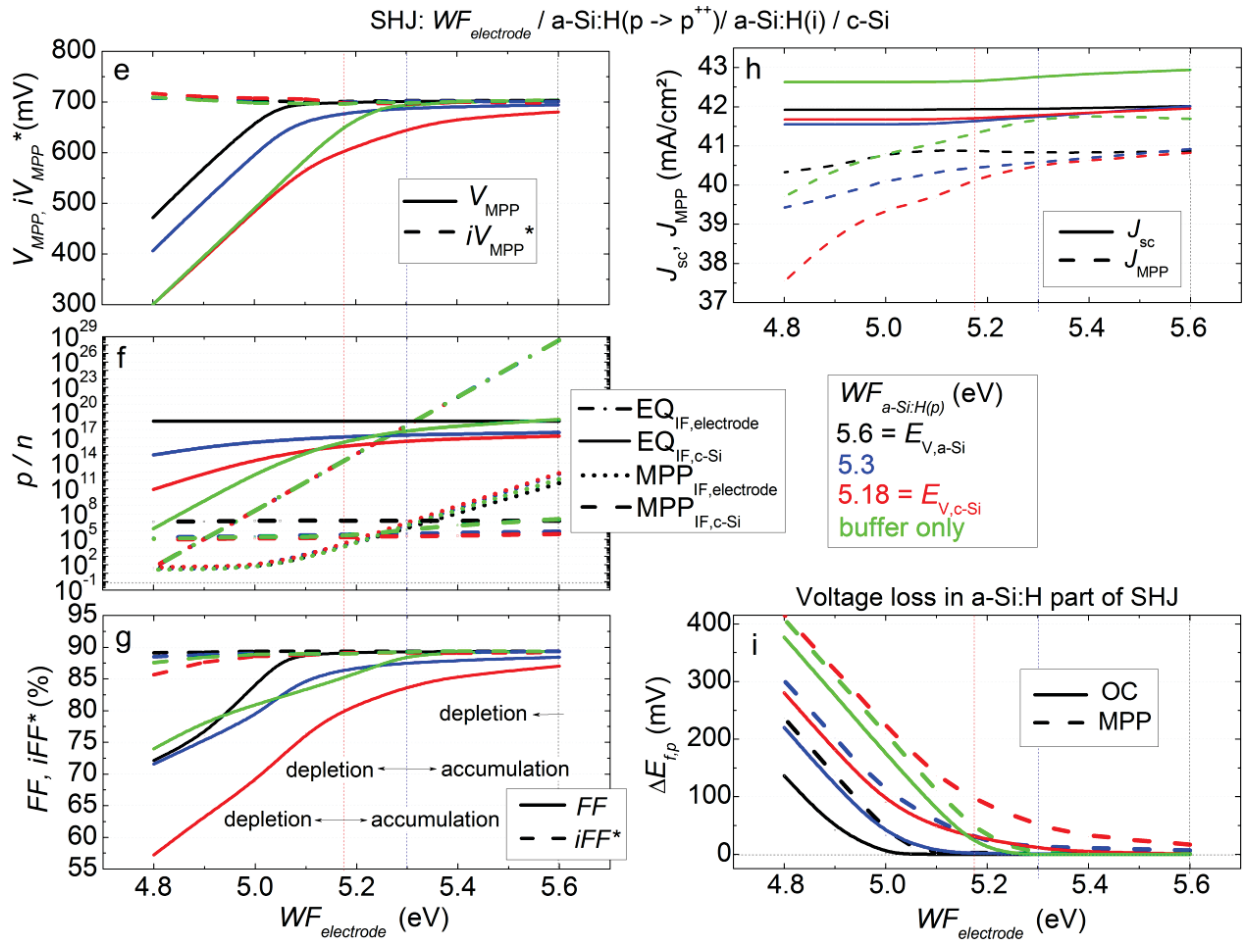


Figure 4.15. Further simulation results for the structure of Figure 4.14 mainly for MPP conditions. h) is representing the voltage lost in the whole contact region for MPP and OC conditions which corresponds to the reduction of the hole quasi Fermi level ($\Delta E_{f,p}$) in the p-contact. This values exactly matches the difference between the implied voltage and the external voltage. No voltage loss takes place in the c-Si part of the contact.

the recombination in the a-Si:H bulk and at the interface to the electrode are also strongly increased for such conditions can be deduced from Figure 4.14d and was shown before in Figure 4.12. The lower the p-doping and $WF_{electrode}$ are, the higher is the parasitic current which flows in the a-Si:H part of the SHJ triggered by the recombination there.

In Figure 4.15i the voltage losses in the contact region for MPP (dashed lines) and OC conditions (solid lines) are shown. It is the difference between the implied and the external voltage for MPP conditions (Figure 4.15e) and OC conditions (Figure 4.14a). The excellent passivation of the c-Si by the contact for OC conditions and the lack of extrinsic c-Si bulk recombination allow for a nearly constant and very high iV_{oc} of 755-765 mV as shown by the dashed lines in Figure 4.14a. The same holds for the MPP conditions, a very high and constant iV_{MPP} of 702-709 mV (Figure 4.15e) is reached. It can clearly be seen in Figure 4.15i that with

lower doping and lower $WF_{electrode}$ the hole contact loses its ability to maintain the hole quasi Fermi level in the SHJ. An important finding is that this voltage loss is always much higher for MPP conditions as compared to OC conditions (dashed and solid lines in Figure 4.15i). Besides the voltage at MPP, the current (density) at MPP is also significantly reduced as compared to short-circuit (SC) as shown in Figure 4.15h. Hence, the FF from the J - V characteristics (solid lines) in Figure 4.15g is well below the implied FF ($iFF^* = iV_{MPP} \cdot J_{MPP} / iV_{oc} \cdot J_{SC}$).

Summarizing the result from above, to match the implied efficiency (Figure 4.14c) and hence preserve low-injection conditions in the contact region either a suited electrode featuring a high $WF_{electrode}$ well above the absorbers valence band has to be applied as shown for the MIS like device. Or, if the latter cannot be ensured, an additional doped layer is needed that partly compensates for the unsuited WF of the electrode. The higher the a-Si:H doping is the higher is the tolerance to $WF_{electrode}$. In general, for the optimization of the SHJ both the a-Si:H and electrode properties have to be considered to maximize the efficiency.

Experimental investigations of the influence of the a-Si:H doping, an improved work function matching and high work function electrodes which allow to omit the doped a-Si:H are presented in chapter 6.

The induced c-Si band bending as an indirect measure for the contact's selectivity

It should be noted that except for the idealized very highly doped p-layer ($WF_{a-Si:H(p)} = 5.6$ eV, Figure 4.14) the equilibrium band bending which is induced into the absorber (φ_{c-Si}) is a good measure for the selectivity of the contact. This is shown in Figure 4.16a where the efficiency is plotted as a function of φ_{c-Si} and the equilibrium p/n ratio at the c-Si surface. The lower the p-doping of the a-Si:H is the more sensitive is the efficiency to φ_{c-Si} . This follows from the fact that with decreasing doping the a-Si:H layer loses its ability to shield the parasitic band bending which is induced by the TCO electrode into the a-Si:H. This is most pronounced for the MIS like structure where φ_{c-Si} is governed solely by the properties of the electrode as a doped layer is omitted. This again explains the close affinity of SHJ cells to the other class of induced junction devices, namely MIS or SIS devices. The most notable difference is that SHJ cells are featuring a semiconductor buffer and that the (lowly) doped and undoped a-Si:H are prone to operate in high-injection conditions. A problem, which is not observed for the metals and degenerately doped TCO or pol-Si films of MIS and SIS cells and their dielectric buffer layers, respectively.

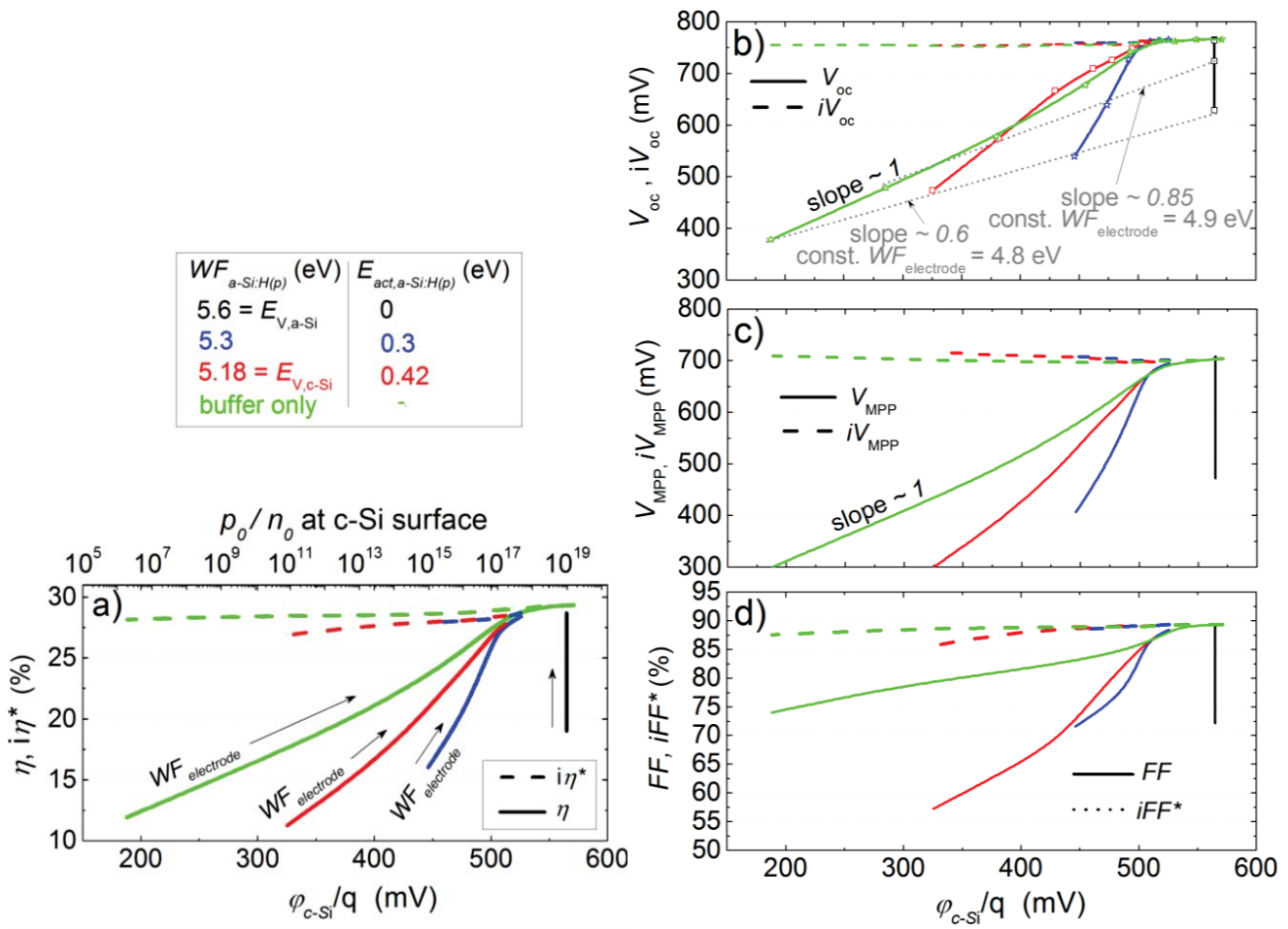


Figure 4.16. Data from Figure 4.14 and Figure 4.15 plotted as a function of the induced c-Si band bending. For a) the corresponding equilibrium hole/electron ratio at the c-Si surface is also given. Results for the different p-type doping levels of the a-Si:H(p) layer are distinguished by the color, the electrode’s work-junction increases from left to right as indicated by the arrows in a). The dotted lines in b) connect the conditions for a comparable work function of the electrode (either 4.8 or 4.9 eV) for the different levels of p-type doping.

For the voltage at open-circuit and MPP conditions a roughly linear dependence on ϕ_{c-Si} for the regime where external voltage is limited by selectivity rather than surface passivation ($V < iV$) is observed. An ideal voltage extraction ($V \approx iV$) is observed for an ϕ_{c-Si} and p_0/n_0 of about 520 meV and $5 \cdot 10^{17} \text{ cm}^{-3}$, respectively. For this conditions p_0 at the c-Si surface is about $1 \cdot 10^{19} \text{ cm}^{-3}$. For $V < iV$ the slope is unity for the case that no doped a-Si:H is present and where ϕ_{c-Si} defined mainly by $WF_{electrode}$. This is similar to the results from Figure 4.9. The presence of the doped layer result in the $WF_{electrode}/a-Si:H(p)$ and $a-Si:H(p)/c-Si$ double junction causing the steeper slope. A slope below unity is observed for the case that $WF_{electrode}$ is constant and that the doping is variable (grey lines in Figure 4.16b). Some band bending is need in this case to account for the parasitic $WF_{electrode}/a-Si:H(p)$ Schottky contact.

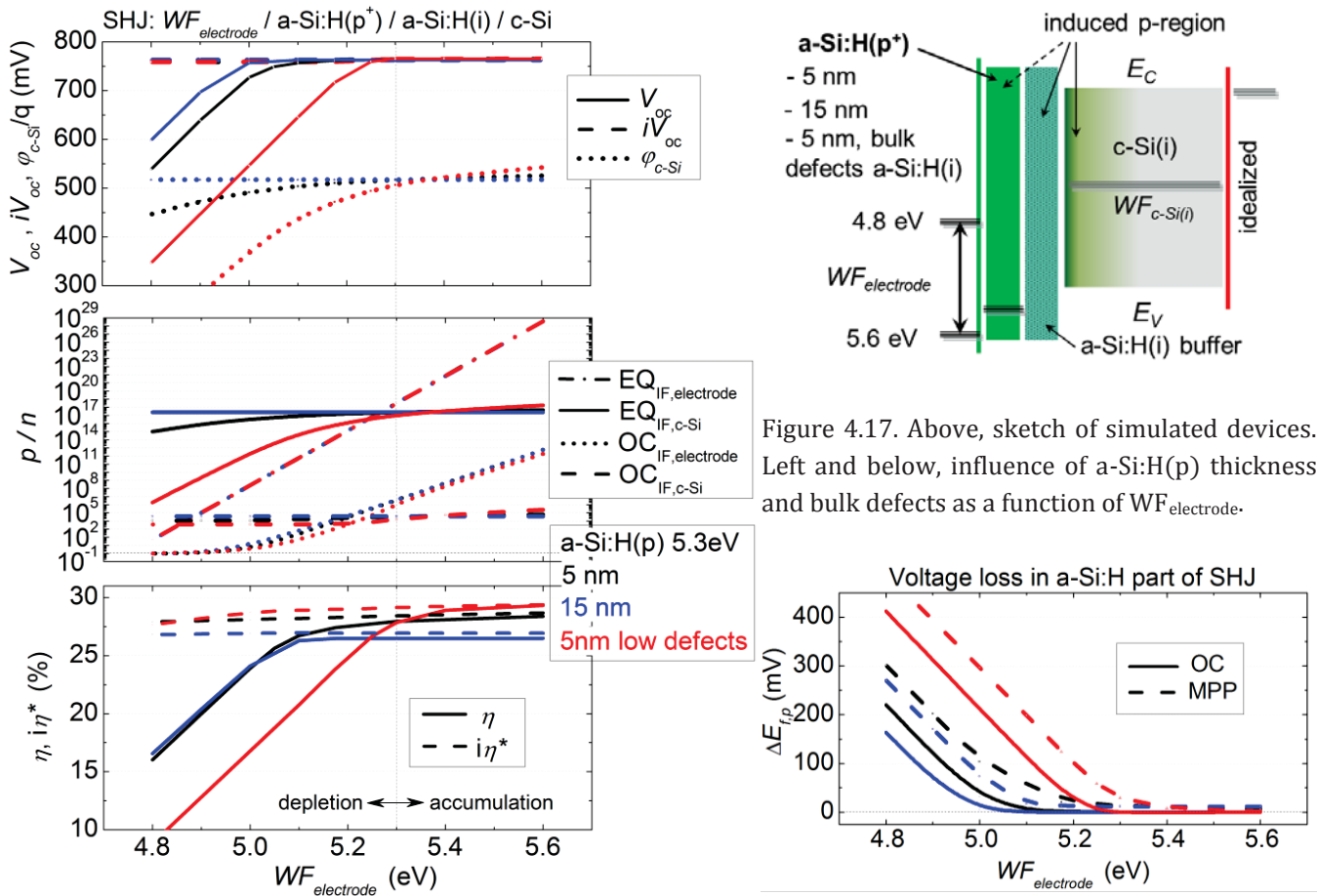
The correlation between φ_{c-Si} and the different cell parameter and the efficiency is an important finding since φ_{c-Si} can experimentally be easily determined e.g. by surface photo-voltage (SPV) measurements [18], [126], [89]. This technique was pioneered for SHJ device at the HZB Berlin and has proven helpful for the analysis of the induced junction which results from the TCO and a-Si:H properties in this thesis. Experimental results are presented in chapter 6.

a-Si:H(p) thickness and bulk defects: Effective screening length

Here, we shall briefly look at two other parameters that influence how the electrode and the doped a-Si:H interact. As indicated in Figure 4.17, (i) the thickness of the p-doped layer was increased from 5 to 15 nm and (ii) a lower defect density for a 5 nm p-doped layer was assumed. For the latter, the defect density corresponds to the one of the undoped a-Si:H buffer. The net doping and thus the free hole density is the same for all p-layers, E_{act} amounts to 0.3 eV which corresponds to $WF_{a-Si:H(p)} = 5.3$ eV.

The results for the three different p-layers are plotted vs. $WF_{electrode}$ in Figure 4.17. It can be seen that in terms of V_{oc} a higher a-Si:H(p) thickness (blue vs. black) can tolerate a lower $WF_{electrode}$ to some extent. This is due to the fact that for the thicker layer the depletion is restricted mainly to the doped layer itself and does not modify the junction properties underneath. This can be inferred from the fact that φ_{c-Si} and the equilibrium p/n ratio at the c-Si surface (solid lines) are not affected by $WF_{electrode}$ for the thicker p-layer. The local depletion of the doped layer can be deduced from the reduced equilibrium p/n ratio at the electrode's interface (dashed dotted lines). The bottom-right graph shows that the voltage loss in the a-Si:H part of the SHJ is reduced for the thicker p-layer for MPP conditions as well. Nevertheless, with regards to the efficiency for an increased thickness of the doped layer (at the illuminated side) the improved external voltage is compensated by the increased parasitic absorption in the thicker p-layer. The current loss in the additional 10 nm is significant and amounts to about 2 mA/cm².

For both 5 nm layers (black and red) comparable conditions are observed for flat-band conditions, i.e. $WF_{electrode} = 5.3$ eV. However, for the more relevant case of a lower $WF_{electrode}$ and a depleted a-Si:H, the a-Si:H(p) with the same net doping but less bulk defects (red) shows a worse performance. The voltage loss in the contact region is much higher for both OC and MPP conditions and the efficiency is strongly reduced for this layer. This is explained by the higher screening length of the less defective layer. As nicely motivated for silicon thin film cells in Ref



[127], for SHJ cells by Varache [23], [125] and by the present author in Ref [95] (equation (2.5)) the reduced density of defects in the a-Si:H bulk also means that the density of rechargeable states is reduced. For the layer with the lower defect density the screening length exceeds its thickness which means that additional rechargeable states in the undoped a-Si:H and the c-Si part of the SHJ underneath are needed to screen the parasitic band bending. Consequently, the depletion is not only restricted to the doped layer but stretches far into the c-Si part of the SHJ. This global depletion can be inferred from the influence of $WF_{electrode}$ on φ_{c-Si} and the equilibrium p/n ratio at the c-Si surface which is much higher for the less defective 5 nm layer (red). Hence, while the bulk defects of the a-Si:H are detrimental in terms of doping efficiency they seem to be essential to mitigate the problem of the opposing Schottky contact.

4.2.6 Role of electric field

A p/n junction without an electric field

In this subsection the relevance of the electric field for the carrier selectivity and the movement of holes and electrons in opposite directions shall be briefly discussed on the basis of the fictive device structure which is also found in chapter 6.8 of the textbook from Würfel [9] and is qualitatively discussed there. It shall be shown that the electric field, that inevitably forms when enabling a highly hole populated device region via doping or by an induced junction, is a side-effect rather than it is actually governing the carrier selectivity.

This issue was also discussed by Cuevas *et. al.* [128] and Würfel *et. al.* [39] more recently. It was also pointed out that while an electric field results from the way in which a high hole density in the contact region is reached. The important fact is that the local hole density is increased while the electron density is decreases and not the presence of the accompanying electric field. Taking into account that the dominant driving force that governs the parasitic current of the “wrong” carrier species (electrons) from the absorber into the hole contact is the diffusive force acting on the electrons. The concentration gradient seen by the electrons of the absorber can be reduced if less electrons recombine at the hole contact. This is reached by the increase and decrease of the equilibrium hole and electron density in the contact region, respectively, according to

$$J_0 = \frac{q n_i^2}{p_{0,maj}} S_0 = q n_{0,min} S_0 \quad (4.7)$$

Hence, the unwanted property of the hole contact to act as a sink for the electrons is diminished in this way. It ensures a small electron current and hence that the total current is dominated by the hole current.

To demonstrate the irrelevance of the electric force acting on the electrons, two p/n junction devices were simulated which are distinguished by their hole contact. The band diagram, the local electric potential (φ), electron affinity (χ) and hole, electron density are shown in Figure 4.18 for EQ (left) and OC (right) for both structures. The reference structure (grey) corresponds to a highly doped p/n homojunction where the p-side is featuring a spatial variation of the acceptor doping density (N_A) as shown by the green line. This p-contact has the constant band gap and the electron affinity of c-Si. For the sake of simplicity, the maximum doping density in the p-doped region and of the n-doped absorber was set to the density of states in the valence and conduction band (degenerately doped). It means that in the highly doped region E_f and the valence and conduction band merge, respectively. Hence, the difference between the work

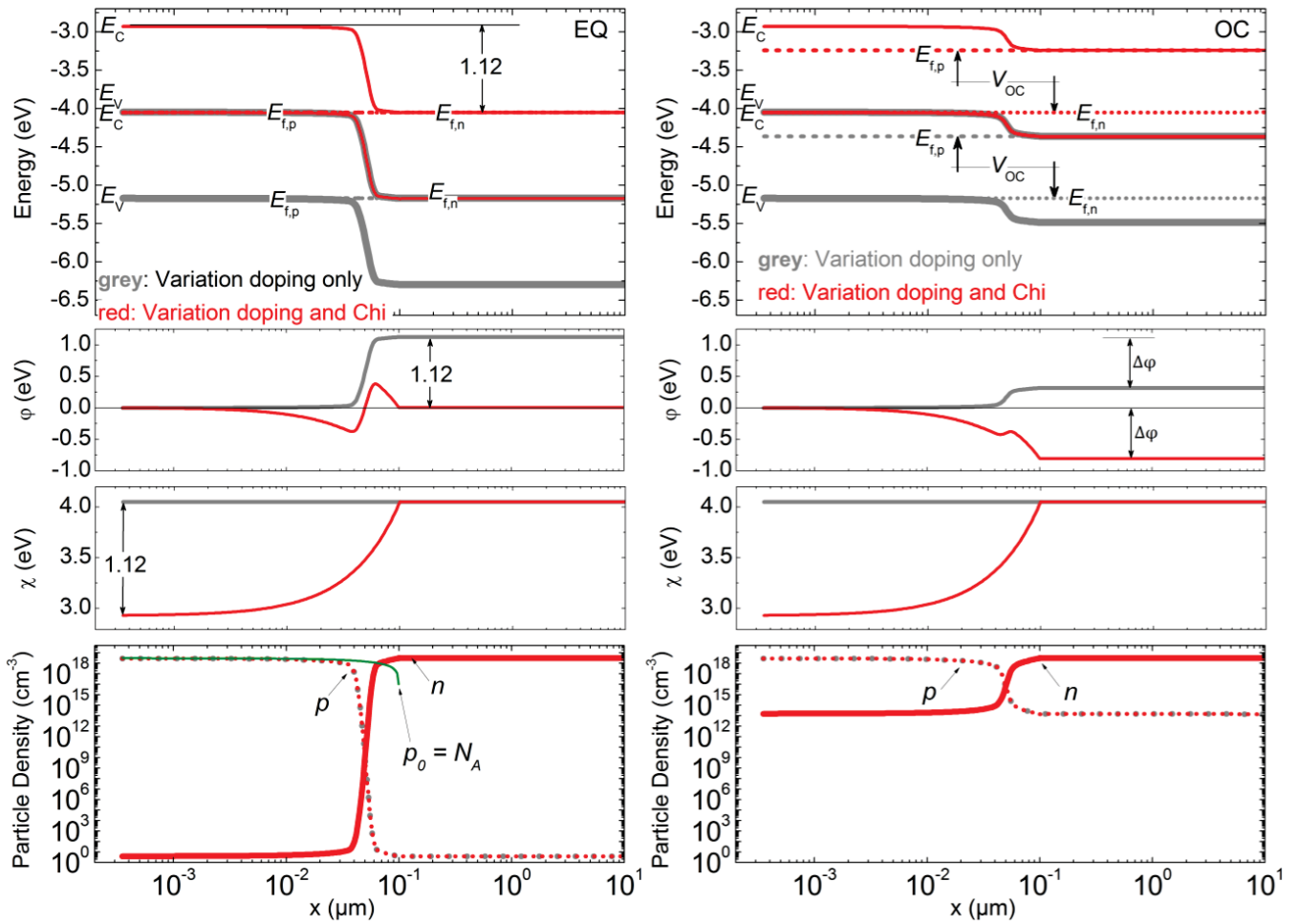


Figure 4.18. Band diagrams, electric potential difference, electron affinity and hole and electron density for EQ (left) and OC (right) of the two structures discussed in the text. The first 100 nm of the devices are the p-doped region which is in contact to an n-absorber. The potential is fixed at $x = 0$ nm.

function of the p- and n-region amounts to the difference of E_V and E_C and thus the band gap. The electric potential difference that results from the contact formation between both materials for EQ is defined by this quantity and thus amounts to 1.12 eV as shown in the middle graph. For the band diagram of the reference structure only this electric potential difference is responsible for the bending of the bands.

To get the same distribution of carriers within the fictive device (red) for EQ conditions but omit the electric field, an identical spatial variation of the acceptor doping (doping profile) was assumed but the accompanied variation of ϕ with p-doping has to be compensated. This is done by a spatial variation of the composition of the material. This means we have to construct a heterojunction that not only as a graded doping but also a grading of χ in the p-layer. To this end, χ at $x = 0$ nm is reduced by 1.12 eV compared to the reference and approaches the values of c-Si

(4.05 eV) at the end of the p-region as shown in Figure 4.18 in red. This results in the parallel shift of the band diagram towards lower energies compared to the reference but the same band bending is observed.

A peculiar shape of the electrical potential is observed at the junction which might be explained by a dipole [128]. Nevertheless, it can be seen that the band bending does not follow this behavior and is identical to the one for the reference structure in grey. Hence, the only difference between both structures visible in the band diagram is that the band diagram of the fictive structure is shifted by the lower χ at $x = 0$ nm. The band bending is identical but originates from the electric field for the reference structure and for the fictive structure only the variation of χ is responsible for the band bending. For the latter an electric field does not exist and the bending of the bands can be understood as a graded conduction (and valence) band offset which is similar to the structure in Figure 2.5.

Looking at the results for OC conditions (right in Figure 4.18), except for the electric field an identical behavior is observed for both structures. For both φ and thus the band bending are reduced by the same amount. However, φ is pointing in opposite directions. The increase of the hole and electron density within the device and the accompanied compensation of the space charges causes the reduction of the internal field. As the recombination parameters (S_0, \dots) and the equilibrium carrier concentrations are identical for both devices the recombination for OC must be identical too. This is actually true and quantified by the external voltage for OC conditions which amounts to $V_{oc} = 810$ mV for both devices (intrinsic c-Si recombination was neglected). The external voltage corresponds to the splitting of $E_{f,p}$ and $E_{f,n}$ in the p- and n-region, respectively, as voltage extraction is ideal, i.e. no gradient in the majority carrier Fermi-level is observed in the contact region. The remaining band bending at OC is defined by $V_{bi} - V_{ext}$ and amounts to 1120 mV $-$ 810 mV = 310 mV for both structures. The fact that the electric field of the fictive structure is pointing in the opposite direction and is also much higher clearly shows that the blocking behavior of the electric field preventing the parasitic electron injection from the absorber into the p-region cannot be the relevant force governing the selectivity of a p/n junction.

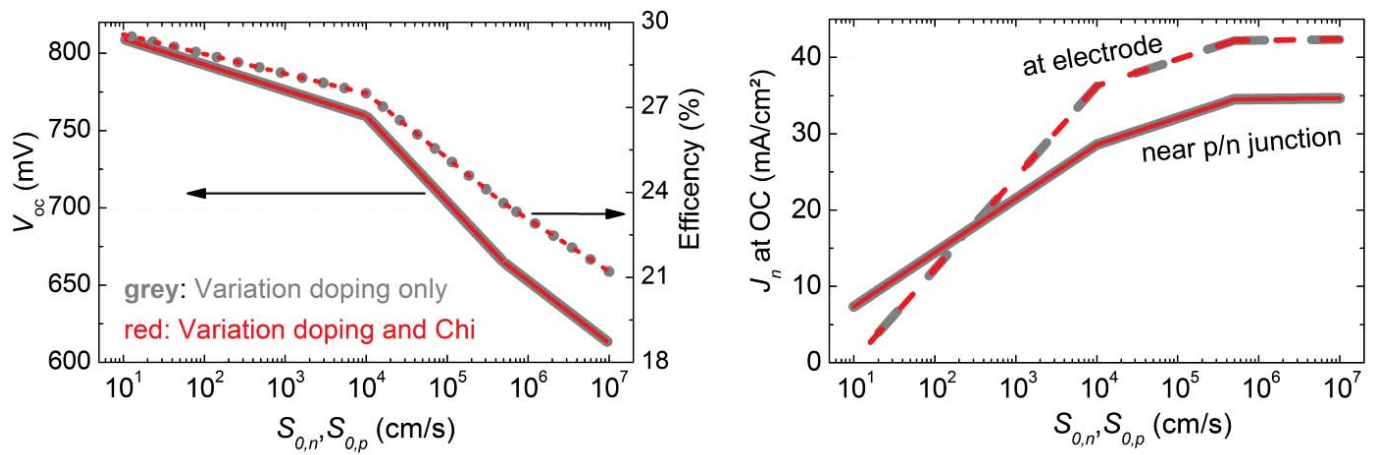


Figure 4.19. Left, external V_{oc} and efficiency of the two structures discussed in the text as a function of S_0 at the interface to the electrode. Right, the corresponding electron current density for OC conditions at the interface to the electrode and near the p/n junction (at $x = 100\text{nm}$ in Figure 4.18). The V_{oc} is above the intrinsic limit of the c-Si absorber as Auger and radiate recombination have not been considered in the whole structure.

These findings are corroborated by the right graph in Figure 4.19 where the parasitic electron current, i.e. the recombination current is shown for OC conditions as a function of S_0 . Two currents are shown, one which is injected from the n-absorber into the p-region (near the p/n junction) and the one at the interface to the electrode for which S_0 was varied. The variation of S_0 was chosen to change the recombination activity of the p-region and to probe how the n-injection from the absorber responds for both systems. No difference is observed. The electron currents are the same irrespective of the chemical passivation and the position in the hole contact. The annihilation of electrons (and holes) by recombination at the surface which increases with S_0 acts as a sink for electrons in the same way, despite the opposing electrical field. The left graph reveals that despite this significant difference in the drift force acting on the carriers, both devices behave exactly alike for OC conditions and the identical high efficiency reveals that this is also the case for MPP and short-circuit conditions.

4.2.7 Important bulk parameters for semiconductor buffer layers

Band gap, mobility and thickness:

Transition between electrically opaque and transparent buffers

In the following the influence of the electrical band gap (E_g), hole and electron mobility (μ_p, μ_n), thickness and bulk defect density of the buffer layer are investigated. This is different from the standard consideration for a buffer layer, which is its chemical passivation of the c-Si absorber. The aim is to point out the important parameters which allow the buffer to decouple the iV_{oc} of the absorber from the abundance of defects at the interface at the electrode. The simulated structure is given in Figure 4.20. As the iV_{oc} is the main concern flat-band conditions have been assumed (no field-effect passivation). Accordingly, the absence of an induced or doped junction limits the external V_{oc} to below 400 mV for all structures. Moreover, when changing E_g of the buffer the conduction and valence band offset are kept similar to avoid asymmetries for the hole

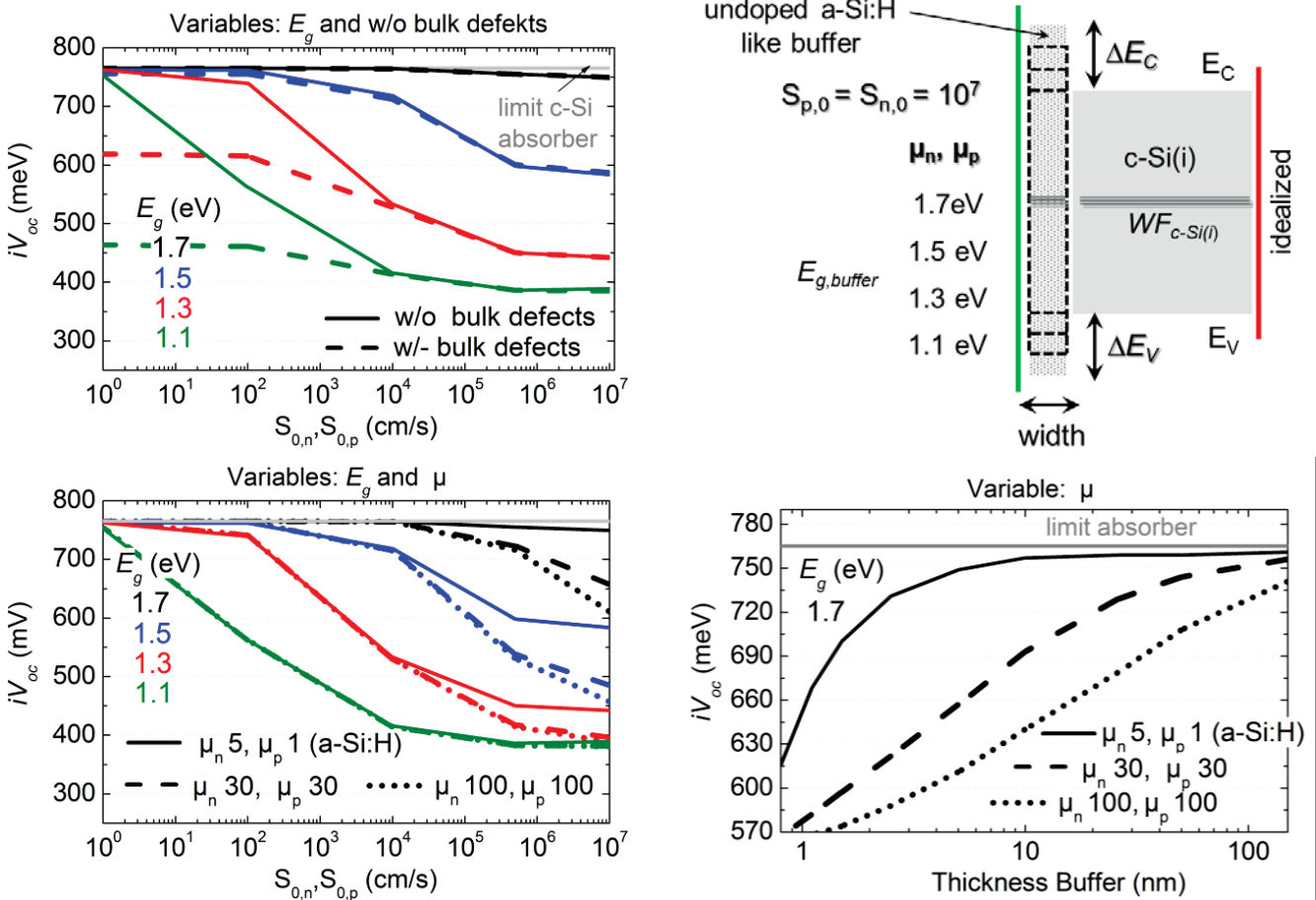


Figure 4.20. Top-right, sketch of simulated structure indicating the variation of the buffer layer's band gap. Left, iV_{oc} as a function of S_0 for 5 nm thick layers of different E_g . Top-left, with and without bulk defects. Bottom-left, different mobility, without bulk defects. Bottom-right, iV_{oc} as a function of buffer layer thickness for different mobility. $S_0 = 10^7$ cm/s, $E_g = 1.7$ eV and bulk defects omitted. Mobility in is cm^2/Vs .

or electron injection from the absorber caused by asymmetric hetero-barriers. It should be remembered that tunneling is not considered in the simulation. However, it is very likely that tunneling is a relevant recombination and transport path for the a-Si:H / c-Si hetero-junction [20], [129], [130]. So the result presented here present an upper limit for the iV_{oc} as additional tunneling related recombination processes are not considered. In Ref [131] important parameters for buffer layers enabling a high iV_{oc} , other than chemical passivation, are also addressed.

The left graphs in Figure 4.20 show the iV_{oc} as a function of S_0 at the interface of the electrode for four different band gaps (different colors) of a 5 nm thick buffer. In the upper graph results with and without defects in the bulk of the buffer are compared. It can be seen that with increasing band gap the iV_{oc} becomes less sensitive to S_0 and the bulk defects. For an E_g of 1.7 eV the iV_{oc} is only about 10 mV below the intrinsic limit for an very high $S_0 = 10^7$ cm/s. The iV_{oc} rises with decreasing S_0 and if bulk defects are neglected the intrinsic limit is reached for $S_0 = 1$ cm/s regardless of E_g . It can be seen that for such a well-passivated interface additional bulk defects do not contribute to recombination for a high band gap. Hence, for a sufficiently high E_g surface and bulk recombination of the buffer are virtually eliminated.

Referring to the intuitive explanations from Ref [16] on the possibilities to lower the recombination current pre-factor and hence the recombination current this can be easily understood by

$$J_0 = \text{charge} \cdot \text{carrier density} \cdot \text{transport velocity} = q \frac{n_i^2}{p_0} \frac{\frac{kT}{q} \mu}{L_{eff}} = q n_0 \frac{\frac{kT}{q} \mu}{L_{eff}} \quad (4.8)$$

It shows that for an electrically opaque region [132] the reduction of n_i which comes along with the increase of E_g (Figure 2.5) yields a lower recombination owing to a decreased electron density (purple in equation (4.8)). The ocher-colored part in the equation above suggests that a low mobility will have a positive influence too. That the low mobility of a-Si:H actually is a key ingredient to allow for a high iV_{oc} is shown in the lower-left graph in Figure 4.20. The results for the high band gap buffer show that a low mobility makes the buffer electrically opaque and prevents the carriers from reaching the recombination active interface. To ensure that the buffer is opaque the width of the buffer must be above the effective diffusion length. The lower-right graph indicates that even for a high band gap, for a too low thickness the buffer becomes transparent and hence sensitive to S_0 . The transition between opaque and transparent for the

layer with the mobility of a-Si:H is at around 10 nm. For higher mobilities thicker layers are required to avoid reaching the recombinative interface. The results for the a-Si:H layer suggest that its effective diffusion length is in the range of 10 nm, for thicknesses below the layer becomes transparent and the iV_{oc} is strongly reduced. Interestingly, this is in the same thickness range for which a saturation of the iV_{oc} is observed experimentally. In short, the high band gap limits the recombination in the bulk of the buffer and the low mobility and a sufficient thickness keep the carriers within the low recombination active bulk which prevents them from reaching the highly recombinative electrode / buffer interface.

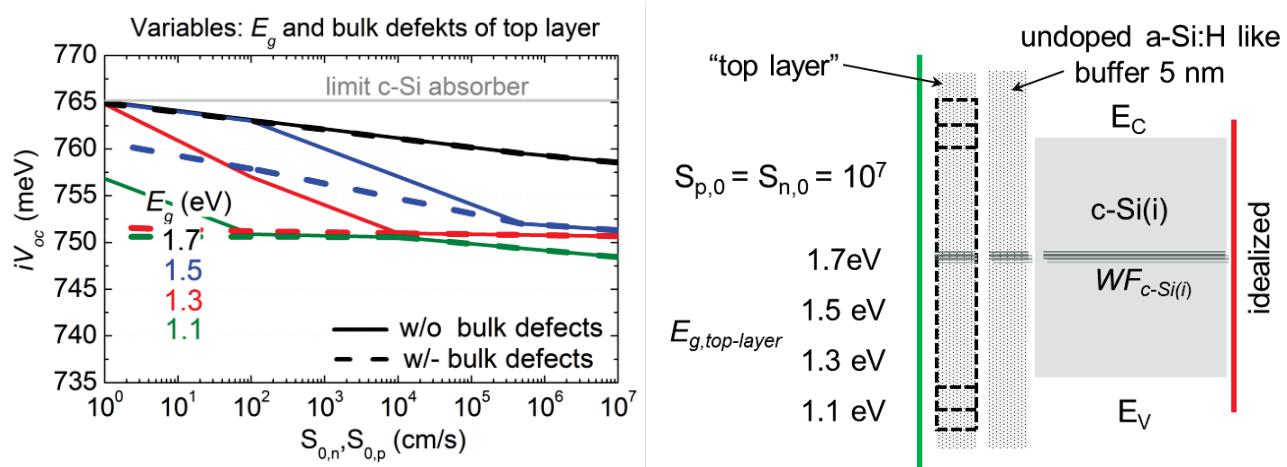


Figure 4.21. Right, sketch of simulated structure indicating the variation of the band gap of the layer on top of the buffer. Left, iV_{oc} as a function of S_0 for top layers with and without bulk defects and different E_g .

In Figure 4.21 it shall be motivated that the buffer decouples the c-Si passivation not only from the properties of the interface shared with the electrode but from the bulk properties of a layer which is placed on top of the buffer as well. This variation is intended to be representative for the case when μ c-Si layers which are featuring a lower band gap (higher n_i) and a higher mobility (electrically transparent) are grown on top of the a-Si:H buffer instead of the commonly applied high band gap amorphous layers. Besides the band gap also the bulk defects of the top layer are variables. It can be seen that the reduction of the band gap of the top layer and thus its increase of n_i has only a small influence on the iV_{oc} . For the 5 nm buffer which is not totally opaque (Figure 4.20 right) the iV_{oc} remains above 750 mV. This however is not a surprising result as for the worst case scenario where the buffer is in direct contact to the electrode and $S_0 \approx 10^7$ cm/s a similar high iV_{oc} was observed for this buffer for the structure investigated before. It should be noted that the reduction of the minority carrier density for the case that a junction is formed leads to further significant reduction of the density term in equation (4.8).

4.2.8 Selectivity from an asymmetric surface recombination velocity

Now we turn to the fictive and rather unrealistic contacts and come back to the issue of ideal voltage extraction. The ability of an asymmetric transition rate for electrons and holes directly at the interface of the electrode to enable an asymmetric hole and electron current into the electrode is discussed here. With this we are aiming to minimize the velocity term of the equation (4.5) and (4.6). It should be noted that the carrier selectivity of all contact schemes discussed before was based on the asymmetry of the density terms.

In theory, the easiest way to ensure that the charge transfer at the interface between the absorber and the external electrode is dominated by holes is to minimize the recombination rate of electrons while keeping the recombination of holes high enough to not limit their transition rate, i.e. the hole current. In this sense, the surface recombination velocity of electrons and holes ($S_{0,n}, S_{0,p}$) at the interface between the absorber and the electrode were changed over an extreme range. The local hole and electron current density at the interface are described by

$$j_{n,IF} = q S_{0,n} n_{IF} \quad (4.9)$$

$$j_{p,IF} = q S_{0,p} p_{IF} \quad (4.10)$$

A sketch of the simulated structure and some key results of the simulations are shown in dependence of $S_{0,n}$ in Figure 4.22. As no p-doping was assumed and the electrode is not characterized by a certain work function (no induced junction), the carrier distribution in the hole contact region is not modified with respect to the bulk of the absorber for equilibrium (EQ) which results in flat-band conditions at the surface of the intrinsic absorber. This is evidenced in the middle graph where $p \approx n$ (dotted lines).

Let's first look at the ability of the contact to passivate the c-Si absorber for OC conditions, i.e. to provide a high excess carrier density within the absorber and a high iV_{oc} (dotted lines upper graph). For $S_{0,p} = S_{0,n}$ (black) a value of 1 cm/s is sufficient to approach the intrinsic limit imposed by the c-Si bulk recombination (~ 760 mV). For $S_{0,p} \neq S_{0,n}$ the iV_{oc} is limited by the higher S_0 over a wide range. Going to extremely low $S_{0,n}$ a very high $S_{0,p} = 10^7$ cm/s can be tolerated in terms of surface passivation. Even though such conditions ($S_{0,p} \gg S_{0,n}$) are unrealistic for semiconductors system, it can be seen that such a contact has the ability to ensure a high external V_{oc} as well (solid lines). However, only for an extremely low $S_{0,n}$ and an extremely high $S_{0,p}$ the gap between iV_{oc} and V_{oc} is small. The middle graph showed that the p/n ratio at the interface is unity for EQ.

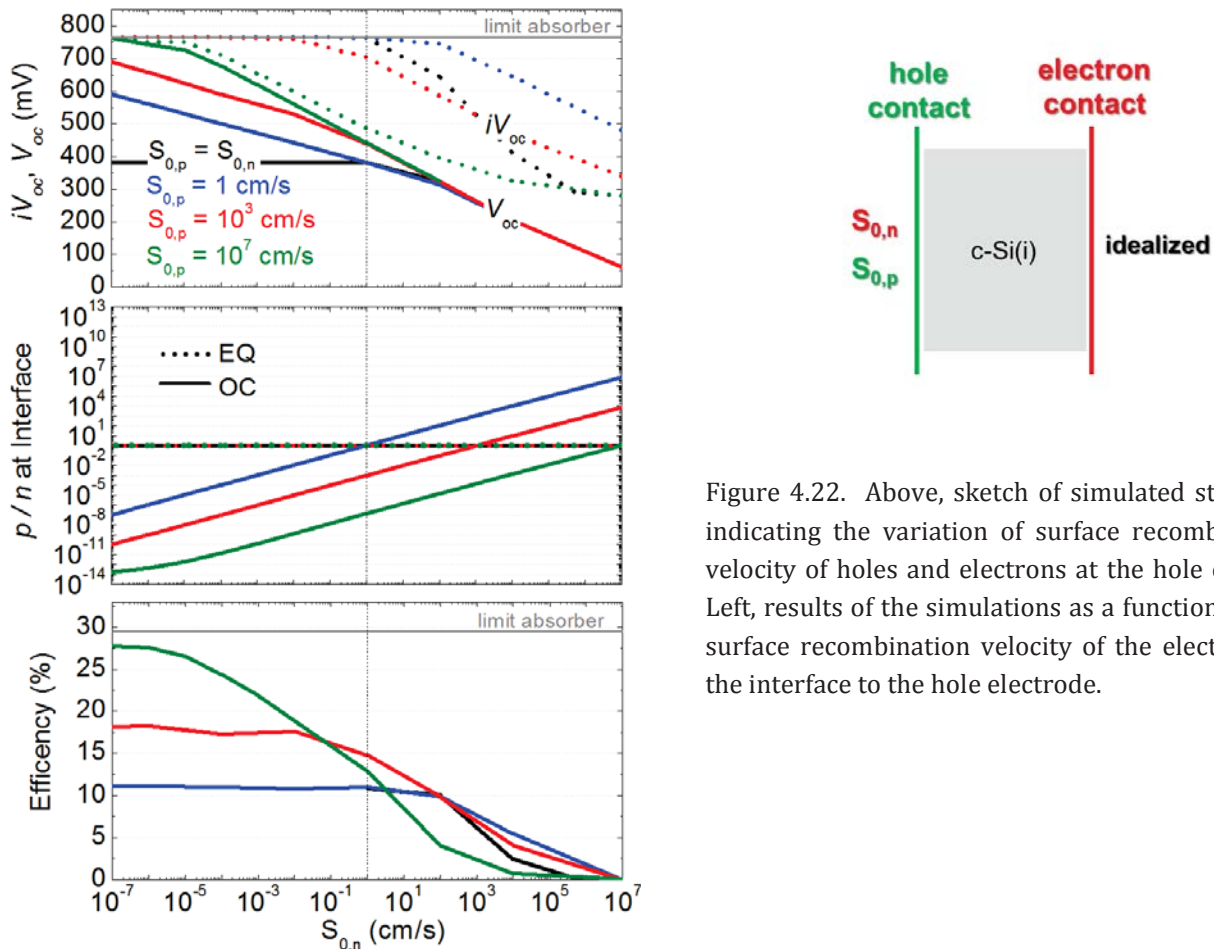


Figure 4.22. Above, sketch of simulated structure indicating the variation of surface recombination velocity of holes and electrons at the hole contact. Left, results of the simulations as a function of the surface recombination velocity of the electrons at the interface to the hole electrode.

During operation, the carrier densities are altered and it can be seen that for the parameters for which a reasonable external V_{oc} is reached the interface is populated predominantly by electrons and not holes ($p/n \ll 1$) for the hole contact. Despite the clear dominance of electrons at hole contact the extremely low transition rate of electrons ($S_{0,n}$) ensures that the overall current is still dominated by the holes. It should be noted as well that the rearrangement of free carriers near the interface during operation causes an electric field which is reflected in a corresponding band bending in the contact region (not shown). This field however, is pointing in the “wrong” direction not blocking the electrons from reaching the interface but rather attracting them.

It should be pointed out that in principle, such a contact can show excellent performance for short-circuit and MPP conditions as well as it is reflected in the efficiency which is approaching the intrinsic-limit of the c-Si absorber for the extreme symmetry between $S_{0,n}$ and $S_{0,p}$. A carrier selective contact scheme that is based on such a pronounced asymmetry of $S_{0,n}$, $S_{0,p}$ is rather of academic importance for semiconductor based systems. Its relevance is discussed for organic systems in literature [133], [134], [135] and might be of some relevance for organic / inorganic hybrid systems [136] as well.

4.2.1 Selectivity from an asymmetric mobilities and hetero-barriers

The ability of two other variables to influence the velocity term in the equations (4.5) and (4.6) and hence rather fictive contacts are investigated. This are the mobilities and the band offsets which are tuned in such a way the electron current is reduced to a minimum without hampering the hole current. Hence, similar to above the possibility to obtain reasonable selectivity by other means than an asymmetric equilibrium p/n ratio is discussed.

Carrer selectivity from asymmetric mobilities

The influence of the mobility and thickness is discussed on the basis of Figure 4.23. The structure is similar to the one from Figure 4.20 but the band gap is fixed to 1.7 eV and the absorption coefficient of the buffer is either the one of a-Si:H ($k_{a-Si:H}$) or is set to zero (k_0) to neglect the influence of photo-absorption and excess carrier generation in the buffer. The equilibrium p/n ratio is close to unity due to flat-band conditions. Hence, low low-injection conditions in the contact region and $p/n \gg 1$ are not maintained during operation.

Accordingly, if a-Si:H like parameters (black) with similar mobilities are assumed for the undoped buffer the V_{oc} (dashed and solid lines) is well below the iV_{oc} (dotted line) and limited to about 350 mV. If the mobility of electrons is significantly reduced (blue and red) the V_{oc} is higher but still limited to below the iV_{oc} . The highest V_{oc} is obtained for the thickest film featuring an extreme asymmetry of the mobilities (red) and only if photon absorption in the buffer is neglected (solid lines). This behavior might be explained as follows. As motivated in section 4.2.1,

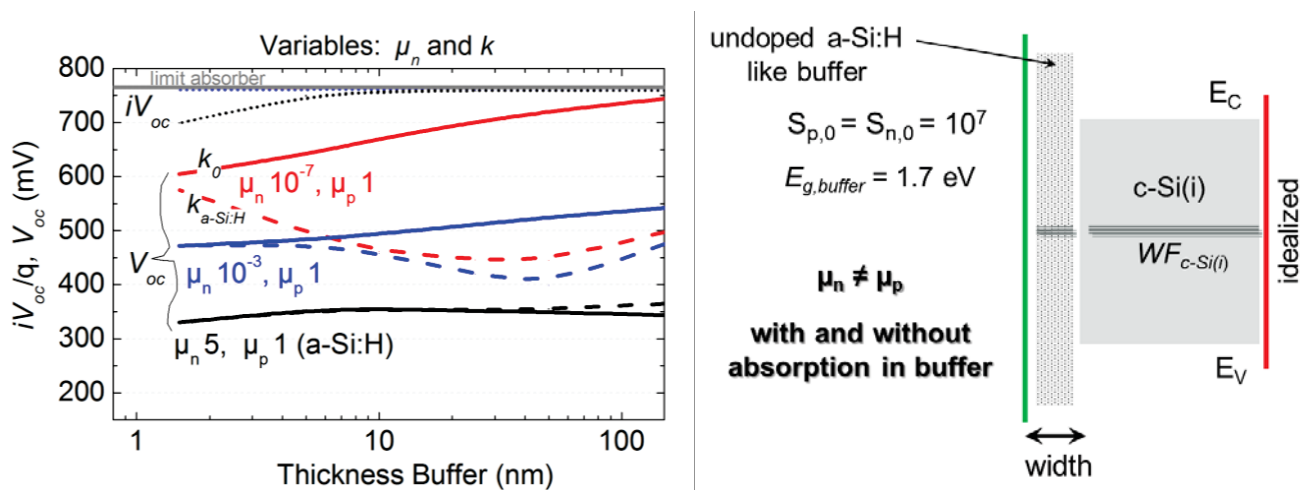


Figure 4.23. Right, sketch of simulated structure indicating the variation of the buffer layer’s thickness and mobility. The absorption coefficient (k) of the buffer is either the one of a-Si:H or is set to zero to neglect photo-absorption in the buffer. Left, iV_{oc} (dotted lines) and V_{oc} as a function of buffer layer thickness. The dots lines correspond to the V_{oc} with absorption in the buffer. For the solid lines photon absorption in the buffer is neglected.

for the hole contact the electron current must be negligible. With a very low electron mobility the absorber’s electrons can not reach the electrode and this becomes even more unlikely the thicker the buffer is. However, this contact only works if the parasitic supply of electrons originating from photon absorption in the buffer itself is switched off (solid lines).

Carrier selectivity from asymmetric hetero-barriers

The basic question here is if an increased conduction band offset hampers the parasitic electron current from the absorber and hence ensures the dominance of the hole current. The investigated structure is sketched in Figure 4.24 and corresponds to the one from above with the exception that the electron affinity (χ) of the a-Si:H like buffer is changed to tune the conduction band offset (ΔE_C). By reducing χ of the a-Si:H(i) buffer while keeping all other parameters constant, an increased conduction band offset between the buffer and the absorber is observed as indicated in Figure 4.24. Again, the equilibrium p/n ratio is close to unity in the contact region due to flat-band conditions.

It can be derived from Figure 4.24 that a ΔE_C of 580 meV is not sufficient to significantly suppress the parasitic electron current. Even, if the additional electron current caused by photon absorption in the buffer is neglected the external voltage remains well below the internal voltage and is limited to about 580 mV (even for much thicker films). It should be noted that the maximum V_{oc} takes a value which is very similar to ΔE_C . However, it is not further investigated if

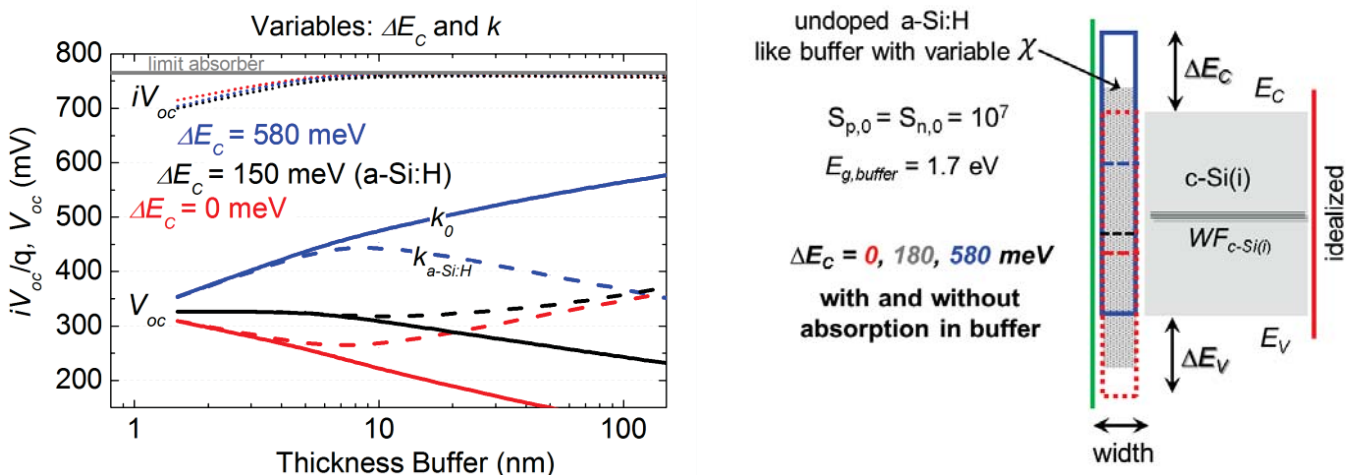


Figure 4.24. Right, sketch of simulated structure indicating the variation of the buffer layer’s conduction and valence band offset and thickness. The absorption coefficient (k) of the buffer is either the one of a-Si:H or is set to zero to neglect photo-absorption in the buffer. Left, iV_{oc} (dotted lines) and V_{oc} as a function of buffer layer thickness. The dots lines correspond to the V_{oc} with absorption in the buffer. For the solid lines photon absorption in the buffer is neglected.

this is a fundamental correlation. The data clearly suggest that carrier selectivity can only be ensured if the asymmetry of the hetero barriers is very high and if the contribution from photon absorption to the current of the wrong carrier species is negligible.

Similar to the investigations in section 4.2.8, the results above clarify that to obtain reasonable selectivity by other means than an asymmetric p/n ratio extreme assumptions have to be made for the material and junction parameters which are not fulfilled by semiconductor based contact systems. This is explained by the fact that a highly asymmetric p/n ratio can be easily obtained experientially by doping or an induced junction. The tunability of the other parameters (S_0 , μ , ΔE , photon-absorption, ...) on the other hand is limited by rather fundamental reason explained by material science. Hence, in terms of contact engineering the density terms in equations (4.5) and (4.6) are the determining factor for carrier selectivity of common systems.

4.3 Chapter Summary

In the first part, the fundamental challenge of balancing the power losses at the front side was addressed by comparing homojunction and heterojunction cells on the basis of spreadsheet calculations (diode model). The complex design trade-off of homojunction cells between a low minority carrier recombination in the metalized and passivated regions, an efficient lateral majority carrier transport (low R_{sheet}) and low optical losses (mainly grid shading) was demonstrated. It was shown that an improved minority carrier recombination is intrinsically linked to a less efficient majority carrier transport and the need for sophisticated device designs for the homojunction. For heterojunction cells this design problem is, in principle, less complex which is explained by the fact that recombination is not increased in the metalized region. This allows for the unique combination of a very low recombination (high V_{oc} and FF_0) and an efficient lateral transport (low $pFF-FF$). It results not only in an intrinsically higher efficiency but also in a much simpler device design.

In the second part, important conditions that allow for the selective excess carrier extraction from a c-Si absorber have been discussed for a variety of hole selective contacts systems on the basis of numerical device simulation. As a unique feature both the ability of the contact to passivate the absorber, i.e. to provide a high implied voltage, and the ability of the contact to extract this voltage from the absorber were analyzed independently. Unlike for the standard

investigations where it is assumed that voltage extraction is ideal (external voltage matches implied voltage) this allowed for an holistic evaluation of the contacts and to assess by which cause the external device characteristic was limited. The results revealed that in principle a variety of material properties can provide an ideal voltage extraction from the absorber. However, for the common contact schemes selective carrier extraction is always based on maintaining low-injection conditions in the contact region. In other words, the majority carrier density needs to remain well above the minority carrier density in the contact region during operation. Such a strong asymmetry of the hole / electron density has to be ensured experimentally by sufficient doping in the contact region and/or materials featuring suited work functions which lead to the formation of an induced junction and hence induced asymmetry of the hole / electron density. It was shown that for fictive contact schemes carrier selectivity can be obtained by other means. However, extreme assumptions had to be made for the material and junction parameters which are far from the one that can be fulfilled by semiconductor-based contact systems. While a highly asymmetric hole / electron ratio can be obtained experimentally, this is not the case for a highly asymmetric hole / electron recombination rate, mobility, hetero-barrier, negligible photon-absorption, etc.. The tunability of these parameters is rather limited due to fundamental aspects explained by material science.

Basically, within this chapter it was clearly demonstrated that non-optimized contact schemes may provide sufficient c-Si surface passivation but may fail to selectively extract the excess carriers of the absorber. This highlights that unlike properly designed cells which obey the standard p/n-junction theory, not only the “classical” losses, i.e. minority carrier recombination and ohmic transport losses might limit the cell characteristic. Hence, a non-ideal voltage extraction must be taken into account for the analysis of the FF and V_{oc} losses of novel / alternative contact schemes as a possible loss mechanism.

5 Limit of the Internal Voltage at MPP and Open-Circuit Conditions: Chemical and Field-Effect Passivation of the Absorber

In this chapter the injection level-dependent surface passivation of an a-Si/c-Si contact is investigated experimentally and using numerical device simulations. The main objective is the interaction between chemical and field-effect passivation which defines the excess carrier density within the absorber and the corresponding implied voltage at maximum power point and open-circuit condition. By doing so, information on the extractable internal voltage for both working conditions and hence the upper efficiency limit imposed by surface passivation is gained. Deep insight regarding the influence of an induced band bending and junction, defects at the c-Si surface and the absorber doping is obtained from numerical simulations. Regarding the experimental investigations, for the first time, field effect passivation at the a-Si:H(i) / c-Si is tuned by the deposition of either positive or negative Corona charges rather than by the deposition of n-type or p-type a-Si:H, respectively. Much attention is paid to the FF limitation imposed by the c-Si surface passivation, an aspect hardly studies so far.

This chapter is partly adapted from publication [137] and the master thesis of Markus Reusch [109], a master student supervised by the author.

5.1 Motivation

If well designed, the recombination at the a-Si:H / c-Si contacts can be suppressed very efficiently for open-circuit (OC) conditions so that the overall recombination of high efficiency SHJ cells is limited mainly by the intrinsic recombination of the high-quality crystalline silicon (c-Si) absorber. This is reflected in very high open-circuit voltages (V_{oc}) of up to 750 mV [80], [3] which are only several mV below the upper limit defined by the crystalline silicon absorber [6]. This clearly demonstrates that SHJ cells can show a nearly ideal device performance for the operation at OC conditions. However, to evaluate the efficiency limitation by surface passivation a more holistic view is needed which takes the surface passivation at maximum power point (MPP) conditions and hence the FF limitation by surface passivation into account. To this end the injection-level dependent passivation of the c-Si is investigated experimentally and by 1D numerical device simulations regarding the influence of chemical and field-effect passivation.

We use a well proven experimental approach, i.e. Corona charging that allows to distinguish between chemical and field-effect passivation [138]. The performed Corona charging and

consecutive QSSPC measurement approach shows some affinity to the interface characterization of gate dielectrics by C-V and SPV measurements. However, for C-V measurements an applied gate-voltage defines the surface band bending and induced junction close to the c-Si surface. For SPV measurements on the other hand the contactless method of Corona charging is used to manipulate the surface band bending and therefore the dominance of a certain carrier species near the surface [139].

It should be noted that previous Corona charging experiments are restricted to dielectric passivation layers⁸ and that the passivation quality is evaluated only for a constant injection-level (typically 10^{15} cm^{-3}) rather than for constant working conditions (MPP or OC). The latter makes it difficult to draw conclusion about its implications on the device efficiency. Accordingly, the presented methods distinguish itself from previous investigations as it allows for the investigation of (i) semiconductor passivation layers (a-Si:H) and (ii) the quantitative assessment of the influence of the junction recombination on MPP and OC conditions. In addition to this, unlike for the investigations from Leendertz *et al.*, field-effect passivation is not tuned by changing the doping type and density of an doped a-Si:H layer which is place on the undoped a-Si:H buffer. Rather, a thin dielectric is deposited onto the a-Si:H buffer and a Corona charge is deposited on top of the SiO_x / a-Si:H(i) / c-Si stack which allows to tune the surface conditions over a wide range from depletion to flat-band and accumulation conditions. The investigations presented here are not aiming for the extraction of exact numbers for the interface defect density and distribution (chemical passivation) and the charge density (field-effect passivation). Rather the qualitative behavior and make a link to the experimental easily accessible parameters like the iV_{oc} and iFF by the QSSPC and other techniques like e.g. the Suns-PLI [106] method are of concern.

Overview: FF limitation by surface passivation

Assuming that the overall device recombination is limited by the same mechanism for both MPP and OC conditions, according to Green's empirical expression [105] the upper FF limit reads

$$FF_0 = \frac{U_{oc} - \ln(U_{oc} + 0.72)}{U_{oc} + 1} \quad \text{with } U_{oc} = \frac{qV_{oc}}{n_{oc} k_B T} \quad (5.1)$$

⁸ Including thermally grown and PECVD SiO_2 [138], PECVD SiN_x [140], ALD Al_2O_3 [141] and ALD HfO_2 [142].

which neglects series resistance and shunt resistance related losses and the change of the dominating recombination mechanism between OC and MPP conditions (constant ideality factor (n_{oc})). Assuming that the device recombination is limited by Auger recombination and that high injection conditions are maintained for MPP this translates into an upper limit of the fill factor (FF_0) of 89% ($n_{oc} = 2/3$ for high-injection Auger). This upper limit is shown in Figure 5.1 as a function of n_{oc} and V_{oc} . It can clearly be seen that FF_0 is increasing with higher V_{oc} and lower n_{oc} . This is related to the fact that with increasing V_{oc} the excess carrier concentration in the absorber and hence the implied voltage increase for both the OC and MPP conditions. Consequently, the increase in V_{oc} is accompanied by an increase of the V_{MPP} which results in a higher FF according to equation (2.29).

Considering the relation between the experimentally achieved FF and the V_{oc} for both homojunction and heterojunction devices in Figure 5.1 a saturation of the FF at around 83 % is observed independent of the V_{oc} . Unfortunately the reason for this FF -limitations remains speculative. According to the right graph in Figure 5.1, it can not be distinguished between a low implied fill-factor (iFF) caused by insufficient surface passivation at MPP, a low pseudo fill-factor (pFF) which results from a low shunt resistance or if transport related losses ($FF-pFF$) are of major concern. However, for our standard SHJ devices and the SHJ cells from EPFL [143] the pFF is hardly exceeding 83 % thereby representing a significant FF limitation considering the relatively high V_{oc} of about 715 mV for the devices from EPFL. It should be noted that a too low

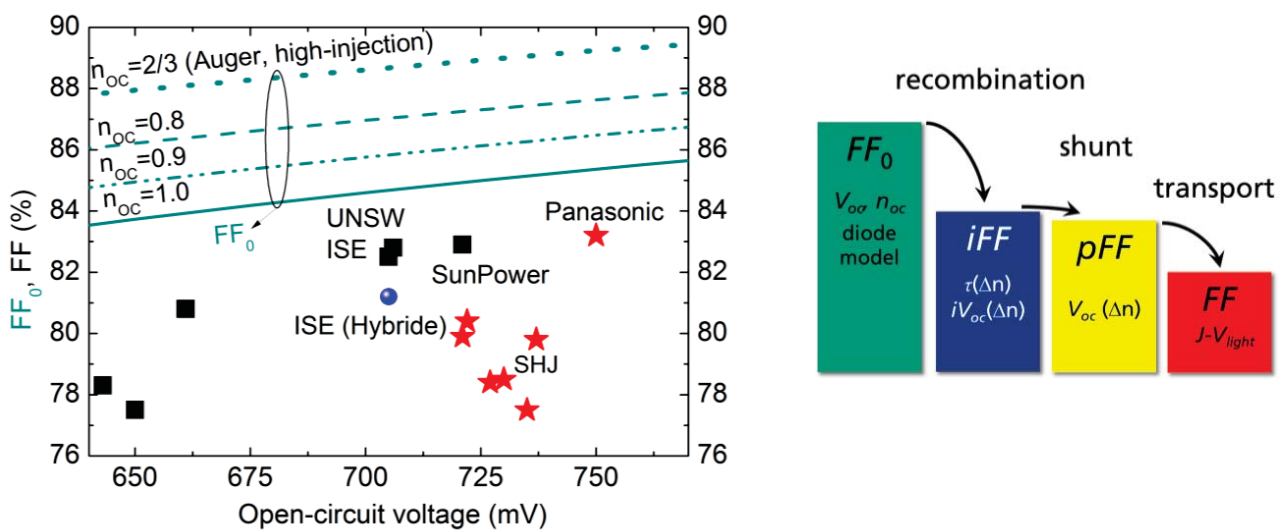


Figure 5.1: Left, FF as a function of V_{oc} . Red symbols correspond to collected data for SHJ cells and black symbols for homo-junction cells. The green lines give the upper FF limite according to Eq. 5.1 for different ideality factors at OC conditions. Right, contribution of different loss mechanisms defining the FF from the $J-V_{light}$ characteristic.

shunt resistance is not limiting these pFF s which clarifies that unlike for OC conditions surface passivation for MPP is representing a significant loss mechanisms.

Basically, the FF limitation by interface recombination is a well-known fact from e.g. (i) high-efficiency homojunction solar cells caused by the $\text{SiO}_2 / \text{c-Si(p)}$ interface [144] (Aberle *et al.* 1993)

“Despite exceptionally high open-circuit voltages, record high-efficiency PERL (passivated emitter, rear locally diffused) silicon solar cells recently developed at the University of New South Wales demonstrated relatively low fill factors. This behavior is shown to result from a surface recombination velocity at the rear Si-SiO₂ interface that increased with reducing voltage across the cell, leading to non-ideal J-V curves with high ideality factors (>1.3) near the maximum power point. When corrected for series resistance losses, the Air Mass 1.5 (AM1.5) fill factor of actual PERL cells is found to be limited to values below 82.9 %, as opposed to the ideal theoretical limit of 85-86 % for silicon cells operation in low injection conditions.”

and (ii) for the early amorphous / crystalline heterojunction devices (HIT) where both an improved V_{oc} and FF was observed if an buffer layer in-between the absorber and the defective doped overlayer was added [75] (Swada *et al.* 1994)

“... V_{oc} is improved by ~30mV and FF of more than 80% (increased from ~72% to 80%) is obtained with the HIT structure. That is clearly due to a reduced surface recombination at the a-Si/c-Si interface.”

Recent results from Descoedres *et al.* [143] explain the observed difference in the pFF for p- and n-type SHJ cells by the asymmetry of the captures cross sections for the a-Si:H passivated c-Si surface (same problem as for SiO_2). Leendertz *et al.* [89] gave an excellent overview on the interplay of chemical and field-effects passivation by the undoped / doped a-Si:H stack over a wider injection range on the basis of “lifetime samples”. Unfortunately, the implications on the iV_{oc} and iFF and thus the efficiency were not discussed in detail.

5.2 Simulation: Influence of interface defects and absorber

The influence of the injection-level dependent chemical and field-effect passivation of the absorber surface on the excess carrier lifetime and the implied voltage are illustrated in the light of the defect recombination at the a-Si:H / c-Si interface. The latter is described by the SRH

formalism which is extended by the influence of a surface band bending equation (2.21) which alters the local hole and electron density at the surface with respect to the bulk. For a more profound description of the interface recombination as described by the extended SRH formalisms the reader is referred to Aberle *et al.* [33]. For an excellent and recent overview of the recombination at the dielectric passivation layer / c-Si interface the reader is referred to the PhD thesis of Richter [27]. More SHJ specific literature where, e.g. the approximation of the amphoteric nature of the dangling bond defects by the SRH statics and the injection-level dependent charge in the a-Si passivation layer are discussed and semi empirical fit routines have been developed to quantify the influence of chemical and field-effect passivation can be found in [145], [146], [147], [148].

5.2.1 Input parameters and qualitative influence of variables

To demonstrate the influence of the different interface parameters 1D numerical device have been performed with AFORS-HET [108] [99]. To this end, the injection-level dependent effective lifetime of double side planar “lifetime structures” was simulated. The illuminated side of an 100 μm thick n-type absorber (5 $\Omega\text{ cm}$ dark resistivity) is featuring an insulator boundary offering the definition of a defect density (D_{it}) and a fixed charge density (Q_{fix}). The non-illuminated side of the absorber is characterized by a very low and constant surface recombination velocity (S) of 0.01 cm / s for holes and electrons. Consequently, the contribution of rear to the total device recombination is neglected. The chemical passivation is governed by the D_{it} at the front which is characterized by one acceptor and one donor like mid-gap defect. This deep defect level corresponds to the maximum “recombination activity” of a defect and thus a worst case scenario according the defect recombination statistics from Shockley and Read [29] and Hall [30] (SRH recombination). The D_{it} is varied from 0 to 10^{11} cm^{-2} . A further very important parameter that is hard to access experimentally but is required to describe the “recombination activity” of a given defect density and distribution is the capture cross section (σ). Unfortunately, only the c-Si interface properties passivated by thermally grown SiO_2 are well investigated for microelectronic MIS/MOS devices [149] and solar cells [138]. A consistent set data for a-Si:H was not found by the author. In addition to this, just like the D_{it} , the capture cross section varies within the band gap and is increasing towards mid-gap [33]. Within this simulations the capture

cross sections of the mid-gap defects was set to 10^{-16} cm^2 for both holes and electrons if not otherwise stated. Thus, σ_n / σ_p is unity. Whilst the characteristics of the defects potentially available as recombination centers is described by the D_{it} and σ the actually recombination that takes place at the interface is also defined by the concentration of holes and electrons at the interface (p_s and n_s). For the simulations the n/p ratio at the interface is manipulated by a fixed charge density (Q_{fix}) which allows n_s and p_s to deviate from its concentration in the bulk of the absorber as carriers are either repelled or attracted by Q_{fix} . This adds another significant degree of freedom to reduce interface recombination. As sketched in Figure 5.2 (bottom), a sufficient high positive Q_{fix} will reduce the concentration of the absorber's holes (minority carrier species) and increase the concentration of electrons (majority carrier species) in the interface region. Thus, if Q_{fix} is sufficient high recombination is limited by the absence of the holes in this device region which makes the recombination of an electron-hole pair less dependent on the actual density and distribution of recombination sites, i.e. the D_{it} . Such conditions correspond to the induced electron selective contact of the absorber ($n_s \gg p_s$). These are conditions similar to the case when a n-doped a-Si:H layer is placed on the absorber. In this case the chemical passivation

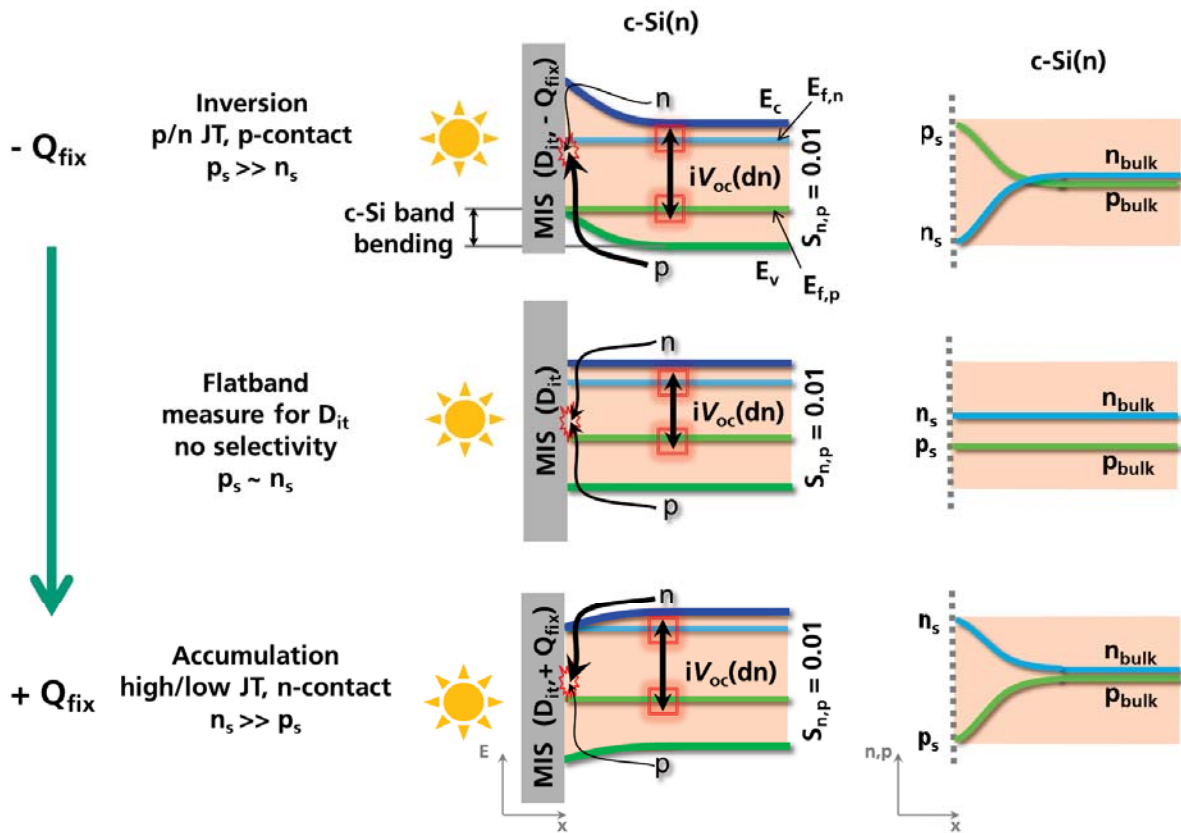


Figure 5.2: Schematic band diagram and local hole/ electron density for OC conditions for an inverted (top), flat-band (middle) and accumulated c-Si absorber surface (bottom).

is supported by the so-called field-effect passivation as the majority carrier of the n-type absorber are accumulated at the interface (high/low junction). For a negative Q_{fix} holes are attracted and electrons are repelled from the interface causing a field-effect passivation as well (Figure 5.2, top). For a high negative Q_{fix} holes are the majority carrier species in the interface region and electrons are the minority carriers ($p_s \gg n_s$). This leads to an inverted interface of the n-type absorber and an induced p/n-junction. It should be noted that similar conditions are observed for the induced p/n-junction formed by the p-doped a-Si:H layer of the standard SHJ. Without a surface charge we have flat-band conditions where the hole and electron density at the interface are not altered as compared to the bulk. The absence of a pronounced field-effect passivation makes such conditions very sensitive to the chemical passivation, i.e. the D_{it} . For the simulations Q_{fix} is varied from 0 to (+/-) 10^{12} cm^{-2} . A comparative value for experimentally observable negative Q_{fix} is reported for highly doped p-type a-Si:H as $-1 \cdot 10^{11} \text{ cm}^{-2}$ [89]. For the only common dielectric passivation layer featuring a negative Q_{fix} (Al_2O_3) a very high Q_{fix} of well below $-1 \cdot 10^{12} \text{ cm}^{-2}$ is reported in Ref. [141].

The contribution of the bulk recombination of the c-Si absorber is either assumed to be limited by the intrinsic recombination (Auger and radiative recombination) or the recombination in the c-Si is neglected. The latter case reflects the academic case where device recombination is limited solely by the chemical and field-effect passivation at the illuminated interface. The presented results include the injection-level dependent lifetime and the corresponding implied cell parameter (e.g. FF , V_{oc} and efficiency) obtained from the corresponding implied J-V curves.

5.2.2 Simulation Results

D_{it} and Q_{fix}

In Figure 5.3 the influence of the D_{it} and Q_{fix} on the overall device recombination at the implied MPP (left) and implied OC conditions (top-right and middle-right) as well as the corresponding implied efficiency⁹ (right-bottom) are shown. It can be seen that the requirements on the interface passivation are much higher for the MPP conditions as compared to the OC condition. To approach the intrinsic limit of the absorber at OC ($iV_{oc} \sim 767 \text{ mV}$) a higher D_{it} and lower Q_{fix} are

⁹. A constant J_{sc} of 41 mA/cm^2 was assumed.

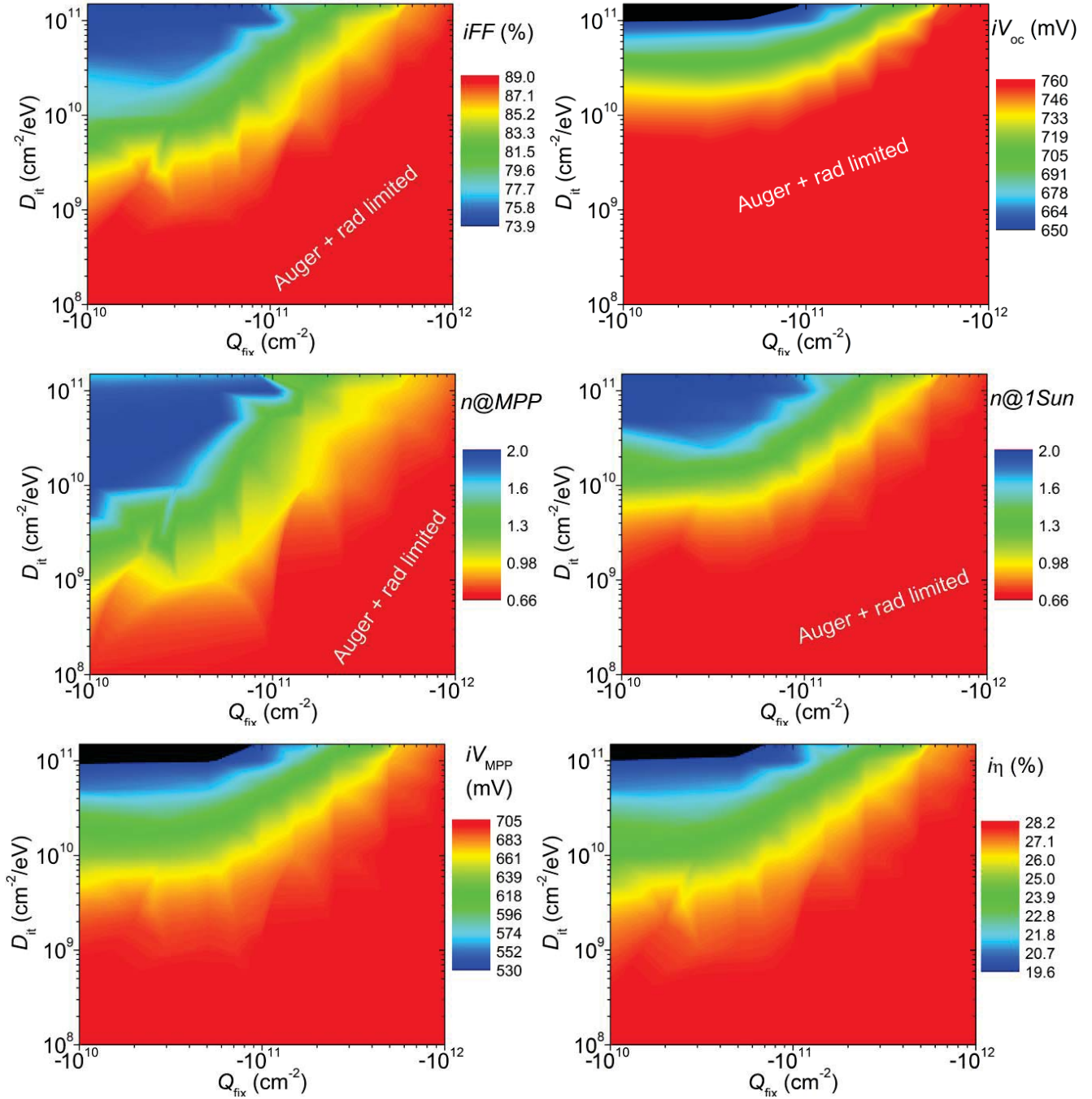


Figure 5.3: Mapping of iFF , iV_{oc} , $n@MPP$, $n@1Sun$, iV_{MPP} and the implied efficiency in dependence of D_{it} and Q_{fix} . Parameters are extracted from implied J-V curves which are based on simulated $\tau_{eff}(\Delta n)$ characteristics. Some of these $\tau_{eff}(\Delta n)$ curves are shown in Figure 5.4. The blurring of the contour plots is explained by the limited amount of data point.

tolerated as compared to the MPP conditions ($iFF \sim 89.4\%$). Consequently, the implied efficiency strongly benefits from a further reduction of interface recombination as the iFF further improves whilst the iV_{oc} is already limited by the intrinsic c-Si recombination. The limitation by the intrinsic recombination within the absorber can also be determined from the local ideality

factors at MPP (left-middle) and OC condition (right-middle). For the chosen absorber dark resistivity of $5 \Omega \text{ cm}$ high-injection Auger and radiative recombination are the limiting recombination path for both working conditions for negligible surface recombination. Accordingly, the ideality factor corresponds to about 0.7 for both OC and MPP [6]. It is also shown in Figure 5.3 (left-bottom) that intrinsic FF limit corresponds to a very high iV_{MPP} of about 700 mV, a voltage well above the V_{oc} of common homojunction devices.

A closer look at the corresponding injection-level dependent effective lifetime characteristics in Figure 5.4 for some of the D_{it} and Q_{fix} combinations from Figure 5.3 might give a more intuitive understanding of the observed behavior. We start with the influence of the D_{it} by moving along the y-axis in Figure 5.3 for a very low and negligible Q_{fix} of $-1 \cdot 10^{10} \text{ cm}^{-2}$. First, it can be seen in Figure 5.4 (top-left) that for high excess carrier densities (Δn) the intrinsic recombination within the absorber (black line) is strongly increased by high-injection Auger recombination which is reflected in the drop of the effective lifetime. The achievable Δn level for 1 sun illumination (diamonds) is limited to about $2.5 \cdot 10^{16} \text{ cm}^{-3}$ which corresponds to the maximum achievable quasi-Fermi level splitting and iV_{oc} of 767 mV. For this 1 sun OC conditions an effective lifetime of about 1 ms is required to reach the intrinsic limit. For the given absorber doping and thickness a higher iV_{oc} can only be reached by increasing the illumination above 1 sun or by decreasing the operation temperature (300 K for this simulations). It can be seen as well that the (implied) MPP conditions (stars) are always shifted to lower Δn and thus to much higher lifetimes. The lower Δn level at MPP for a real device is explained by the fact that a current and thus excess carriers are extracted from the device ($J_{\text{MPP}} > 0$) whilst the illumination and thus the excess carrier generation rate are virtually constant. For the (implied) MPP conditions here, no carriers are extracted (OC conditions) but the lower Δn is reached by lowering the illumination intensity and thus the generation rate. For the intrinsic MPP limit which is still dominated by high-injection Auger recombination Δn amounts to about $7 \cdot 10^{15} \text{ cm}^{-3}$ which corresponds to the iV_{MPP} of about 700 mV from Figure 5.3 (left-bottom). A much higher lifetime of 12 ms is required to maintain such a high excess carrier density. This shows that for maintaining the intrinsic limit for such low Δn the requirements on the interface passivation are extreme and much higher for MPP as compared to OC conditions.

In terms of interface defects, it can be seen in Figure 5.4 (top-left) that the defect recombination is less pronounced the lower the D_{it} . Such conditions, i.e. when the recombination is limited

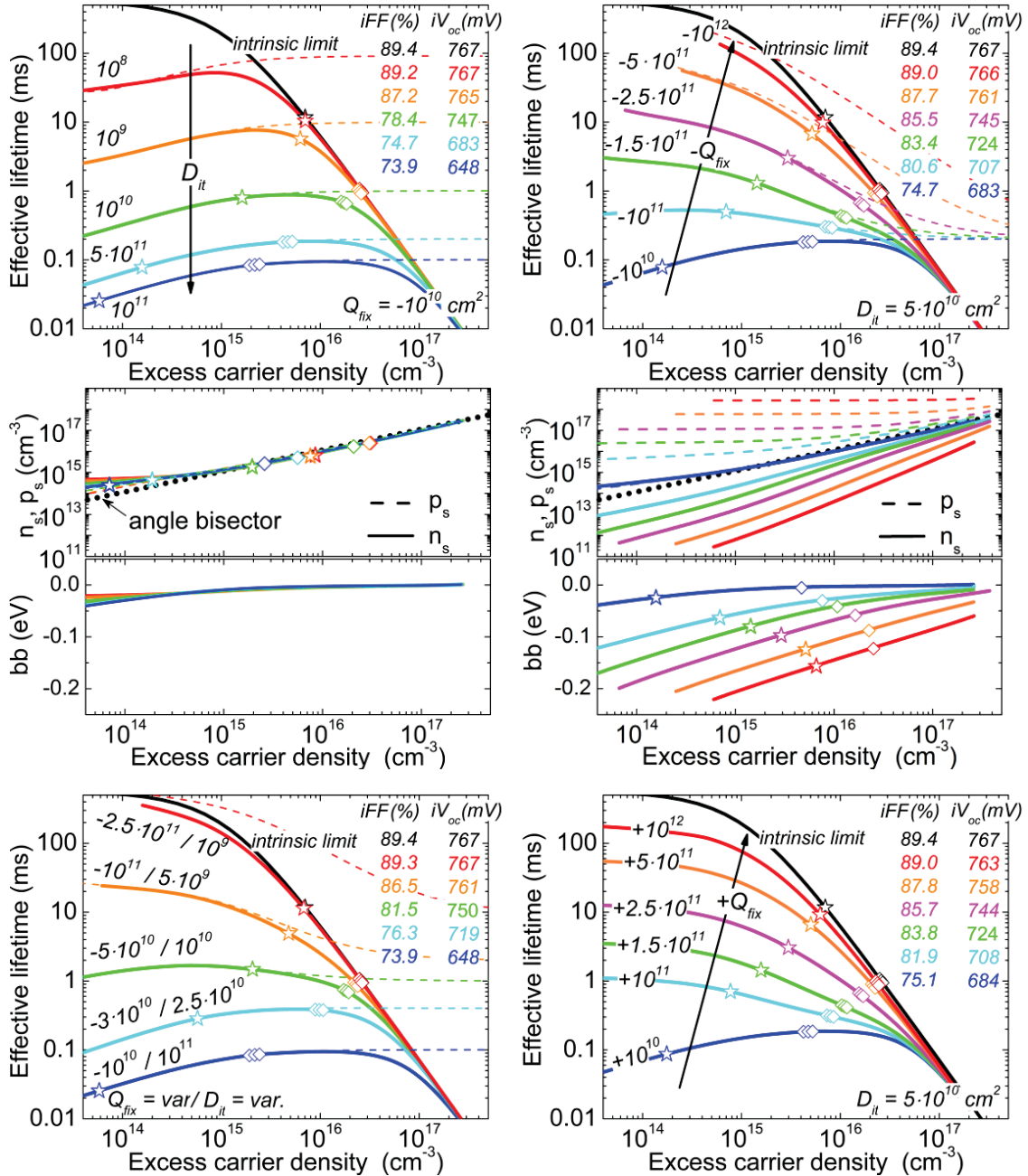


Figure 5.4 Simulated $\tau_{eff}(\Delta n)$ characteristics which are the basis for the results from Figure 5.3. Stars and diamonds on each line correspond to the MPP and OC conditions of the respective implied j-V curve. Multiple diamonds result from the fitting of the V_{oc} . The dashed lines correspond to the contribution of the surface to the $\tau_{eff}(\Delta n)$ characteristics.

Top-left and middle-left, $\tau_{eff}(\Delta n)$ and surface carrier density and band bending for a constant and negligible Q_{fix} of $-1 \cdot 10^{10} \text{ cm}^{-2}$ and variable D_{it} . Top-right and middle-right, same for a constant and very high D_{it} of $5 \cdot 10^{10} \text{ cm}^{-2}/\text{eV}$ and a variable negative Q_{fix} . Bottom-left, $\tau_{eff}(\Delta n)$ for a variable Q_{fix} and D_{it} . Bottom-right, variation of positive Q_{fix} for a very high D_{it} of $5 \cdot 10^{10} \text{ cm}^{-2}/\text{eV}$.

rather by the amount of the available recombination sites than by the availability of the holes or electrons are reflected in a parallel shift of the $\tau_{\text{eff}}(\Delta n)$ characteristics towards higher lifetimes. This becomes even more obvious from the SRH lifetime which is limited solely by surface recombination (dashed lines) as here the c-Si bulk limitation is not observed for high excess carrier densities.

The corresponding injection-level dependent hole and electron concentration at the c-Si surface and the band bending (bb) which is induced in c-Si are shown in Figure 5.4 (left-middle). As Q_{fix} is negligible the induced bb is low and the ratio of p_s/n_s is close to unity. The concentration of both species at the interface is increasing with Δn . It thus becomes clear that a lower D_{it} does not modify the p_s/n_s ratio but allows for a higher concentration of both excess holes and electrons at the surface and in the bulk for a given generation rate and working condition. For a Δn above of 10^{15} cm^{-3} the small bb vanishes and p_s and n_s are equal to the hole and electron concentration in the bulk. The latter is indicated by the fact that p_s and n_s lie on the angle bisector (black dotted line) and thus match Δn which is dominated by the excess carrier density in the bulk. For low Δn a small bb is observed which is higher the higher the D_{it} . This bb is caused by the charge of the defect states at the interface. Accordingly, a slightly depleted surface instead of flat-band conditions are observed for low Δn . This fact can at least partly explain the reduction of lifetime for Δn below 10^{15} cm^{-3} as the hole concentration (minorities of absorber) at the interface is increased as compared to the bulk. However, the influence for a negligible Q_{fix} is not of relevance for the SHJ cell as for the formation of the hole and electron contact always a highly hole and electron populated surface and thus an inversion and accumulation of the c-Si surface is present. The results discussed so far thus correspond to case when only an undoped buffer layer is present and chemical passivation is the dominant passivation mechanism.

Conditions similar to a hole contact for a constant but moderate chemical passivation by the buffer layer are shown in Figure 5.4 (right-top). In this graph we move parallel to the x-axis in Figure 5.3 by changing Q_{fix} for a high D_{it} of $5 \cdot 10^{10} \text{ cm}^{-2}$. It can be seen that besides a low D_{it} the Q_{fix} at the c-Si surface can reduce surface recombination considerably. With increasing Q_{fix} mainly the low Δn regime and thus the MPP conditions benefits from a lower recombination and higher lifetime. This is explained by the fact that for a moderate density of excess electrons and holes the dominance of holes at the surface, i.e. the inversion can be easily maintained which is not the case for higher Δn levels. As can be seen in Figure 5.4 (right-middle) the bb decreases with increasing

Δn and the p_s/n_s ratio is approaching unity. Consequently, the highest bb is observed in the dark due to the lack of excess carriers (not shown). This shows that the reduction of surface recombination by suppressing a certain carrier species, in this case electrons (solid lines) is more efficient the lower Δn . Accordingly, for very high Δn the lifetime defined solely by the surface recombination (dashed lines in Figure 5.4 right-top) converges to a constant level that is defined only by the D_{it} of $5 \cdot 10^{10} \text{ cm}^{-2}$.

The result above are indicating that in principle both a very low D_{it} or a very high Q_{fix} alone are sufficient to allow for excellent surface passivation. Nevertheless, for all passivation schemes which also have to provide a carrier selective transport a moderate thickness of the buffer (undoped a-Si:H or tunnel oxide) and a highly hole and electron populated device region near the interface have to be provided at the same time. Unfortunately, chemical passivation (D_{it}) and the induced junction (Q_{fix}) are coupled to some extent. This also holds for the SHJ in which a doped a-Si:H layer is present on top the undoped a-Si:H buffer. The increased doping, which means increasing Q_{fix} , is related to the doping and Fermi-level induced defect formation [150], [151]. This defects can partly be “seen” by the c-Si minority carriers close to the surface. This deteriorates the chemical passivation by the SHJ depending on the buffer layer and doped layer properties. The combined influence of the D_{it} and negative Q_{fix} on the surface recombination is shown in Figure 5.4 (left-bottom). Here we move along a line from a Q_{fix} and D_{it} of -10^{10} cm^{-2} and $10^{11} \text{ cm}^{-2}/\text{eV}$ towards $-2.5 \cdot 10^{11} \text{ cm}^{-2}$ and $10^9 \text{ cm}^{-2}/\text{eV}$ in Figure 5.3.

For the sake of completeness, Figure 5.4 (right-bottom) shows the case of a buffer layer with a moderate chemical passivation and a positive charge. The charge corresponds to conditions similar to the electron contact formed by an n-doped overlayer. It can be seen that the characteristic for the field-effect passivation obtained for accumulation is very similar to the one for the negative charge which causes inversion conditions (right-top).

Capture cross section

So far, the capture cross section was set to 10^{-16} cm^2 for both holes and electrons. This means that a preferred capture of either holes or electrons by the mid-gap defects was not taken into account. First the influence of a symmetric ($\sigma_n / \sigma_p = 1$) but reduced capture cross sections is shown, then the case of asymmetric capture cross sections is investigated.

In Figure 5.5 the influence of the capture cross section is shown. The top-left graph shows results for a constant D_{it} and near flat-band conditions, i.e. a negligible Q_{fix} . The reduction of the capture cross sections has a similar influence like reducing the density of defects (Figure 5.4 top-

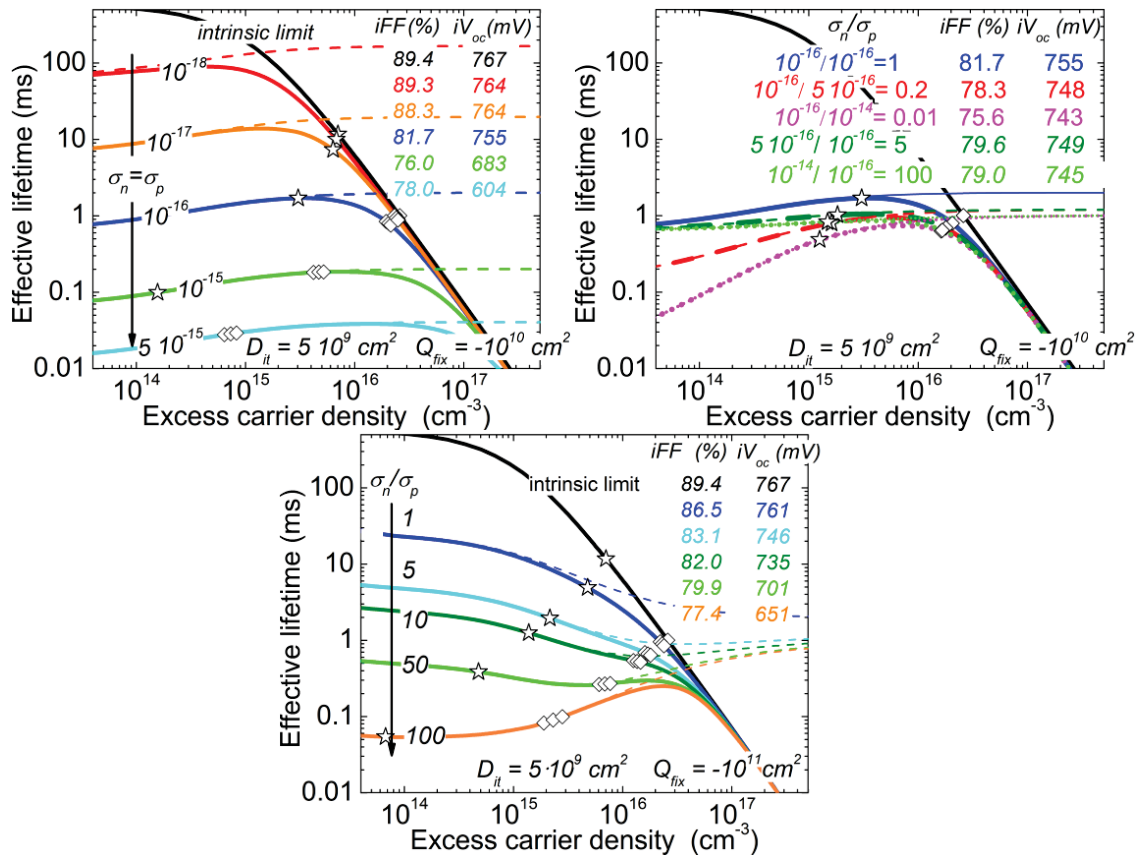


Figure 5.5: Simulated $\tau_{eff}(\Delta n)$ characteristics revealing the influence of the capture cross section on the effective lifetime. Stars and diamonds on each line correspond to the MPP and OC conditions of the respective implied J-V curve. Multiple diamonds result from the fitting of the V_{oc} . The dashed lines correspond to the contribution of the surface to the $\tau_{eff}(\Delta n)$ characteristics. Top-left, $\sigma_n = \sigma_p$ for a negligible charge and a very low D_{it} . Top-right, $\sigma_n \neq \sigma_p$. Bottom, $\sigma_n > \sigma_p$ for a high negative charge and a very low D_{it} .

left). The only difference here is that for the constant D_{it} the defect charge remains constant which explains why the drop in the effective lifetime in the lower Δn range is less pronounced as compared to Figure 5.4 (top-left). This reflects that chemical passivation is defined by both the D_{it} and σ .

The influence of asymmetric capture cross sections is shown in the top-right graph in Figure 5.5. The increase of the capture cross section of the minority carrier species at the interface (σ_p), holes for the flat-band conditions, is assumed for the red and magenta case. It leads to an increased defect recombination which is reflected in a drop in the low-injection lifetime and the iFF . The influence of the majority carrier capture cross section (σ_n , green and light green) on the low-injection lifetime is less pronounced and dominant for the high-injection and transition regime where the recombination becomes limited by both the electrons and holes. Accordingly,

the drop in iFF is less severe. Thanks to the low D_{it} OC conditions are limited by intrinsic c-Si bulk recombination for all variations. This explains why the iV_{oc} is hardly affected by the properties of the surface defects.

The influence of an increased capture cross section of the minority carrier species for a highly hole populated / inverted c-Si(n) surface (σ_n) is shown in the bottom graph in Figure 5.5. This setup corresponds to a p-emitter stack with a very low D_{it} . It can be seen that σ of the minority carrier species at the surface (electrons) shows a strong influence mainly in the lower Δn region and is thus counteracting the positive influence of the high negative Q_{fix} . In the corresponding Δn region SRH recombination is the dominating recombination channel which is more pronounced the more efficient the capture of the local minority carriers, i.e. the higher σ_{min} . As the influence of σ_n / σ_p and Q_{fix} are superimposed it is hard to clearly separate both effects. Based on simulations not shown here the dip in the effective lifetime for σ_n / σ_p of 5, 10 and 50 between OC and MPP is explained by the fact that for Δn below 10^{15} cm^{-3} the high Q_{fix} is keeping the lifetime on a higher level. But for Δn between 10^{15} to 10^{16} cm^{-3} the bb is already strongly reduced and the influence of σ_n is dominating. For above $\Delta n = 10^{16} \text{ cm}^{-3}$ the p_s/n_s ratio (not shown here but can be deduced from the middle-right graph in Figure 5.4) is approaching unity and a specific minority carrier species at the surface does not exist anymore. Consequently, the recombination becomes limited by the capture of both the holes and electrons as the interface gets into high-injection. As σ_p is below σ_n the hole capture is limiting the recombination for this conditions and the lifetime increases again for very high Δn . For $\sigma_n / \sigma_p = 100$ the low Δn region is totally dominated by the high σ_n and not superimposed by the field-effect passivation. Accordingly, the increase of the lifetime towards the high-injection regime is more pronounced. The dashed lines are indicating the contribution from surface recombination only and are converging towards a constant value at very high Δn which is defined by the constant D_{it} .

Finally, Figure 5.6 shows the influence of an asymmetric capture cross section for the following six junction configuration: Near flat-band conditions, inversion and accumulation for an n-type absorber (left) and the same for an p-type absorber (right). Conditions similar to a hole selective contact, e.g. a p-doped layer ($p_s \gg n_s$) forming the p/n or high/low-junction are denoted in green in both graphs. Conditions similar to a electron selective contact, e.g. a n-doped layer ($n_s \gg p_s$) forming the high/low-junction or p/n in red. Flat-band conditions ($n_s \sim p_s$) are illustrated in blue.

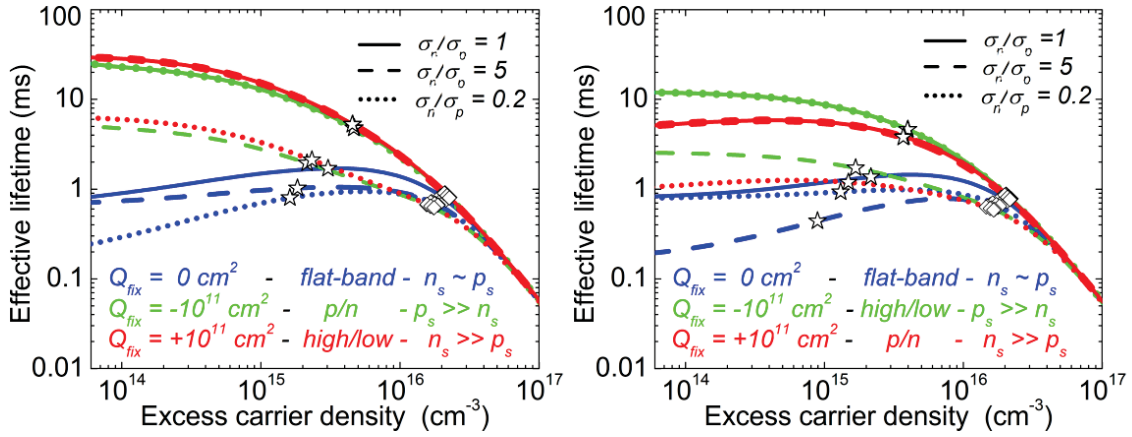


Figure 5.6: Simulated $\tau_{\text{eff}}(\Delta n)$ characteristics revealing the influence of an asymmetric capture cross sections for flat-band, inversion and depletion for an 5 Ω cm n-type absorber (left) and p-type absorber (right). D_{it} is 10^{10} cm^2/eV . Stars and diamonds on each line correspond to the MPP and OC conditions of the respective implied J-V curve. Multiple diamonds result from the fitting of the V_{oc} .

As discussed before for the n-type absorber, the low injection lifetime suffers from an increased defect recombination for the case that $\sigma_{\text{Min},s} > \sigma_{\text{Maj},s}$, i.e. if the capture cross section of the minority carrier species at the interface is

higher than that of the majority carrier species. In Figure 5.6, the dominance of the minority carrier species at the surface is tuned by both the sign of Q_{fix} and the doping type of the absorber. Consequently, for flat-band $\sigma_p > \sigma_n$ (blue dotted line, left) and $\sigma_n > \sigma_p$ (blue dashed line, right) have a detrimental influence for an n- and p-type absorber, respectively. The same holds for accumulation (red dotted line, left and green dashed line, right). For both cases, flat-band and accumulation, the minority carrier species at the interface is the minority carrier species of the absorber. For the inverted interface it is the other way around and interface recombination is limited by the majority carrier species of the absorber for low-injection conditions. Consequently, $\sigma_n > \sigma_p$ (green dashed line, left) and $\sigma_p > \sigma_n$ (red dotted line, right) have a detrimental influence for an n- and p-type absorber, respectively. These results point out that defect recombination is always sensitive to the capture cross section of the local (induced) minority carrier species. It holds for a hole or electron selective contact which is presenting the p/n-junction (inversion) or high/low-junction (accumulation) of an n- or p-type absorber.

Absorber doping

Another parameter that determines the excess carrier density at MPP and OC and thus the iV_{MPP} and iV_{OC} is the doping concentration (N_d) or dark resistivity (ρ_{dark}) of the absorber. Its influence on $\tau_{eff}(\Delta n)$ is shown in the top of Figure 5.7. An excellent p-contact for an n-type absorber has been assumed, i.e. a high $Q_{fix} = -10^{11} \text{ cm}^{-2}$ and a low $D_{it} = 5 \cdot 10^9 \text{ cm}^{-2}/\text{eV}$. The lower graphs show the corresponding iFF and the implied voltage at MPP and OC. These parameters are plotted either versus ρ_{dark} (left) or the ratio of the average excess carrier density within the absorber (Δn) at the respective working condition (MPP and OC) to N_d (right). The graphs include the results without surface recombination, i.e. the intrinsic limitation by the c-Si bulk recombination (orange and grey dashed lines).

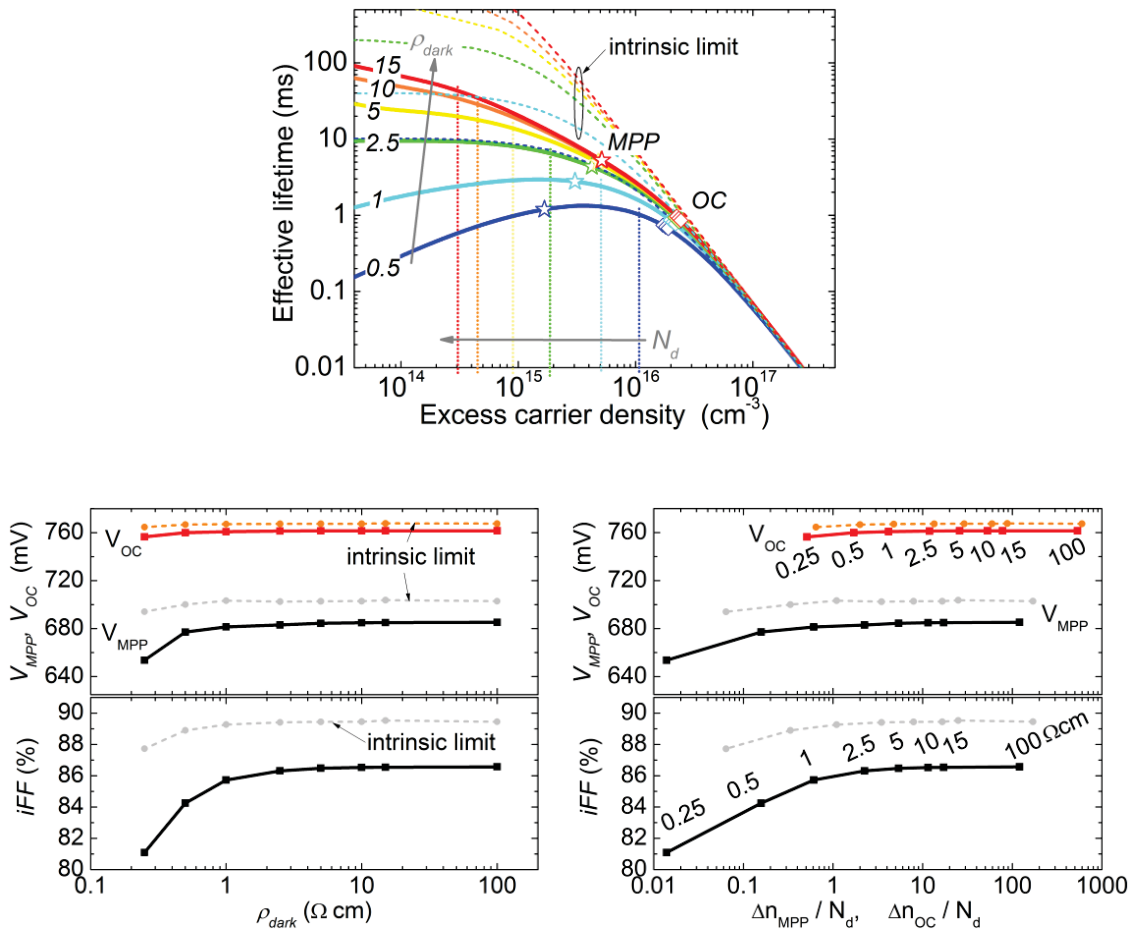


Figure 5.7: Top, $\tau_{eff}(\Delta n)$ for different absorber dark resistivity's for a constant $Q_{fix} = -10^{11} \text{ cm}^{-2}$ and $D_{it} = 5 \cdot 10^9 \text{ cm}^{-2}/\text{eV}$. Bottom-left, the corresponding V_{OC} , V_{MPP} and FF as function of absorber dark resistivity. Bottom-right, same vs. the ratio of the absorber excess carrier density for corresponding working conditions (MPP or OC) and the absorber donor doping density. The orange and grey dashed lines correspond to the result without surface recombination, i.e. the upper limit imposed by the c-Si bulk recombination.

For the assumed interface parameters, defect recombination at the interface is sufficiently suppressed so that the excess carrier density can reach values above the absorber doping density. Accordingly, the overall device recombination at OC conditions is limited mainly by high-injection Auger recombination within the absorber. This is indicated in the bottom-right graph by the fact that $\Delta n_{OC} / N_d > 1$ for the V_{oc} (red line). The excess carrier density at MPP on the other hand is always lower which makes the occurrence of high-injection conditions less likely. Nevertheless, for a reduced absorber doping a lower excess carrier density is needed to reach high-injection conditions. This is reflected by the fact that for ρ_{dark} above $1 \Omega\text{cm}$ $\Delta n_{MPP} / N_d > 1$ for V_{MPP} . Accordingly, a pronounced increase in iV_{MPP} and iFF are observed for sufficient low doping of the absorber. That this is linked to the intrinsic bulk recombination is shown by the dashed grey lines which reveal a similar behavior.

It can be concluded that for a sufficient low interface recombination, a low absorber doping helps to push the MPP conditions towards the intrinsic limit of the absorber and thus to higher Δn and iV_{MPP} . For a high absorber doping the demands on the interface passivation are much higher to allow for an excess carrier density high enough to approach the limit of high-injection Auger recombination for MPP conditions.

Further approaches to increase the iFF

Another approach to increased Δn and thus iV_{MPP} and iV_{oc} on cell level is to lower the thickness of the absorber and/or to increase the generation rate. In terms of efficiency, for lowering the thickness the gain in voltage at MPP and OC might be superimposed by a loss in current due to reduced carrier absorption. In addition it should be noted that while for thinner wafers the contribution from the absorber to the overall recombination becomes less pronounced. The influence of the surface recombination becomes stronger which leads to even higher demands on the c-Si passivation. It was shown experimentally that the surface passivation is sufficient to increase the V_{oc} for thinner absorbers [80], [152]. However, an increase in FF has not been observed which is most likely explained by the insufficient passivation quality which fails to maintain high-injection conditions at MPP, i.e. to increase not only the V_{oc} but the iFF and hence pFF as well. The simulation results in Figure 5.8 predict such a behavior. For the ideal case that defect recombination is neglected (black lines) an increase of the V_{oc} and FF with decreasing absorber thickness and recombination volume is observed. The local ideality factor remains slightly below 0.7 (right graph) thereby indicating that high-injection Auger recombination in the

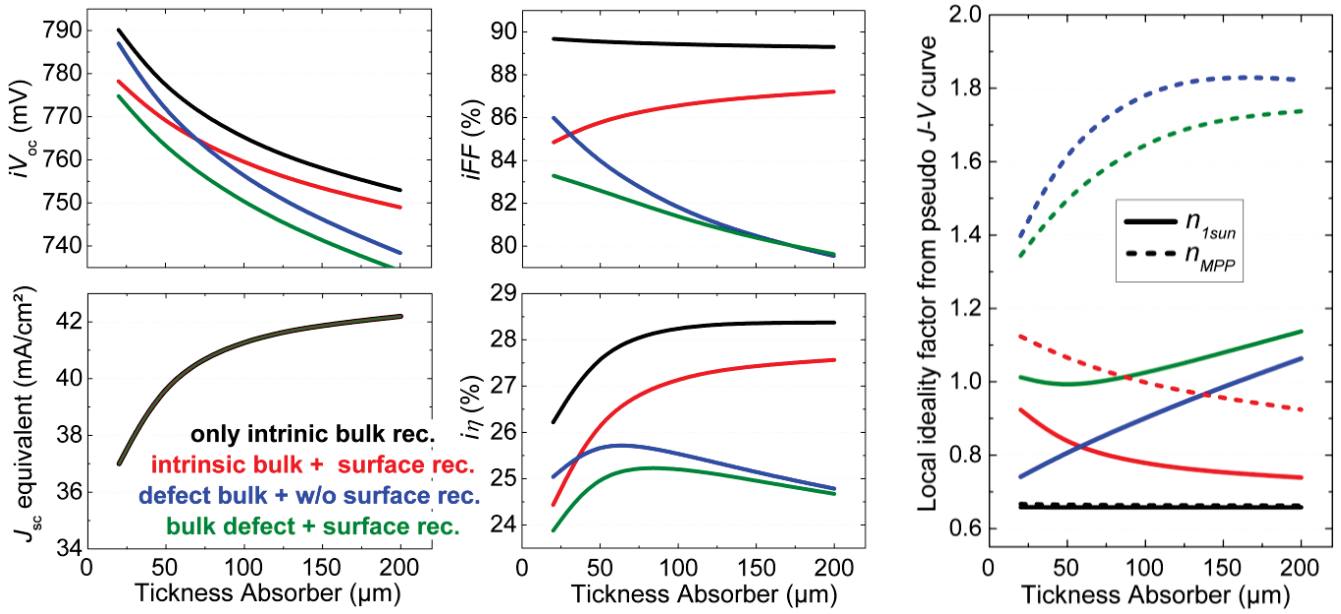


Figure 5.8: Dependence of implied cell parameters on the thickness of a 5 Ωcm c-Si absorber derived from the respective $\tau_{\text{eff}}(\Delta n)$ characteristic. For the black lines extrinsic recombination in the bulk and at the surface are neglected. For the red lines the influence of defect recombination at the surface is added ($Q_{\text{fix}} = -10^{11} \text{ cm}^{-2}$, $D_{\text{it}} = 5 \cdot 10^9 \text{ cm}^{-2}/\text{eV}$). For the blue line only intrinsic and defect recombination in the bulk are considered (mid-gap defect, $N_{\text{tr}} = 10^{10} \text{ cm}^{-3}$). For the green lines the combined influence of defect recombination in the bulk and at the surface are shown. J_{sc} is identical for all variations.

absorber is the dominant recombination path for all thicknesses. If defect recombination at the surface is present (red lines), the influence of the surface recombination becomes more pronounced the thinner the absorber is. This is reflected in the increase of the local ideality factor with decreasing wafer thickness. As defect recombination is less pronounced for OC conditions compared to MPP conditions. The V_{oc} increases but the FF drops the thinner the absorber gets. It should be noted that with respect to the MPP conditions the opposite is the case if defect recombination in the absorber is dominating (blue lines). Both V_{oc} and FF benefit from thinner wafers as the influence of defect recombination in the bulk become less pronounced. The green lines are presenting the case where defect recombination in the bulk of the absorber and at its surface are present. For the conditions assumed here, still a gain in FF for thinner absorbers is observed. This follows from the stronger influence of defect recombination in the bulk. The influence of defect recombination in the bulk on the FF is discussed in more detail in section 7.2.2.

Another approach to increase Δn for the relevant working conditions which is not based on lowering the recombination is to increasing the generation rate. This can be achieved by improving the light management of the device and more important by increased the illumination intensity as it is done for concentrator devices. The latter might be an appealing approach to maintain both MPP and OC in high-injection condition as it is briefly discussed in section 7.2.4.

5.3 Experimental: Influence of a-Si:H(i) thickness and Corona charge

This experimental section highlights that excellent passivation of the c-Si absorber is a fundamental prerequisite for a very high upper FF limit imposed by the c-Si surface passivation by a contact scheme.

5.3.1 Motivation

Figure 5.9 shows the typical behavior observed for Corona charging experiments for three dielectric passivation layers [141]. The effective surface recombination velocity (S_{eff}) at a fixed Δn level is plotted as a function of the deposited Corona charge density. For a maximum interface recombination, i.e. a maximum S_{eff} the fixed charge of the passivation layer is compensated and field effect passivation is ineffective. This condition serves as a measure of the chemical passivation provided by the film which is defined by σ_n , σ_p and D_{it} . The best chemical passivation is obtained for the Al_2O_3 followed by the SiN_x and SiO_x as indicated by the lower S_{eff} at the local maximum. The graph also reveals the positive charge of SiN_x and SiO_x and the negative charge of Al_2O_3 . An inverse charge is required to nullify the charge of the respective passivating dielectric.

The purpose of the experiments performed in this section is to use such Corona charges to manipulate the field effect passivation at the a-Si:H(i) / c-Si(n) interface without the need to apply doped a-Si:H layers on top of the undoped a-Si:H buffer. By doing so the influence of the doped overlayer and a potential damage of the a-Si:H(i) / c-Si(n) interface by subsequent a-Si:H(n/p), TCO or metal depositions can be ruled out. The chemical passivation is influenced by changing the thickness of the of the undoped a-Si:H buffer [89]. This allows to access the passivation properties determined solely by the nominally undoped buffer layer. For the SHJ cell the buffer layer properties define the trade-off between the improved field effect passivation with higher a-Si:H doping [89] and a potential decrease of the chemical passivation. The negative

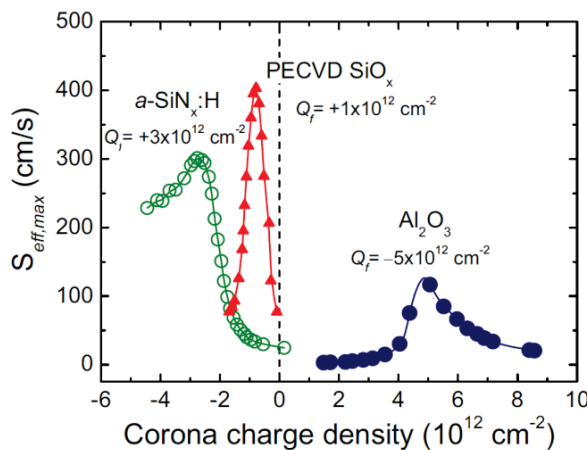


Figure 5.9: Effective surface recombination velocity vs deposited corona charge density for three dielectric passivation layers. Adapted from Ref [141].

influence of the doped a-Si:H on the chemical passivation is explained by (i) tunneling of excess carriers from the c-Si in the defective doped overlayer [153] and/or an increased defect density at the c-Si surface and within the a-Si:H bulk caused by the modification of the Fermi-level by the presence of the doped layer. The latter is explained by the Fermi-level dependent defect equilibration [150] and Fermi-level dependent hydrogen rupture [151] which connects to the early work of Dean *et. al.* [154] and Powell *et. al.* [155] on a-Si:H based thin film transistors. For very thin buffer layers a non-closed film or a film with a high void fraction and a diffusion length of the a-Si:H which is higher than its thickness (section 4.2.7) might influence the interaction of the c-Si excess carriers with the defective doped layer as well.

It should be mentioned that initially the experimental investigations of Corona charging have been triggered by the three questions below.

- i. **Can we use Corona charging to achieve flat-band conditions for a stack of intrinsic and doped a-Si:H, i.e. nullify the charge which induces the band bending?** This would allow to determine the charge of a-Si:H stack. It would be helpful to learn more mainly about the doped layer properties, i.e. its net doping. However, it turned out that this is only possible for very low a-Si:H doping as the Corona charge that can be applied to the investigated dielectrics are insufficient to fully compensate the charges of the doped a-Si:H and thus reach flat-band condition.
- ii. **Can we investigate the Fermi-level dependent defect formation/equilibration without a doped layer on top?** In previous work on a-Si:H based transistors [155] and SHJ cells [151], [150] the Fermi-level within the a-Si:H and at the a-Si:H /c-Si interface was manipulated either by changing the gate voltage or the doping of the a-Si:H layer on top of the intrinsic buffer. The objective here was similar to experiments on the thin-film transistors. Change the Fermi-level by changing the Corona charge (not external bias). Then anneal the samples to allow for the defect equilibration under specific conditions and positions of the Fermi-level. This would be a nice experiment to distinguish between effects from the doped overlayer and effects attributed solely to the position of the Fermi-level in the undoped a-Si:H buffer and at the c-Si interface. Unfortunately, irreversible changes of the dielectric layer upon annealing with deposited Corona charges gave inconsistent results so far.
- iii. **Can we manipulated the p/n ratio at the interface for an undoped a-Si:H buffer layer?** By depositing external Corona charges on the a-Si:H buffer layer the influence of chemical and

field-effect passivation can be investigated independently. This issue could be investigated as a suitable dielectric was found that meets the (less demanding) requirements.

5.3.2 Device fabrication – Suitable Dielectric Capping Layer

For the experimental investigations we follow a similar approach as presented in the simulation section. “Lifetime structures” have been fabricated from shiny etched, (100) oriented, 200 μm , n -type, 4.3-5.8 $\Omega\text{ cm}$, float-zone (FZ) silicon wafers. At the illuminated front side the a-Si:H(i) layer is featuring a thickness of 5, 8, 14 and 27 nm. An increasing thickness is representing a lower D_{it} [89]. It should be noted that the same buffer layer is subjected to the different Corona charging and subsequent lifetime measurements. The recombination at the rear side is strongly suppressed by the application of either a very thick (27 nm) a-Si:H(i) layer or a stack of (10 nm) a-Si:H(i) and (10 nm) phosphorus doped a-Si:H(n). Subsequently on both sides a 1000 nm thick SiO_x insulating film was deposited in a parallel-plate PECVD reactor powered at 13.56 MHz. A dielectric layer is required to maintain a stable external Corona charge Q_{ex} . It should be noted that the applicability of thin low temperature high quality dielectrics is restricted. A variety of dielectric single layers and stacks as well as photoresists have been tested for the following basic requirements [109]:

- i. No damage of the a-Si:H / c-Si IF during subsequent deposition of the dielectric.
- ii. A low pinhole density, a low charge of the dielectric itself and a minimum layer thickness to allow for a stable and high Q_{ex} close to the a-Si:H / c-Si interface. A stable Q_{ex} for several minutes is required to perform the injection-level dependent lifetime measurements.
- iii. No damage of the a-Si:H / c-Si interface during deposition of Q_{ex} , i.e. via Corona charging, to allow for multiple charging events with the same sample and to obtain the same lifetime characteristics after rinsing off the charges.
- iv. During annealing, e.g. on a hot plate the properties of the dielectric layer should not significantly change and Q_{ex} should be stable. This would be important for investigating the influence of annealing on the a-Si:H / c-Si interface properties with Corona charges deposited on the dielectric.

In conclusion, the best compromise was made by a thick 1000 nm thick PECVD SiO_x single layer for investigating the influence of Q_{ex} . As mentioned above investigating the influence of doped overlayers and of annealing were not possible as requirement (ii) and (iv) gave non satisfying results.

To manipulate the surface band bending external charges were deposited onto the dielectric using a Corona discharge [138], [156]. In short, a voltage of 10 kV is applied to a tungsten needle. At the tip air particles are ionized. The charges are attracted by the grounded sample and the resulting surface potential is measured using a Kelvin probe. From the measured surface potential the deposited corona charge is calculated assuming the SiO_x dielectric as a simple plate capacitor.

5.3.3 Experimental Results

The influence without and with positive and negative external Corona charges on the $\tau_{\text{eff}}(\Delta n)$ characteristic for the four different a-Si:H(i) buffer layer thicknesses is shown in Figure 5.10. Without an Q_{ex} (black symbols) an increase of the iV_{oc} and iFF with increasing thickness of the a-Si:H(i) buffer is observed. For this case the surface band bending is defined mainly by the interplay of the a-Si:H(i) and the fixed charges of the PECVD SiO_x insulating film. It should be noted that a-Si:H(i) alone does not introduce a significant band bending as shown in Figure Figure 6.1. For PECVD SiO_x Q_{ex} is positive and in the range of 10^{12} cm^{-2} ([157] and Figure 5.9). For the very thick buffer layer (27 nm, bottom-right, black curve) OC conditions are clearly dominated by the intrinsic recombination of the absorber and the excellent passivation allows the operation at MPP conditions close to the intrinsic limit as well. The corresponding iV_{oc} and iFF are 743 mV and 87.0 %, respectively. The deposition of positive external charges on the same buffer layers corresponds to the conditions caused by an a-Si:H(n) layer (high/low junction, red curves). It leads to the accumulation of electrons (majority carriers of the absorber) at the c-Si surface. For such conditions, iV_{oc} and iFF are improved to excellent values regardless of the buffer layer thickness. For the 5 nm buffer iV_{oc} and iFF are improved by 48 mV and 3 %_{abs} by the additional field-effect passivation. The application of moderate negative external charges (blue curves) is assumed to induce flat-band or depletion at the c-Si interface as some negative charges should be required to compensate the positive charges of the SiO_x. This assumption is supported by the fact that maximum surface recombination for all buffer layer thicknesses is observed for a negative Q_{ex} in the range of $0.5 - 1 \cdot 10^{12} \text{ cm}^{-2}$ which is in good accordance with the fixed charge of the PEVCD SiO_x. A strong increase of the recombination is observed which is attributed to the fact that the p/n ratio at the a-Si:H/c-Si interface is close to unity, i.e. $n_s \approx p_s$ for this conditions. Accordingly the lowest iV_{oc} and iFF are observed. For the 5 nm buffer, iV_{oc} and iFF are reduced by 101 mV and 11 % as compared to accumulation. The strong dependence on the buffer layer

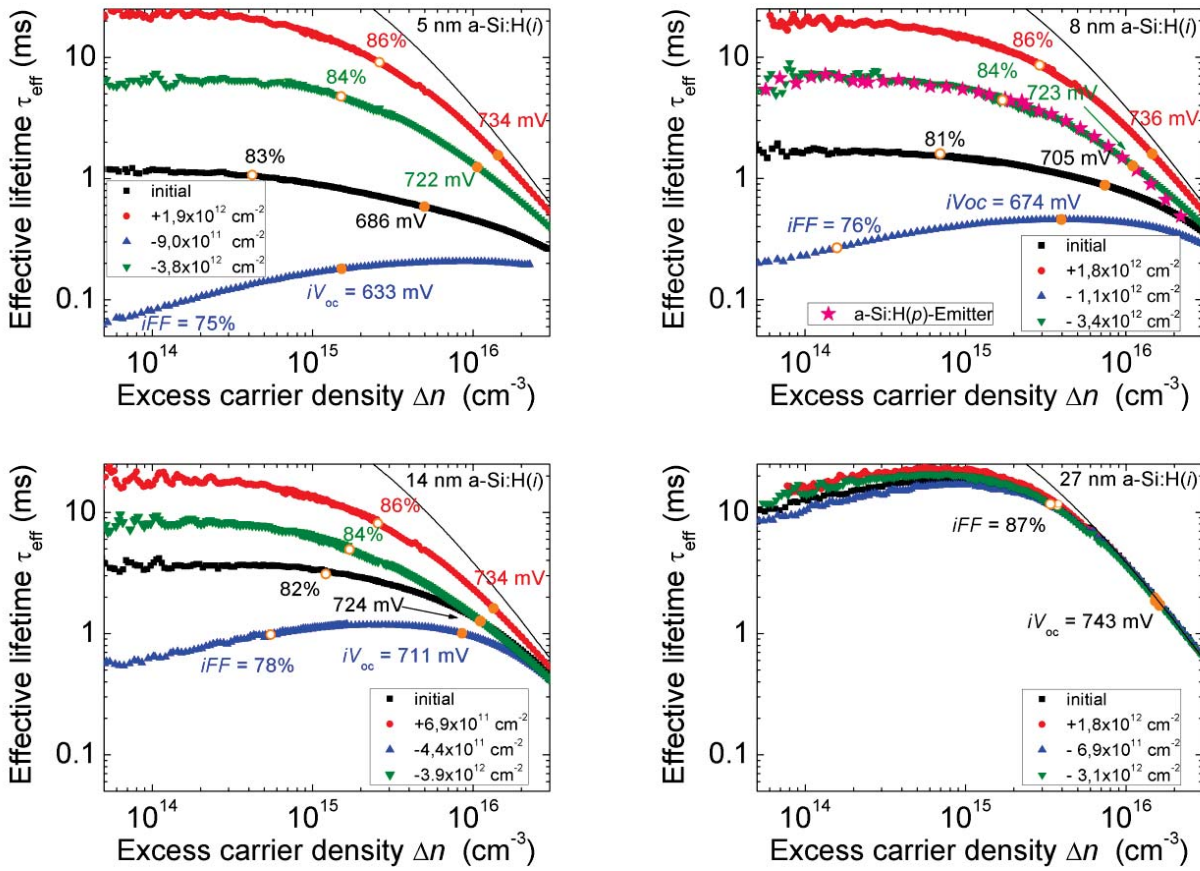


Figure 5.10: Measured $\tau_{\text{eff}}(\Delta n)$ characteristics for different surface charges (colors). Each graph corresponds to a different i -layer thickness. The solid circles are presenting the 1 sun conditions the open circles the pseudo MPP conditions.

thickness shows that such conditions are a measure for the chemical passivation which is increasing with buffer layer thicknesses. A further increase of the negative charge density leads to inversion of the c -Si surface and thus a highly hole populated interface (green curves). An increase of the effective lifetime is observed. The electron concentration at the interface is significantly reduced and the holes are the majority carrier species at the interface ($p_s \ll n_s$). This corresponds to recombination conditions introduced by the p/n junction in SHJ solar cells when a p -doped a -Si:H layer is present. A good correlation between the recombination characteristics of the sample with strong negative external charges (green curve) and a reference sample with a moderately doped a -Si:H(p) (pink stars) is found for the 8 nm buffer. This proves that our approach to mimic the field-effect passivation with external corona charges instead of doped layers is principally valid. The external charge has a strong influence on the recombination characteristics which is more pronounced for lower excess carrier densities. Hence, field effect passivation adds a positive influence to the chemical passivation and is thus a basic requirement

to obtain both a high V_{oc} and iV_{MPP} . This is in qualitative agreement with the simulation (Figure 5.4 and findings in literature e.g. Ref [89]).

The data from Figure 5.10 is shown again in Figure 5.11 where each graph is representing the $\tau_{eff}(\Delta n)$ characteristics for comparable Q_{ex} for the four different buffer layers. The two graphs in the bottom show the typical representation of the results of Corona charging experiments (Figure 5.9). However, the y-axis is representing iV_{oc} and iFF and not the effective lifetime or surface recombination velocity for a fixed Δn level.

For depletion (top-left) a shift of the $\tau_{eff}(\Delta n)$ characteristics towards higher lifetimes for thicker films can be seen. This is in accordance to the near flat-band conditions in the simulation section (Figure 5.4 (top-left)), thereby clearly indicating the reduction of the D_{it} with increasing a-Si:H(i) thickness. For these conditions the lowest iV_{oc} and iFF and a very strong dependence on the buffer layer thickness are observed. This can be interfered from the graphs in the bottom as well where iV_{oc} and iFF are plotted as a function of Q_{ex} . For both the minimum is centered at around -10^{12} cm^{-2} which can be well explained by the charge required to compensate the positive charge of the PECVD SiO_x capping layer. Except for the thick buffer OC and MPP are dominated by the poor or moderate chemical passivation and are far off the intrinsic limit. For such conditions the absence of field-effect passivation calls for an outstanding D_{it} to suppress surface recombination. For a strong inversion (top-right and negative Q_{ex} in the bottom) field-effect passivation is efficient making recombination at OC and MPP conditions less sensitive to the D_{it} and buffer layer thickness, respectively. However, a significant reduction of the D_{it} , represented by the 27 nm buffer is required approach the intrinsic limit for such conditions as well.

It is important to note that the behavior for the thin buffer layer (5 nm) is in strong contrast to the one observed for the case when a highly hole populated interface is obtained by the additional p-doped a-Si:H overlayer (not shown here). Our buffer layers thinner than about 7 nm cannot ensure an efficient decoupling of the chemical c-Si passivation from the doping of the a-Si:H(p) layer above. For our too thin layers the increased of the field-effect passivation by the doped layer is superimposed by the loss of chemical passivation. This does not only lead to a significant V_{oc} loss but also the iFF and thus pFF of our cells do not benefit from the deposition of

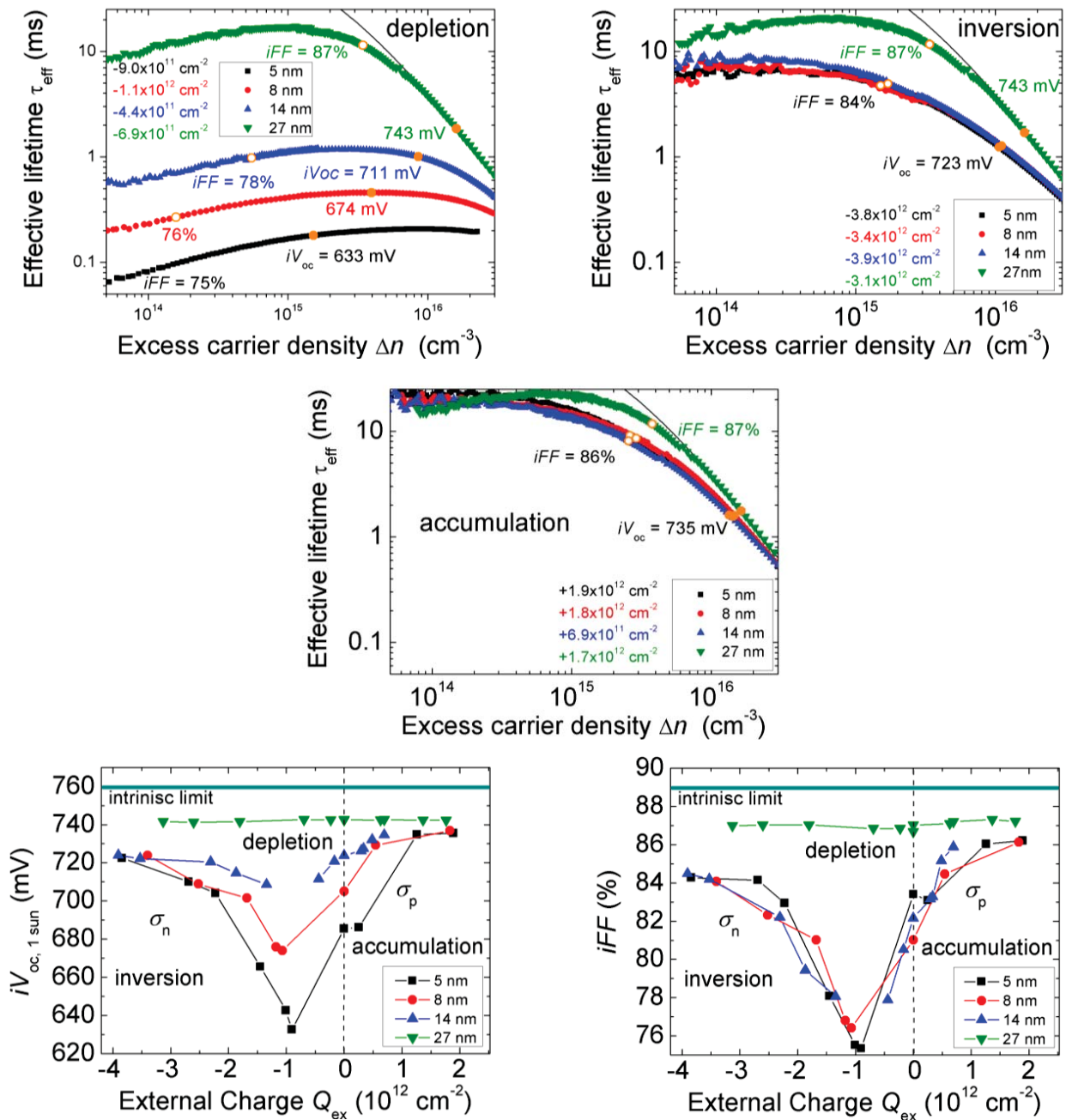


Figure 5.11: Top and middle, measured $\tau_{eff}(\Delta n)$ characteristics for depletion, inversion and accumulation for four different buffer layer thicknesses. 1 sun conditions and the pseudo MPP conditions are marked by the filled and open symbols, respectively. Bottom, the corresponding iV_{oc} and the iFF as a function of the deposited Corona charge.

the p-doped a-Si:H. A direct interaction of the minority carriers at the c-Si side of the junction with the defects on the a-Si:H side of the junction can explain such a behavior. A buffer layer with insufficient thickness behaves similar to the case when the buffer is omitted [75], [18], [158], [151], [159], [89], i.e. where the highly defective doped layer is in direct contact to the c-Si. So, in terms of c-Si passivation a buffer layer thickness / quality has to be chosen allowing for an

efficient decoupling of the field effect passivation from the chemical passivation. However, with increasing layer thickness iFF has to be traded for J_{sc} and FF as parasitic absorption [158], [119] and transport induced losses [160], [130] will start to lower the efficiency. This makes clear that improving the buffer layer quality rather than its thickness is of major importance. Where the lower limit for the thickness of the buffer might be the tunneling length by which the a-Si:H defects are seen by the c-Si carriers and the thickness when a closed film is developed, improving the doped layer properties might add another degree of freedom for the junction engineering.

Figure 5.11 shows that for accumulation (graph in the middle and positive Q_{ex} in the bottom graph), field effect passivation is very efficient reducing the influence of the buffer layer thickness significantly. In addition, the gap to the 27 nm buffer and the intrinsic limit which is at about 760 mV and 89.0 % for the applied absorber [6] is smaller compared to inversion and depletion conditions. For the thinner buffer layers accumulation leads to significantly higher $iFFs$ and iV_{oc} s of about 2 %_{abs} and 10 mV as compared to inversion. This is in accordance to the common experimental finding that the influence of the n-doped overlayers is less detrimental as compared to its p-doped counterparts for an n-type absorber. However, the experimentally behavior observed here should be related to a more intrinsic effect as a doped overlayer is omitted and the same buffer is used for inversion, depletion and accumulation.

A plausible explanation for the better passivation for accumulation as compared to inversion is a less efficient field-effect passivation for inversion. However, this is not in line with simulation results presented in Figure 5.4 (compare right-top and right-bottom) which suggest that a similar external charge results in similar iV_{oc} and iFF . Further investigations are needed to draw a definite conclusion. Another possible cause can be an asymmetry of the capture cross section for holes and electrons of the defects dominating the recombination. As motivated in the simulation section above, according to SRH statistics the recombination is limited by the minority carrier species in low-injection conditions and low-injection conditions are still dominant for MPP conditions. Under inversion conditions electrons are the minority carriers at the interface, whereas holes are the minority carriers under accumulation conditions. In accordance to the simulations in Figure 5.6, the experimental findings can be understood by the fact that electrons are more easily captured than holes at the a-Si:H /c-Si interface. This means $\sigma_n / \sigma_p > 1$ for the defects dominating the recombination. A similar conclusion was drawn from the comparison of textured (111) oriented n- and p-doped absorbers [161] passivated by stacks of doped and

undoped a-Si:H. These results shall be briefly discussed. A lower iFF for p-type absorbers was observed in Ref [161] which was reflected in a lower pFF and FF of the solar cells. However, it should be noted that the reduced low-injection lifetime in Ref [161] was observed only for p-type absorbers and irrespective of whether the SHJ is forming the p/n-junction (niPin), high/low-junction (piPip), or depletion conditions (iPi) of symmetric structures and for the asymmetric solar cells structures (niPip). For n-absorbers no reduction of the lifetime for the lower Δn regime was observed. This experimental findings do not match the behavior predicted by the simulation results shown in Figure 5.6. There it has been shown that a higher capture cross section for electrons ($\sigma_n / \sigma_p > 1$) should adversely affect the low-injection lifetime for all hole selective contacts, i.e. for all cases when electrons are the minority carrier species at the interface. So, always when the pi stack is present, irrespective if placed on a n-type or p-type absorber. Accordingly, the fact that the niPin structure which does not include the pi stack shows the reduction and the piNin not, is not in line with the simulation results. If the discrepancies between the simulations and the experimental findings in Ref. [161] are caused by the incorrect description of the experimentally observed interface recombination by the simulations or if the reduced low-injection lifetime in Ref [161] is caused by other effects than an asymmetric capture cross section remains open.

Regardless of whether a higher capture cross section for electrons, a less efficient field-effect passivation or other factors are responsible for the inferior passivation for inversion conditions of an n-type absorber observed here. It results in an intrinsic limitation which can only be mitigated by a significant reduction of the density of defects. Such conditions are reached for the experimental investigations by the 27 nm thick intrinsic a-Si:H buffer layer where both the iV_{oc} and iFF are on a very high level and close to the intrinsic limit.

Parasitic effects

As a defective doped layer is omitted here, recombination is limited to the bulk of the absorber, its space charge region and the a-Si:H / c-Si interface. It is expected that depending on the tunneling length and the a-Si:H thickness the a-Si:H bulk defects and the defects at the SiO_x / a-Si:H interface will be seen by the excess carriers as well [153]. However, further aspects might contribute to the overall device recombination.

One aspect might be an increased recombination in the c-Si space charge region caused by a surface-damaged region (SDR) near the interface (~ 100 nm). This is discussed for inverted or depleted c-Si surfaces as observed for SiN_x passivated p-type or Al₂O₃-passivated n-type

absorbers in Ref. [140]. As this damaged region lies within the space charge region it significantly influences the overall recombination. The influence of artificial effects arising from depletion region modulation (DRM) [162] and the recombination at the edge of the samples or local inhomogeneities [107] can influence $\tau_{\text{eff}}(\Delta n)$, too. It is shown in Ref. [163, 164] that inversion layer shunting at the sample edge caused by an emitter diffusion or the charge of the dielectric passivation can have a negative influence on the relevant Δn range. However, compared to our results, no surface damage region and inversion layer shunting seems to be present for the 27 nm a-Si:H(i) layer as a comparable and high iFF is observed for both accumulation and inversion. Based on this, it seems that such parasitic effects do not have to be taken into account for the interpretation of the experimental data.

5.3.4 Conclusion

To summarize the results from the experimental investigations, in Figure 5.12 iFF is plotted as a function of iV_{oc} . The color is indicating the i-layer thickness and the numbers correspond to depletion (1), inversion (2) and accumulation (3) conditions at the a-Si:H(i)/c-Si interface. With increasing the a-Si:H(i) thickness the slope of the iFF become steeper. This is explained by the fact that mainly the recombination at depletion (1) benefits from an improved chemical passivation which comes along with increasing buffer layer thickness. For the 27 nm buffer an outstanding chemical passivation allows to push the iFF towards the intrinsic limit, i.e. above 86 %. Except for the 27 nm buffer, the iV_{oc} and the iFF are higher for accumulation (3) as compared to inversion (2) conditions. A plausible explanation is a higher capture cross section for electrons which are representing the minority carrier species at the inverted interface. This might be an intrinsic property of the c-Si surface states as faster capture of electrons is observed for the SiO₂ / Si [33], [165], the Al₂O₃ / Si interface [166], [167] and the a-Si:H / c-Si interface as well [161].

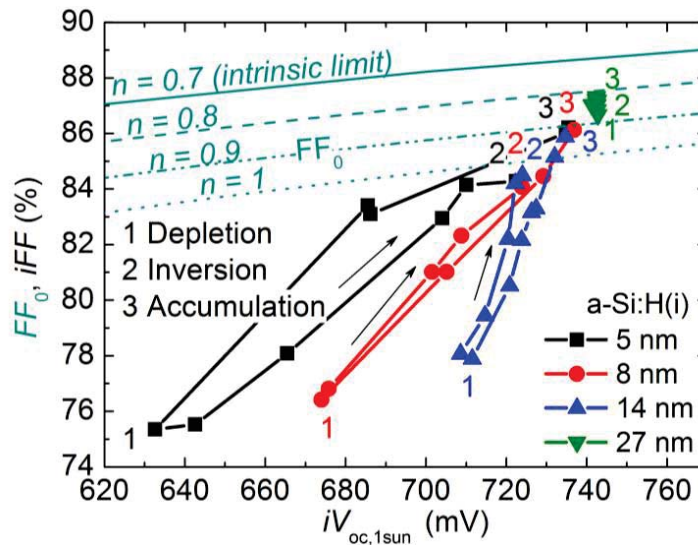


Figure 5.12: iFF vs iV_{oc} obtained from the measured $\tau_{eff}(\Delta n)$ characteristics of Figure 5.11. The FF_0 as a function of iV_{oc} is shown as well. The numbers along the measured points are indicating the corresponding surface conditions, i.e. depletion, inversion, accumulation.

5.4 Chapter Summary

In this chapter the interplay between the chemical and field-effect passivation of c-Si by undoped a-Si:H was investigated on the basis of device simulations and experimentally with idealized lifetime test structures. The main concern was to link the injection level dependence of the c-Si surface passivation to the upper limit of the extractible internal voltage at MPP and OC conditions.

Unlike for the solar cell structures, the field-effect passivation and thus the p/n ratio at the interface was manipulated via the deposition of external Corona charges instead of changing the doping of an additional a-Si:H film on top. The chemical passivation was altered by changing the thickness of the undoped a-Si:H buffer layer. This novel approach enabled manipulating the field effect passivation without adding any contributions to the chemical passivation from the doped a-Si:H top layer and its deposition process. In this way a model system was created that allows to decouple both passivation mechanisms. It was shown that the requirements on the c-Si passivation are less stringent for OC conditions as compared to MPP conditions. This is explained by the fact that for high excess carrier densities the iV_{oc} becomes limited rather by the intrinsic recombination in the bulk of the c-Si absorber than by the defect recombination at the a-Si:H / c-Si interface. The opposite is the case for the lower excess carrier densities at MPP conditions where the intrinsic recombination in the bulk of the absorber is much lower. This makes the overall recombination for MPP more sensitive to the defect recombination at the interface as compared to OC conditions. Especially, if the MPP is shifted into the transition region, while OC is still in high-injection, a significant reduction of the FF is observed while the V_{oc} loss remains moderate. Hence, to also approach the intrinsic limit for MPP conditions, the requirements on the c-Si passivation are extreme and much higher as compared to the OC conditions. In addition to this intrinsic issue, an asymmetry of the hole and electron capture cross sections of the limiting defects at the a-Si:H / c-Si interface seems to increase recombination at inversion conditions as compared to accumulation conditions for a n-type absorber. This leads to even higher demands and thus calls for an outstanding chemical c-Si passivation. Nevertheless, a very high iFF of 87% was experimentally demonstrated for inversion conditions proving the very high FF potential of SHJ devices. As the pFF of current SHJ is well below such values it becomes clear that much FF can be gained if surface passivation is improved substantially.

Referring to solar cells, a very important aspect is the decoupling of chemical passivation and field-effect passivation. Whilst the former is mainly defined by the buffer which also has to allow

for efficient carrier transport, the latter is strongly defined by doped layer properties and the need to form the selective hole and electron contacts. If such a decoupling can not be ensured, the field-effect passivation gained by the doped layer might be superimposed by a drop of the chemical passivation which will not allow to achieve the outstanding passivation properties needed to operate near the intrinsic limit for MPP conditions as well.

6 Carrier Extraction from the Absorber: Realization and Evaluation of Different Carrier Selective Contact Schemes

The objective of this chapter is twofold. Firstly, different contacts systems are evaluated regarding their ability to form a carrier selective contact. Secondly, simple experimental approaches which allow for this already in the early stage of device engineering are presented.

After a short introduction, an a-Si:H doping variation, from undoped to highly p-doped, is presented of the standard SHJ. It showcases that the external voltage of a poor designed contact schemes can be limited by the excess carrier extraction from the absorber rather than the passivation of the absorber, conditions which are hardly obtained for homojunction cells. In this case the external terminal voltage is significantly lower than the internal voltage in the absorber (For simplicity this effect is called non-ideal voltage “extraction” in the following). The suitability of analyzing the illumination level dependence of the external open-circuit as a simple means to predict both V_{oc} and FF losses caused by inappropriate work functions, insufficient net doping and other factors adversely affecting the selective carrier extraction is pointed out. Other non-idealities of the J-V characteristic are also discussed. As an attempt to improve the work function matching at the ITO / doped a-Si:H contact results for an ITO doping variation are presented.

Thereafter, different metal layers and materials adopted from organic electronics (e.g. metal oxides) are tested for their ability to form a hole or electron selective contact. The suitability of analyzing the asymmetry of the external V_{oc} obtained if the same material is forming either the hole or electron contact is pointed out. Two promising materials, namely molybdenum and tungsten oxide, are investigated in detail. It is proven that materials adopted from organic electronics are interesting candidates for alternative contact schemes for future c-Si based solar cells.

6.1 a-Si:H doping variation as a showcase for a non-ideal voltage extraction

This chapter is linked to simulations in section 4.2.5 where the voltage and excess carrier extraction from the absorber by the TCO/doped a-Si:H / a-Si:H(i) / c-Si contact of the SHJ was investigated. More precisely, the ability of the SHJ to passivate the absorber’s surface and to extract excess holes is analyzed in detail for an a-Si:H(p) emitter doping variation. The experimental findings are underpinned by numerical simulations with *Sentaurus Device* (Synopsys) [168] which have been instructed by the author and have been performed by

Sebastian Schröder, a diploma student supervised by the author (diploma thesis [100]) and Heiko Steinkemper a PhD student working with *Sentaurus Device* simulations. A large share of the experimental data was acquired in the course of the master thesis from Markus Reusch [109] likewise supervised by the author.

This section is based on the author's publications [169], [170], [171], [172], [94].

6.1.1 Motivation

Optimization of doped a-Si:H

Whilst the major work on SHJ optimization in the past was related to improve the surface passivation of the a-Si:H / c-Si heterojunction (mainly V_{oc} improvement) comparatively little attention was paid to the heterojunction formed between the TCO and the doped a-Si:H. However, the excellent V_{oc} s achieved by many companies and institutes shifts the attention towards J_{sc} and FF improvements. This calls for a more integral understanding of the SHJ taking the tight interplay of both heterojunctions (TCO / a-Si:H and a-Si:H / c-Si) into account. In this respect, a proper engineering of the SHJ particularly at the illuminated front is crucial. A low screening length of the doped a-Si:H is needed to screen the parasitic band bending which results from the work function mismatch between the TCO and the doped a-Si:H (Ref [94] and section 4.2.5). The low screening length ensures an efficient tunneling transport at the parasitic Schottky contact and prevents the global depletion of the a-Si:H. It follows that the screening length defines the lower limit for the a-Si:H thickness. This means that a low screening length is also beneficial in terms of optical properties as it allows for thinner films that show less parasitic absorption. This can result in a trade-off between J_{sc} and FF [119], [173], [174]. But in Refs [175], [158], [176], [177], [94] it is also reported that the V_{oc} is reduced if the layer thickness is below the screening length, i.e. when the a-Si:H doping is insufficient and/or the work function mismatch too high for the applied layer thickness. However, it is known from a-Si:H that doping is far from degeneracy and that a high doping often interferes with the c-Si interface passivation [150] and the optical properties [178], [179], [180]. Thus, it is obvious that the implementation of only several nanometer thin layers featuring both a high doping and a high transparency is a challenging task. For example, the layer's transparency can be improved by alloying (a-SiO_x:H, a-SiC:H) but comes at the expense of an even lower doping efficiency [178], [179], [180], [102]. The growth of ultra-thin materials featuring a crystalline fraction (nc-Si:H, μ c-Si:H) potentially facilitating the doping efficiency and transparency is challenging as well [181], [182]. Concerning the TCO work function, optimization of the bulk properties (high mobility) is of major concern to

balance the losses from the lateral transport and the parasitic absorption. The additional optimization of the interfacial TCO properties to adapt the work function without adding significant optical losses, process complexity and costs might also be a challenging task.

When characterizing doped SiTFs it should be considered that even for quasi homogeneous amorphous layers the determined activation energy typically shows a strong thickness dependence [183], [184]. This is even more true for $\mu\text{-Si}$ films for which the incubation layer and the evolution of the crystallinity in the growth direction lead to a strong thickness dependence of the material properties [182]. Since device relevant layers are only a few nanometers thick, the characterization of thicker layers can lead to e.g. an overestimation of the net doping. Thus, for the quantitative investigation of device relevant layers more sophisticated techniques are required [185]. Another important factor that should be considered for the optimization of the doped layers are the interfacial TCO properties, more precisely the actual work function which results after contact formation at the interface. The quantitative determination of the actual interface properties is very challenging. In various publications [186], [93], [187], [188] it is shown that for example the work function of the TCO in contact to air or vacuum can be modified. However, unlike for other thin film devices where the doped SiTFs are deposited onto the (modified) TCO, for SHJ cells the TCO is deposited onto the doped layer. Thus, it is relatively unknown to which extent these findings apply to the interface formed for the inverse process sequence of the SHJ. Another important fact is that subsequent processing can have a significant influence on the actual bulk and interface properties of the SiTFs and TCO. Thus, for the contact characterization and optimization one should not depart too far from the actual system, which is used in the solar cell. Such an approach is suggested in the following.

6.1.2 Illumination-level dependence of open-circuit voltage

Suns- V_{oc} measurements at high illumination have already proven their basic suitability and usefulness for the characterization of the metal / semiconductor (Schottky) contacts of homo junction solar cells [103] [189]. In Ref [189] FF losses caused by insufficient c-Si doping below the local metal electrode have clearly been identified by this method. So far, only few publications are dealing with the characterization of SHJ devices [190], [191], [192], [177], [171] using the Suns- V_{oc} setup [103]. The net doping of the SiTFs is especially for amorphous layers well below that of the highly-doped regions in c-Si homojunction cells which makes the formation of a

parasitic Schottky contact and the depletion of the contact from majority carriers more likely for SHJ cells.

The basic idea behind analyzing the Suns- V_{oc} curve: Thick buffer layers

For an ideal voltage extraction and the avoidance of high-injection conditions in the contact region three basic requirements exist as outlined in section 4.2. To motivate these requirements experimentally Figure 6.1a shows the injection level dependent implied V_{oc} , (iV_{oc} , solid lines) and the corresponding external V_{oc} (symbols) for an a-Si:H(p) emitter doping variation. Figure 6.1b shows the corresponding equilibrium band bending induced in the c-Si(n) absorber. Figure 6.1c shows a non-ideal voltage extraction in hole contact.

Requirement 1): c-Si surface passivation: High quasi Fermi-level splitting in the absorber.

The iV_{oc} characteristic for the B_2H_6 gas phase doping variation of the a-Si:H(p) emitter is shown by the solid lines in Figure 6.1a. In this experiment a relatively thick buffer layer (~ 10 nm) was applied to prevent a degradation of the chemical c-Si passivation with increasing doping. The iV_{oc} (lines Figure 6.1a) is only slightly affected by the emitter doping and a high level of surface passivation is observed regardless of the illumination intensity. For one sun condition the iV_{oc} amounts to about 730 mV for all doping levels.

Requirement 2) Induced band bending and hole density: Constant majority carrier quasi Fermi-level in the undoped buffer and at the c-Si surface.

The band bending (inversion) of an a-Si:H(p)/a-Si:H(i)/c-Si(n) structure determined from surface photo voltage (SPV) measurements [193], [89] as a function of the B_2H_6 gas phase doping of the a-Si:H(p) layer is plotted in Figure 6.1b. For a gas phase doping concentration below 2000 ppm the band bending increases strongly with doping and saturates for higher doping concentrations at about 800 meV. Most of this band bending is induced into the c-Si and the undoped a-Si:H forming a highly hole populated device region and the induced p/n-junction. The results also indicate that the work function of the a-Si:H(p) which is responsible for the induced band bending increases with doping.

Requirement 3) High hole density in the doped a-Si:H: Constant majority carrier quasi Fermi-level in the doped a-Si:H and at the interface to the TCO electrode.

Despite the relatively high work function of the a-Si:H(p) which induces a highly hole populated c-Si region, a sufficiently high hole density in the doped a-Si:H needs to be ensured as well. This free hole density results from the interplay between the net doping of the a-Si:H(p) and the work function of the TCO which causes the depletion of the a-Si:H(p) from free holes. However, unlike

for the two requirements above, this free hole density is hardly experimentally accessible for the device relevant structure.

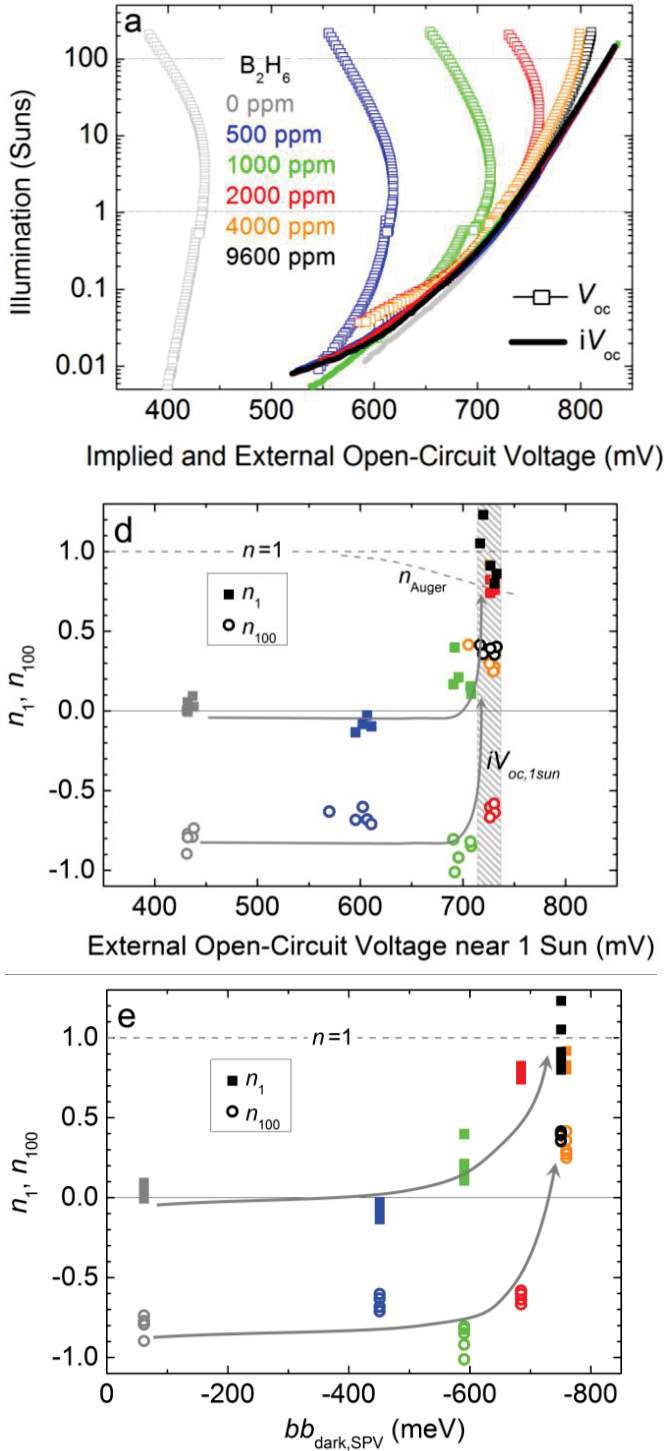


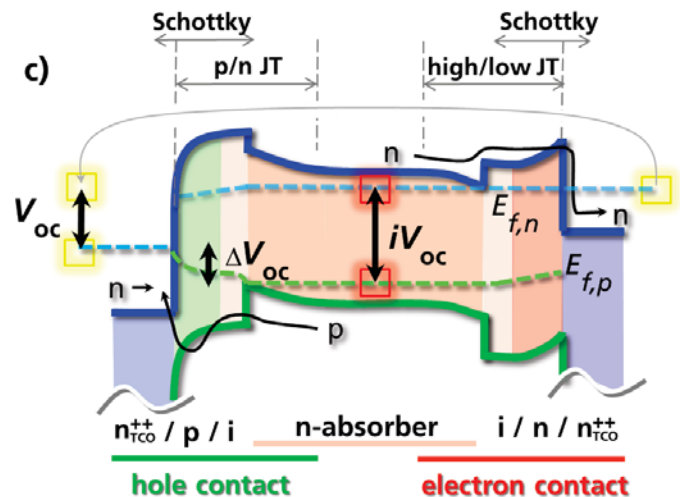
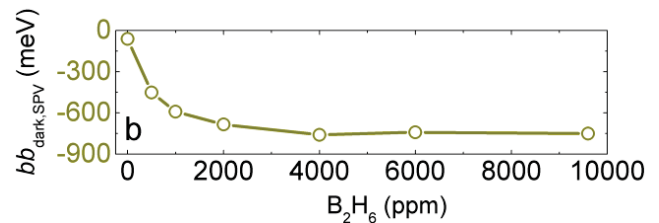
Figure 6.1: a) Measured influence of a-Si:H(p) emitter B_2H_6 gas phase doping on the Suns- iV_{oc} (solid lines) and Suns- V_{oc} (open squares) characteristic of ITO/piNin/ITO Suns- V_{oc} samples featuring a ~ 10 nm thick buffer layer below the emitter.

b) Induced c-Si band bending in the dark of piN SPV samples.

c) Sketch of TCO/piNin/TCO solar cell band diagram at open-circuit conditions featuring a gradient of the majority carrier QFL in the p-SHJ and no gradient in the n-SHJ.

d) Slope of Suns- V_{oc} curves near 1 and 100 suns vs. external V_{oc} near 1 sun. The shaded area denotes the implied V_{oc} near 1 sun. n_{Auger} is the voltage dependent ideality factor of the 1 sun V_{oc} limited by the intrinsic c-Si bulk recombination [6].

e) Slope of Suns- V_{oc} curves near 1 and 100 suns vs. the induced c-Si band bending from b).



As extensively discussed in section 4.2, the case that the contact region provides a too low hole density and is operating in high-injection manifests itself in a voltage loss (ΔV_{oc}) mainly in the a-Si:H (hole contact in Figure 6.1c). This voltage loss can be determined directly by the comparison of implied and external V_{oc} with the QSSPC and *Suns*- V_{oc} setup. The measured illumination level dependence of the external V_{oc} for the a-Si:H(p) emitter doping variation is shown in Figure 6.1a. A difference between the iV_{oc} (solid lines) and the external V_{oc} (open symbols) can be observed which increases for decreasing gas phase doping. However, this voltage loss can also be determined in an indirect way when analyzing only the slope of the external V_{oc} at a certain illumination intensity. A voltage loss caused by high-injection conditions in the contact region is indicated by the fact that the slope of the *Suns*- V_{oc} curve drops below the one predicted by the standard p/n-junction theory, where it is assumed that the V_{oc} is determined solely by surface and c-Si bulk recombination and hence the iV_{oc} . If this assumption is fulfilled, i.e. if low-injection conditions in the contact region are preserved, depending on the prevalent minority carrier recombination path, the slope can range from 0.7 to 2.0 [44] (see also Figure 5.3) but will not fall below 0.7. The latter is indicating the intrinsic limit imposed by high-injection Auger recombination in the absorber. In Figure 6.1d it is shown that for insufficient doping (grey, blue, green) the slope of the external V_{oc} near 1 and 100 suns (n_1 and n_{100}) drops well below this lower limit of 0.7 (grey dashed lines). In accordance with the direct comparison between the iV_{oc} and the external V_{oc} in Figure 6.1a, this clearly shows that the low external V_{oc} 's of these contacts are not limited by a poor surface passivation. Figure 6.1d reveals that for increasing doping (red, orange, black) and when the external V_{oc} approaches the limit imposed by the iV_{oc} (shaded area) n_1 and n_{100} strongly increase. n_1 takes a value of about 0.8 which is close to 0.7, indicating that voltage extraction is ideal. This is evidenced in Figure 6.1a where the external V_{oc} matches the iV_{oc} for 1 sun conditions. However, for all cases n_{100} is below n_1 . This is explained by the much higher excess carrier density in the contact region which results from such high illumination intensities. Accordingly, operation in high-injection conditions is more likely and the voltage loss is more pronounced. This is in line with the fact that the external voltage remains below the internal voltage for 100 suns in Figure 6.1a. To highlight the importance of the induced p/n-junction for an ideal voltage extraction, in Figure 6.1d n_1 and n_{100} are plotted as a function of the induced c-Si band bending obtained for the different a-Si:H(p) doping levels. The trends are very similar to Figure 6.1d and it becomes obvious that a sufficient high band bend is needed for an ideal voltage extraction.

As shown in Figure 6.1a for the undoped emitter (0 ppm) a high level of c-Si passivation (iV_{oc}) is achieved but regardless of the illumination level the contact does not have the ability to extract the high iV_{oc} provided by the well passivated absorber. In this case the contact properties are dominated by the ITO / a-Si:H Schottky contact and a poor hole contact is formed as the contact region is depleted from holes. This is explained by the fact that the work function of the ITO is close to mid-gap rather than close to the valence band of the a-Si:H and the c-Si absorber (more in section 6.3). At 1 sun the external V_{oc} is limited to about 430 mV for the case that the selectivity is dominated by the TCO work function only. The selectivity of the contact to holes is increased as with higher doping the a-Si:H / c-Si p/n-junction starts to dominate over the opposing TCO / a-Si:H Schottky contact.

For 1 sun conditions a doping of about 2000 ppm is required for our layers to fully extract the voltage provided by the passivated absorber. An external V_{oc} of ~ 730 mV is reached which agrees well with the iV_{oc} which in turn is limited by the c-Si passivation provided by the p- and n-SHJ and the intrinsic bulk recombination of the planar 5 Ω cm, 200 μ m thick, FZ absorber [6]. However, for illumination intensities above 1 sun, a voltage loss within the SHJ occurs which causes a deviation of the external V_{oc} from the iV_{oc} characteristics. Basically, the voltage loss in the contact region is more pronounced for lower doping and higher illumination intensities.

6.1.3 Correlation with the fill-factor

Solar cells: Thinner buffer layer

In this section a B_2H_6 gas phase doping variation of an ITO / a-Si:H(p) / a-Si:H(i) emitter for an only ~ 7 nm thick intrinsic buffer layer is studied and the qualitative relation between the Suns- V_{oc} characteristic at high illumination intensities of non-metallized Suns- V_{oc} test samples and the FF of finished devices is presented. n_{100} is preferred over n_1 as it is more sensitive to a voltage loss in the contact region as motivated above.

Contrary to the previous section our thinner buffer layer cannot ensure an efficient decoupling of the chemical c-Si passivation from the doping of the a-Si:H(p) layer above. In Figure 6.2a it can clearly be seen that due to additional B_2H_6 during deposition of the a-Si:H the c-Si absorber becomes significantly depassivated [151], [150]. Consequently, the iV_{oc} at 1 sun is reduced from about 720 mV (600 ppm) to 630 mV (9600 ppm) by increasing the doping. Thus, for our p-SHJ with too thin buffer layers a fundamental trade-off between a-Si:H doping and c-Si passivation is

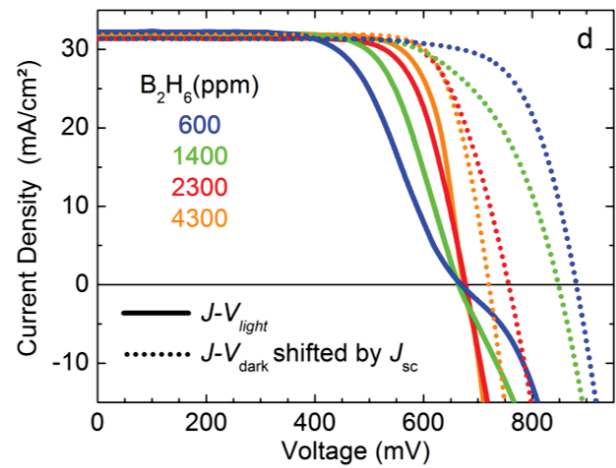
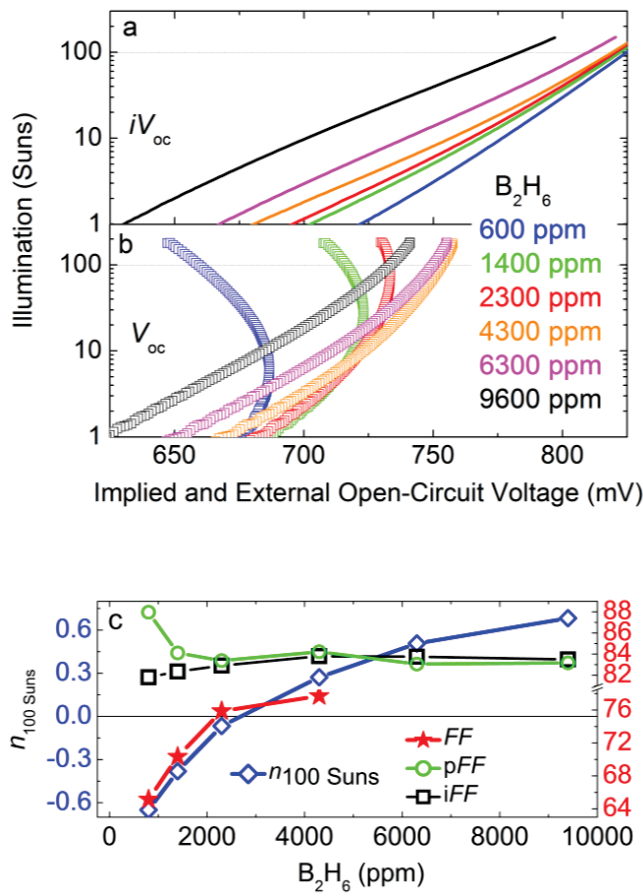


Figure 6.2: Left, a) measured influence of a-Si:H(p) emitter gas phase doping on the $Suns-iV_{oc}$ and b) on the $Suns-V_{oc}$ characteristic of ITO/piNin/ITO $Suns-V_{oc}$ samples featuring a ~ 7 nm thick buffer layer below the emitter. c) The corresponding slope of the external V_{oc} at 100 Suns and the FF of finished. Additionally, the iFF from QSSPC and the pFF from $Suns-V_{oc}$ measurements of corresponding $Suns-V_{oc}$ samples are shown. Above, d) measured $J-V_{light}$ characteristic and $J-V_{dark}$ shifted by the J_{sc} .

observed. The local ideality factor at 100 suns ($n_{100\text{Suns}}$, blue) of this ITO/piNin/ITO $Suns-V_{oc}$ sample and the FF of finished devices (red) featuring metal electrodes at the front and rear are shown in Figure 6.2c. Reflecting the V_{oc} characteristic for high illumination intensities from Figure 6.2b, $n_{100\text{Suns}}$ is increasing from -0.6 to 0.6 with doping. More importantly, the same trend can be observed for the FF of the corresponding cells (no cells were fabricated with a-Si(p) layers exceeding 4300 ppm B_2H_6 gas phase concentration). This demonstrates experimentally that there is a correlation between the $Suns-V_{oc}$ characteristic at high illumination intensities and the FF of actual solar cells. In terms of maximum efficiency for this buffer layer an optimum doping has to be found that serves best the trade-off V_{oc} vs. FF .

In Figure 6.2c the corresponding iFF from QSSPC (black) and the pFF from $Suns-V_{oc}$ measurements (green) are shown to assess behavior of the devices near MPP and for lower illuminations, i.e. lower excess carrier densities. The iFF is slightly increased with doping from about 81.5 to 84.0 % reflecting the improved field effect passivation [194], [89] (section 5) that results from the higher band bending in the c-Si part of the SHJ (Figure 6.1b). A poor selectivity of the SHJ is also indicated by a pFF which is well above the iFF . This “too high pFF ” is explained by

the much lower excess carrier density for the pseudo MPP conditions (~ 0.03 suns) compared to the 1 sun conditions. Accordingly, the voltage loss for the pseudo MPP conditions is much lower which means that reduction of the V_{oc} by a non-ideal voltage extraction is much stronger than that of the V_{MPP} from the $Suns-V_{oc}$. According to equation (2.29) this results in the increase of the pFF . However, this is observed only for very low doping, i.e. if already a significant voltage loss at 1 sun OC conditions is observed (600 and 1400 ppm in Figure 6.2a, b).

It can be seen in Figure 6.2d that for “real” MPP conditions, i.e. when a current is drawn from the device, insufficient doping is reflected in an S-shaped behavior of the $J-V$ curve and that the superposition principle fails (section 4.2.5). Finally, Figure 6.3a and b shows the slope of the $Suns-V_{oc}$ curves near 1 and 100 suns plotted vs. the FF and the V_{oc} , respectively. It can be clearly seen that with increasing doping n_1 and n_{100} are increased which is indicating that losses caused

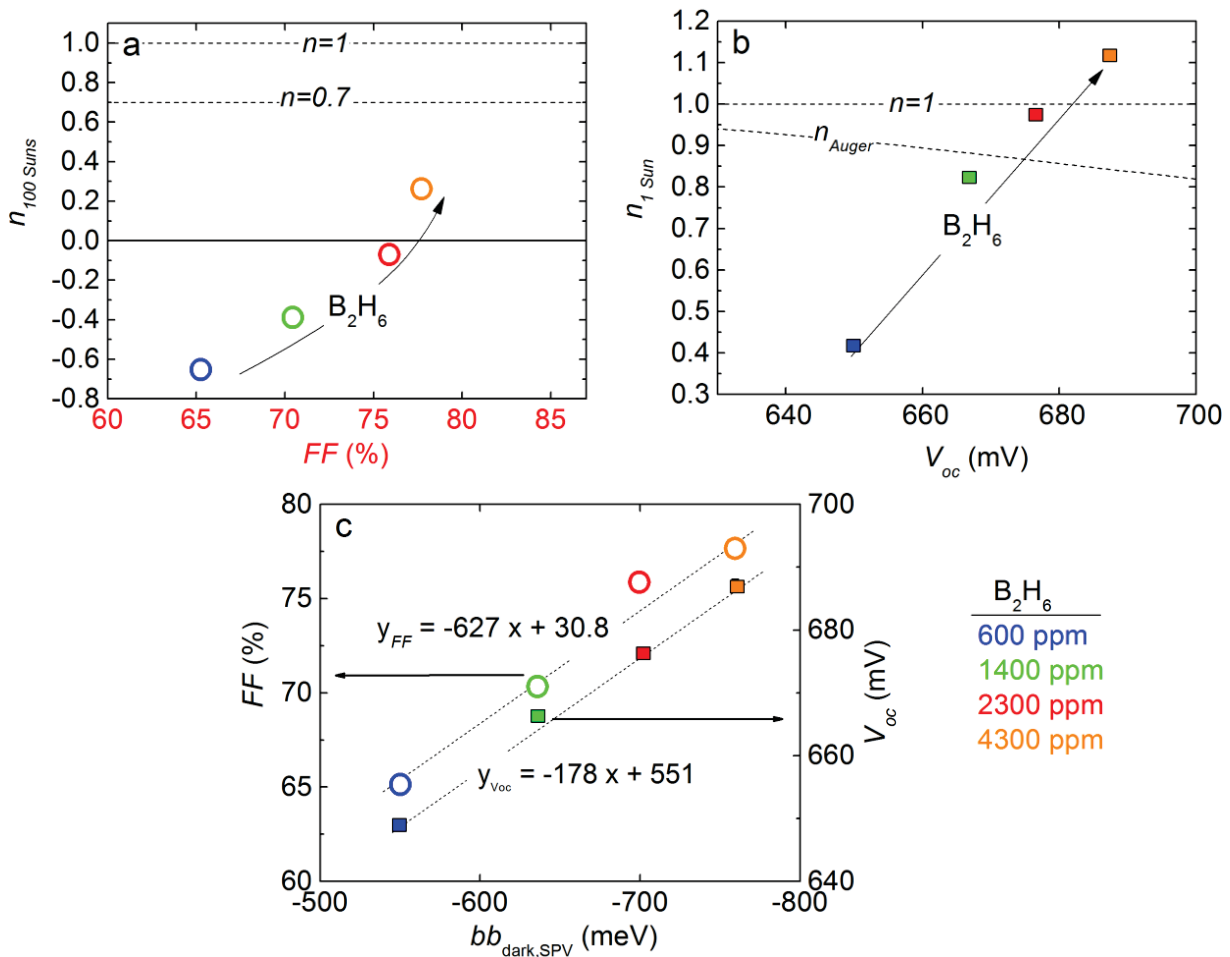


Figure 6.3: a) Slope of $Suns-V_{oc}$ curves near 100 suns vs. FF for the four different emitter gas phase doping levels. b) Slope of the $Suns-V_{oc}$ curves near 1 sun vs. V_{oc} . n_{Auger} in b) is the voltage dependent ideality factor of the 1 sun V_{oc} limited by the intrinsic c-Si bulk recombination [6]. c) FF and V_{oc} as a function of the induced c-Si band bending obtained for the different a-Si:H(p) doping levels and a linear fit of the data.

by high-injection conditions in the contact becomes less pronounced with increasing gas-phase doping. With respect to the importance of the induced p/n-junction, Figure 6.3c reveals a linear dependence of the V_{oc} and FF on the induced c-Si band bending. The linear dependence of the V_{oc} is in line with the simulation results in section 4.2.3 and 4.2.5 where such a behavior was predicted for the regime where the external voltage is limited by the selectivity rather than surface passivation. That the slope is below unity results from the fact that the increase of the induced band bending is not only responsible for improvement of the a-Si:H(pi) / c-Si p/n-junction but that the parasitic ITO / a-Si:H Schottky contact must also be taken into account (see Figure 4.16b grey dotted lines).

Correlation with the fill-factor: Device Simulations

To corroborate the conclusions drawn from experimental findings above, device simulations with *Sentaurus device* were performed. Unlike for the AFORS-HET simulations in section 4 tunneling transport is included here yielding an even better agreement with the experimental results. Furthermore, in Refs [96] and [195] it has been shown that tunneling at the TCO/a-Si:H(p) interface has to be taken into account to obtain realistic J - V and QSSPC characteristics. Here an a-Si:H(p) emitter doping variation for an TCO/piNin/TCO structure was simulated. Defects at the interface to the absorber were omitted and a constant defect density and defect characteristic of the p-layer was assumed. Hence, the iV_{oc} is limited mainly by the intrinsic recombination of the absorber and like in section 6.1.2 only a minor influence of the emitter doping on the iV_{oc} is observed. We did not treat the TCO as an individual n-type semiconductor, but as a conductive layer characterized only by its interface work function, conductivity and optical properties. Barrier tunneling at the TCO/a-Si:H(p) interface was considered. To take the depletion of the a-Si:H(p) by the TCO into account the TCO work function is set to 4.93 eV which is 670 meV below the valence band of the a-Si:H. The net doping of the a-Si:H(p) is quantified by its activation energy (E_a) which is varied over a wide range from undoped (860 meV \sim mid-gap) to a very high net doping (200 meV below the valence band energy). A lumped series resistance of $0.5 \Omega\text{cm}^2$ was assumed. More simulation parameters can be found in Ref. [94].

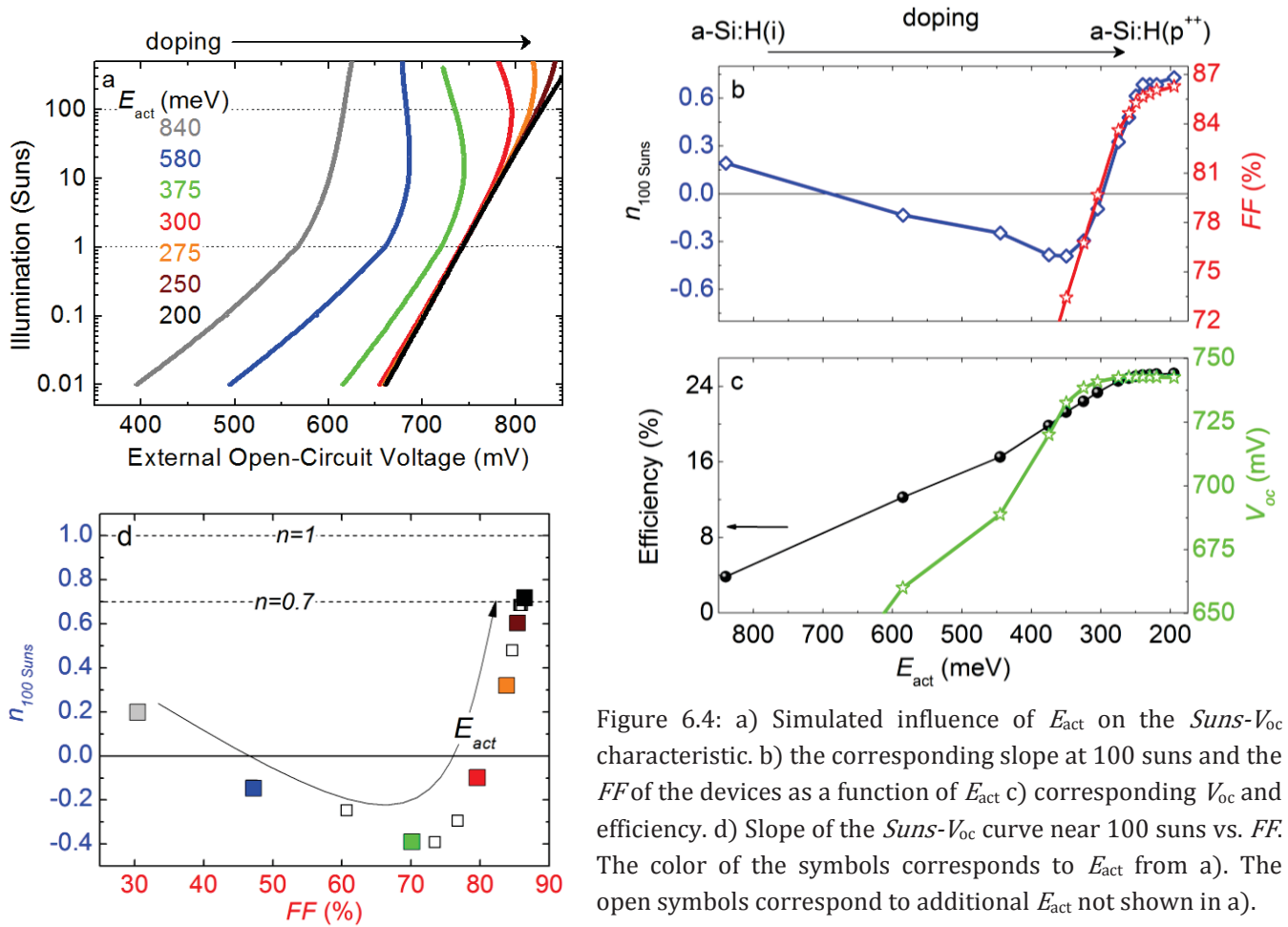


Figure 6.4: a) Simulated influence of E_{act} on the $Suns-V_{oc}$ characteristic. b) the corresponding slope at 100 suns and the FF of the devices as a function of E_{act} c) corresponding V_{oc} and efficiency. d) Slope of the $Suns-V_{oc}$ curve near 100 suns vs. FF . The color of the symbols corresponds to E_{act} from a). The open symbols correspond to additional E_{act} not shown in a).

The simulated $Suns-V_{oc}$ characteristics are shown in Figure 6.4a. Good qualitative agreement between the simulations and the experimental results for a thick buffer layer (Figure 6.1a) are observed. With increasing doping the V_{oc} loss in the contact region is reduced. Regarding the $V_{oc,1Sun}$ (Figure 6.4a, c) a sufficient selectivity is observed if E_a approaches 300 meV. The $V_{oc,1Sun}$ saturates at about 740 mV limited by the iV_{oc} (not shown). The corresponding FF is plotted in Figure 6.4b, d. Again a clear correlation between the FF and n_{100} can be observed for moderate to high doping ($E_{act} > 400$ meV). It can be seen in Figure 6.4b, c that the FF still significantly increases for E_{act} below 300 mV while the increase in V_{oc} is only negligible. This shows again that optimal 1 sun MPP conditions require a much higher doping than optimal OC conditions. That this also applies to the optimal TCO work function is shown in Ref [94] from the present author by the present author which substantiates that the requirements on the selective carrier extraction are more challenging for MPP conditions as compared to OC conditions.

Similar to the experimental findings, Figure 6.4a reveals that exposing the SHJ to illuminations well above 1 sun even for OC conditions a clear signature of the lack of doping can be observed

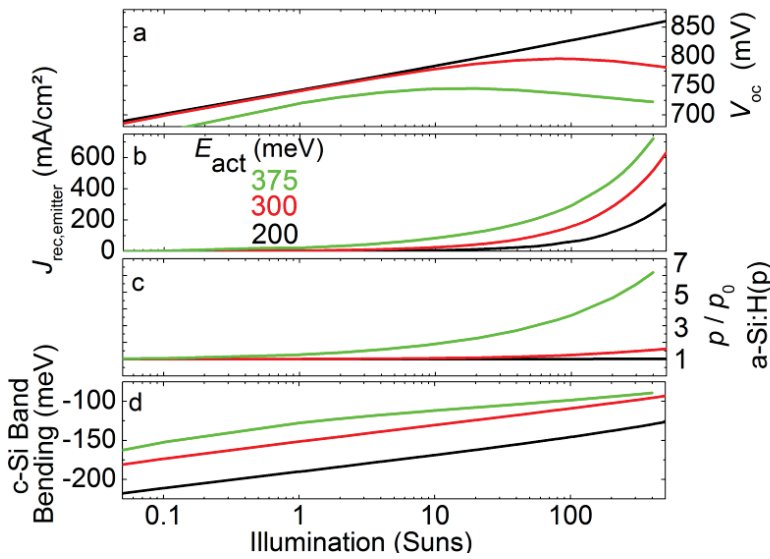


Figure 6.5: a) Simulated influence of E_{act} on the *Suns*- V_{oc} characteristic, replotted from Figure 6.4a. b) The recombination current density within the TCO/a-Si:H(p)/a-Si:H(i) emitter stack. c) The ratio of the actual hole concentration to the equilibrium hole concentration within the a-Si:H(p). d) The band bending in the c-Si space charge region.

for layers featuring relatively high doping levels ($E_a < 300$ meV). By making use of this effect a clear correlation between the current-less *Suns*- V_{oc} characteristics at high illumination intensities and the 1 sun MPP conditions is observed (Figure 6.4b, d). However, it can be seen that this correlation is observed only for the case that doping is sufficient to prevent a voltage loss for the 1 sun OC conditions. For very low doping ($E_a > 400$ meV) when $V_{oc,1Sun}$ is significantly affected by a non-ideal voltage extraction a different behavior is observed. However, these layers would be excluded for further device optimization anyway as already the $V_{oc,1Sun}$ is limited by insufficient doping. In combination with the very low *FF* it would result in a very low cell efficiency (Figure 6.4c).

In Figure 6.5 a more detailed loss analysis for three distinctive doping levels is presented. $E_a = 200$ meV represents optimum doping where low-injection conditions are maintained irrespective of the work conditions and the contact characteristic is dominated by minority carrier recombination, i.e. the implied V_{oc} . $E_a = 300$ meV yields only optimum OC conditions and $E_a = 375$ meV represents insufficient doping of the a-Si:H(p) emitter for MPP and OC conditions. It can be seen in Figure 6.5a that the reduction of V_{oc} for higher illuminations (compared to the highly-doped with 200 meV layer), comes along with an increasing recombination current within the TCO/a-Si:H(p)/a-Si:H(i) part of the p-SHJ (Figure 6.5b). The emitter recombination current

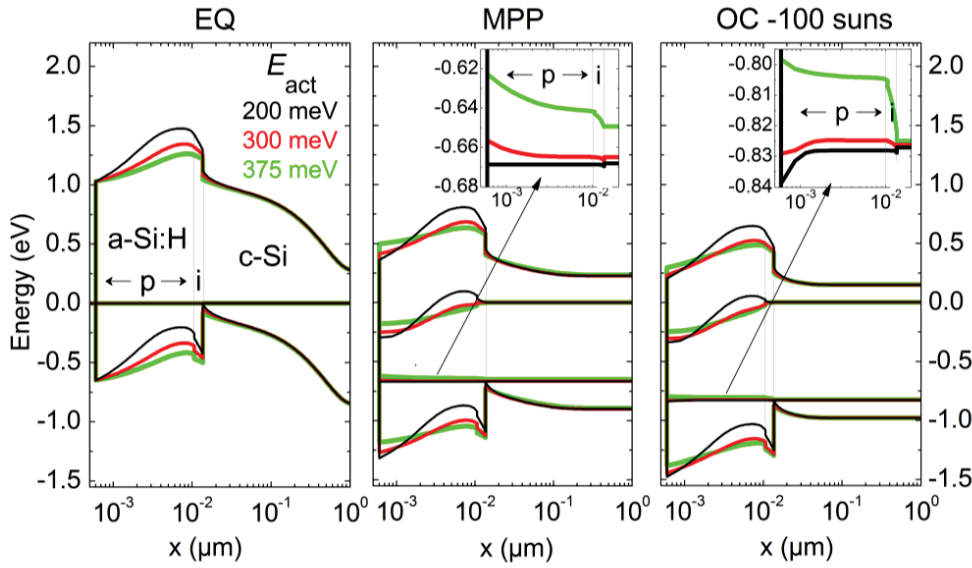


Figure 6.6: Influence of E_{act} on the band diagram at EQ, 1 sun MPP and 100 suns OC conditions. Shown are the a-Si:H and c-Si part of the p-SHJ. Diagrams are plotted in respect to the electron QFL. The insets show the hole QFL within the a-Si:H(p)/a-Si:H(i) stack.

density in Figure 6.5b corresponds to the sum of the defect recombination within the a-Si:H(p)/a-Si:H(i) and at the TCO/a-Si:H(p) interface. The recombination within the a-Si:H(p) dominates the total recombination of the TCO/a-Si:H(p)/a-Si:H(i) stack (not shown). That this is not only true for OC but also for MPP conditions was shown by the author in Ref [94]. It follows that for a low doping or high work function mismatch the recombination within the a-Si:H(p) is responsible for the low FF . More precisely, it is caused by the fact that depleted contact region is operating in high-injection conditions. For such conditions the majority carrier density in the contact region is reduced by recombination as well which is linked to a significant gradient in the majority carrier quasi Fermi-level. Figure 6.5 reveals that the voltage loss at OC correlates well with the onset of high-injection conditions in the a-Si:H(p) layer, i.e. when the actual majority carrier density (p) exceeds the equilibrium majority carrier density (p_0). p_0 for the investigated layers ($E_{act} = 200, 300, 375$ meV) amounts to $2 \cdot 10^{16}$, $1 \cdot 10^{14}$ and $5 \cdot 10^{12}$ cm $^{-3}$. This significant difference in p_0 can be attributed to the lower doping and the higher depletion caused by the TCO work function. The corresponding band bending in the space charge region of the c-Si absorber is shown in Figure 6.5d as well. It can be seen that very high illumination intensities exceeding 100 suns do not cause flat-band conditions within the c-Si absorber.

In Figure 6.6 the band diagrams for equilibrium (EQ), 1 sun MPP and 100 sun OC conditions for the three E_{act} are depicted. The depletion of the a-Si:H(p) near the TCO/a-Si:H(p) interface and the inverted c-Si can be observed for all working conditions. The lower E_{act} is the lower is the a-Si:H depletion and the higher is the c-Si inversion, respectively. That the parasitic band bending at the TCO/a-Si:H(p) interface increases with a-Si:H doping results from the increased work

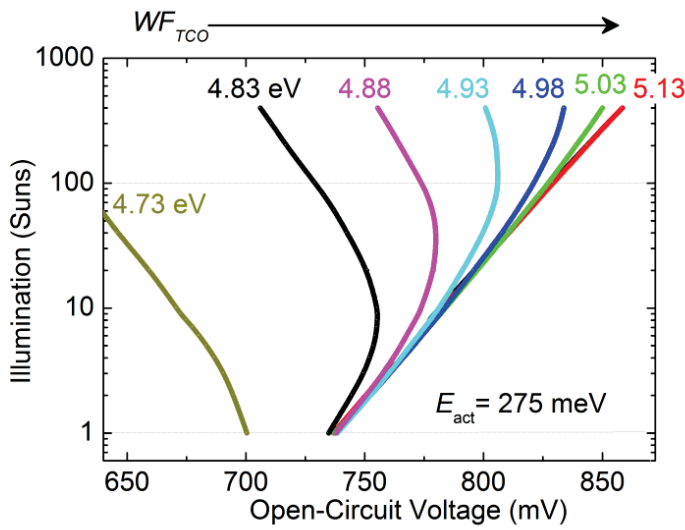


Figure 6.7: Simulated influence of TCO's work function on the Suns-Voc characteristic at high illumination intensities for a constant a-Si:H(p) doping.

function mismatch between the TCO and a-Si:H(p) [94]. With increasing doping work function matching becomes even worse but the higher doping reduced the screening length and hence the effective Schottky barrier height as the barrier becomes narrower [95]. For an E_a of 300 meV and 375 meV the depletion of the a-Si:H(p) is not only restricted to a small region near the TCO/a-Si:H(p) interface but a global depletion of the a-Si:H(p) is observed as the a-Si:H(p) thickness is below the respective screening length. This is indicated by the difference between the hole quasi Fermi-level and the valence band energy within the a-Si:H(p) near the a-Si:H(i) layer. For EQ this difference is higher than E_a of the a-Si:H(p) featuring medium and low doping. It amounts to 200, 335, and 415 meV for the layers with an E_a of 200, 300, and 375 meV, respectively. In accordance with results from section 4.2.5, with the onset of high injection conditions in the contact region for MPP and OC a gradient in the majority carrier (hole) quasi Fermi-level is observed which is responsible for reduction of the external V_{MPP} and V_{oc} .

Finally, it should be noted that a variation of the TCO work function for a constant a-Si:H doping yields a behavior of the $Suns-V_{oc}$ characteristic (Figure 6.7) which is similar to the one observed for the variation of the a-Si:H doping for a fixed work function of the TCO from above. In accordance with the results from section 4.2.5 this highlights the tight interplay between the TCO work function and the a-Si:H doping (and thickness) with respect to the SHJ properties.

To sum up, the experimentally observed results could be well reproduced by numerical device simulations and recombination within the TCO/a-Si:H part of the SHJ coupled to the occurrence of high-injection conditions in the contact region were identified to cause the deviation of the

external voltage from the implied voltage. To prevent a voltage loss within the contact region and allow for a high FF and V_{oc} , a high equilibrium density of the contacts majority carrier species is mandatory. This requires a high net doping and a negligible depletion of the doped a-Si:H by the TCO work function. Furthermore, a direct comparison of the QSSPC and Suns- V_{oc} characteristic is not mandatory to identify if surface passivation or voltage extraction is the limiting factor. Analyzing only the slope of the illumination level dependence of the external voltage obtained with Suns- V_{oc} allows for a meaningful evaluation of the contact scheme as a clear correlation between the local slope and FF and V_{oc} loss caused by a non-ideal voltage extraction exist.

6.1.4 Temperature dependence of cell parameters

The more common approach for the identification of such a non-ideal voltage extraction is to analyze the temperature dependence of J - V_{light} curve of finished solar cells. However, compared to the current-less Suns- V_{oc} measurement it leads to much higher demands on the sample and measurement setup. Some cell parameters obtained from J - $V_{light}(T)$ and J_{sc} - $V_{oc}(T)$ measurements are plotted in Figure 6.8 for the a-Si:H(p) emitter doping variation.

The most striking feature is the temperature dependence of the V_{oc} and the FF which reveals the non-ideal behavior of the cells featuring insufficient doping of the a-Si:H(p). Both deviate from the linear reduction with temperature, which is governed by the increase of minority carrier recombination at MPP and OC conditions and the correspond reduction of the FF_0 and V_{oc} with temperature [196]. The emitter with the highest doping (blue) on the other hand follows the behavior predicted by the standard p/n-junction theory and shows a linear reduction of the V_{oc} and FF with increasing temperature.

While a satisfactory explanation for the non-linear reduction of the V_{oc} with increasing temperature for the lowly doped emitters cannot be given. Device simulations assuming similar c-Si passivation by the hole contact but different doping levels cannot reproduce the experimental findings. Hence, the fact that for the experimentally investigated emitters the c-Si surface passivation and doping are not decoupled might explain this behavior. The lowly doped and less defective emitters provide much better c-Si passivation and are thus characterized by a much higher iV_{oc} as compared to their highly doped counterparts (Figure 6.2). This higher iV_{oc} level is linked to a lower reduction of the iV_{oc} with temperature [196]. Thus, the reduction of the iV_{oc} with temperature, which defines the upper bound of the external V_{oc} , is expected to be lower

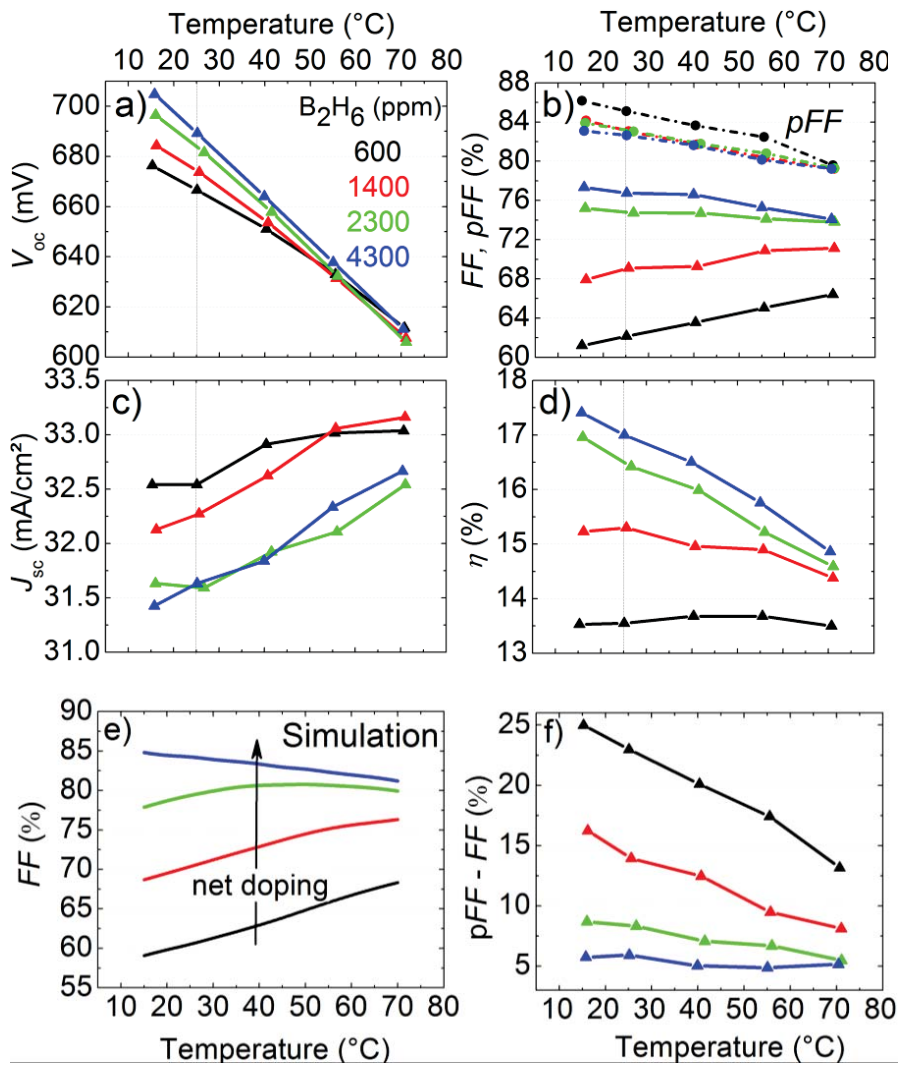


Figure 6.8: Temperature dependent parameters from measured J-V and Suns- V_{oc} characteristic for the a-Si:H(p) emitter doping variation. e) FF from Sentaurus device simulations for an emitter doping variation.

for the lowly doped emitters. This would result in a lower slope of the $V_{oc}(T)$ dependence. However, such a behavior is observed only for the moderate temperature range up to 40 $^{\circ}C$. For higher temperatures a changing slope is observed for the lowly doped emitters which is indicating that a second mechanism is involved which yields a higher reduction of the V_{oc} with increasing temperature. The fact that all lines start to merge at higher temperatures might be related either to an increased minority carrier recombination rate or an increased voltage loss in the contact region which are more pronounced for the lowly doped emitters. An increased voltage loss in the contact region with temperature might be caused by the fact that high-injection conditions become more pronounced the higher the density of thermally generated excess carrier is. This is similar to the case when additional excess carriers are generated by photon-absorption. However, more detailed investigations are needed for a clear explanation of this interesting behavior.

The explanation for the FF which is increasing rather than decreasing with temperature for insufficient doping is more straightforward. This behavior can be reproduced qualitatively by device simulations (Figure 6.8e) and according to a loss analysis not shown here this behavior is explained as follows: For the highly doped emitter the hole extraction is dominated by tunneling which provides an efficient transport path which does not benefit from an increased temperature. Accordingly, the difference between pFF and FF , which quantifies the fill factor losses caused by transport related issues (Figure 6.8f), is not affected by the temperature (blue line). The drop in the FF with temperature (Figure 6.8b) follows the reduction of the pFF caused by the increase of minority carrier recombination, i.e. the reduction of FF_0 . On the other hand, for the lowly doped emitters hole extraction is poor because tunneling is inefficient. Thermionic emission is the domination transport path, which becomes more efficient the higher the temperature is. Accordingly, the transport related FF loss is reduced with increasing temperature for these emitters (Figure 6.8f). For the moderate doping (green) the improved majority carrier (hole) extraction (reduction of $pFF - FF$) and the increased minor carrier recombination (reduction pFF) are superimposed which yields an almost constant FF (Figure 6.8b) in the range from 15°C to 70°C. For the low and very low doping this interplay results in an increase of the FF and hence a positive slope of $FF(T)$ as the reduction of the transport related FF losses clearly dominates over the losses caused by the increased minority carrier recombination.

With respect to the J_{sc} the typical linear increase with temperature [196] is observed irrespective of the emitter doping. The fact that even the very low emitter doping (black) which leads to significant losses at MPP and OC, the J_{sc} shows a normal behavior illustrates that the demands on the selective carrier extraction from the absorber are the lowest for short-circuit conditions. This can be explained by the fact that the excess carrier density in the contact region takes its lowest value (most excess carriers are extracted externally) which makes the contact region unsusceptible to operate in high-injection. The higher J_{sc} for the very low (black) and low (red) emitter doping might be partly explained the higher optical band gap of the less defective lowly doped a-Si:H which reduced parasitic absorption (not shown). Representative for all emitter doping levels, Figure 6.9 shows the temperature dependence of the external quantum efficiency (EQE) and the corresponding 1-reflection (1-R) data. The shift of the optical c-Si band gap towards lower energies / higher wavelength is depicted in the graph. The latter makes the absorption of long wavelength photons in the c-Si absorber more likely with increasing temperature. This is reflected in the increased EQE for wavelength above 900 nm and the

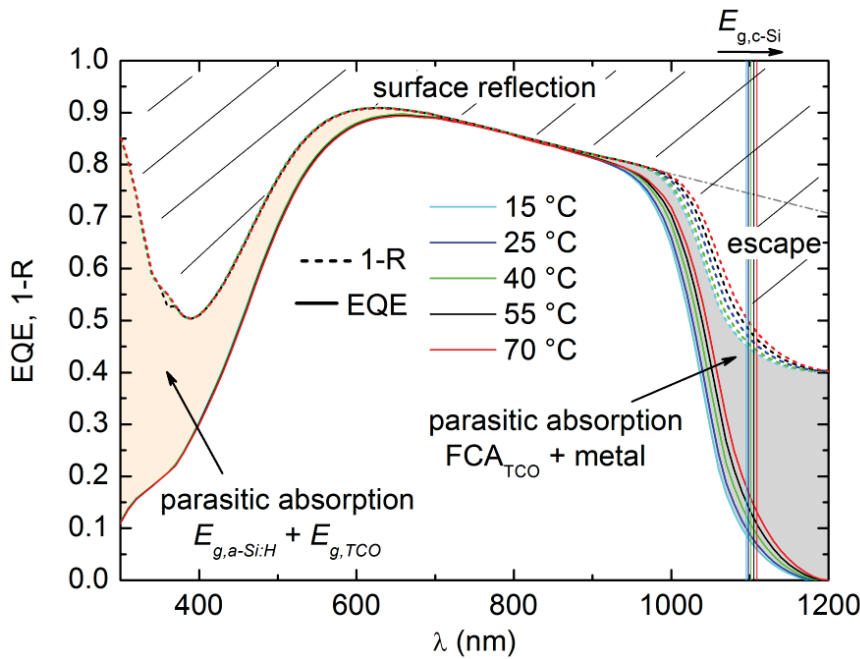


Figure 6.9: Temperature dependence of measured external quantum efficiency and 1-reflection of a planar cells.

reduced escape reflectance. The latter is indicating that less long wavelength photons exit the absorber at the front of the solar cells. The shaded area between the EQE and 1-R curves is indicating the parasitic photon absorption. It is rather constant and not affected by the temperature. Hence, the current gain with temperature is dominated by the decrease of the optical band gap of the c-Si absorber which makes photon absorption in the long wavelength regime more likely. Figure 6.8d shows that in terms of efficiency, the gain in J_{sc} does not outweigh the loss in V_{oc} and FF . Interestingly, for 70°C a similar efficiency is observed for the low (red), medium (green) and high (blue) emitter doping.

6.1.5 Further investigations and remarks

Amorphous silicon compounds for p/n and high/low junctions

It shall be pointed out below that the proposed method of analyzing the *Suns*- V_{oc} characteristic at certain high illumination intensities to probe the selectivity of a contact is not only restricted to investigations of the hole contact and that it is applicable to both the p/n junction and the high/low junction. To this end, the influence of alloying of n-doped a-Si:H films on their doping efficiency is investigated for the electron selective contact. The latter is formed by an ITO/a-SiO_x:H(n)/a-Si:H(i) stack which is depicted in Figure 6.10. A doping variation for the a-SiO_x:H(n) layer is presented which forms either the front emitter (stack placed on p-absorber) or the front surface field (stack placed on n-absorber). The net doping of the a-SiO_x:H(n) film is

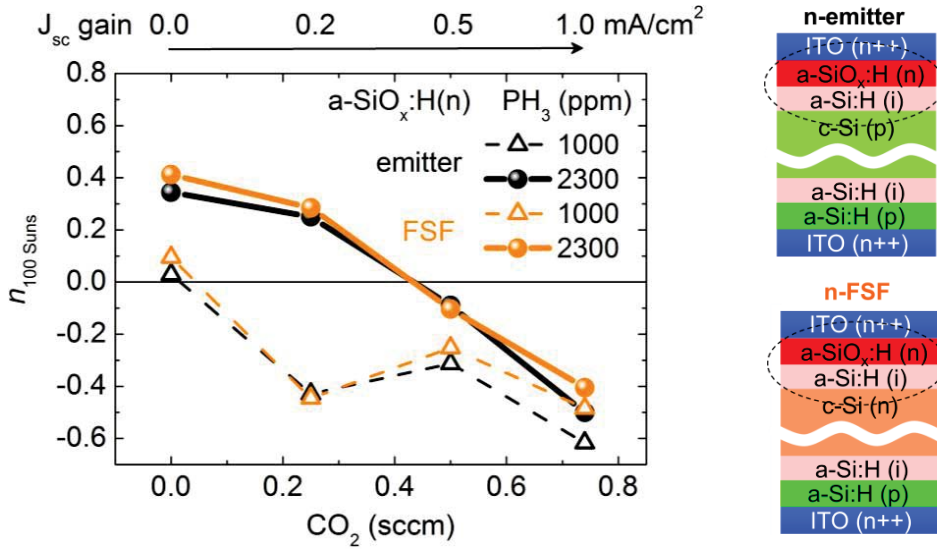


Figure 6.10: Experimentally obtained slope of the *Suns*- V_{oc} curve at 100 suns as a function of the CO_2 gas flow for an a-SiO_x:H(n) front emitter (black symbol) and front surface field (orange symbols). The PH_3 gas phase doping concentration is denoted by the open and closed symbols. The numbers above the graph correspond to the simulated J_{sc} gain with increasing alloying.

manipulated by both the PH_3 (n-doping) and the CO_2 (alloying) flow in the process gas. Consequently, the net doping is a function of the amount of active phosphorus (n-doping) and oxygen (alloying) incorporated in the layer. The motivation for alloying the ~10 nm thick a-SiO_x:H(n) layer is to increase its optical band gap. This lowers the parasitic absorption in the a-SiO_x:H film and, thus, increases the photocurrent available for absorption in the c-Si. However, typically a trade-off between the net doping and the optical properties is observed for a-SiO_x:H [178] which has to be carefully balanced to maximize the efficiency. The results shown here are determined on *Suns*- V_{oc} samples.

To determine the potential J_{sc} gain with increasing alloying the corresponding refractive indices and extinction coefficients of the a-SiO_x:H(n) films have been extracted from spectroscopic ellipsometry measurements by fitting the data to a Tauc-Lorenz model and were implemented in *Sentaurus device* simulation. As shown in Figure 6.10, a significant J_{sc} gain of up to 1.0 mA/cm² is expected for the maximum CO_2 flow for a 10 nm layer. However, the experimentally obtained slope of the *Suns*- V_{oc} curve at 100 suns indicates a strongly increasing voltage loss in the contact region at 100 suns with increasing CO_2 gas flow. This can be interpreted as a strong decrease of the doping efficiency with alloying. It can be seen that a higher PH_3 content in the process gas (spheres) has a positive influence on the net doping for a moderate CO_2 content as the slope at 100 suns is increased with respect to the lower PH_3 content in the process gas (open triangles). However, for a high CO_2 content, which yields the best optical properties, the doping efficiency is poor and seems to be determined solely by the high CO_2 content. As the band gap is changed by alloying, a change of the band offsets is expected, too. This might be of importance for MPP conditions when a significant current transport takes place. However, it is expected that this is of

minor importance for the current less $Suns-V_{oc}$ measurements that are used here. This is confirmed by the fact that for device simulations a variation of the electrical band gap and thus a change of the band offsets at the conduction or valence band are not required to reproduce the behavior from Figure 6.10.

Furthermore, it should be noted that even for the layer without CO_2 $n_{100Suns}$ is well below the limited of 0.7 which would indicate sufficient doping of the n-layer. Just as for the p-layers from the previous section, a strong dependence on the gas phase doping is observed for our n-layers. Subsequent optimization of the a-Si:H(n) layer has revealed that for a further increase of the PH_3 gas phase doping (not shown) $n_{100Suns}$ approaches 0.7. However, the negative influence of the gas phase doping on the c-Si surface passivation and hence the implied V_{oc} is much lower as compared to our p-doped layers. Hence, the trade-off between c-Si passivation (high iV_{oc}) and excess carrier extraction (low voltage loss in contact) is less pronounced for our electron selective contacts. This might be partly explained by the higher doping efficiency of n-type a-Si:H [197] which yields a higher net doping for lower defect densities as compared to the p-type layers. The need for a relatively high doping of the a-Si:H at the electron contact is partly explained by the parasitic Schottky contact formed with the ITO. As will be shown below the work function of our ITO is at around mid-gap of a-Si:H. Hence, a mismatch is observed for both p- and n-doped a-Si:H layers which must be compensated for by sufficient doping. Hence, these results underline the importance of sufficient net doping for the ITO/a-Si:H(n/p) Schottky contact regardless of the doping type of the a-Si:H layer.

A very important finding which proves the general validity of the proposed method is the comparable behavior of the $Suns-V_{oc}$ characteristics irrespective of whether the ITO/a-SiO_x:H(n)/a-Si:H(i)/c-Si(p/n) stack forms the p/n junction (black symbols) or the high/low junction (orange symbols).

Remarks and General Considerations

A metallization of the sample is not a prerequisite for $Suns-V_{oc}$ measurements. Having sufficiently conductive TCOs at the front and rear is satisfactory. However, a higher scattering on non-metallized samples is observed which requires averaging over the sample area. The typical approach, which has been established in this work for the initial optimization of the SHJ or other related contacts like TOPCon [52] regarding their ability to maintain low injection condition, is based on such $Suns-V_{oc}$ samples. The sample preparation and characterization is relatively simple

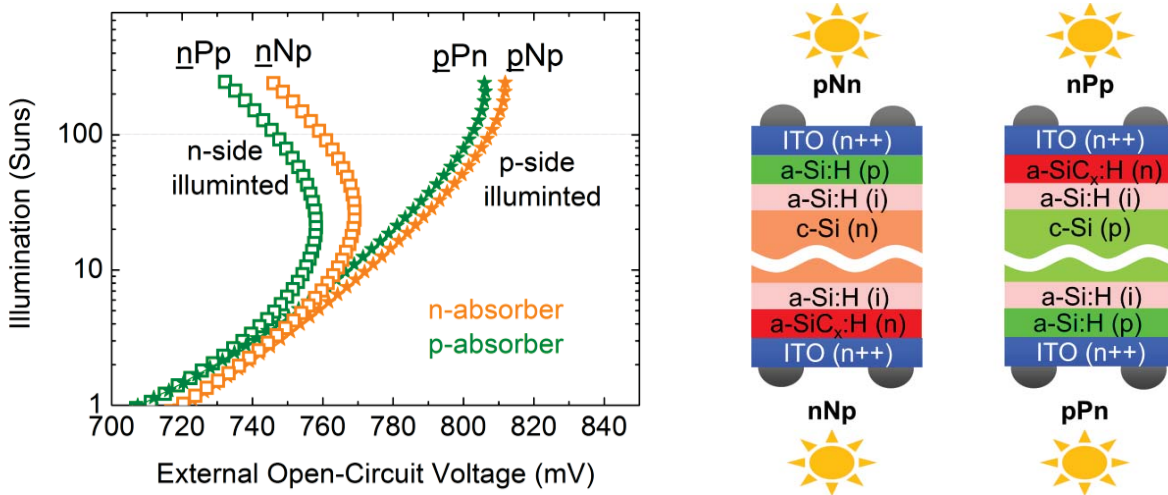


Figure 6.11: Experimentally obtained Suns- V_{oc} curve for bifacial cells featuring an n-type absorber (orange) or a p-type absorber (green). Cells are illuminated either at the p-side (stars) or the n-side (squares). The capital letter denotes the type of absorber doping.

which allows to screen a large parameter space and to identify layers which are subsequently investigated in more detail on solar cell level.

Obviously, the injection level within the SHJ is an important parameter for these measurements. Thus, typically white light (standard flash without any filters) is used to ensure a significant absorption within the SHJ (mainly below ~ 700 nm) and to allow for a high excess carrier density within the contact region. In this configuration, the measured *Suns- V_{oc}* characteristic is dominated mainly by the SHJ facing the light source as the excess carrier density in the non-illuminated contact is much lower. This offers the big advantage that both contacts on either side of non-metallized *Suns- V_{oc}* samples or bifacial cells can be investigated relatively independently from each other. By simply flipping the device. Figure 6.11 shows results for bifacial cells featuring either a n-type absorber (orange) or a p-type absorber (green). A similar characteristic is observed for illumination from the n-side (squares) and the p-side (stars). However, n-side illumination reveals the characteristic of a voltage loss in the contact region. Hence, for these devices the electron selective contact needs to be optimized in terms of electron extraction from the absorber.

Another approach to change the sensitivity of the front or rear junction to high-injection effects are *Suns- V_{oc}* studies with different excess carrier density within the specific contact region. This is realized by illumination with either blue, white or infrared light [191], [192] which however limits the illumination intensity to relatively low values. Moreover, care must be taken if the investigated SHJs feature distinctive optical properties, which result into different injection

levels. For a comparison of contacts featuring different levels of minority carrier recombination (e.g. c-Si passivation) it must take into account that for high illumination intensities the intrinsic c-Si bulk recombination might not be the limiting recombination path which means that the upper limit of $n_{100\text{Suns}}$ is above 0.7 and rather limited by the ideality factor of dominating defect recombination.

Other layer optimizations (not shown) in which the method could already prove its suitability include the alloying of doped a-Si:H by carbon via adding CH_4 in the process gas [102], [92], the growth of thin layers featuring a significant crystalline fraction (nc-Si:H, $\mu\text{c-Si:H}$) [182], [198] as well as the comparison of different TCOs (unpublished). Results for the modification of the interfacial ITO properties can be found in section 6.2 and 6.4 and in Refs [199], [200], [201]. Furthermore, the influence of subsequent process steps has been investigated successfully. This is important for example to monitor the influence of thermal treatments on the contact properties as such process steps are an integral part of the device fabrication and required, e.g. for annealing of the sputter damage caused by the TCO deposition [202], crystallization of the TCO [97] and for sintering and contact formation of the metal electrodes.

6.1.6 Conclusion

The basic requirements in terms of the selective carrier extraction from the absorber were motivated experimentally. It was shown that non-optimized contact schemes may provide excellent c-Si surface passivation but may fail to selectively extract the absorber's excess carriers. It has been shown that the *Suns*- V_{oc} method is a well-suited technique for the characterization and optimization of silicon heterojunction. It was proven that a correlation between the *Suns*- V_{oc} characteristic at certain illumination intensities and the FF and V_{oc} of SHJ solar cells exists. This finding facilitates junction engineering as FF and V_{oc} losses can easily be predicted in the very early stage of device optimization. Even though this method yields only qualitative information about the microscopic interface and bulk properties, it is a powerful method to gain profound insight into the interplay between these properties. Numerical device simulation provided the base for the interpretation of the experimental results and facilitated the understanding of the underlying physical phenomena.

6.2 Interfacial ITO doping variation: An attempt to modify the parasitic Schottky contact

While in the previous section the influence of a-Si:H doping was investigated, the influence of the ITO doping is in the focus here. Results for an ITO(n) doping variation as an attempt to improve the work function matching between the ITO and the doped a-Si:H are presented. A combined analysis of the hole and electron contact is conducted. This is an important fact as it allows to verify whether a variation of the work function at the interface is responsible for the modification of the external contact properties. A motivation for the experiments is given in Figure 6.12. The upper part shows the front side of the investigated cell structures. A double layer ITO stack is applied. An about 60 nm thick layer is highly doped and optimized for the lateral transport. A thin layer (8-10 nm) in contact to the doped a-Si features a doping variation over a very wide range. This doping variation is intended to manipulate the vertical transport at the TCO / doped a-Si:H contact mainly by an improved work function matching. In the lower part (middle), the desired variation of the ITO contact layer work function with doping is shown. A low doping (ITO(n)) is intended to yield a low free electron density and thus a high work function

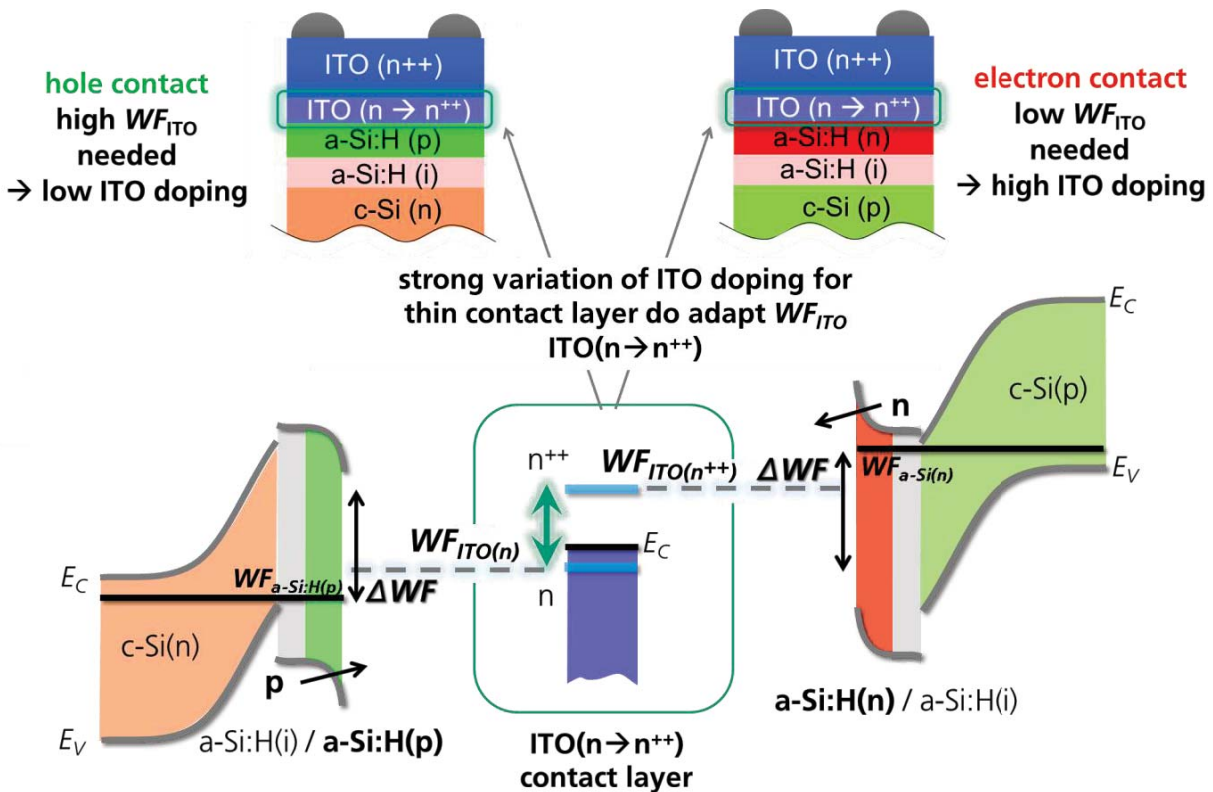


Figure 6.12: Top, sketched front side of experimentally investigated solar cells. The thin ITO layer contacting either p- or n-doped a-Si:H is highlighted. Below the desired variation of the ITO contact layer work function via changing its n-type doping. Left, for a low ITO doping the work function mismatch between ITO and p-doped a-Si:H is reduced. Right, for a high ITO doping the work function mismatch between ITO and n-doped a-Si:H is reduced. The parasitic band bending induced in the doped a-Si:H by the Schottky contact is shown as well.

for the n-type TCO as the Fermi-level moves towards or even below the conduction band [203]. For this condition the higher work function should yield better contact properties for the ITO(n)/a-Si:H(p) hole contact of the n-type absorber (Figure 6.12, left). A low ITO work function is expected to follow from a high doping (ITO(n⁺⁺)) as the Fermi-level is shifted further into the conduction band. Consequently, improved contact properties for the electron contact of the p-type absorber are expected (Figure 6.12, right).

To observe an influence of the work function on the contact properties for the experimental investigations two prerequisites must be fulfilled: (i) The effective work function at the interface between the ITO contact layer and the doped a-Si:H must be tunable by the modification of the deposition conditions and the ITO doping. Besides an adjustability of the TCO work function this also implies that Fermi-level pinning is moderate. (ii) The work function has to be a determining factor for the actual contact properties. For example, for a sufficiently high a-Si:H doping the work function at the interface should be of minor importance as tunneling is efficient. Hence, lowering the barrier height by an improved work function matching might hardly effect the contact properties for such conditions. For this reason, a moderate doping of the p- and n-doped a-Si:H was chosen (2300 ppm gas phase doping for both). The doping and free electron density (n_e) of the 8-10 nm ITO contact layer is changed by adapting the oxygen content ($OC = O_2 / (O_2 + Ar)$) in the sputter gas during DC sputtering from an In₂O₃:SnO₂ (90:10) target. The 60 nm thick highly doped ITO layer is deposited on top without breaking the vacuum. A narrow pitch of 800 μm of the grid electrode and the low sheet resistance of this upper ITO layer ensures that the contact properties are not affected by the lateral carrier collection at the front. Hence, the vertical transport via the ITO / ITO_{contact layer} / doped a-Si:H stack is the decisive factor.

This section is partly adapted from publication [111] of the present author and the visual presentations from the 26th EU PVSEC and the 4th SiliconPV 2015 (no publication submitted there).

6.2.1 Probing the tunability of the effective work function

To probe the actual work function that results upon contact formation at the interface for the deposition condition of the ITO contact layer, SIS like *Suns-V_{oc}* samples were used. The hole and electron selective contacts of these test structures are realized in a similar fashion as the standard SHJ from Figure 6.12. With the only difference that the doped a-Si:H layer is omitted. Consequently, the selectivity of the contact to either holes or electrons is quantified by the

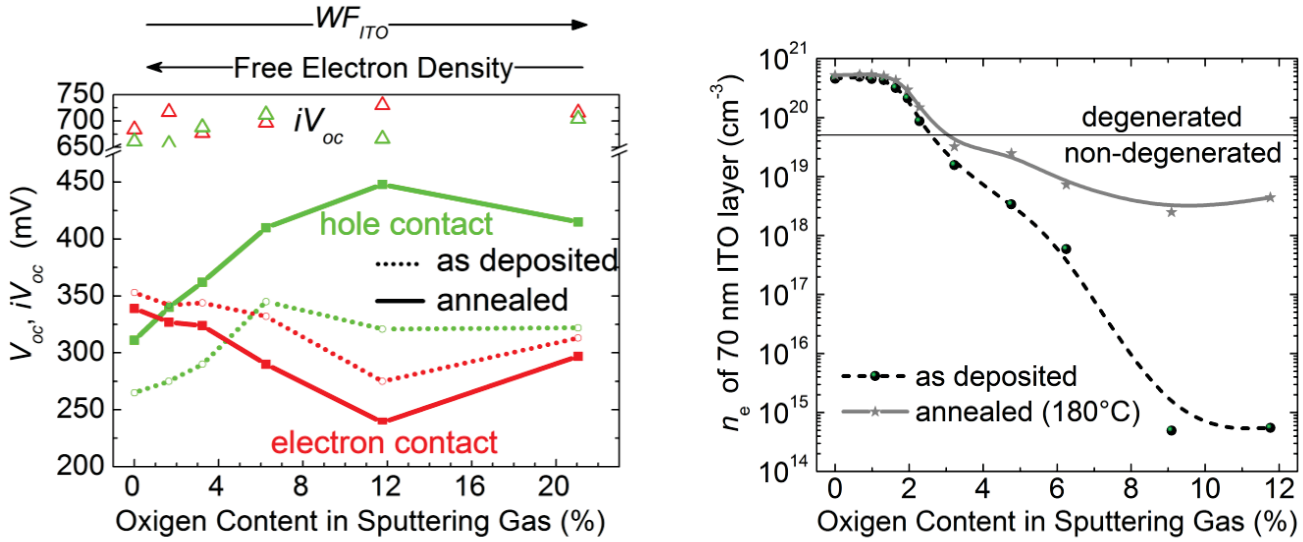


Figure 6.13: Left, V_{oc} and iV_{oc} of SIS like test structures before and after annealing as a function of the oxygen content in the sputter gas during deposition of the ITO contact layer. The “ITO emitter” forms either the hole contact of an n-absorber (green) or the electron contact of a p-absorber (red). Right, free carrier density of thick ITO layers (~70nm) before and after annealing. The vertical line is indicating the transition between degenerated and non degenerated films according to [203].

external V_{oc} which follows from the induced junction and the level of c-Si passivation by the contact (iV_{oc}) as motivated in section 4.2. For a rough estimate of the free carrier density of the thin ITO contact layer, the average free carrier density of 70 nm thick films is shown in Figure 6.13 (right) as a function of the oxygen content applied during ITO deposition.

In Figure 6.13 the V_{oc} and iV_{oc} as a function of the oxygen content applied during contact layer deposition are shown. The iV_{oc} (open symbols) is not affected by the ITO contact layer properties and is well above the external V_{oc} . Consequently, the c-Si passivation does not limit the external V_{oc} . After annealing (solid lines) a clear trend is observed for the V_{oc} . For a low oxygen content, i.e. a high n_e the V_{oc} for a hole contact of an n-type absorber (green) decreases and vice versa for electron contact of an p-type absorber (red). It follows that the work function at the interface to undoped a-Si:H can be tuned and that this behaviour is in qualitative agreement with the one observed for the variation of the ITO surface work function in contact to air or vacuum [203], [93]. Another interesting feature is that with annealing the V_{oc} is increased for the hole contact while it is decreased for the electron contact for all oxygen contents. This can be interpreted as a global increase of the effective work function at the interface with annealing. Hence, an improved hole extraction and a deterioration of the electron extraction with annealing is expected for solar cells where this films are applied as additional contact layers. However, this is in conflict with the

increase of the free electron density with annealing which is expected to result in an reduction of the work function as the Fermi-level is pushed further into the conduction band of the ITO [186]. Consequently, rather a reduction of the work function with annealing would be expected considering the bulk properties of thick ITO films which shown an increase of n_e with annealing (Figure 6.13, right). The annealing behaviour clearly indicates an opposing modification of the ITO bulk and interface properties which however, cannot be explained here.

It should be kept in mind that the doping variation performed here is covering a very wide range. Unfortunately, no literature data is available that provides information about the actual compositions and work function of such films. Another important fact is that the properties of the thin ITO films used here (below 10 nm) should be strongly influenced by the initial growth. Whereas the overall properties of the thicker films typically investigated in literature and in the right graph in Figure 6.13 are dominated rather by its bulk properties [204]. Furthermore, it is well known that besides the variation of the free electron density, low temperature annealing can also cause a structural transition of the films. This includes the transition from amorphous to crystalline [205] which can influence the work function at the interface as well [206]. Mobile hydrogen which is available in the a-Si:H underneath [207] acts as dopant as well. For results not shown here with thick film we observed a significant addition increase of n_e with annealing compared to samples without a-Si:H underneath the ITO. Indeed, in most cases hydrogen may increase the net doping of TCOs and metal oxides as it acts as a donor and passivates acceptor like defects [208], [66]. However, the lowly doped ITO contact layers may loose its metal-like behaviour which makes him prone to depletion. In this case the Fermi-level in the ITO might drop below a certain level where hydrogen tends to act as an acceptor rather than a donor. In this case the free electron density and hence the net doping of the n-type contact layers might be rather reduced [208]. For the lowly doped films a large part of the band bending might actually be screened in the ITO contact layer. This band bending is not available to induced the junction in the a-Si:H / c-Si region. If annealing increases n_e of the thin films the band bending will be shifted further into the a-Si:H / c-Si part of the junction. This makes the V_{oc} more sensitive to the actual work function difference and might explain the global increase and decrease of the V_{oc} with annealing.

Another possible explanation is that the variation of the effective work function is governed by the modification of the Fermi-level pinning. With increasing oxygen content in the sputtering gas an oxide rich film could be created at the interface alleviating the effect of Fermi-level pinning by

reducing the pinning factor (equation (2.32)). This would make the effective work function more sensitive to the actual work function of the ITO contact layer. Mobile oxygen in the ITO films might also be involved in the annealing induced changes causing e.g. a de-pinning of the Fermi level.

It should be noted that similar results were obtained for much thinner films of below 5 nm. However, typically the 8-10 nm films were investigated as for a thickness below 8 nm a non-closed film was expected.

Even though that for the modification of the external V_{oc} with annealing a reasonable explanation cannot be given here, the results indicate that the effective work function at the ITO interlayer / a-Si:H(i) interface can be tuned by changing the deposition conditions of the ITO contact layer. This is the key prerequisite for the desired work function engineering on solar cell level which is presented in the following. Hence, if work function matching is relevant on cell level, an inverse dependence of the FF on the oxygen content applied during sputter deposition and on the annealing is expected for the investigations of the hole and electron contact.

6.2.2 SHJ cells with modified hole and electron Schottky contact

In Figure 6.14a the FF as a function of oxygen content in the sputtering gas of the SHJ cells featuring either an a-Si:H(p) (left) or an a-Si:H(n) (right) layer below the ITO contact layer (Figure 6.12) is shown. The results are shown before and after hotplate annealing in ambient air.

A comparable FF dependence is observed in Figure 6.14a. Irrespective of whether the ITO contact layer is part of the hole (left) or electron contact (right). For both, the highest FF is observed for the lowest oxygen content and annealing leads to a significant reduction of the FF . The FF drop with annealing is more pronounced the higher the oxygen content is. Basically, the FF dependence for the a-Si:H(n) electron contact could be explained by the work function matching which improves for a lower oxygen content as the work function of the ITO contact layer decreases. Conversely, for the a-Si:H(p) an increase of the FF with increasing oxygen content and work function would be expected if the work function of the contact layer would be the determining factor. However, this does not seem to be the case for the investigation here.

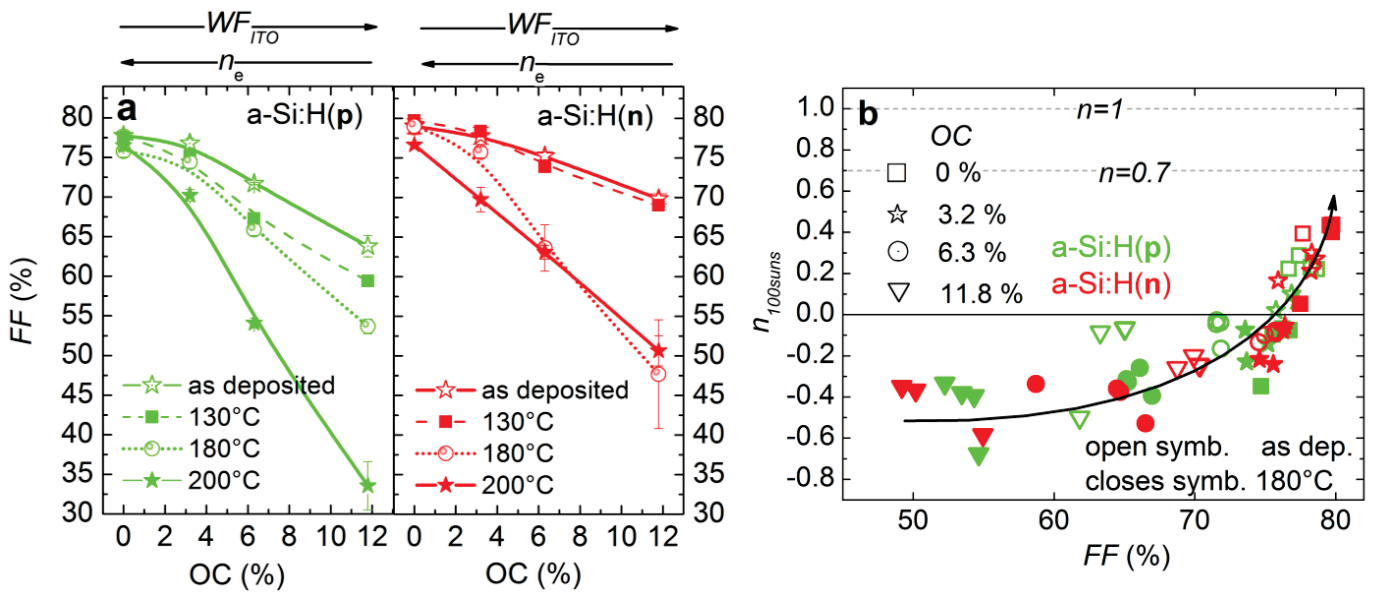


Figure 6.14: a) FF of SHJ cells as a function of the oxygen content in sputtering gas before and after annealing. In green, where the ITO contact layer is a part of the ITO(n) / a-Si:H(p) hole contact. Red where it is part of the ITO(n) / a-Si:H(n) electron contact. b) slope of the $Suns-V_{oc}$ curves near 100 suns vs. the FF for the four different oxygen content (different symbols), before annealing (open symbols) and after annealing at 180°C (closed symbols).

A FF reduction from the lateral carrier transport at the front can be ruled out as a comparable and sufficiently low R_{sheet} is observed for all variations. Furthermore, this R_{sheet} is even reduced by annealing. The FF loss for high oxygen contents is clearly dominated by a non-ohmic contribution as indicated by the S-shaped $J-V$ characteristic in Figure 6.15a and the failure of the superposition principle. It can be seen that the V_{oc} is not effected which is explained by the fact that sufficient doping of the a-Si:H underneath is applied to prevent the global depletion of the doped a-Si:H. The correlation between the slope of the V_{oc} at 100 suns from the $Suns-V_{oc}$ curve and the FF (Figure 6.14b) also reveals that the FF reduction is dominated by the increases of non-ohmic transport losses and that the behaviour is similar for the hole and electron contact. The temperature dependence of the FF is shown in Figure 6.15b. A similar yet not as clear behaviour is observed. Only for the a-Si:H(n) and the lowest oxygen content the behaviour of a well working contact is observed, i.e. a negative slope of $FF(T)$. For the others a very similar $FF(T)$ dependence is observed and only the overall FF level is influence by the oxygen content. Based on the findings from section 6.1.3 (a-Si:H(p) doping variation) a more pronounced change of the slope from negative to positive would be expected with increasing oxygen content and decreasing FF level. The fact that $FF(T)$ is rather constant shows that the increase of the thermally activated transport

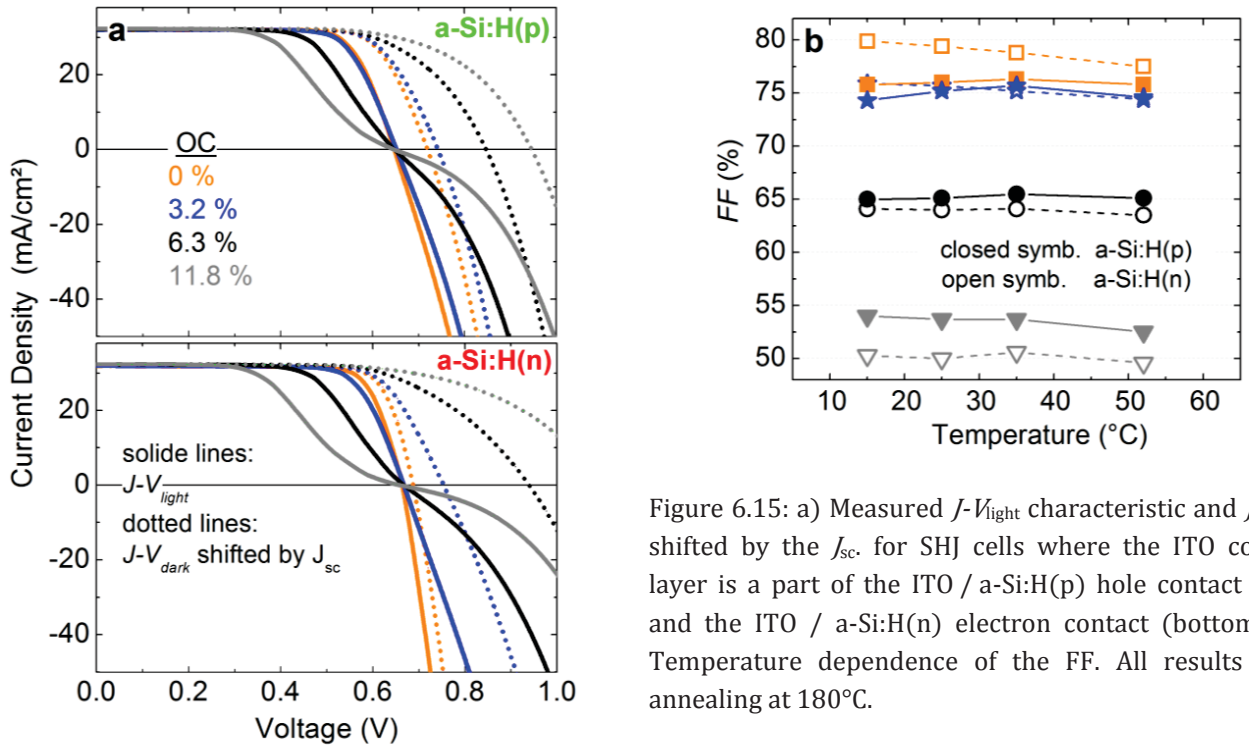


Figure 6.15: a) Measured $J-V_{light}$ characteristic and $J-V_{dark}$ shifted by the J_{sc} , for SHJ cells where the ITO contact layer is a part of the ITO / a-Si:H(p) hole contact (top) and the ITO / a-Si:H(n) electron contact (bottom). b) Temperature dependence of the FF. All results after annealing at 180°C.

path can compensate for the reduction of the pFF with temperature (latter not determined here). However, the thermally activated transport paths do not become efficient enough to result in a positive slope of $FF(T)$. The fact that the $FF(T)$ characteristic is hardly effected by the oxygen content is indicating that the low a-Si:H doping results in pronounced Schottky barrier which cannot be overcome by the additional thermally activated transport path. Simulation results (not shown) indicate that the significant reduction of the overall FF level while maintaining the $FF(T)$ dependence is linked to a classical ohmic series resistance. Hence, unlike the results in Figure 6.14b and Figure 6.15a, the $FF(T)$ dependence does not unambiguously reveal that a similar increase of non-ohmic transport losses with increasing oxygen content is the cause for the FF reduction.

While the results above indicate a modification of the Schottky contact with changing oxygen content in the sputtering gas during ITO interlayer deposition and annealing. In contrast to the results from the preliminary investigation with the SIS like test structures, the influence of an improved work function is not observable on cell level. This is concluded from the fact that an inverse behaviour of the FF is not apparent. The opposite is the case as a similar FF dependence on the oxygen content and annealing for the hole and the electron selective contact is observed. The highest FF is reached for the lowest oxygen content and a significant drop in FF with increasing oxygen content and annealing is observed. Hence, a similar or the same mechanism

seems to hamper the carrier extraction from the p-type and n-type a-Si:H with increasing oxygen content and annealing.

Unfortunately, the origin for the detrimental modification of the Schottky contact of the hole and electron contact is unclear. However, in section 6.4.3 a successful approach to modify the parasitic Schottky contact for the hole contact is presented. Before moving to the next section, a brief discussion on the possible origins for the *FF* limitation is found below.

6.2.3 Possible origins of the fill factor limitation

Unfortunately, the actual origin of the *FF* reduction with increasing oxygen content in the sputtering gas and with annealing could not be identified. However, possible causes should be mentioned briefly and are summarised below and in Figure 6.16.

- 1) The vertical transport through the ~10 nm ITO contact layer, i.e. the contact layer conductivity might limit the transport. Unfortunately, this cannot be assessed as e.g. Hall measurements on such thin films gave no meaningful results. However, the facts that the investigation of much thinner films (below 5 nm) resulted in a similar slope of the *Suns-V_{oc}* curve and that an increased of n_e with annealing is observed (for thick films) are arguments against a limitation by the ITO contact layer bulk conductivity.
- 2) An interfacial oxide which becomes thicker / denser with increasing oxygen content in the sputter gas and annealing. Besides mobile oxygen from the ITO such an oxide might also result from the oxidation of the doped a-Si:H by the oxygen containing sputtering atmosphere. Similar to the intention alloying of doped a-Si:H, the oxygen could result in a reduced net doping of the a-Si:H if incorporated into the films. For both, the presence of an oxide-rich interlayer or a reduced a-Si:H net doping a less efficient tunnelling is expected. While a clear statement would require the application of more advanced structural and chemical investigations of device relevant stacks. Further below, two simple experiments are presented aiming for the indirect identification of such an oxide-rich phase.

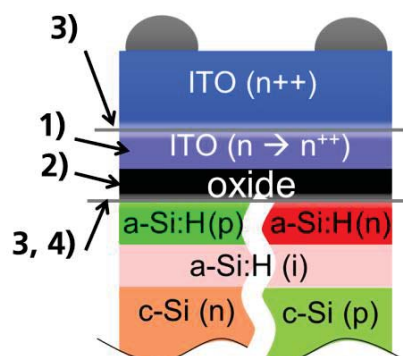


Figure 6.16: Indication of possible causes for the *FF* reduction of the SHJ cells with increasing oxygen content in the sputter gas during the ITO contact layer deposition and annealing. The numbers correspond to the numbering of the possible reasons in the text.

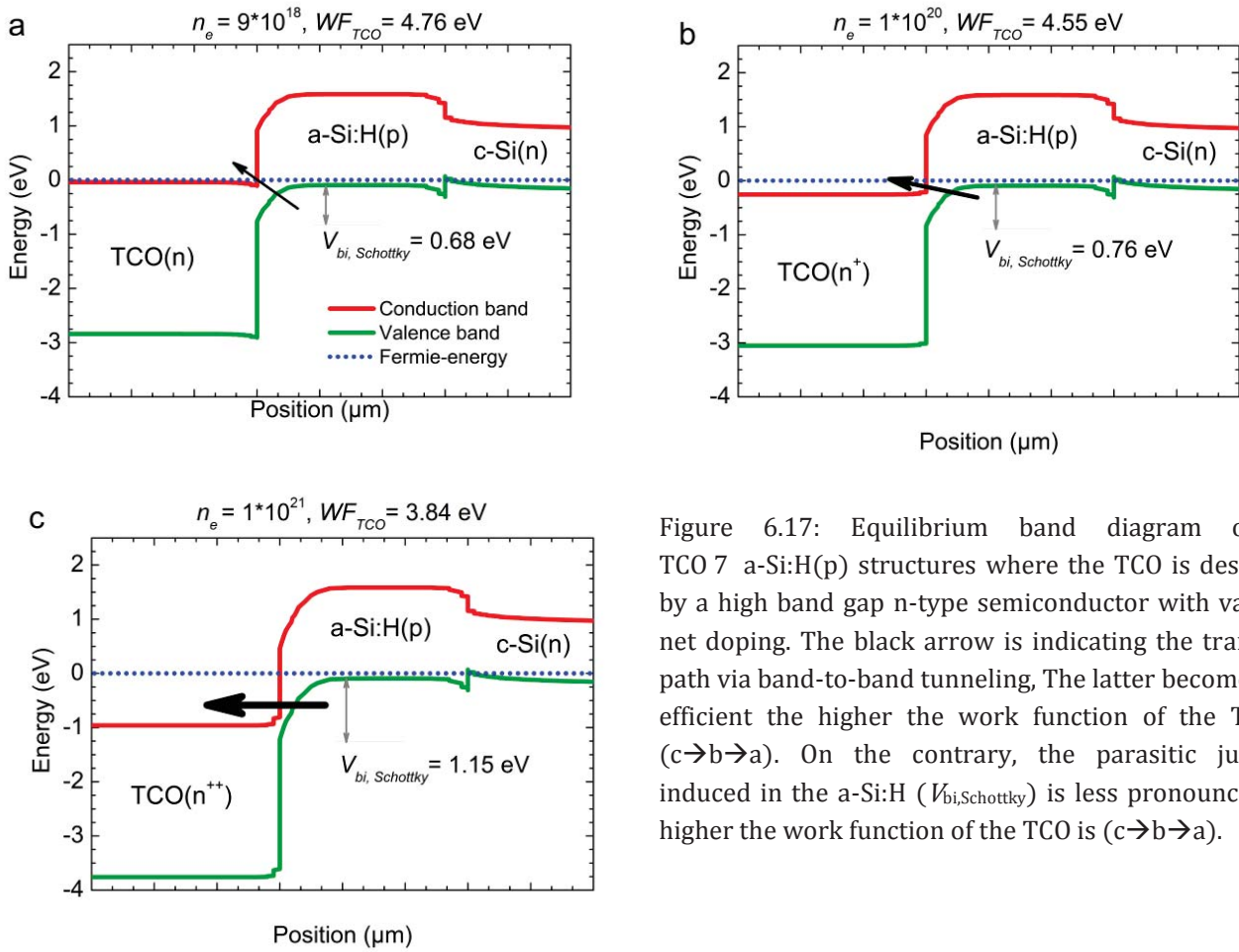


Figure 6.17: Equilibrium band diagram of an TCO 7 a-Si:H(p) structures where the TCO is described by a high band gap n-type semiconductor with variable net doping. The black arrow is indicating the transport path via band-to-band tunneling, The latter becomes less efficient the higher the work function of the TCO is ($c \rightarrow b \rightarrow a$). On the contrary, the parasitic junction induced in the a-Si:H ($V_{bi, \text{Schottky}}$) is less pronounced the higher the work function of the TCO is ($c \rightarrow b \rightarrow a$).

- 3) For a very low doping of the $\text{ITO}_{\text{contact layer}}$ the films might lose its metal-like behaviour. A non-negligible screening length would lead to a significant depletion in this part of the junction. Hence, tunnelling would be less deficient. While this is a likely explanation, reliable n_e data for the thin $\text{ITO}_{\text{contact layer}}$ would be needed for a meaningful evaluation. It follows that the contact should be described rather by a complex $\text{ITO}(n^{++}) / \text{ITO}_{\text{contact layer}} / \text{doped a-Si:H}$ double heterojunction. This leads to two important implications. The approximation of the $\text{ITO}_{\text{contact layer}} / \text{doped a-Si:H}$ junction by a Schottky contact would be an oversimplification of the problem. And, the $\text{ITO}(n^{++}) / \text{ITO}_{\text{contact layer}}$ junction might contribute to FF loss as well.
- 4) Results from device simulations in which the $\text{ITO}_{\text{contact layer}} / \text{doped a-Si:H}$ contact is described by a heterostructure rather than by a Schottky contact [100] suggest that the unexpected FF reduction for the a-Si:H(p) could be related to the fact that with decreasing doping band-to-band tunnelling becomes less efficient, and that this effect dominates over the positive influence of an improved work function matching. As intended experimentally, Figure 6.17 reveals that with decreasing ITO doping ($c \rightarrow b \rightarrow a$) work function mismatching is improved

which leads to a reduction of the parasitic junction induced in the a-Si:H ($V_{bi, Schottky}$). However, band-to-band tunnelling into the TCO becomes less efficient as the overlap between the valence band of the a-Si:H(p) and the conduction band of the TCO vanishes. Indeed, for certain conditions the inverse FF dependence for the hole and electron contact vanished and reasonable qualitative agreement with the experimental results was observed by the simulation. However, the fact that a very similar FF behaviour is observed experimentally for the hole and electron contact ($J-V$, $J-V(T)$ and $Suns-V_{oc}$) suggest that one and the same mechanism is responsible for the limiting transport barrier. Other simulations reveal that the tunnelling transport via defects in the a-Si:H and TCO band gap can also play an important role and it is likely that those are also modified by the oxygen content and annealing.

The fact that work function matching shows no clear influence on cells level but for the test structures could be explained by the Fermi-level pinning. It might be more pronounced for the doped and more defective a-Si:H films compared to the undoped and less defective a-Si:H used for the test structures. The charge neutrality level (equation (2.32)) itself might also be influenced in an inverse fashion by p- and n-doping [66], [67]. Basically, it could adversely affect the actual modification of the effective work function and Schottky barrier compared to the case of the undoped a-Si:H.

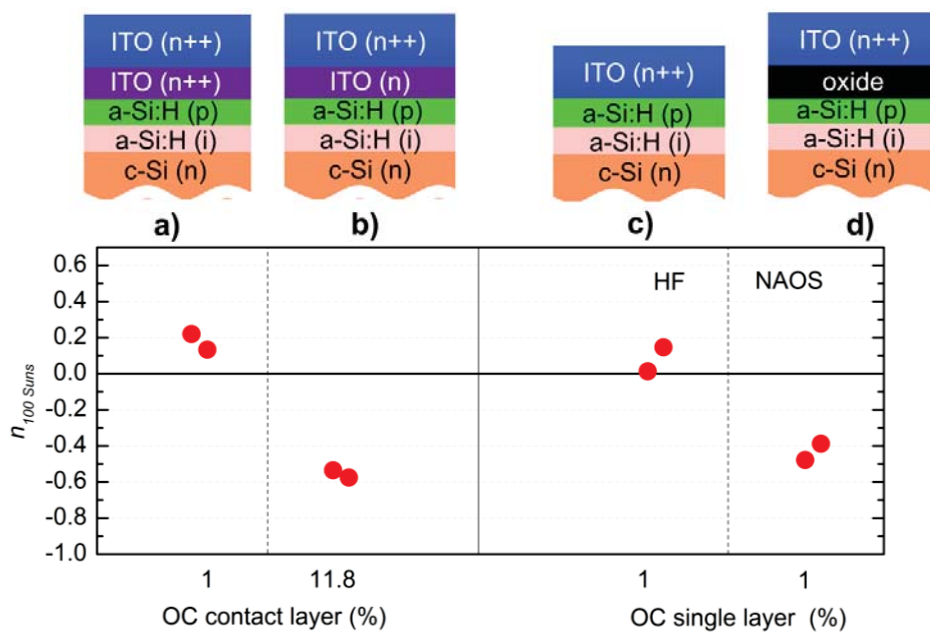


Figure 6.18: Top, design of investigated $Suns-V_{oc}$ samples.

Below, corresponding slope of the $Suns-V_{oc}$ curve at 100 suns after annealing at 180°C.

Finally, the results from two small experiments, which have been conducted to probe the possible influence of point 2 shall be briefly presented.

First the objective was to find out whether a ITO contact layer featuring a high oxygen content and an oxide layer which was intentional grown show a similar slope of the $Suns-V_{oc}$ curve at 100 suns. Figure 6.18 shows the investigated $Suns-V_{oc}$ samples.

Comparing the results of structure a) and b) from the cell batch reveals the know behavior. A high oxygen content results in a much lower and negative slope at 100 suns. For d) were the ITO contact layer is replaced by a wet chemically grown oxide (nitric acid oxidation) which is featuring a thickness of ~ 1.4 nm on c-Si, results similar to b) are observed. Hence, the intentionally grown oxide shows an influence similar to the ITO contact layer deposited with a very high oxygen content. The reference samples c), without any layer in-between behave similar to a), the structure featuring the highly doped ITO contact layer.

The results illustrate that in principle the FF limitation of the cells deposited with a high oxygen content could be caused by the presence of an oxide film at the interface between the ITO and the doped a-Si:H.

The second experiment was an attempt to prove the existence of such an oxide film by the selective wet chemical etching. As shown in Figure 6.19, for samples with different oxygen content first HCl is used to etch off the ITO and subsequently HF is used to etch the remaining oxide, if present. However, it should be noted that such a selectivity for the etching can not be guaranteed, e.g. as the structural composition of the oxide is unknown. The presence of a

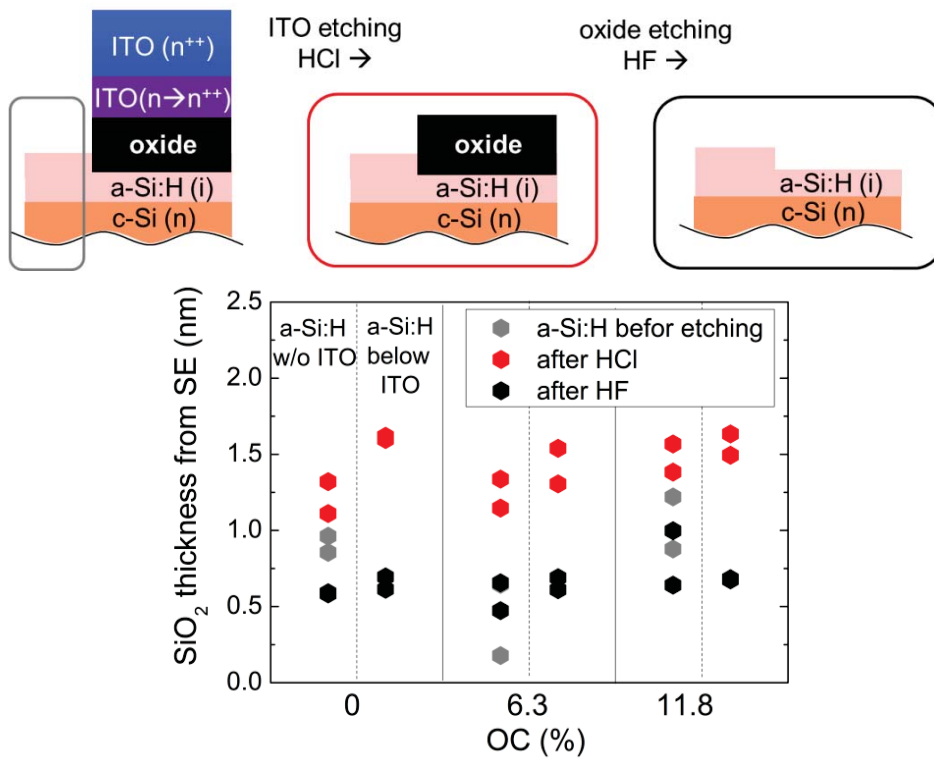


Figure 6.19: Top, design of test samples. Below, SiO₂ thickness from spectral ellipsometry (SE) for the conditions discussed in the text.

potential oxide is monitored by spectral ellipsometry (SE) measurements. A shadow mask was used for the ITO depositions to allow for measurements in the covered and uncovered regions of the sample. The SiO_x thickness estimated from SE are shown in Figure 6.19 for the different configurations, i.e. the areas without ITO which were covered by a shadow mask (first box for each oxygen content) and with ITO (second box), after HCl (red) and HF (black) etching.

Basically, very similar results are obtained for the different oxygen contents. The red symbols indicate a similar oxide thickness after HCl etching, irrespective if ITO was deposited on-top or not. The comparison between the red and grey symbols reveals that the oxide thickness on the a-Si:H which was not covered with ITO is rather increased by the HCl. An oxide growth on the a-Si:H is reasonable since c-Si is also oxidized by HCl, e.g. by the RCA clean. After HF etching (black) the overall oxide thickness is reduced, but again a similar thickness is observed for all oxygen content. Hence, an oxide grown on top or partly inside the a-Si:H could not be verified by this approach.

6.2.4 Conclusion

It was shown on test structures that for a very wide variation of the oxygen content in the sputtering atmosphere during deposition of an additional ITO contact layer, the work function at the ITO / undoped a-Si:H interface could be manipulated in the expected manner. However, if implemented in solar cells, the FF is not affected by the intended work function engineering. For the hole and electron contact a similar transport barrier results which reveals that other effects than the work function dominate the contact properties. The highest FF is obtained for the same ITO contact layer deposition conditions for p- and n-doped a-Si:H, i.e. for the lowest oxygen content. Unfortunately, the exact cause for the strong FF drop with increasing oxygen content and annealing could not be identified. The formation of an oxide rich film at the interface or a too low free electron density in the ITO contact layer, blocking the efficient hole and electron extraction from p- and n-doped a-Si:H (likely by an inefficient tunnelling) are plausible explanations, respectively. More investigations on cell level with higher a-Si:H doping and more data points for moderate oxygen contents would be needed for a final evaluation of this approach. More important, advanced characterization techniques are needed to link the electrical and structural contact properties.

6.3 Replacing the TCO by a metal: An approach to improve the Schottky contact ?

The two sections above revealed that a parasitic junction is formed at the ITO / a-Si:H contact irrespective of the doping type of a-Si:H. It was shown that the most important requirement to deal with this is to apply a sufficient high doping of the a-Si:H to allow for a narrow Schottky barrier width. This enables an efficient tunneling transport and prevents the global depletion of the a-Si:H / c-Si junction underneath. While in the previous section an unsuccessful attempt to change the ITO properties rather than the doped a-Si:H properties was presented. In this and the following section the ITO is replaced by other materials. Here, different metal films are investigated for their suitability to form an efficient contact.

This section is based on the publications [171] and [199].

6.3.1 Motivation

It was argued in section 4.2.3 that for the hole selective contact a material with a work function close to the valence band of the c-Si absorber (5.17 eV) and for the electron contact with a work function close to the conduction band of the absorber (4.05 eV) are needed to form a properly working induced junction. Plenty other devices exist where the preferred hole or electron conductivity / transport is tuned in a similar way. The most prominent is the field-effect transistor where the p/n ratio in the channel is defined mainly by both the work function of the gate stack and the applied gate voltage. Put simply, for solar cells the induced junction enables a preferred transport of either holes or electrons in a vertical direction, for the transistor in the horizontal direction (see Figure 6.20). Furthermore, for both devices an additional buffer layer is applied to lower the defect density at the metallurgical junction (c-Si surface). A huge store of knowledge was acquired in the last decades for the transistor technology which is very helpful for the design of related silicon solar cells. This class of devices is ranging from the classical MIS approach where a metal forms the gate to the SIS approach where a degenerately doped poly silicon or metal oxide / TCO layer forms the gate, electrolyte based systems also exist [46]. As motivated in section 2.5 and 4.2 properly designed SHJ devices show a great affinity to the SIS approach (if doped a-Si:H behaves metal like, no high-injection conditions in contact region). One important aspect for all approaches is the issue of surface interactions and surface modifications during contact formation. The most prominent factor might be the Fermi-level pinning which describes this microscopic effects. It is caused by the fact that besides the bulk properties of the contact partners their surface near properties will contribute to the resulting band alignment and the contact properties as well [66], [67]. Such effects might complicate an efficient work function

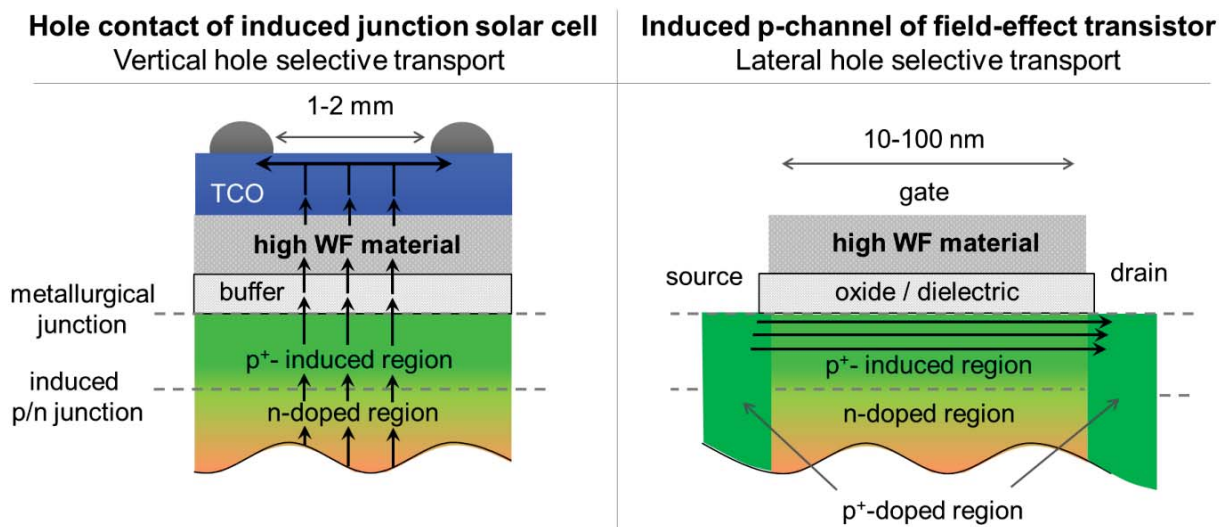


Figure 6.20: Left, sketched hole contact of induced junction solar cell. Right, sketch of depletion mode (normally on) p-channel metal-oxide like field-effect transistor. A (positive) voltage must be applied to the gate to deplete the channel from holes, i.e. to minimize the lateral conductivity. The light green regions are the inverted and highly hole populated device region which are externally induced by the high work function material for the equilibrium conditions for both devices. For the solar cell, the electron density in the induced p-region is parasitically increased by applying an external voltage or by illumination. For the field-effect transistor, the hole density and hence the conductivity of the channel are altered by the gate voltage.

engineering as the effective work function is pinned rather close to mid-gap than to the valence / conduction band of the absorber.

Several publications exist which show a positive influence for manipulating the interface work function for doped a-Si:H by changing the contact layer properties. For example, for silicon thin film cells high work function metallic nano dots have been applied at the ZnO:Al(n)/ SiC:H(p) interface [209] or a low TCO doping was used [210], [211], [212] to improve work function matching at the hole contact (similar to section 6.2). A positive influence of a high work function metal as a contact layer for a-Si:H(p) was shown in Ref [159] for SHJ cells as well. A high / low work function metal showed a positive / negative influence on the hole extraction (FF) of SHJ cells. However, with increasing doping of the a-Si:H(p) the overall level of the FF was increased and the influence of the contact layer work function was less pronounced. This is explained by the fact that the effective Schottky barrier height seen by the contact's majority carriers is defined by both the height and the width of the induced parasitic junction [95]. Accordingly, an improved work function matching helps to reduce the barrier height but a certain doping level is mandatory to ensure that the barrier is sufficiently narrow.

In this section, first MIS like test structure are used to gain insight in the adjustability of the effect work function at the metal / a-Si:H interface. Taking the optical properties and the stability during a low temperature annealing of such contacts into account, one suitable metal and ITO are compared on cell level.

6.3.2 Probing the effective work function

Fermi-level pinning at the metal/a-Si:H(i)/c-Si contact

Simple MIS like test structure (Figure 6.21) which allow to measure the external V_{oc} have been used to assess the ability of different metals to form a carrier selective contact. More precisely, the effective work function that result after contact formation between the metals and a ~ 10 nm thick undoped a-Si:H(H) buffer which induces a certain junction in the a-Si:H(i) / c-Si underneath should be probed by this experiments. It should be noted that unlike for the classical MIS structure the buffer here is a high band gap semiconductor (a-Si:H) and no insulator. But a thin native oxide is expected to present at the a-Si:H(i) surface. The metal films have been deposited by thermal evaporation at moderate temperature to ensure a soft deposition. It follows that the chemical c-Si passivation by the undoped buffer before metal deposition is on a high level (iV_{oc}

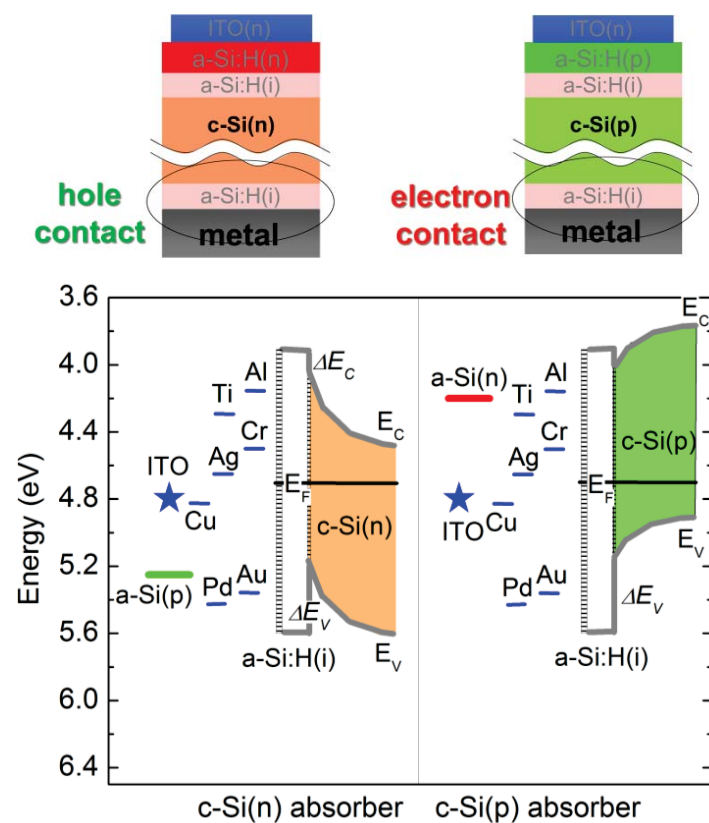


Figure 6.21: Top, schematics of investigated MIS like *Suns-V_{oc}* samples to probe different metal layers regarding their ability to induce a hole or electron selective contact.

Bottom, the band alignment at the metal/a-Si:H(i)/c-Si(n) contact (left) and the metal/a-Si:H(i)/c-Si(p) contact (right) before contact formation with the metals. The vacuum work function of the metals under investigation is depicted by the blue lines (metals) and is taken from [213]. The data for a-Si:H and c-Si are taken from AFORS-HET [20]. The work function of ITO (blue) is set to 4.8eV a values often quoted for device relevant ITO films [93]. For both configurations the c-Si surface is depleted by a junction induced by the undoped a-Si:H buffer. This is explained by the work function of the undoped a-Si:H (4.7 eV) which is close to mid-gap of the c-Si absorber.

~700 mV) and is not adversely affected by the deposition process itself. Owing to the opacity of the metal films, the junction under investigation is placed at the non-illuminated rear side (rear emitter configuration). The same metal films (100nm Au, Pd, Cu, Cr, Ti or 1000nm Ag and Al) have been applied to both n- and p-type shiny etched c-Si absorbers forming either the hole or electron selective contact, respectively (Figure 6.21). Some samples received an 70 nm layer of highly doped reactively sputtered ITO(n) (~60 Ohm/sq) instead of a metal contact layer resulting in an SIS like structure. This test structures investigated are similar to those from section 6.2 where different ITO contact layers were investigated. Basically, the ITO / doped a-Si:H emitter stack of a standard SHJ featuring a n-type or p-type absorber is placed at the rear and replaced by the metal films under investigation.

The experimental results are shown in Figure 6.22 where the measured V_{oc} of the hole contact (green) and the electron contact (green) is plotted vs. the bulk or vacuum work function of the different metal films. For comparison, the behavior predicted by the device simulations¹⁰ from section 4.2.3 is depicted in grey.

A linear dependence of the external V_{oc} on the work function of the contact layer is observed by fitting the experimental data with a linear regression line. For the hole contact of a n- absorber (green) the V_{oc} increases with increasing work function. For the electron contact of a p-absorber (red) the opposite is the case, the V_{oc} decreases with increasing work function. Similar to the simulation results for the idealized MIS structure without buffer layer (light grey) the intersection of the linear regression lines is near mid-gap of the c-Si absorber (4.61 eV). The V_{oc} in this work function regime is about 350 mV for the simulations and the experiment. A comparison of this V_{oc} level with the results from section 4.2.3 (Figure 4.9b) indicates that good surface passivation is obtained experimentally by the a-Si:H(i) buffer. Amongst other points, this justifies the assumption that the external voltage of the samples is limited by the ability of the contact layer to induce a sufficiently high hole / electron density in the a-Si:H(i) / c-Si contact region than by the c-Si surface passivation. This is substantiated by the fact that the V_{oc} of the hole and electron selective contacts show an inverse dependence on the work function. Or in other words, the built-in potential of the induced junction sets the upper limit of the external V_{oc} and not the minority carrier recombination and iV_{oc} .

¹⁰ The simulation results for the structure without an a-Si:H(i) buffer have been taken from Figure 4.9. The results with the 5nm buffer for the hole selective contact correspond to the results from Figure 4.14 (green line).

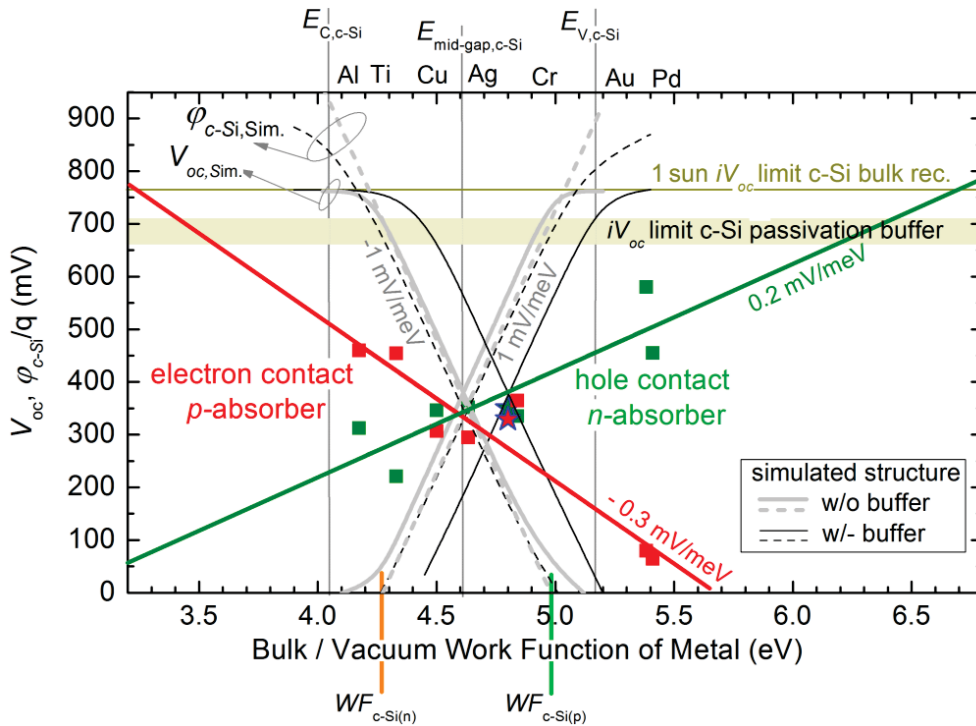


Figure 6.22: External V_{oc} vs. vacuum work function of the metal contact layers (squares) and for an highly doped ITO (star). Results for the hole selective contact of an n-absorber in green. For an electron contact of an p-absorber in red. The grey/black lines correspond to the external V_{oc} (solid lines) and the induced equilibrium c-Si band bending (dashed lines) from simulations (AFORS-HET) of a structure with (black) and without (grey) an 5nm a-Si:H(i) buffer.

Unlike for work functions close to mid-gap, for contact layers featuring work functions close to the valence / conduction band of the c-Si absorber, the experimentally obtained V_{oc} is well below the one predicted by the simulations. This is explained by a pronounced Fermi-level pinning at the metal / a-Si:H interface. Owing to these effects the actual work function which induces the junction is pinned rather close to mid-gap and does not correspond to the bulk (or vacuum) work function of the contact layer anymore which is plotted at the abscissa. The degree of pinning is expressed by the slope of the linear regression lines (Equation (2.32 and Figure 2.9) which is well below the one for the simulations where surface effects have been neglected ($S=1$). Accordingly, for the simulation the effective metal work function at the interface ($WF_{M,eff}$) matches the vacuum work function of the metal ($WF_{M,vac}$) which is not the case for the experiment. The absolute value of the slope is unity for the simulations until the external V_{oc} becomes limited by the iV_{oc} for high external V_{oc} s. That the V_{oc} is changed by 1 mV if the work function is changed by 1 meV is explained by the fact that the work function difference between the 1 Ω cm absorber (WF_{c-Si} marked at the abscissa) and the contact layer is changed by 1 meV as well with increasing or decreasing work function. As shown in section 4.2.3 and 4.2.4, this work function difference basically corresponds to the induced equilibrium c-Si band bending (ϕ_{c-Si} , grey dashed line) which defines the built-in potential of the junction to a great extent and hence the V_{oc} ($|WF_{M,eff} - WF_{c-Si}| = |\phi_{c-Si}| \approx |V_{bi}| \approx V_{oc}$). For the experimental data the slope is 0.2 / -0.3 mV/eV

indicating that the induced built-in potential of the junction is much lower for a contact layer with a vacuum work function other than mid-gap.

Another important finding from the experimental investigations in Figure 6.22 is that for our highly doped ITO (stars) a comparable V_{oc} for the hole and electron contact is observed at a work function level near 4.8 eV. Furthermore, these V_{oc} s fit reasonably well in the behavior observed for the other metal contact layers. A work function of 4.8 eV is in good agreement with the work function often specified for such highly doped films [93]. This work function is close to mid-gap of the a-Si:H buffer and hence does not match the work function of the p- or n-doped a-Si:H as illustrated in Figure 6.21 and Figure 6.12. This work function difference amounts to about 0.5 eV for the ITO/a-Si:H(p) and the ITO/a-Si:H(n) which has to be compensated by a sufficient a-Si:H doping. This highlights, that in terms of work function matching ITO is neither an ideal contact layer for the hole nor the electron contact.

Table 6-1 collects the parameters that need to be chosen for equation (2.32) to match the linear dependence of the V_{oc} on the vacuum work function from Figure 6.22. The experimental trends are very well reproduced if E_{CNL} is set to mid-gap of the c-Si absorber and if WF_{c-Si} is chosen to match the value of the 1 Ω cm n- and p-type absorber. For the simulated structure without buffer E_{CNL} has no influence as S takes an value of unity. S from the experimental investigations shows reasonable agreement with the value of 0.28 determined from the hole contact of a-Si:H thin film Schottky diodes [214]. It follows that the metal / a-Si:H(i) / c-Si contact is characterizes by a pronounced Fermi-level pinning which, however, is lower as compared to the bare c-Si surface ($S \approx 0.05$ [65]) but much higher than for SiO_2 ($S \approx 0.9$ [65]). This means that compared to the

Table 6-1: Parameters chosen for Eq. (2.32) to describe the linear dependence of the V_{oc} on the contact layer work function in Figure 6.22 for the experimental data and results from simulations (without buffer).

		<i>Linear regression lines</i> <i>Figure 6.22</i>	<i>Parameters Eq. 2.32</i>		
			<i>S</i>	E_{CNL} (meV)	WF_{c-Si} (meV)
<i>Hole contact</i>	<i>Sim.</i>	$V_{oc}=1 WF_{vac}-4.28$	1	-	4.28
	<i>Exp.</i>	$V_{oc}=0.2 WF_{vac}-0.59$	0.2	4.61	
<i>Electron contact</i>	<i>Sim.</i>	$V_{oc}=-1 WF_{vac}+4.98$	-1	-	4.98
	<i>Exp.</i>	$V_{oc}=-0.3 WF_{vac}-1.78$	-0.3	4.61	

simulated case where Fermi-level pinning is neglected, for the hole contact to the vacuum work function of the contact layer must be much higher than the valence band energy of the absorber to form an efficient junction. Extrapolating the linear V_{oc} dependence reveals that for an V_{oc} of 700 mV the vacuum work function of the contact layer must be 6.4 eV. For the electron selective contact the work function must be much lower than the conduction band energy. For a V_{oc} of 700 mV a suitable material with a vacuum work function of 3.5 eV is needed. However, it should be noted that for contact materials other than metals the Fermi-level pinning might be different. This is an important point which needs to be investigated to judge the relevance of Fermi-level pinning for the contact engineering with other materials.

The deviation between the results for both simulated structures, with a 5 nm a-Si:H buffer layer (black) and without (grey) in Figure 6.22 should be briefly addressed. It can be seen that by adding the buffer layer (black vs. grey) the V_{oc} 's are shifted to higher work functions (~ 0.2 eV) and that the induced band bending (ϕ_{c-Si}) is reduced especially if the work function is close the conduction or valence. It can also be seen that that the slopes remains the same. It was demonstrated in section 4.2.4 that the presence of the buffer increases the demands on the work function as a highly hole / electron populated device region has to be induced in the buffer as well. Actually, only for very high / low work functions a large share of the induced band bending is accommodated in the buffer as can be seen in Figure 6.22 from the comparison of ϕ_{c-Si} with and without buffer (black and grey dashed lines). However, adding the buffer also leads to additional hetero-barriers which have the potential to suppress the parasitic injection of the "wrong" carriers from the absorber into the contact (section 4.2.1). This means that in terms of external voltage, adding the buffer can have a positive influence by adding hetero-barriers. However, this can be superimposed by the negative influence that an additional band bending needs to be induced in the buffer as well. Results from simulation (not shown) indicate that the much higher conduction band offset at the a-Si:H(i) / c-Si interface (~ 450 meV, Figure 6.21) impedes the parasitic hole injection for the electron selective contact much more than the parasitic electron injection for the hole selective contact as the hetero-barrier in the conduction band is much smaller (~ 150 meV). Hence, for the hole selective contact the additional hetero-barrier is too small to compensate for the additional band bending and work function needed to induce the junction in the buffer. On the other hand, for the electron contact the demands on the work function are lowered as the positive influence of a higher hetero-barrier dominates. However, it

is important to note that the influence of such an asymmetric hetero-barrier is not reflected in the experimental findings. This can most likely be explained by the fact that the blocking behavior of the hetero-barriers is much lower for the experimental structures. For the latter a tunneling transport might be involved which makes the hetero-barriers more transparent for the “wrong” carriers. Thereby representing an additional transport / recombination paths which was not taken into account for the device simulation.

6.3.3 Limited applicability of metal films as contact layers

The results above showed that a direct hole or electron contact can not be formed for the investigated films. Hence, a doped a-Si:H is needed below the metal to enable a carrier selective contact. However, for the application of the metal films to solar cells some other important properties need to be taken into account as well. In terms of efficiency, the contact layer must provide excellent optical properties and must be compatible to the subsequent process steps.

Regarding the optics, the opacity of metal films forbids their application to the illuminated front side. For the rear side, metals with a low reflective index (n) in the NIR wavelength regime (significantly below c-Si, $n \sim 4$) are needed for a high internal back reflection of the photons reaching the metal film at the rear. This limits the choice of the metals investigated in Figure 6.22 to Ag ($n \sim 0.23$), Au ($n \sim 0.28$), Cu ($n \sim 0.33$), Al ($n \sim 1.5$) to avoid significant optical losses. However, parasitic plasmonic absorption on rough surfaces limits the application of all metal films to smooth rear sides like for shiny etched c-Si surfaces. For industrially relevant textured rear surfaces and probably also for saw damaged etched surfaces TCO films have to be sandwiched between the rough surface and the metal to minimize parasitic absorption in the metal [215], [216]. This means in terms of optics using metal films as direct contacts layers for a-Si:H is only of minor importance for industrial relevant structures which are characterized by rather rough surfaces where plasmonic absorption is significant.

The results from optical simulations are shown in Figure 6.23. In qualitative agreement with the experimental investigations presented in Ref. [171] by the present author, it can be seen that a rear side metal with a low refractive index is mandatory to avoid significant optical losses. It can also be seen that adding a layer with a low refractive index and low parasitic absorption (e.g. TCO, SiO_x) partly elevates this problem.

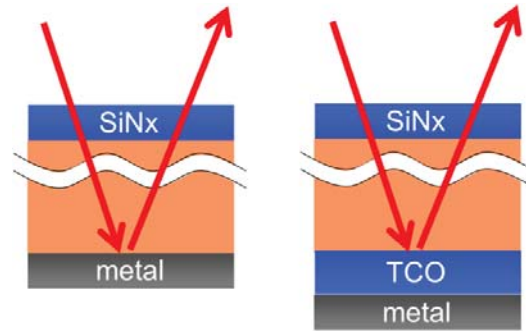
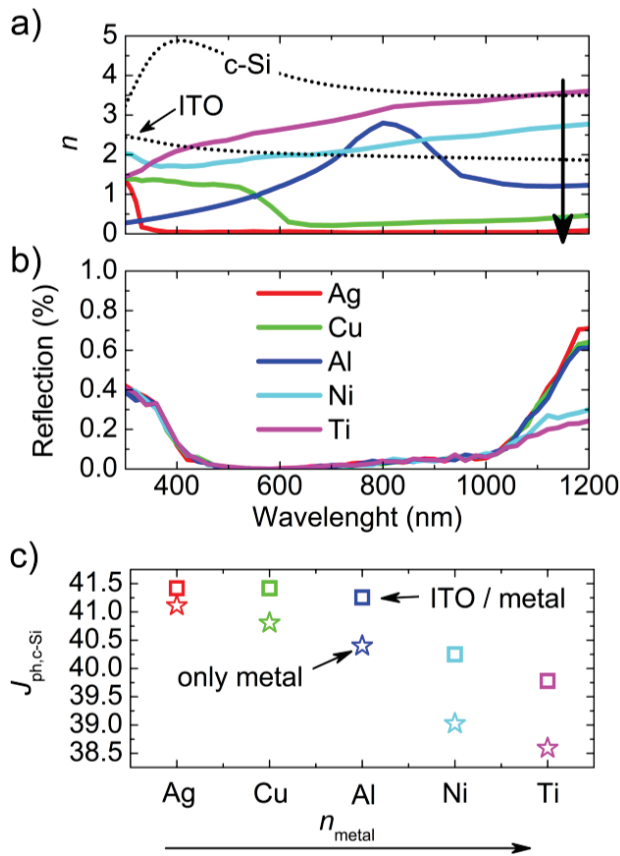


Figure 6.23: Above, structure used for optical simulations with Sunrays [217]. A texture is assumed for the simulations at the front and the rear.

Left: a) Spectral refractive indices used as input parameters for the optical simulations. b) Spectral reflection for different rear side metals. c) The photocurrent generated in the c-Si absorber for the different rear side metals. For the squares an additional TCO in-between the metal and the c-Si was assumed as it is shown in the right structure above. The influence of plasmonic absorption is not considered by the simulations.

Another problem with metal films placed directly on a-Si:H is a detrimental chemical modification, diffusion, or spiking through the a-Si:H and the mechanical junction properties (adhesions). Such issues were observed already at moderate annealing temperatures deteriorating the electrical properties. For annealing the structures from Figure 6.22 at 200°C for some minutes, a significant degradation of the V_{oc} was observed for Au, Pd, Cu and Al which is mainly caused by the depassivation of the c-Si upon annealing. Only Ti, Cr and Ag show stable performance in terms of V_{oc} , while Ag showed only moderate adhesion.

Summing up, the electrical degradation of the junction properties limits the choice of a metal layer to Ti, Cr and Ag. While Ti is preferred because of its good electrical and mechanical contact properties (for both p- and n-doped a-Si:H) Ag offers excellent rear side reflection but only moderate adhesion on planar / smooth surfaces.

6.3.4 High efficiency hybrid rear emitter cells: ITO vs. metal films

For the comparison of ITO, Ti and Ag as rear side contact layer the so-called hybrid SHJ solar cell was used. A sketch of the cell design which was established through this work by the present author [172], [171], [218] is shown in Figure 6.24. It is featuring a high efficiency homojunction front side with low optical and electrical loss. This allows to concentrate on the losses caused by

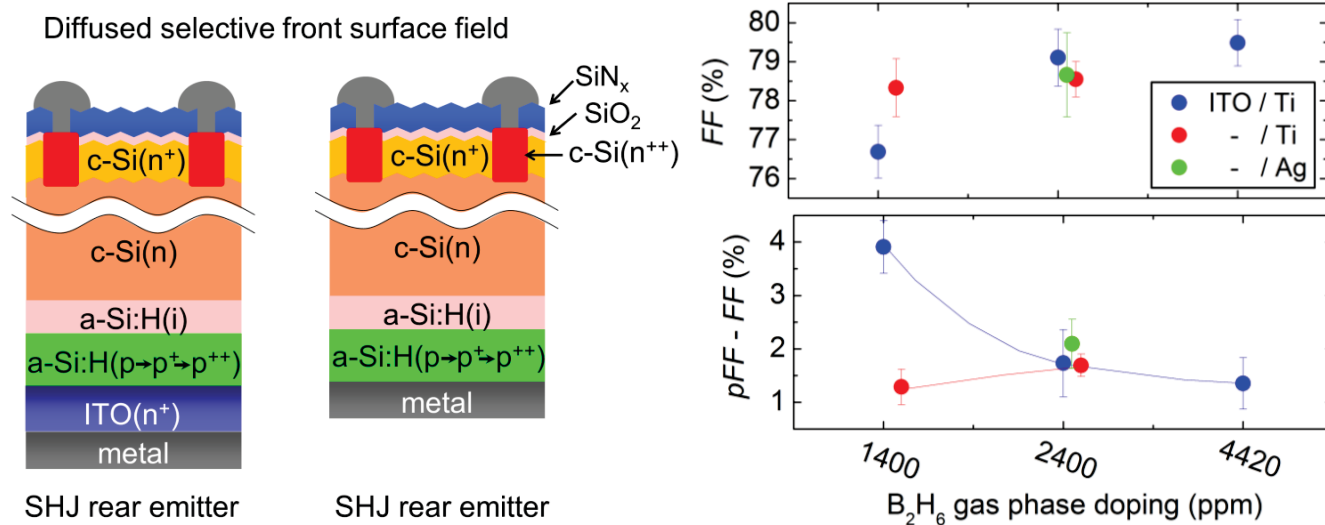


Figure 6.24: Left, investigated hybrid SHJ solar cells featuring different rear sides. Right, FF and transport related FF loss ($pFF-FF$) for three different a-Si:H(p) doping levels and different contact layers. Lines are guides to the eyes.

the SHJ at the rear. The rear emitter consist of the a-Si:H(i)/a-Si:H(p) emitter which is capped either with a highly doped ITO, Ti or Ag. Furthermore, three different gas phase doping level are used during a-Si:H(p) deposition.

Figure 6.24 shows the FF and the transport related FF loss ($pFF-FF$) for three different doping levels of the rear emitter. For the very low doping level of 1400 ppm the FF loss for the Ti is much lower compared to the ITO contact layer despite the fact that work function of Ti (4.3 eV) is well below the one for ITO (4.8 eV, Figure 6.22). Accordingly, with respect to work function matching the inverse behavior would be expected. Increasing the gas phase doping to 2400 ppm, the net doping of the a-Si:H(p) seem to be sufficiently high as the FF loss becomes independent from the contact layer and a similar FF loss is observed for ITO, Ti and Ag. The ITO contact layer benefits from the increased doping which is not the case for the Ti. An even higher gas phase doping yields some further improvement for the ITO which is in agreement with the results from Figure 6.2.

A plausible explanation for the behavior of lowly doped a-Si:H where a much higher FF with Ti which is featuring a lower work function than ITO is observed cannot be given here. But possibly effects caused by a chemical modification of the interface, like a silicide or oxide formation or a partial crystallization are involved lowering the effective Schottky carrier height for Ti. Such modifications are known for example from the Cr/a-Si:H interface [219]. Also for the ITO contact layer the work function might not be the only determining factor as already argued in section 6.2.

The majority carrier extraction from the doped a-Si:H into the TCO might be impeded by additional effects like hetero-barriers and by the fact that the screening length of the TCO is below the one of a metal films. However, a good contact with Ti to lowly doped a-Si:H(p) was also observed in Ref [159]. Ti (4.3 eV) showed a much higher FF compared to Al (4.2 eV) and the FF with Ti was even close to the one obtained for Pd which features a much higher work function (5.4 eV).

The results with ITO from above are in agreement with a-Si:H(p) doping variation performed for the SHJ in section 6.1. The results with Ti for the low doping suggest that the contact layer's work function is not the only determining factor. This was also concluded from the results in section 6.2 for the ITO interlayer doping variation.

By combining a sufficiently doped a-Si:H(p) rear emitter (4400 ppm) with an Ag contact layer an maximum efficiency of 22.8 % ($V_{oc} = 705$ mV, $J_{sc} 39.9$ mA/cm², FF 81.2%) was reached.

6.3.5 Conclusion

It was shown that metal films are not suited as contact layers for the a-Si:H bases SHJ. A pronounced Fermi-level pinning between the metal films and the a-Si:H was observed. This permits there application as a direct hole or electron contact and calls for an additional doped a-Si:H which forms the actual junction. With respect to contacting the doped a-Si:H, the unsuited work function of the metals does not seem to be fundamental problem since a very high FF was observed for a low work function metal (Ti) in contact to the high work function a-Si:H(p). More intrinsic limitations are set by the deterioration of the chemical c-Si passivation already at moderate annealing temperatures, poor adhesions and the poor optical properties in terms of rear side reflection. Hence, metal films like Ti can be beneficial in terms of FF . However, in terms of stability and efficiency only Ag gave good results with an efficiency of 22.8%. With respect to the industrial relevance, the moderate adhesion of Ag is an issue which must be overcome. Another point is that in terms of an efficient light management it is expected that a TCO will always be a part of the SHJ at the rear side as well.

6.4 Contact materials adopted from organic electronics

In the previous section pure metal films and ITO were investigated and proved to be unsuitable to form carrier selective contacts for a c-Si absorber if directly placed on the buffer. An additional doped a-Si:H in-between these material and absorber was mandatory to form a proper junction. In the search for other contact materials, some materials applied to devices from organic electronics are investigated in the following. First different materials are investigated with test structures and two promising candidates are investigated in more detail on cell level.

This section is partly adapted from publications [220] and [221].

6.4.1 Motivation

Very helpful in finding novel contact materials is the work on organic and inorganic thin film devices like transistors, LEDs and solar cells. Material research triggered in this field reveals interesting materials, which might be candidates for forming carrier-selective contacts for silicon wafer based solar cells. These materials are ranging from organic films and TCOs / metal oxides [222], [223], [224] to dipole layers [67], [66]. This applies, in particular, to the high work function metal oxides used for the formation of the hole selective contacts [188]. Some of these materials are shown in Figure 6.25 and in Figure 6.26. Their actual work function strongly depends on the chemical composition [222], [223] but work functions well below the valence band of the c-Si absorber have been reported. With work functions well above 6 eV such films could even

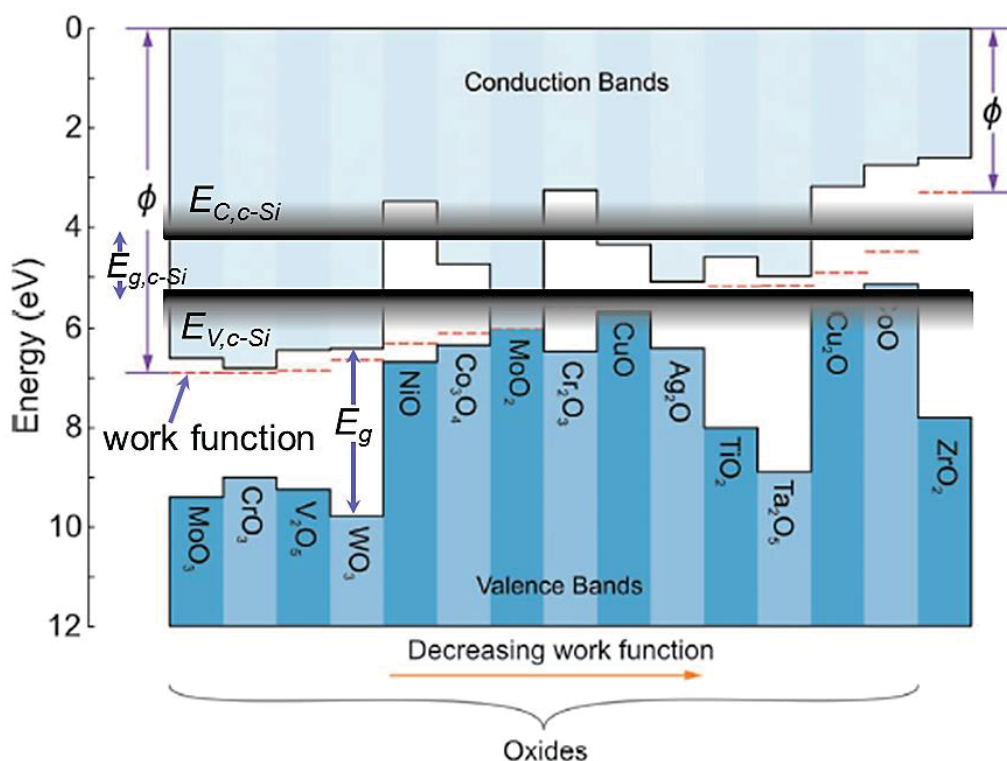


Figure 6.25: Schematic band diagram and energy levels of different materials applied to organic electronics. Adopted from [222]. The conduction and valence band energy of the c-Si absorber are added by the present author.

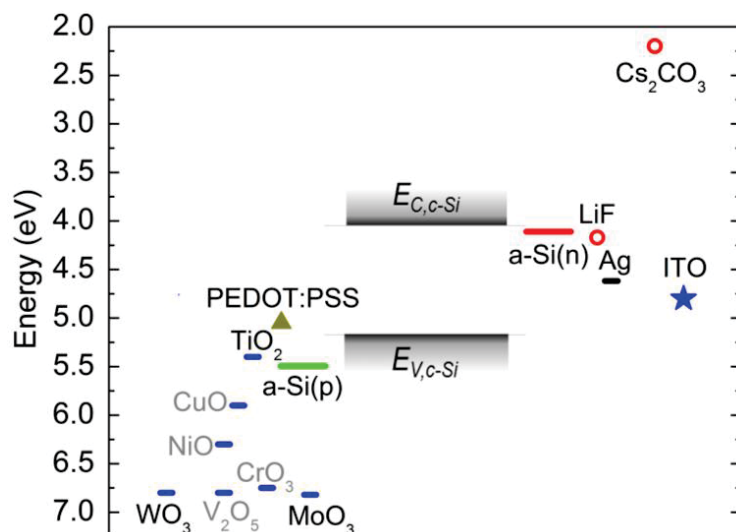


Figure 6.26: Work function of different contact layers used for organic electronics and the conduction and valence band energy of the c-Si absorber. The work function values for the metal oxides are taken from [222] and correspond to the stoichiometry with the highest work function. Data for PEDOT:PSS from [228] and Cs₂CO₃ from [225]. No work function data was available for LiF and its work function was assumed to match the one of Al (more in the text). Reference for the metals and ITO are given in Figure 6.21.

compensate for the pronounced Fermi-level pinning which was observed for pure metal films in the previous section (Figure 6.22). For the electron selective contact LiF and Cs₂O₃ are used for organic electronics [224]. However, the function of LiF is not based on its low work function but rather on the fact that it lowers the work function of the Al electrode which is typically applied to the electron contact [225], [224]. Another candidate for the electron contact is titanium oxide [226], [227] (not shown).

Promising results for silicon thin film absorbers have been obtained recently for the high work function molybdenum oxide and the low work function LiF/Al that replaced the p-doped and n-doped a-Si:H films, respectively [229]. For wafer based silicon absorbers the basic applicability of Poly(3,4-ethylenedioxythiophene) : poly(styrenesulfonate)(PEDOT:PSS) [230] and molybdenum oxide (MoO_x) [231], [232] as a hole selective contact was shown recently. However, it should be noted that the application of such TCOs / metal oxides to a silicon absorber, more precisely, of MoO_x was proposed already in 19680 [60] and more recently by numerical device simulations by the present author [94].

6.4.2 Assessing the suitability of different contact materials

Suns-V_{oc} samples

Suns-V_{oc} samples in the rear emitter configuration (Figure 6.27) have been used to probe the ability of different contact materials to form a hole or electron selective contact. The investigated materials are labeled black in Figure 6.26. Films of 10-15 nm thickness were thermally evaporated from MoO₃, WO₃, TiO₂, LiF, Cs₂O₃ precursors and were capped by thermally

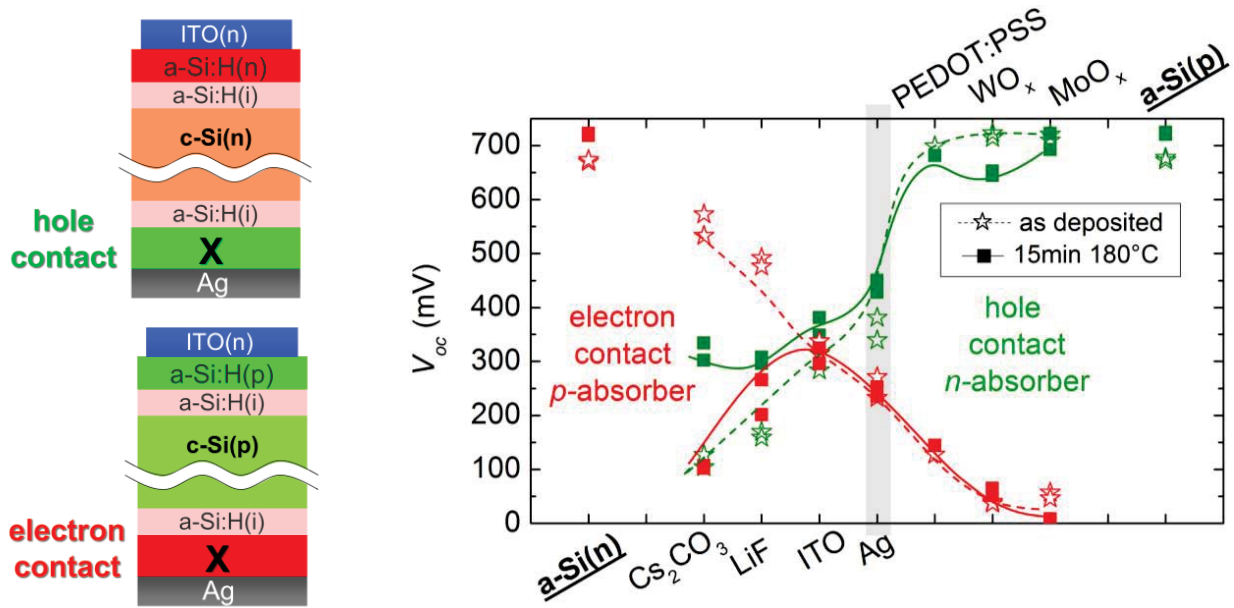


Figure 6.27: Left, schematics of investigated Suns- V_{oc} samples to probe the ability of different contact layers to form a hole (top) or electron (bottom) selective contact. Right, external V_{oc} obtained for the different contact materials before (open stars) and after annealing (closed squares). In green, the results for a holes selective contact. In red, for an electron selective contact, lines are guide to the eye.

evaporated Ag without breaking the vacuum. The thermal evaporation of the Ag capping ensures a soft deposition (compared to TCO sputtering) and Ag showed negligible chemical degradation of the underlying aSi:H(i) buffer compared to other metals (see section above). Additionally, PEDOT:PSS, another hole selective contact material from organic electronics, was deposited by spin-coating, a highly doped ITO was deposited by reactive magnetron sputtering and n- and p-doped a-Si:H films were used as reference. The latter films were capped by thermally evaporated Ag as well (with breaking the vacuum).

The experimental results are shown in (Figure 6.27)Figure 6.27. Before annealing (open stars) an invers behavior of the V_{oc} for the hole (green) and electron contact (red) is observed. This is again indicating that the V_{oc} is dominated by the voltage extraction from the absorber rather than surface passivation. The structures where Ag is in direct contact to the a-Si:H(i) buffer can be regarded as the reference and adding different contact layers in between changes the contact properties with respect to Ag. For the Ag contact layer a similar V_{oc} is observed for both the hole and electron contact which can be explained by the work function of Ag which is close to mid-gap of the c-Si absorber. The same holds for the highly doped ITO. Regarding the other contact materials, the behavior before annealing (stars) follows the one expected from their work function values taken from literature. For the hole selective contact the V_{oc} level of the p-doped a-

Si:H is reached for PEDOT:PSS, WO_3 , MoO_3 . For the electron selective contact the V_{oc} is well below the one of the n-doped a-Si:H meaning that LiF and C_2O_3 are forming a poor electron selective contact in this configuration.

After annealing the V_{oc} for the n- and p-doped a-Si:H was lightly increased which is explained by improved c-Si surface passivation by the undoped a-Si:H buffer. However, regarding the hole contact the V_{oc} for MoO_3 , WO_3 and PEDOT:PSS is reduced to some extent which is most pronounced for WO_3 . For the electron selective contact the reduction of the V_{oc} for LiF and C_2O_3 is even more pronounced while the V_{oc} for the hole contact for the same contact layers is increased. This is indicating that during annealing the properties responsible for the voltage extraction are significantly modified.

It should be noted that the thickness of LiF and C_2O_3 is well above ~ 1 nm which is the thickness typically applied [225]. Furthermore, an Al capping instead of an Ag capping is typically used. Hence, further investigations are needed for these materials in order to finally evaluate their suitability to form an electron selective contact.

SPV samples

Above, MoO_3 and WO_3 have been identified to be interesting candidates to form a hole selective. To verify that a highly hole populated contact region is induced at the c-Si surface and in the buffer layer by the these films, surface photo-voltage (SPV) measurements [193], [18], [89], [126] were performed. To allow for a better quantitative interpretation of the data, in addition to the investigated a-Si:H(p) (doping 4400 ppm), MoO_x and WO_x films the results for an a-Si:H(p) doping variation are shown in Figure 6.28a.

It can be seen that the induced equilibrium band bending (φ_{SPV}) and hence the inversion of the c-Si surface are similar for the highly doped a-Si:H(p) films and the two metal oxides, i.e. MoO_x and WO_x . After annealing (open stars) the induced band bending is reduced for MoO_x and rather constant for WO_x . This suggests that the bulk and/or interface properties of MoO_x are adversely affected during annealing. However, a value of about 800 meV is observed for all conditions which indicates that the work function which results after contact formation is high. The latter is presented graphically in Figure 6.28b. A value of 900 meV would result if the effective work function would match the valence band edge of the absorber (5.17 eV) and if no buffer layer would be present. However, it has to be taken into account that a φ_{SPV} below 900 meV must not necessarily follow from a lower effective work function. This is explained by the fact that some

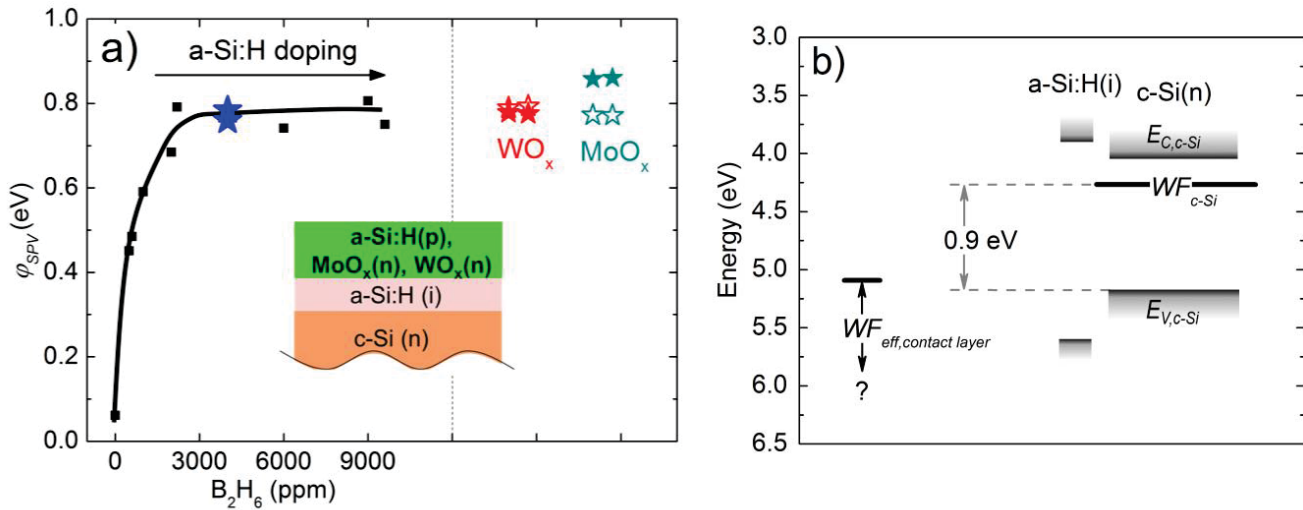


Figure 6.28: Left, equilibrium band bending induced into the n-type c-Si absorber by p-type a-Si:H, WO_x and MoO_x contact layers determined from SPV measurements. The open symbols for the metal oxides correspond to after annealing at 180°C, all other results before annealing. The investigated sample structure is shown in the graph. Right, schematic of the band diagram for the measured structure before contact formation. Energy with respect to vacuum level

band bending will be induced in the a-Si-H buffer as well, which will not be probed by the SPV setup.

6.4.3 SIS like cells and modification of the parasitic Schottky contact

In the final step MoO₃ and WO₃ are implemented in solar cells for a more detailed investigation of the electrical and optical contact properties. In accordance with the device simulations from section 4.2.5 and in Ref. [94] of the present author the presumably high effective work function of MoO₃ and WO₃ should be sufficiently high to replace the p-doped a-Si:H (4300 ppm) of the standard SHJ. This is investigated experimentally by an SIS like solar cell structure (see Figure 6.29b). The case where such a high work function material is used as an additional contact layer, sandwiched between the p-doped a-Si:H and the ITO, is investigated as well (see Figure 6.29c). This should result in an improved Schottky contact which should be beneficial mainly for the FF. The case where the a-Si:H buffer is omitted is investigated as well (d in Figure 6.29). This is mainly motivated by the results from section 4.2.4 which have shown that the presence of the a-Si:H buffer increased the demands on the work function of the contact layer. This was explained by the fact that a high hole density has to be induced in the buffer as well. As only WO_x showed reasonable surface passivation without a-Si:H buffer investigations on cell level have been performed only with WO_x. This results in an SS like solar cell structure. It should be mentioned

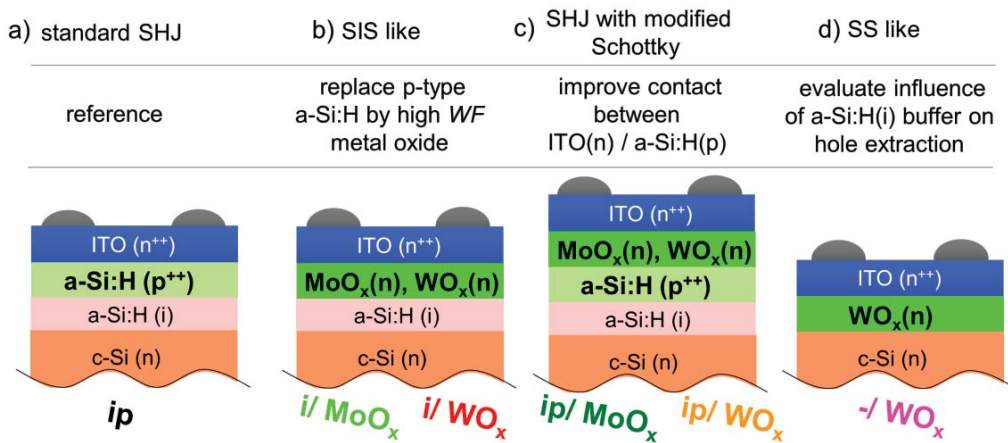


Figure 6.29: Schematic of investigated solar cell front sides and the motivation/aim for the respective structure. The electron selective contact at the rear is formed by and a-Si:H(i/n) stack.

that for the structures above it is assumed that the contact formed between the n-type ITO and the n-type metal oxides performs well, i.e. shows an ohmic and low resistive characteristic. This has not been investigated so far. The results for all variation from the $J-V_{light}$ characteristics are summarized in Figure 6.30 (different colors). The individual cell structures (SIS, modified SHJ) are discussed consecutively and the standard SHJ featuring only an p-doped a-Si:H is presenting the reference structure. The results before / after annealing at 180°C are shown in Figure 6.30. The data in the first box of each group corresponds to the results before annealing, in the second box after annealing. To evaluate if the V_{oc} s and FF s shown here are affected by a non-ideal contact behavior regarding the selective hole extraction, the slope of the illumination level dependent V_{oc} is plotted in Figure 6.31a and b. Figure 6.31c und d show the temperature dependence of the V_{oc} and FF which is also used to identify non-ideal junction properties. Finally, Figure 6.32 shows the $J-V_{light}$ characteristics at STC conditions from which a non-ideal behavior can be readily identified, e.g. by an S-shaped or double-diode behavior. For comparison with the investigated cells, the parameters of two homojunction cells (stars) which show ideal device performance in terms of excess carrier extraction (well described by the two diode model) but different levels of minority carrier recombination and hence different V_{oc} s, are shown as well. The optical losses are discussed separately below.

Starting with the V_{oc} and the FF for the SIS like structures in Figure 6.30 it can be seen that before annealing MoO_x (light green) outperforms the p-doped a-Si:H (black) in terms of both V_{oc} and FF . On the contrary, WO_x (red) shows a lower V_{oc} and no gain in FF . The lower V_{oc} for WO_x might be partly attributable to an inferior c-Si passivation by the contact. However, Figure 6.31b reveals that n_1 is only at about 0.65 (red, open symbols) which is well below the 1.0-1.1 of MoO_x , the a-Si:H(p) reference (open light green and open black symbols) and the homojunction cells

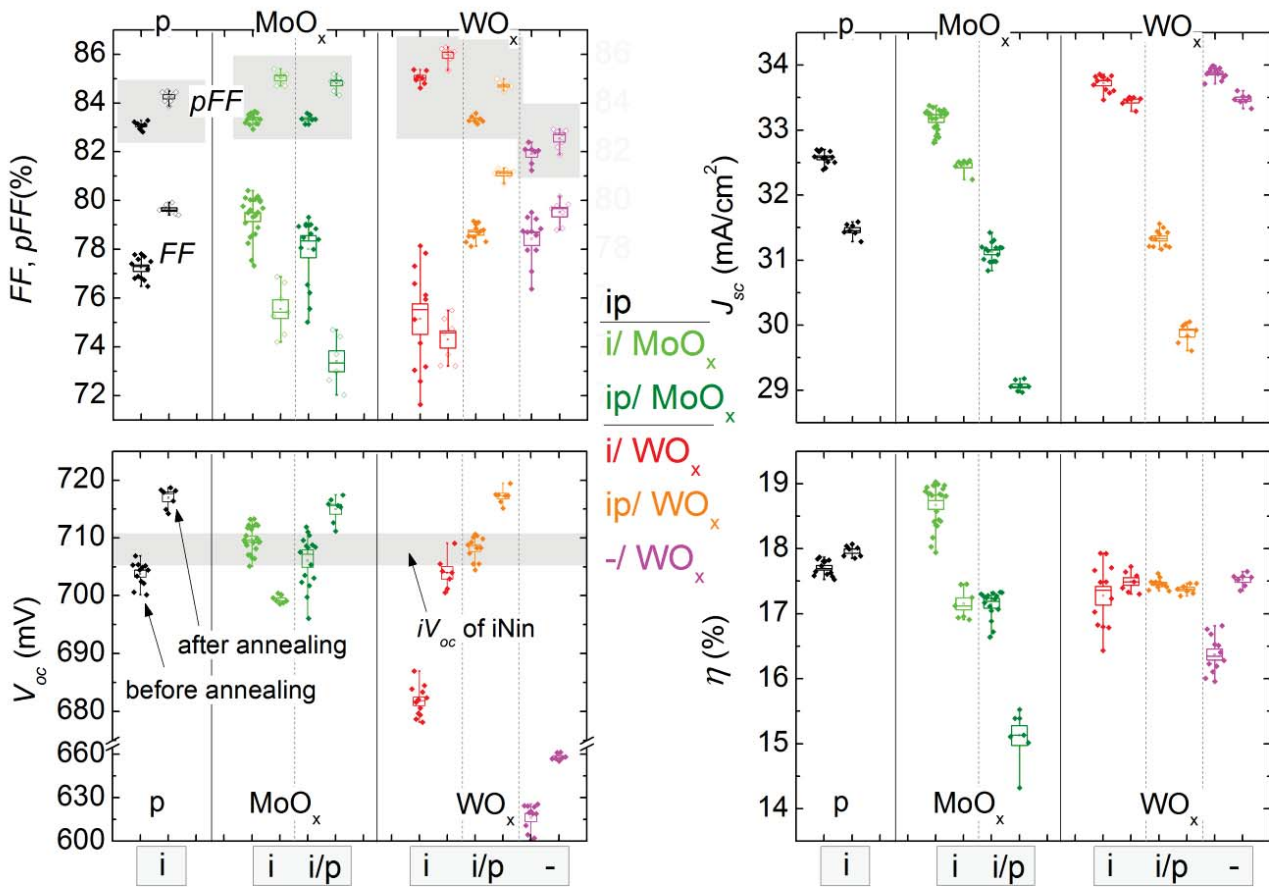


Figure 6.30: Cell parameters from J - V_{light} for the different structures shown in Figure 6.29. The first values in each box correspond to before annealing, the second one corresponds to after annealing at 180°C in ambient air.

(stars). Accordingly, unlike for MoO_x the work function of WO_x does not seem to be sufficiently high to induce a highly hole populated a-Si:H(i)/c-Si contact region or other factors hamper the hole extraction.

Annealing should lead to an improved c-Si surface passivation of all samples, which is explained by the rearrangement of hydrogen and the curing of the sputter damage caused by the ITO deposition. Accordingly, the V_{oc} of the a-Si:H(p) reference and of the SIS like samples featuring WO_x is increased (Figure 6.30). On the other hand for MoO_x the V_{oc} is reduced during annealing which is not explained by the depassivation of the c-Si absorber but rather by a deterioration of the selective hole extraction as indicated by n_1 (Figure 6.31b). It drops well below unity after annealing (closed light green symbols). This is potentially caused by an increase of the effective work function of MoO_x which leads to a depletion and hence high-injection conditions in the contact region similar to WO_x. After annealing the FF is limited by such non-ideal conditions for both metal oxides. This is indicated by n_{100} which is well below 0.7 (Figure 6.31a). That the

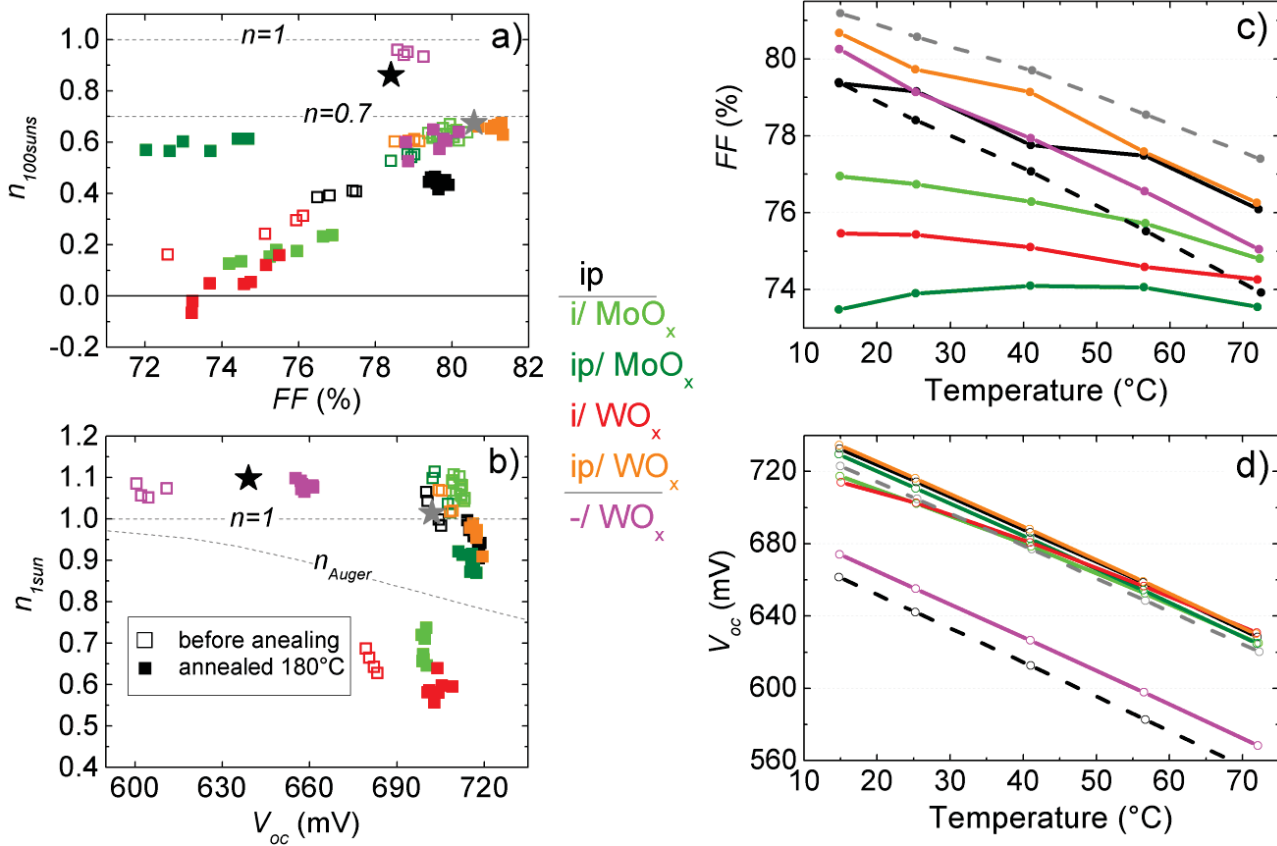


Figure 6.31: a) Slope of V_{oc} near 100suns from $Suns-V_{oc}$ vs. FF from $J-V_{light}$. b) Slope of V_{oc} near 1sun from $Suns-V_{oc}$ vs. V_{oc} from $J-V_{light}$. c) Temperature dependence of FF for cells after annealing. d) Dependence of 1 sun V_{oc} from $J-V_{light}$ on the temperature for cells after annealing. The black and grey symbols in a) and b) and the dashed lines in c) and d) corresponds to experimental results of two homo-junction cell featuring a diffused boron emitter and a diffused phosphor BSF or an n-TOPCon BSF, respectively. Both shows ideal behavior in terms of selective hole extraction but the V_{oc} level is higher for the latter homo-junction cell.

transport related FF losses increased with annealing can also be deduced from the difference between the pFF and the FF in Figure 6.30 which increases with annealing. However, care must be taken when interpreting the pFF of such non-ideal devices. Similar to the very low a-Si:H(p) doping from section 6.1.3 (Figure 6.2) the pFF might be overestimated due to non-ideal contact properties rather than reflecting good surface passivation. The non-ideal contact characteristics for both SIS like contact schemes after annealing can also be recognized from the temperature dependence of the FF and especially the V_{oc} (Figure 6.31c, d) and the S-shaped $J-V_{light}$ characteristic (Figure 6.32). They show similar features like a-Si:H(p) films with insufficient

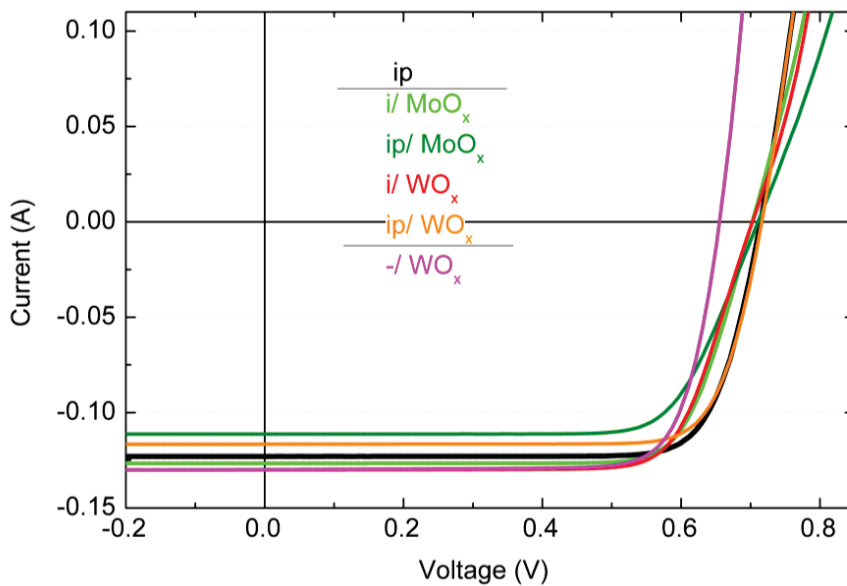


Figure 6.32: J - V_{light} characteristic for the different structures shown in Figure 6.29. Measured at 25°C after annealing at 180°C.

doping from section 6.1.3. With respect to the efficiency, despite the improved J_{sc} ¹¹ which is explained by the improved blue response caused by the higher band gap of the metal oxides compared to a-Si:H(p), the efficiency after annealing is not improved if a-Si:H(p) is replaced by MoO_x or WO_x. However, before annealing MoO_x clearly outperforms the reference.

A very important observation is that by omitting the aSi:H(i) buffer the semiconductor-semiconductor (SS) like heterojunction formed between WO_x and c-Si (magenta) shows an ideal contact characteristic. The lack of chemical surface passivation by the buffer leads to a reduced V_{oc} and pFF reflecting the lower implied voltage at OC and MPP, respectively. However, despite the lower pFF the FF is comparable to the a-Si:H(p) reference with buffer indicating lower transport related FF losses. The local ideality factors, the temperature dependence of the V_{oc} and FF and the J - V_{light} characteristic unambiguously indicate ideal performance in terms of selective hole extraction. This clearly shows that the function of the buffer goes well beyond providing excellent chemical passivation and that the buffer layer properties have to be taken into account when optimizing the overall contact properties with respect to the selective carrier extraction. A possible explanation for this behavior might be that the work function of the WO_x investigated here is not sufficiently high to provide the additional band bending which needs to be induced in the buffer. It should be noted that the efficiency of the very simple ITO(n)/ WO_x(n)/c-Si(n) hole contact where both the doped a-Si:H and the buffer are omitted, is similar to that of the reference

¹¹ The J_{sc} reduction with annealing for all samples is dominated by the increase of reflection which in turn is caused by the increase of the free carrier density of the ITO which result in a reduction of the reflective index.

structure. In addition, the V_{oc} level is well above that of a structure where a highly doped a-Si:H(p) is directly placed on the absorber. For the latter the V_{oc} with our highly doped a-Si:H(p) layers is typically limited to 630 mV, which is in accordance with the results from Ref. [159]. The moderate V_{oc} level of 660 mV with WO_x directly placed on the absorber shows that surface passivation by metal oxides can be superior to that of highly doped a-Si:H(p) films.

We now turn to the structures where the selective hole extraction from the absorber should be ensured by the highly p-doped a-Si:H and MoO_x (olive) and WO_x (orange) are applied as additional contact layers to improve the parasitic Schottky contact formed between a-Si:H(p) and ITO. Again, before annealing MoO_x shows an improved V_{oc} and FF with respect to the a-Si:H(p) reference but after annealing the FF is significantly reduced. The presence of the a-Si:H(p) prevents a degradation of the V_{oc} and the increase of the V_{oc} with annealing can be attributed to the improved iV_{oc} . Accordingly, n_1 drops slightly below unity. Unfortunately, the reduction of the FF with annealing is not reflected by n_{100} which cannot be explained. However, the fact that the FF is reduced while n_{100} remains constant indicates that the increase of the transport related FF loss ($pFF-FF$) is rather dominated by increased ohmic losses. However, this behavior is not necessarily in line with the assumption of a decreasing work function of MoO_x with annealing. The latter was assumed to be the major cause for the FF and V_{oc} reduction of the SIS like structure with MoO_x . Considering that the MoO_x bulk properties play an important role for the effective work function, a reduction of the work function would correspond to a Fermi-level which is pushed further towards the conduction band energy for non-generated n-type material or further above the conduction band energy for degenerated material. This would correspond to an increase of the free electron density and hence an increase of the layers conductivity. Accordingly, if the bulk conductivity of MoO_x is the limiting factor, annealing should lead to a decrease of the ohmic losses rather than to their increase. However, the temperature dependence of the FF shows a clear signature of the non-ideal carrier extraction. The FF slightly improves with temperature which means that the contact characteristic is dominated rather by thermally activated processes than tunneling. For the cells where WO_x is used as an additional contact layer (orange), a better V_{oc} and FF before annealing is also seen. However, both are further increased above the level of the reference featuring only the highly doped a-Si:H(p). The contact to ITO is improved for this contact layer which results in a significant FF improvement from ~ 79.5 to $\sim 81.0\%$. This is also reflected in n_{100} , which is approaching 0.7 and the temperature dependence of the FF . However, while the electrical properties benefit from inserting such an WO_x contact

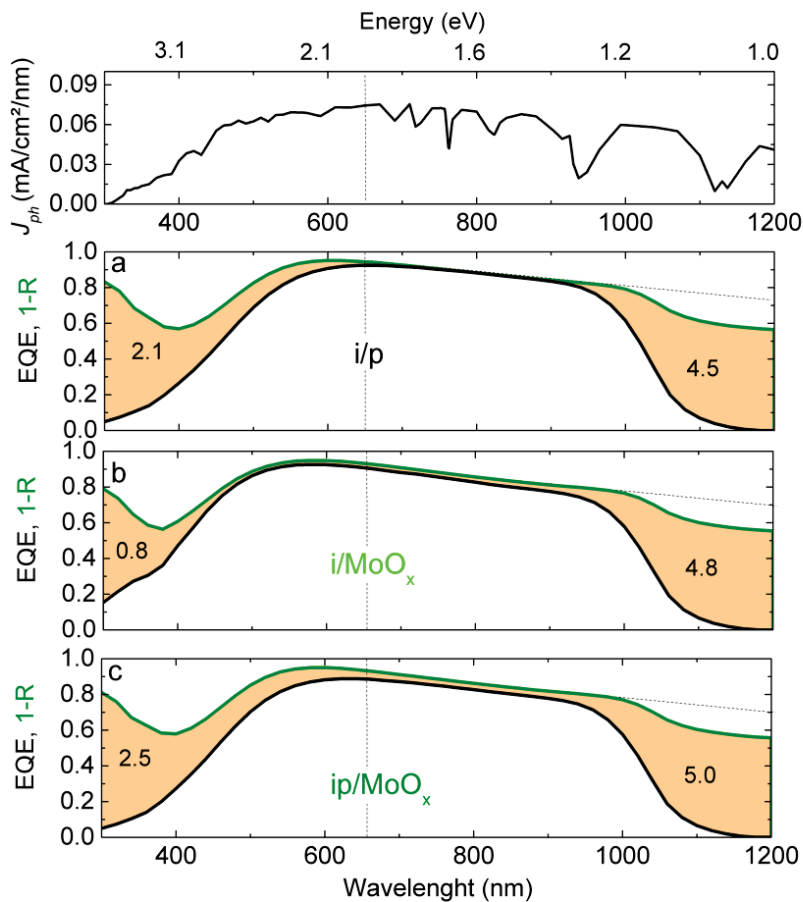


Figure 6.33: External quantum efficiency and 1-reflection of the planar cells. The shaded area denotes the parasitic absorption. The numbers correspond to the current loss in mA/cm^2 by parasitic absorption for wavelength below/above 650 nm.

layer, parasitic absorption in the WO_x layer adversely affects the current. Hence, despite better electrical properties the efficiency remains slightly below the one of the reference structure. It should be noted that the slightly higher V_{oc} for the cells with additional MoO_x and WO_x layers before annealing is most likely linked to a reduction of the sputter damage caused by the ITO depositions. It is expected that for thinner a-Si:H films, which are typically applied to minimize parasitic absorption losses, this shielding of the sputter damage is more pronounced.

To evaluate the optical losses caused by parasitic photon absorption some characteristic EQEs are shown in Figure 6.33. For the SIS like and the modified SHJ structures MoO_x , and WO_x show a similar behavior. Hence, only the results for MoO_x are shown here. To obtain a similar reflection of all structure the ITO thickness was reduced by the thickness of the metal oxide film (similar refractive index).

In terms of optical properties, the SIS structures where 10 nm of p-doped a-Si:H are replaced by the 15 nm thick metal oxides (b in Figure 6.33) reveals that the transparency of the metal oxides is much better than the one of the doped a-Si:H (a in Figure 6.33). This leads to current gains for

wavelength below about 650 nm but parasitic absorption above 650 nm is slightly increased. The SHJ cells with the modified Schottky contact where 15 nm of ITO are replaced by the metal oxides (c in Figure 6.33) reveal that the transparency of the metal oxides is inferior to the highly doped ITO. The parasitic absorption below and above 650 nm is increased compared to the a-Si:H(p) reference. Hence, the optical properties of the metal oxides in terms of parasitic absorption need to be improved, e.g. by reducing the thickness.

6.4.4 Conclusion

The presented results revealed that materials adopted from organic electronics are interesting candidates to form carrier selective contacts for silicon solar cells. MoO_x and WO_x were investigated in more detail and were used for the hole selective contact of an SIS like structure to replace the a-Si:H(p). Furthermore, as an additional contact layer to improve the parasitic Schottky contact formed between the ITO and the a-Si:H(p). A simple semiconductor-semiconductor (SS) structure for which any a-Si:H was omitted and where WO_x is in direct contact to c-Si was also investigated.

Before annealing the MoO_x investigated showed optical and electrical properties superior to that of the a-Si:H(p). For the SIS structure the efficiency was significantly higher ($\sim 1\%_{\text{abs}}$) compare to the reference with a-Si:H(p). However, annealing at 180°C lead to a degradation of the properties responsible for the selective hole extraction for both the SIS like structure and the SHJ structure where MoO_x was used as an additional contact. However, this shows that there is no intrinsic limitation for the application of MoO_x but the modification of the material properties with annealing need to be understood to allow for an efficient engineering of the MoO_x and contact properties. If the WO_x films investigated here are implemented in an SIS like structure the presence of our roughly 7 nm thick undoped a-Si:H buffer layer prevents an efficient hole extraction from the absorber. Moderate surface passivation and a high *FF* are obtained if WO_x is directly placed on the c-Si absorber. Such a simple hole contact (no PECVD) where the metal oxide is directly placed on the absorber might be an appealing approach to replace the Al-BSF or the boron doped selective emitter of homojunction cells. The application of dielectric tunneling buffer layers, which are not prone to depletion, might further improve passivation. Other important questions are whether the better c-Si passivation by such metal oxides (as compared to a-Si:H(p)) would lower the demands on the buffer layer properties in terms of chemical passivation and whether for a thinner a-Si:H(i) buffer layer the hole extraction would be

significantly improved. It was also shown that if WO_x is applied as an additional contact layer to the standard SHJ, an improved contact to the ITO (and AZO) electrode and a screening of the sputter damage are observed. Additional significant parasitic absorption was observed for the 15 nm thick films investigated here. Accordingly, for the front side, thinner films need to be applied while for the rear side the layer thickness should be of less importance. Hence, an appealing approach might be the application of WO_x to an a-Si:H(p) rear emitter improving the contact to AZO. It should also be checked if thicker films can be applied replacing the ITO or AZO at the rear.

Furthermore, it was shown that simple surface photo voltage and Suns- V_{oc} measurements are an easy means for the assessment of such contact schemes. It was also shown that low temperature annealing does not only modify minority carrier recombination and thus the c-Si surface passivation by the contact scheme but also material and contact properties governing the selective carrier extraction were strongly affected.

Investigations (not presented) revealed that for this WO_x films the contact between AZO and p-doped a-Si:H is also improved. In a follow up experiment the influence of the a-Si:H doping (1400/2300/4400 ppm) for WO_x and ITO contact layers was compared [201]. The experimental results were in qualitative agreement with the simulation results in Figure 4.15 and Ref. [94] of the present author where it was predicted that a high work function electrode improves the FF and that this improvement is more pronounced the lower the a-Si:H doping is. We have also shown that sputter deposited WO_x films can improve the contact to ITO [199]. Furthermore, we have applied this MoO_x and WO_x films to the TOPCon [200].

It is important to note that the investigation of metal oxides for silicon solar cells is very novel. Further fundamental understanding of the relevant contact and material properties governing both the selective carrier extraction and the c-Si surface passivation is crucial for an efficient engineering and tailoring of such interesting contact systems. More precisely, the band line up, including hetero-barriers and the chemical properties of the films implemented in device relevant structures needs to be investigated in detail. A characterization approach based on photo-electron spectroscopy (PES) similar to the one presented in Ref. [233] might be helpful. More advanced characterization approaches combined with adequate device simulation might provide a more holistic view. To change the work function of the films, a doping variation similar to the one presented in the section 6.3 should be performed and alternative buffer layers should be investigated. Generally, the tunability of the material properties by reactive evaporation and

alternative deposition schemes needs to be investigated. Finally, more work is needed to identify other suitable contact materials. This also holds for materials capable of forming an electron selective contact.

6.5 Chapter Summary

In this chapter the basic requirements in terms of external voltage and selective carrier extraction from a c-Si absorber have been motivated experimentally. Different contact schemes were analyzed using metals, metal oxides or doped amorphous silicon.

A doping variation of amorphous silicon which forms the hole contact of a standard silicon heterojunction was performed. This experiment was useful to motivate the basic idea behind analyzing the contact properties with respect to a non-ideal voltage extraction from the absorber. It was shown that non-optimized contact schemes may provide excellent c-Si surface passivation but may fail to selectively extract the absorber's excess carriers. It was clearly shown that V_{oc} and FF losses can be caused by such effects and that the *Suns*- V_{oc} method is a well-suited technique for the characterization and optimization of such contacts. A certain minimum doping was needed to avoid the global depletion of the a-Si:H / c-Si part of the SHJ by the TCO electrode and to ensure an efficient tunneling transport into the TCO.

This was followed by an attempt to change the TCO properties, rather than the doped a-Si:H properties, to improve the excess carrier extraction at both the hole and electron contact. The ITO doping near the p-type and n-type doped a-Si:H was varied over a very wide range aiming for an improved work function matching to improve the parasitic Schottky contact. While on test structures it could be shown that the work function can be tuned in the desired way. On cell level, work function matching has shown no influence and other effects governed the carrier transport into the TCO.

In the next step, the metal / a-Si:H contact was investigated. It was shown that metal films are unsuitable as contact layers. Besides a pronounced Fermi-level pinning, more fundamental limitations by the deterioration of the chemical c-Si passivation already at moderate annealing temperatures, poor adhesions and the poor optical properties in terms of rear side reflection were observed. Only Ag combined good optical and reasonable electrical results if placed on doped a-Si:H. It was used to replace the ITO electrode of the standard SHJ. This a-Si:H(p) / Ag hole contact was applied to the rear side of a so called hybrid SHJ cells, a concept which was established in the course of this thesis. An efficiency of 22.8 % could be achieved.

Some alternative and novel contact materials adopted from organic electronics were investigated on test structures. Two candidates have proven their capability to form carrier selective contacts for c-Si absorbers. Molybdenum oxide (MoO_x) and tungsten oxide (WO_x) were successfully integrated in solar cells either to form a direct hole contact or to improve the parasitic Schottky

contact formed with the TCO. With MoO_x the efficiency, before annealing, could be significantly improved compared to the reference ($\sim 18.7\%$ vs. $\sim 17.6\%$) as both optical and electric properties were improved when the a-Si:H(p) is replaced. For WO_x as an addition contact layer, the parasitic Schottky contact of the standard cell structure could be improved, presumably by an improved work function matching. This was quantified by a significant FF gain compared to the reference ($\sim 81.1\%$ vs. $\sim 79.6\%$). Finally, for an a-Si:H less hole contact with WO_x an efficiency comparable to the reference was observed ($\sim 17.6\%$ vs. $\sim 17.5\%$). This simple structure might be an appealing approach to replace the Al-BSF of the standard homojunction cell. So, very encouraging results could be demonstrated for this new class of materials.

In this chapter it was clearly demonstrated that non-optimized contact schemes may provide sufficient c-Si surface passivation but may fail to selectively extract the excess carriers of the absorber. This highlights that not only the “classical” losses, i.e. minority carrier recombination and ohmic transport losses might limit the performance of such novel / alternative contact schemes. This must be taken into account for the analysis of the FF and V_{oc} losses. A simple characterization approach, based on analyzing the illumination level dependence of the V_{oc} , was presented which allows to distinguish between both loss mechanisms. FF and V_{oc} losses can be easily predicted which facilitates junction engineering. This can be performed in the early stage of device optimization as the current-less measurement allows for simple test structures (*Suns- V_{oc}* samples) which can be produced with little effort. Unlike for solar cells, a grid electrode is not needed and lower demands on the definition of the active cell area exist. This allows the screening of a large parameters space before the final evaluation is done on solar cell level. On cell level, the analysis of standard J - V characteristic and eventually their temperature and the illumination level dependence (results for letter not presented here) enables a further evaluation of non-idealities and the quantitative assessment of the efficiency limitation. It should be pointed out that for very basic investigations with the test structures and for the case that the contact under investigation can not be placed at the illuminated front side. The analysis of the test samples might be limited to analyzing the asymmetry of the external V_{oc} obtained if the same material is forming either the hole or electron contact. Another simple and valuable tool are surface photo voltage (SPV) measurements as they enable the quantification of the induced band bending and, indirectly, of the effective work function which results after contact formation at the interface.

Regarding future work, more efforts are needed to characterize the actual microscopic material and interface properties on device relevant structures. This enables a more fundamental understanding to link these properties to the losses caused by minority carrier recombination and the selective carrier extraction. In term of the selective hole/electron extraction from the absorber, other factors than the effective work function like hetero-barriers, non-metal like behavior of the contact layer (depletion of TCO and metal oxide) and the actual transport paths governing minority and majority transport in the contact region need to be analyzed. Such data are also needed to establish a simulation setup which adequately describe such contact schemes. This opens up the possibility for a sensitivity analysis of various parameters which is indispensable for an holistic interpretation of the experimental findings and to define design rules for such novel contact schemes.

7 Lateral Carrier Transport at the Front: Mitigating the Associated Losses

In this chapter the fundamental challenge of balancing the contradictory requirements on excess carrier generation in the absorber and the lateral transport at the front side of heterojunction solar cells is addressed. A detailed comparison between classical both side contacted SHJ cell design, i.e. an n-type absorber having the emitter located the front side (front emitter) or a novel approach having the emitter at the rear side (rear emitter) is carried out. It is demonstrated with the help of 2D simulations that for the rear emitter design an additional lateral transport path via the absorber exists which leads to a higher degree of freedom for the choice of the front side TCO and the metal grid electrode. This opens up different optimization routes for the cells design which can be beneficial in terms of efficiency and economics. A higher FF potential for the rear emitter cells, resulting from a more efficient lateral carrier transport is experimentally demonstrated.¹²

This chapter is based on the publications [235], [236], [237], [218] and the diploma thesis from Sebastian Schroer [100], a diploma student supervised by the author.

7.1 Motivation

The efficiency of SHJ devices is typically dominated by a pronounced trade-off between the optical and electrical losses at the front side [119]. This is explained by both 1D and 2D effects. 1D effects are basically originating from the challenge of optimizing the silicon thin films (SiTFs) at the front towards a high J_{sc} by reducing parasitic absorption. The increase of J_{sc} by reducing the SiTF thickness [119] or increasing its transparency [180] typically comes at the cost of FF and V_{oc} as the influence of the parasitic Schottky contact formed between the TCO and the doped SiTF becomes more pronounced. In terms of 2D losses a trade-off between the FF and J_{sc} caused by the lateral carrier collection at the front is observed [119]. Unlike for high efficiency homo-junction devices which are characterized by complex 2D and 3D features (local diffusions, contact openings) for monofacial SHJ cells a 2D transport is caused only by the local metal grid electrode at the front, more precisely its pitch (Figure 7.1). With increasing pitch the shading by the metal

¹² The 2D numerical simulations were performed with Sentaurus Device (Synopsys) [168]. Most of the 2D numerical device simulations have been performed by Sebastian Schröer, a diploma student supervised by the author (diploma thesis [100]). The 2D simulations comparing the different TCOs (ITO, AZO, IO:H) were performed by Heiko Steinkemper a PhDT student working on Sentaurus Device simulations. Certain intrinsic 1D aspects are investigated on the basis of 1D simulations with QSS-Model v4 (ANU) [234] and AFORS-HET by the present author.

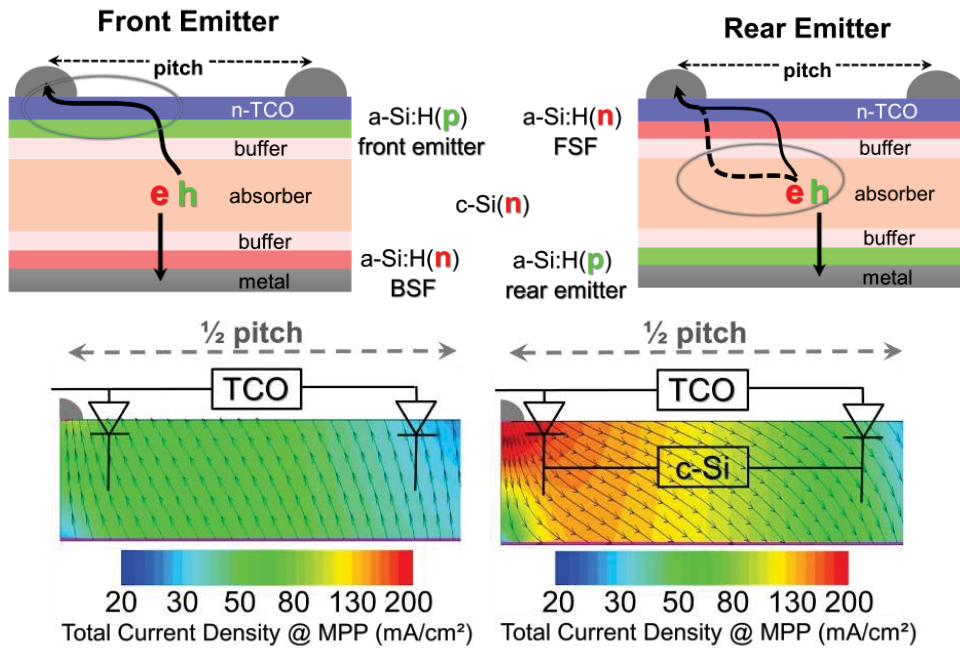


Figure 7.1: Top, sketch of simulated and experimentally investigated cell structures. Bottom, simulated current paths (arrows) and current densities (color) within the absorber at MPP for a symmetry element featuring a R_{sheet} of $105 \Omega/\text{sq}$ and a pitch of $2000 \mu\text{m}$ indicating that a large part of the lateral transport is shifted from the TCO (not visible) into the absorber. The series and parallel connection between the absorber and the TCO for the FE and RE design are indicated as well, respectively.

grid electrode is reduced as the total amount of fingers is reduced (higher J_{sc}). However, this leads longer lateral transport path within the solar cell (TCO and absorber) and hence increasing transport losses (lower FF). The common approach to balance these opposing requirements and to maximize the efficiency is to carefully adapt both the sheet resistance (R_{sheet}) of the TCO electrode and the pitch of the metal electrode. This was already discussed in section 4.1 on the basis of analytical calculations. However, the fact that lowering $R_{\text{sheet}} = 1/(q \cdot n \cdot \mu \cdot t)$ of the TCO comes at the cost of J_{sc} especially if the free carrier density (n_e) rather than the mobility (μ) of the TCO is increased [98] was not considered there. Thus, the findings from section 4.1 are valid only for a high mobility TCO where optical properties are of minor importance and do not change with R_{sheet} . In this section more detailed investigations are carried out as 2D device simulation are performed. Unlike for the analytic calculations, the interplay between the optical and electrical TCO bulk properties are taken into account and more detailed investigations and loss analyses can be performed. It is shown that utilizing the lateral conductivity of the absorber by placing the high/low junction at the front side and the p/n junction at the rear has the potential to lower the power losses caused by the 2D transport as compared to the conventional front emitter (FE) design. This is explained by the fact that for the rear emitter (RE) design the lateral transport is

partly shifted from the front side TCO into the absorber. However, reduced 1D losses are expected for the RE design of a n-type absorber as well (not investigated here). This is attributed to the fact that the optimization of the n-SHJ is typically less demanding as compared to the optimization of the p-SHJ (lower doping efficiency, higher defect density, etc.). Having the more complex p-SHJ at the non-illuminated rear allows concentrating on the optimization of its electrical properties whereas the trade-off between the optical and electrical properties for the n-SHJ at the front is less stringent.

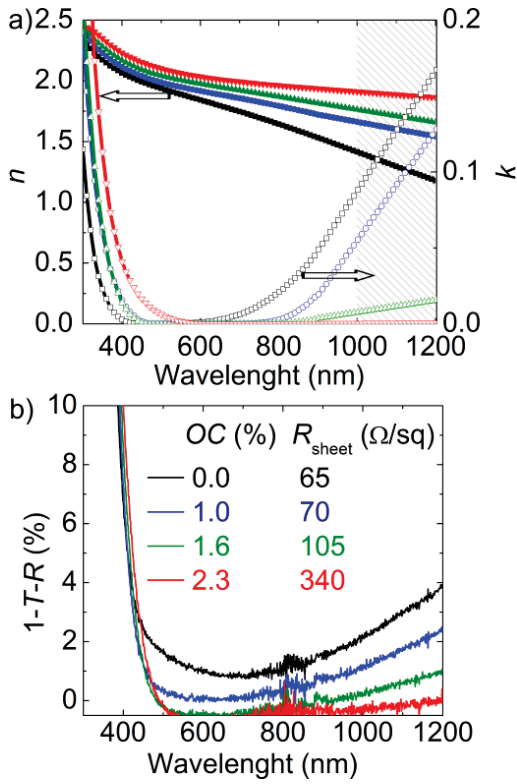
So far only few publications on SHJ RE exist [238], [159], [143], [172], [171], [218] (letter three from author of this these). However, the possibly to mitigate the 2D losses by this approach was first discussed by Ref [237] which is based on work presented here. An experimental verification was performed later on in Ref [239] and [235] (letter from author of this these).

Finally, it should be noted that a similar approach has already been described for homojunction rear emitter cells in Ref [240]. Furthermore, it should be noted that utilizing the absorber for a 2D or even 3D transport over several hundreds of microns is standard for the rear side of more advanced homojunction cells designs. PERL and PERC cells are featuring partial rear contacts of the high/low junction and for all back contacted solar cells both the majority and minority carriers have to travel several hundred microns within the absorber to their respective contacts.

7.2 Simulation: Front vs. rear emitter

7.2.1 Simulation details

2D numerical device simulations for double side planar n-type SHJ solar cells featuring (i) either a front emitter (FE) or a rear emitter (RE), (ii) a variable pitch of the metal grid electrode and (iii) variable electrical and optical TCO properties were performed. As input parameters we took the refractive indices (n) and extinction coefficients (k) estimated from spectroscopic ellipsometry measurements by fitting the data to a Drude-Tauc-Lorenz model [241] and the measured $R_{\text{sheet, glass}}$ data of four distinctive ~ 70 nm ITO thin films deposited at different oxygen flow ratio $OC = O_2 / (O_2 + Ar)$ during the sputtering process [186] (Figure 7.2). It should be noted that the free carrier absorption (FCA) absorption of this layers is expected to be underestimated due to fitting errors caused by the Drude model and the linear extrapolation of the data for the relevant wavelength regime that was performed due to the absence of measured data for above 1000 nm. The corresponding spectrophotometer measurements for co-deposited layers on glass and the μ and n_e determined from Hall measurements are shown as well in Figure 7.2. In accordance to



OC (%)	$R_{sheet,glass}$ (Ω/sq)	μ (cm^2/Vs)	n_e (cm^{-3})
0.0	65	32	4.5×10^{20}
1.0	70	47	3.5×10^{20}
1.6	105	50	1.5×10^{20}
2.3	340	49	0.7×10^{20}

Figure 7.2: (a) Spectral n and k dependence for ~ 70 nm as-deposited ITO films on c-Si deposited at different OC. The shaded area denotes the wavelength regime where the fitted n and k data have been linearly extrapolated. (b) Measured absorption spectra of the corresponding films on glass. The table collects R_{sheet} and the mobility and electron concentration from Hall measurements for samples deposited on glass.

[119], [216] FCA is low if n_e drops below $10^{20} cm^{-3}$. The pitch of the front side metal grid electrode was varied from 800 to 5000 μm . The finger width was fixed to 60 μm . The increase of the pitch corresponds to a decrease of the shading by the grid electrode from 7.4 to 1.2 %. Furthermore, some simplifications allowed to focus on the 2D transport issues. We omitted an intrinsic a-Si:H(i) buffer layer between the 150 μm thick n-type c-Si absorber featuring a dark resistivity of 5 Ωcm and the doped 10 nm a-Si:H layers as well as defects at the corresponding interfaces and in the bulk of the absorber unless otherwise stated. Furthermore, tunneling transport was not considered within the whole device. Further simplification were made concerning the ITO layer, its bulk properties and the interface to the metal and a-Si:H layers. (i) We did not treat the TCO as an individual n-type semiconductor, but as a transparent metal like layer characterized only by its work function, conductivity (R_{sheet}) and n, k values. (ii) The work function of the TCO was matched to that of the doped a-Si:H, resulting in flat-band conditions at the TCO / doped a-Si:H contact. A surface recombination velocity of 10^7 cm/s for holes and electrons is assumed for this interface. Thus, an low ohmic characteristic is observed for the TCO / doped a-Si:H contact. (iii) We also assumed a low ohmic contact characteristics for the metal / TCO contact. To account for the ohmic power losses caused by the TCO / doped a-Si:H contact, the metal / TCO contact and the finger and busbar resistivity, an additional constant and

quit high lumped series resistance of $0.5 \Omega\text{cm}^2$ was assumed for all pitches and all R_{sheet} . As boundary conditions for the optical simulations we chose a textured front and a shiny etched rear side featuring the excellent optical properties of an Ag single layer [171]. Consequently, in the simulation study the FE and RE design are distinguished only by the fact that the p-emitter is located either at the illuminated and locally contacted front or at the non-illuminated fully contacted rear side of the device as sketched in Figure 7.1.

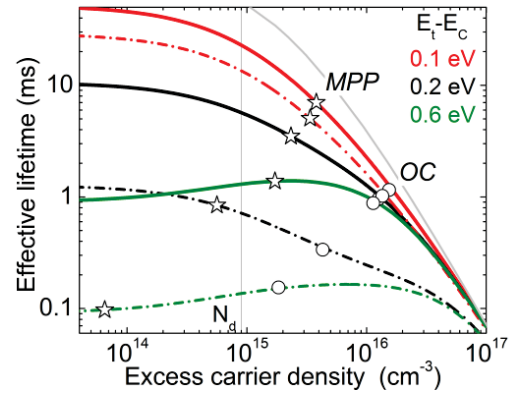
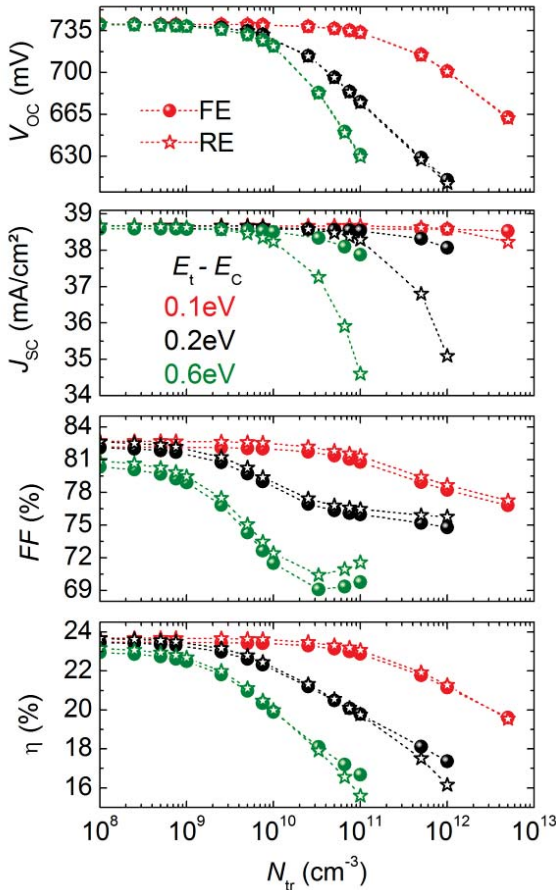
For Section 7.2.2, in which the influence of the defect recombination in the bulk of the c-Si absorber is investigated, the following defect parameter have been chosen. As the limiting SRH bulk defects are not well known for as-grown (Cz) n-type mono crystalline silicon (no high temperature treatment for a-Si:H based HJ cells) and as they will change for different feedstock, we chose the following scenarios to demonstrate the influence of the c-Si bulk recombination on the cell performance: (i) A very pessimistic scenario, in which a deep defect level (E_t) at mid-gap is assumed, thereby strongly affecting the low injection bulk lifetime and the corresponding diffusion length. Two shallow defect levels (ii) 0.2 eV and (iii) 0.1 eV below the conduction band (E_C). The SRH trap density (N_{tr}) was varied from 10^8 to $5 \times 10^{12} \text{ cm}^{-3}$. In all scenarios we assumed equal minority and majority carrier capture cross sections of 10^{-14} cm^2 . According to SRH theory [29], [30] the low values of E_t for (ii) and (iii) result in a strongly reduced recombination activity especially for the low injection conditions compared to (i) for a given N_{tr} .

7.2.2 Collection of absorber's minority carriers at the rear emitter

Does a rear emitter design require a higher absorber quality ?

For all types of RE solar cells [242], [243], [172], including all back contacted solar cells, the requirements on the recombination in the bulk of the absorber and at the illuminated junction at the front are typically higher compared to its FE counterparts. This leads to the fact that typically a higher material quality of the absorber is required for RE devices. To discuss this issue with respect to SHJ cells, first the relevance of the SRH bulk recombination of the c-Si absorber for the cell output parameters is compared for FE and RE devices based on 2D numerical device simulations. Then, general considerations regarding the V_{oc} and FF limitation by SRH bulk recombination are discussed on the basis of 1D simulation. The latter shows similarities to section 5 where the V_{oc} and FF limitation by defect recombination at the absorber surface was investigated.

The results from 2D simulations comparing the cell output parameters of FE (closed symbols) and RE (open symbols) devices are shown in Figure 7.3, left. It is shown that for a lower absorber quality, i.e. for a higher N_{tr} and deeper defect levels (coloring of the symbols) a drop of the short circuit current density (J_{sc}) is observed which is much stronger for the RE devices. This is attributed to the fact that the corresponding bulk lifetime and diffusion length of the 150 μm thick absorber under short circuit (SC) conditions are insufficient to allow for an efficient minority carrier collection at the p/n junction. The stronger influence for the RE design is explained by the fact that the p/n junction is situated far away from the front side where most of the carriers are photo-generated. For the V_{oc} on the other hand no significant difference between the FE and RE devices is observed. For N_{tr} above 10^{10} cm^{-3} the V_{oc} starts to drop well below



$E_c - E_t$ (eV)	N_{tr} (cm^{-3})	iFF (%)	n_{MPP} (-)	iV_{oc} (mV)	n_{OC} (-)
0.1	10^{10}	87.0	0.87	749	0.79
	10^{11}	86.3	0.90	743	0.83
0.2	10^{10}	84.4	1.06	740	0.95
	10^{11}	82.3	1.09	689	1.26
0.6	10^{10}	80.1	1.70	736	1.08
	10^{11}	77.7	1.13	655	1.87

Figure 7.3: Left, simulated influence (Sentaurus) of N_{tr} on V_{oc} , FF, J_{sc} and efficiency (η) for FE (closed symbols) and RE (open symbols) devices featuring a pitch of 2000 μm and R_{sheet} of 105 Ω/sq . The color denotes E_t of the SRH defect with respect to the conduction band. Right, QSSPC-Model simulated absorber bulk recombination limited effective lifetime for N_{tr} of 10^{10} cm^{-3} (solid lines) and 10^{11} cm^{-3} (dashed dotted lines) for $E_t - E_c$ of 0.1, 0.2 and 0.6 eV. Highlighted are the MPP (stars) and OC (circles) conditions. The grey line corresponds to the intrinsic limit of the absorber and N_d the absorber donor doping concentration.

The table collects the corresponding iFF, iV_{oc} , local ideality factor (n) at MPP and OC.

700 mV regardless of the device design. For the FF a comparable characteristic is also observed for FE and RE devices while the absolute FF is slightly higher for the RE devices (discussed in the next section). A strong FF drop well below 80 % with decreasing material quality is clearly visible. Reflecting the behavior of the V_{oc} , J_{sc} and FF a strong reduction of the efficiency with increasing N_{tr} is observed which is more pronounced the deeper the defect level is. The comparison of the efficiency of FE and RE cells reveals that a small drop in J_{sc} by up to ~ 0.3 mA/cm² can be compensated by the slightly higher FF ~ 0.6 %. Nevertheless, it can be seen that for poor material the efficiency of the RE device falls below that of the FE device. The latter is caused by the higher sensitivity of the J_{sc} to the SRH bulk recombination within the c-Si absorber for the RE cells. In terms of absolute efficiency it can be derived from Figure 7.3 that regardless of the position of the p/n junction the requirements on the absorber quality are always higher for the MPP and OC conditions as compared to the SC conditions. This is attributed to the very low junction recombination enabled by the simulated SHJ p/n and high/low junction which, compared to homojunction devices, allows the operation near the intrinsic limit of the absorber for both MPP and OC conditions where the influence of defect recombination is small. A more detailed view on the FF and V_{oc} losses caused by the SRH recombination in the absorber is given in the right graph of Figure 7.3 where the injection-level dependent bulk lifetime for two SRH defect densities (10^{10} and 10^{11} cm⁻³) and for the three defect levels is shown. The table in Figure 7.3 summarizes the corresponding bulk recombination related limit of the V_{oc} and FF . For very high quality material ($N_{tr} = 10^{10}$ cm⁻³ and $E_C - E_t = 0.1$ eV) the intrinsic recombination is dominating the bulk recombination and thus allows for a V_{oc} and FF of 749 mV and 87 % which is close to the intrinsic limit of the 150 μ m thick, 5 Ω cm absorber [6]. The dominance of the intrinsic recombination is expressed also in the corresponding local ideality factors for MPP and OC conditions which are well below unity approach 0.7. This indicates that the absorber is operating in high-injection and near the intrinsic limit dominated by Auger recombination [6]. The latter fact becomes obvious from the corresponding effective lifetime characteristics in Figure 7.3 as well. The MPP and OC conditions for the high quality material are close the intrinsic limit of the absorber (grey line). However, when SRH bulk recombination becomes significant, both MPP and OC conditions are subjected to a transition between two different recombination paths. Consequently, this is reflected in the V_{oc} s and FF s shown in the table. For lower material quality both the recombination at MPP and OC become affected by the increasing SRH recombination. However, attributed to the lower excess carrier density at MPP compared to OC conditions, the

influence of the SRH recombination is much higher for the MPP as compared to OC conditions. Especially, if the MPP is shifted into this transition region, while OC is still in high-injection, a significant reduction of the FF is observed while the V_{oc} loss remains moderate. This is made clear in the table where for a constant N_{tr} of 10^{10} cm^{-3} the V_{oc} drops only by $\sim 9 / 13 \text{ mV}$ ($1.2 / 1.7 \%$) with the depth of the defect level but the corresponding reduction of the FF is much higher and amounts to $2.6 / 6.9 \%$ ($3.0 / 7.9 \%$). Thus, as the low junction recombination of SHJ devices permits operating near the intrinsic limit of the absorber for all working conditions and injection levels, maintaining this condition not only for OC but also for MPP conditions is a basic requirement to reach high FF s. It is shown in other publications that defect recombination in the absorber [244], [245], [246], [247] and at the interface [144], [194], [143], (section 5) can have a strong influence on the FF . Finally, it should be mentioned that the 2D simulations reveal a comparable FF characteristics for the FE and RE devices irrespective of the bulk defects. It is therefore concluded that 1D effects are dominating the FF characteristics and that for well designed devices the influence of defect recombination within the absorber on the lateral carrier transport of the majority carriers (RE) and minority carriers (FE) is small.

To sum up, the simulations indicate that in terms of maximum cell efficiency, for SHJ cells the requirements on the absorber quality are not higher for the RE design as high quality material is required anyway to prevent FF and V_{oc} losses caused by defect recombination in the bulk of the absorber. For this high quality material the corresponding diffusion length is sufficient high to allow an efficient minority carrier collection at the RE. However, as with all RE devices the J_{sc} is more sensitive to the bulk quality. Thus, for poor material quality a lower efficiency will be observed as compared to its FE counterpart. It should be noted, that for thinner wafers the influence of the bulk recombination on the J_{sc} is less pronounced and that for the application of a 2D or 3D RE design (line or point-like features for all back contacted solar cells or homo-junction RE cells) the requirements on the bulk recombination are more stringent compared to the 1D SHJ RE design due to longer transport paths for the minority carriers. In summary, considering high efficiency devices with high quality absorbers, it is expected that the RE design can fully exploit its higher FF potential, which will be discussed in the next sections.

7.2.3 Improved 2D carrier collection for the rear emitter design

Within the second simulation study we investigated the influence of the electrical and optical losses caused by the front side TCO electrode and the metal grid electrode. Again, by comparing FE and RE cell structures regarding their cell output parameters.

Qualitative explanation of the more efficient 2D carrier collection for the rear emitter

In the lower graphs of Figure 7.1 the 2D carrier transport within the absorber under MPP conditions for a FE cell (left) and a RE cell (right) is shown. The coloring denotes the total current density within the absorber; the arrows correspond to the technical direction of current. It can clearly be seen that the current density inside the absorber is higher and that the lateral part of the current within the absorber is more pronounced when the device is featuring a RE instead of a FE design. Consequently, for the RE design a substantial part of the lateral current flow is shifted from the front side TCO (not visible) into the absorber. However, for the FE a lateral component in the absorber is observed, too. The positive influence of such an lateral current component within the absorber of FE cells on the FF was investigated for high efficiency homojunction devices from *UNSW* in Ref [248]. It was shown that for high efficiency devices this effect leads to lower losses as predicted by 1D theory.

For the conventional FE cell design the minority carriers of the absorber (holes) are subjected to the lateral transport towards the front side metal grid electrode as it is indicated in the upper graphs in Figure 7.1. In this configuration the front side TCO and the absorber are horizontally decoupled via the p/n junction which results in a series connection of the absorber and TCO. At the induced p/n junction the holes are separated from the absorber. Thus, the lateral carrier transport towards the local grid electrode takes place mainly within the front side TCO¹³.

As far as RE devices are concerned the majority carriers of the absorber (electrons) are subjected to the lateral transport towards the metal grid electrode (Figure 7.1). In this case the front side TCO and the absorber are horizontally coupled via the high/low junction which results

¹³ The lateral minority carrier(hole) transport within the absorber should be influenced by the ratio of the effective diffusion length to the pitch. Hence, an effective diffusion length well above half of the pitch might facilitate the lateral minority carrier current within the absorber just as it is the case for partial rear emitters in all back contacted solar cells. It should be noted that for high quality c-Si and high quality hole and electron contacts the effective diffusion length can be in the range of several mm for MPP conditions.

The contribution of a lateral component of the hole current in the inverted c-Si region close to the interface, where the holes are majority carriers is investigated in Ref [249] for SHJ cells. The results are indicating the R_{sheet} of the induced p⁺⁺-region is above 1000 Ω/sq and thus of minor importance for the lateral hole collection of SHJ FE devices.

in a parallel connection of the TCO and the absorber. This leads to a more advantageous current flow pattern for the carrier collection at the local grid electrode as a significant part of the lateral transport can be realized inside the absorber. As will be shown below, the higher lateral component of the current for the RE design allows to decouple the influence of R_{sheet} of the TCO electrode and the pitch of the grid electrode on the FF to some extent. It should be mentioned that this is valid only for the mono-facial SHJ design for which the metal electrode covers the whole TCO electrode at the rear enabling a 1D transport at this side of the device. For a bifacial design where the lateral transport within the TCO is required at both the front and the rear sides the achievable FF gain will also depend on the pitch of the grid electrode at the rear side [239].

Cell output parameters

In Figure 7.4 the cell output parameters as a function of the pitch of the grid electrode and R_{sheet} of the front side TCO, for the FE (left) and RE (right) cells are shown. These graphs quantify the aforementioned advantage of the RE design concerning the lateral carrier collection at the local grid electrode. For both structures an increasing pitch as well as an increasing R_{sheet} have a negative influence on the lateral carrier transport and therefore the FF . However, this effect is less pronounced for RE devices particularly when the limitation of the lateral transport in the TCO electrode becomes more relevant, i.e. for high R_{sheet} and large pitches. Concerning the influences of the pitch and R_{sheet} on the optical properties, a closer look reveals that the shading of the metal grid electrode and the optical properties of the TCO electrode are affecting the J_{sc} in the same way for FE and RE devices. With increasing pitch, the J_{sc} is increased due to lower shading by the grid electrode. In order to interpret the J_{sc} gain with increasing R_{sheet} the spectral device absorption for a 70 (top) and 105 Ω/sq ITO (bottom) are plotted in Figure 7.5. It can be seen that the current gain with lower TCO doping and therefore higher R_{sheet} is caused mainly by the decrease of the parasitic FCA in the NIR. This was indicated before in Figure 7.2 by the fitted k and the R/T measurements. A comparable behavior is experimentally observed in Ref [216]. Concerning the V_{oc} , Figure 7.4 shows a comparable behavior for FE and RE cells. The simulations do not reveal any significant influence of the pitch or R_{sheet} on the cell performance at open-circuit conditions. It should be noted that this is in sharp contrast to homojunction devices where the pitch and, thus, the metallization fraction and R_{sheet} have a strong influence on the recombination losses caused by the metal / semiconductor interface (e.g. [250] and section 4.1). This intrinsic drawback of homojunction cells is explained by the fact that a low R_{sheet} can be reached only by increasing the doping of the active c-Si region as the mobility is more or less fixed for the c-Si.

This in turn leads to an increased carrier concentration and, thus, Auger recombination within the bulk as well as an increased SRH recombination at the interface to the dielectric passivation layer adversely affecting both the V_{oc} and J_{sc} with decreasing R_{sheet} [117,

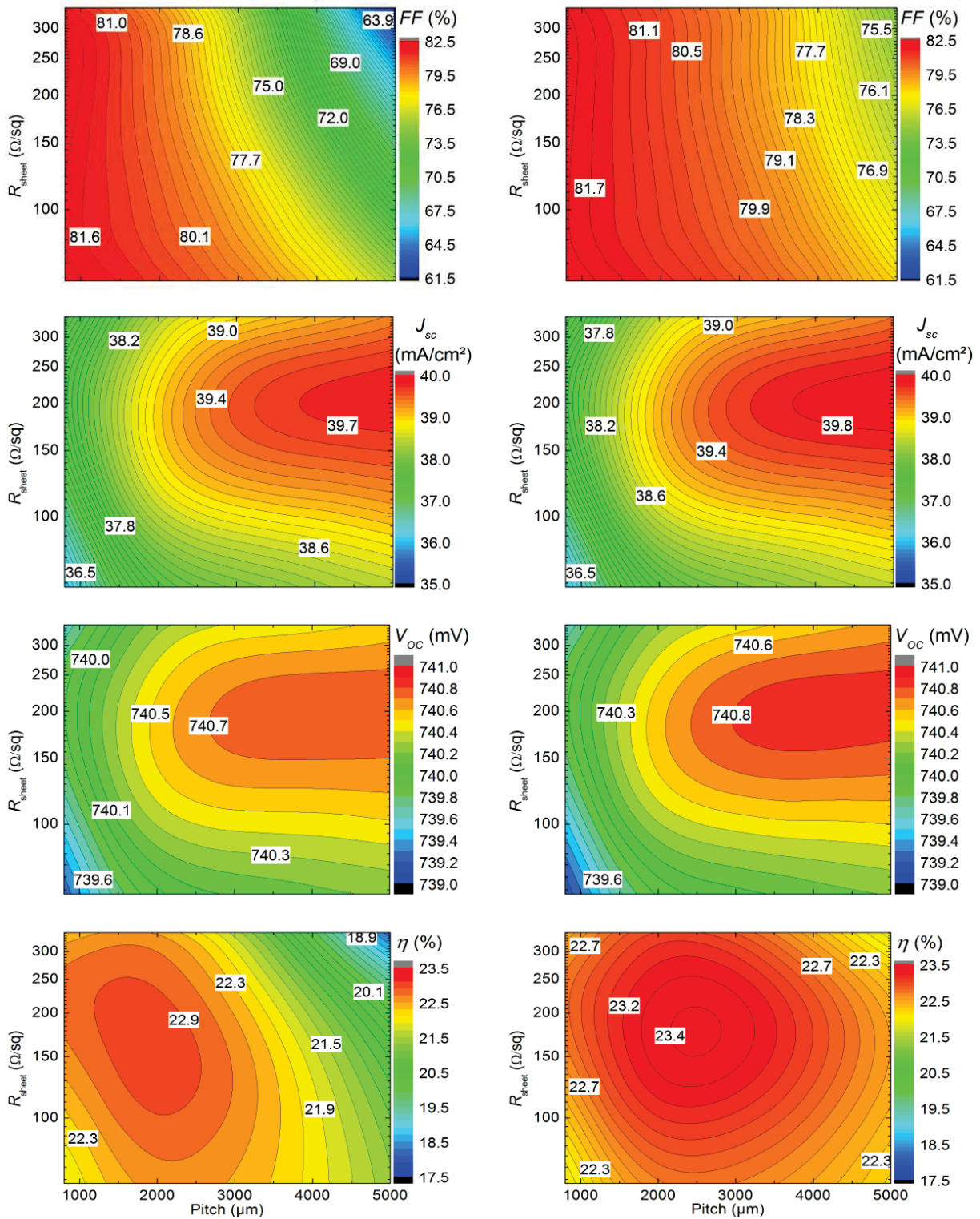


Figure 7.4: Simulated output parameters of FE (left) and RE (right) cells in dependence of R_{sheet} of the TCO electrode and the pitch of the grid electrode.

251]. On the other hand, the contact resistance of the metal / semiconductor interface [252] and the lateral carrier transport are improved with higher c-Si doping [117]. Consequently, highly doped c-Si regions only below the metal are mandatory for high efficiency homojunction solar cells at both the front and rear to overcome this trade-off [253]. For SHJ cells, such a compromise has not to be made as a direct relation between the metallization fraction, the doping of the TCO layer (situated on top of the active junction) and the V_{oc} [216] does not exist. The fact that the mobility of the TCO can be changed adds another degree of freedom to tune the lateral conductivity. Thus, another very important intrinsic advantage of SHJ cells, regardless of the position of the emitter, is that they allow for the combination of a very efficient lateral transport (low R_{sheet}) and a very low junction recombination. However, optical losses caused by FCA are observed for both homo- and heterojunction devices if a low R_{sheet} is realized via high carrier concentration. The efficiency contour plot from Figure 7.4 is discussed in the following.

Efficiency: Implications for device optimization

Comparing the efficiency contour plots from Figure 7.4 it becomes obvious that due to identical J_{sc} and V_{oc} dependencies for FE and RE devices the FF is the determining factor for the cell efficiency. As a conclusion, it can be stated that the application of the RE design opens up a wider range of possibilities in order to optimize the device without compromising or even improving the cell efficiency. In accordance with the FF , not only a shift in the optimum efficiency to regions of higher R_{sheet} and larger pitches is observed, but a slightly higher maximum efficiency is

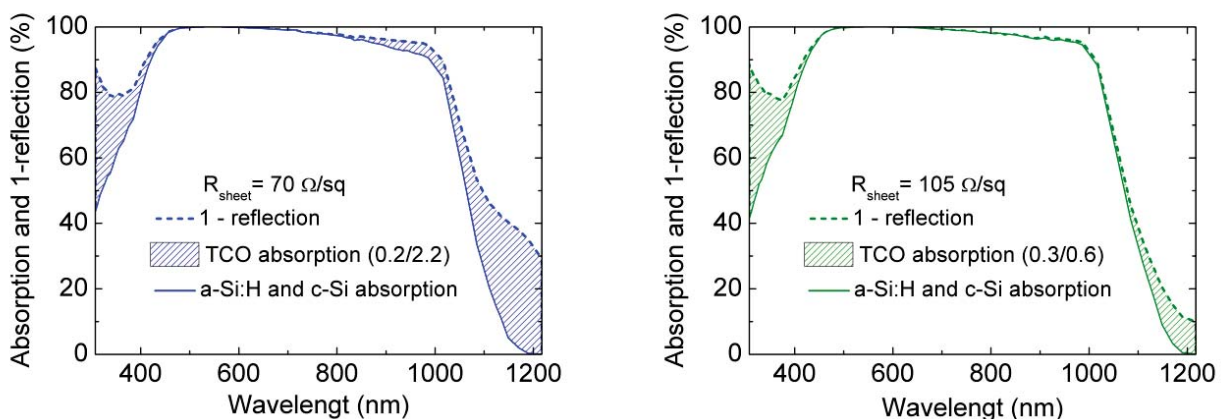


Figure 7.5: Simulated total device absorption (dashed line), absorption in a-Si:H and c-Si absorber (solid line) and parasitic absorption in the front TCO (shaded area) for an R_{sheet} of $70 \Omega/sq$ (left) and $105 \Omega/sq$ (right). The numbers in the parenthesis correspond to the parasitic generation current density (in mA/cm^2) in the front side TCO in the UV and NIR, respectively.

predicted by the simulations as well. Furthermore, the efficiency distribution is much broader for the RE design. Table 7-1 collects the cell data of three different optimization routes that might be chosen to benefit from the advantages of the RE design. Route I compares the two cells with the highest efficiencies. It can be seen that by simply changing the position of the p/n junction from the front to the rear, a small gain in cell efficiency can be achieved. As no negative influence on J_{sc} and V_{oc} is observed, the higher FF of the RE cell is responsible for the higher efficiency (slightly J_{sc} due to better optical a-Si:H(n) properties). Routes II and III are dealing with the economic potential of the RE design, i.e. a lower metal consumption and the implementation of indium free TCOs. For route II it can be seen that the RE design allows to significantly increase the pitch from 2000 to 3600 μm while keeping the efficiency at the level of the FE cell featuring the highest efficiency and a pitch of 2000 μm . For the RE design the FF loss with increasing pitch is only moderate (77.2 % for the corresponding FE cell featuring a pitch of 3600 μm) and this loss can be compensated by a gain in J_{sc} caused by the lower shading by the grid electrode. However, to fully benefit from the increased pitch a metallization technique has to be applied that is not limited by the finger resistivity. In this respect Cu plating [180], [254] has already demonstrated to be a good candidate for metallization of SHJ cells. Another approach is the application of narrow Cu wires embedded in a polymer film [255]. Route III shows that at comparable pitches a much less conductive TCO can be applied if the RE design is used without compromising on the FF . This fact should be of importance especially for the application of low- μ (indium free) TCOs featuring a more pronounced trade-off between the optical and electrical properties. As will be discussed below, for these materials the combination of the low μ and low n_e (latter is required for good optical properties) will result in TCOs featuring a higher R_{sheet} . For FE devices an experimental comparison of a low and medium μ -TCO (AZO and ITO) was carried out in Ref [256]. In Ref [44] R_{sheet} was varied from 57 to 287 Ω/sq leading to an increase in J_{sc} . It could be shown

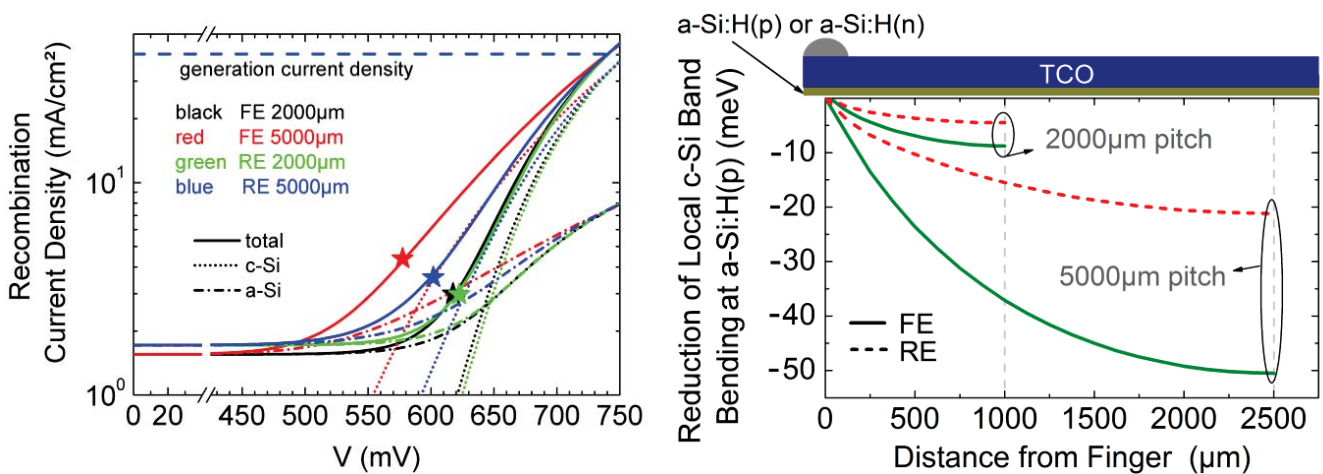
Table 7-1: Simulated cell results for different optimization routes from Figure 7.4.

Route	Device	Pitch (μm)	R_{sheet} (Ω/sq)	V_{oc} (mV)	J_{sc} (mA/cm^2)	FF (%)	η (%)
I	FE	2000	105	740	38.6	80.5	23.0
	RE			740	38.7	81.1	23.2
II	FE	2000	105	740	38.6	80.5	23.0
	RE	3600		741	39.2	79.3	23.0
III	FE	2000	70	740	38.1	81.0	22.8
	RE		340	740	38.6	80.8	23.1

experimentally that for FE devices, even for a medium μ -TCO (ITO), a relatively high R_{sheet} of 100 Ω/sq is required to balance the optical and electrical losses (pitch unfortunately not specified).

MPP – Detailed loss analysis.

A more detailed view on the losses at MPP conditions caused by the lateral carrier transport towards the local grid electrode at the front side is given in Figure 7.6. In the left graph, the relevant global device recombination current densities of two FE and two RE cells featuring an R_{sheet} of 105 Ω/sq and a pitch of either 2000 or 5000 μm as a function of the external terminal voltage are shown. It can be seen that the overall device recombination (solid lines) under SC conditions (0 mV) is dominated by the defect recombination, i.e. parasitic absorption within the SiTFs (dashed-dotted lines, 1.7 mA/cm^2).



Device	Pitch (μm)	R_{sheet} (Ω/sq)	$V_{\text{OC}}/V_{\text{MPP}}$ (mV)	$J_{\text{SC}}/J_{\text{MPP}}$ (mA/cm^2)	FF (%)	η (%)
FE	2000	105	740 / 618	38.6 / 37.3	80.5	23.0
RE	2000		740 / 623	38.7 / 37.3	81.1	23.2
FE	5000	105	740 / 578	38.6 / 35.9	72.6	20.7
RE	5000		740 / 602	38.7 / 36.7	77.1	22.1

Figure 7.6: Left, simulated total recombination current density (solid lines, sum of Auger and SRH whole device) for FE and RE devices with a pitch of 2000 and 5000 μm and a 105 Ω/sq front TCO, respectively. Furthermore, the corresponding Auger recombination in the absorber (dashed-dotted lines), SRH recombination in the silicon thin-films (dotted lines) and the corresponding MPP conditions (stars) are shown. Right, reduction of local c-Si band bending at the FE (solid lines) and at the RE (dashed lines) at MPP conditions as a function of the distance from the grid electrode for a pitch of 2000 or 5000 μm and for a 105 Ω/sq TCO. Table, simulated cell results for cells from Figure 7.4. Deviating from Figure 7.4, for a better comparison of the recombination loss analysis a constant shading and therefore comparable generation current are assumed here for all cells.

Under OC conditions (total recombination current matches generation current) Auger recombination in the c-Si absorber (dotted lines) is dominating the device recombination as ideal hole and electron contacts have been assumed. Under SC and OC conditions a comparable total recombination is observed for all devices leading to the comparable V_{oc} 's and J_{sc} 's (table in Figure 7.6). However, regarding the MPP conditions (stars) the application of a higher pitch leads to an increased (local and) global device recombination which is less pronounced for the RE devices. The recombination losses within the SiTFs and the absorber are lower compared to the respective FE device. Consequently, $P_{MPP} = V_{MPP} \cdot J_{MPP}$ and the $FF = V_{MPP} \cdot J_{MPP} / (V_{OC} \cdot J_{SC})$ are higher for RE devices as shown in the table. The increase of device recombination at MPP with increasing pitch is attributed to the fact that the lateral carrier transport will cause a corresponding voltage drop and consequently the formation of a non-equipotential region in between the fingers of the local grid electrode at the front side which reaches its maximum at half the pitch as reported in Ref [257], [258]. This voltage drop will cause the local junction voltage far away from the fingers to be above the terminal voltage. This means that the p/n junction in between the fingers is locally more forward biased as compared to near the fingers. Consequently, the selectivity and rectifying behavior of the p/n junction are locally reduced. This can be inferred from Figure 7.6 where the variation of the band bending along the p/n junction, either at the front or rear, from underneath the fingers to in between fingers (half pitch) is shown. A comparison of two FE and RE devices featuring a pitch of either 2000 or 5000 μm exhibits a stronger reduction of the band bending for the global MPP conditions at half pitch for FE devices. This effect is more pronounced the higher the pitch is. For the cell with the higher pitch this corresponds to a significant reduction of the local selectivity of the junction. Thus, an increase of the local and consequently of the global device recombination is observed at MPP conditions (Figure 7.6). However, this additional recombination path only exists if a current is extracted from the device (i.e. not for open-circuit conditions) as only in this case the local inhomogeneity of the junction voltage is observed. Thus, besides ohmic power losses induced by Joule heating, these so-called non-generation losses are affecting the MPP conditions and, therefore, the FF of the device [257],[258]. In section 4.2.5 and section 6 it was shown that the TCO / doped SiTF contact properties can have a significant influence on the selectivity of the junction and the FF of the device, too. Accordingly, it is expected that for poor TCO / doped SiTF contact properties the reduction of the (local) junction voltage by the aforementioned 2D effects, would lead to even higher non-generation losses as compared to the case of flat band conditions

at the TCO / doped SiTF contact which are considered here. However, these facts require further experimental and simulative investigations which go beyond the scope of the investigations performed here.

7.2.4 Further aspects

Influence of absorber doping: Conductivity modulation

The main question of this subsection is whether or not RE cells are subjected to specific limitations regarding the applicable absorber doping.

For sufficiently low device recombination, which is commonly observed for well designed SHJ cells, the absorber is operating near high-injection conditions at MPP ($\Delta n = n \gg N_d$) and can therefore provide a high conductivity ($\sigma = q n \mu \gg q N_d \mu$) even for lowly doped absorbers. This effects is known as conductivity modulation [259], [260], [261], [218]. In Figure 7.7 the effective absorber resistivity and the corresponding average hole and electron concentration of the absorber at MPP for three levels of c-Si surface passivation by the p-SHJ are shown. Within this 1D numerical *AFORS-HET* simulations the V_{oc} and, thus, V_{MPP} are changed by changing the D_{it} at the a-Si:H(p/i) / c-Si interface. The corresponding V_{oc} 's are 755, 715 and 660 mV. As a lower device recombination comes along with a higher carrier concentration within the absorber this is reflected in a reduction of the effective absorber resistivity at MPP. It can be seen in the upper graph that under non-equilibrium conditions (solid lines) the effective resistivity of the absorber is strongly decoupled from its value in the dark (dashed lines) and that this is especially true for lowly doped absorbers. This effect (conductivity modulation) is well known from concentrator

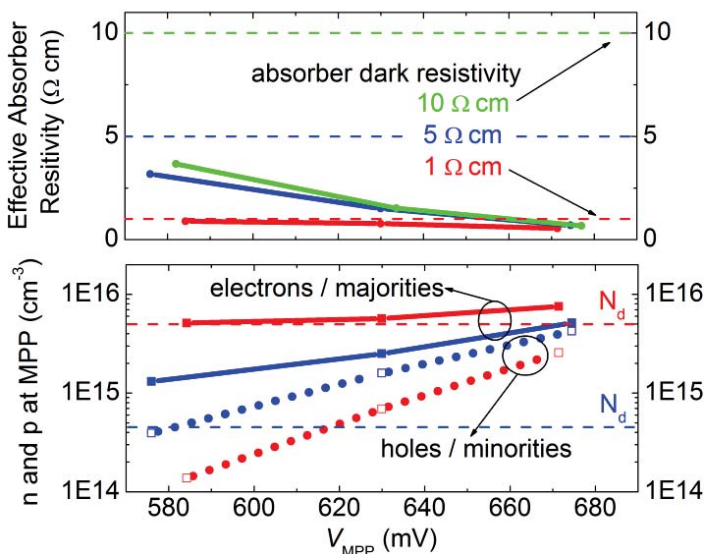


Figure 7.7: Top; effective absorber resistivity as a function of V_{MPP} for an absorber dark resistivity of 1, 5 and 10 Ω cm. Bottom, electron (solid lines) and hole (dotted lines) concentration at MPP as a function of V_{MPP} for an absorber dark resistivity of 1 and 5 Ω cm. V_{MPP} was changed by changing the D_{it} at the a-Si:H(p/i) / c-Si interface, a lumped series resistance was not considered for the AFORS-HET simulations.

devices [262] where a high generation rate ensures a high excess carrier density and thus allows the absorber to operate in or near high-injection conditions. For SHJ cells the low contribution from the hole and electron selective contacts to the overall device recombination allows for similar conditions already for lower illumination intensities (1 sun) as can be seen in Figure 7.7. The lower graph shows that the majority carrier (electron) concentration (straight lines) is well above its equilibrium concentration (dashed lines) which is defined by the ionized doping / impurity concentration of the absorber (N_d). For the very low device recombination and very high V_{MPP} a comparable effective resistivity of the absorber of slightly below $1 \Omega \text{ cm}$ is observed for the dark resistivity's of 1, 5, and $10 \Omega \text{ cm}$ as can be seen in the upper graph.

Results from 2D device simulations for variation of the absorber dark resistive from very low ($0.1 \Omega \text{ cm}$) to very high ($100 \Omega \text{ cm}$) are shown in Figure 7.8. The output parameter of FE and RE cells featuring a pitch of either 2000 or $2800 \mu\text{m}$ (gray and red lines) are compared. To assess the limitation of the cell output parameters by 1D effects like the intrinsic recombination of the c-Si absorber (SRH neglected) 1D *QSS-Model* simulations have been performed as well (blue lines).

For all devices a drop in efficiency for highly doped absorbers, i.e. for below $1 \Omega \text{ cm}$ is observed in Figure 7.8. The implied cell parameters from *QSS-Model* (blue lines), reflecting the limitation by the intrinsic absorber recombination, reveal that this behavior can (qualitatively) be explained by the increase of the intrinsic c-Si recombination and 1D effects. To clarify this effect the corresponding injection-level dependent absorber bulk lifetime from *QSS-Model* is presented in the lower graph. Especially the low injection Auger lifetime is reduced with increasing absorber doping which shifts both the MPP and OC to lower excess carrier densities, i.e. towards lower iV_{oc} and iV_{MPP} .¹⁴ Similar results have been presented before in section 5.2.2. For a dark resistivity below $1 \Omega \text{ cm}$ the absorber recombination is clearly limited by low-injection Auger recombination at MPP, for below $0.5 \Omega \text{ cm}$ the same holds for OC conditions. The c-Si bulk recombination for even lower excess carrier density, i.e. for SC conditions is increased as well as can be inferred from the drop in J_{sc} from the 2D simulations. The higher sensitivity of the RE design to corresponding bulk diffusion length has already been discussed in Section 7.2.2. The recombination at the illuminated high/low junction of the RE cells is expected to increase with high absorber doping too. This effect is known from homojunction devices and is attributed to

¹⁴ The fact that the V_{oc} from *QSS-Model* drops below the V_{oc} from Sentaurus for highly doped absorber is most likely explained by differences in the applied BGN and/or Auger parameters.

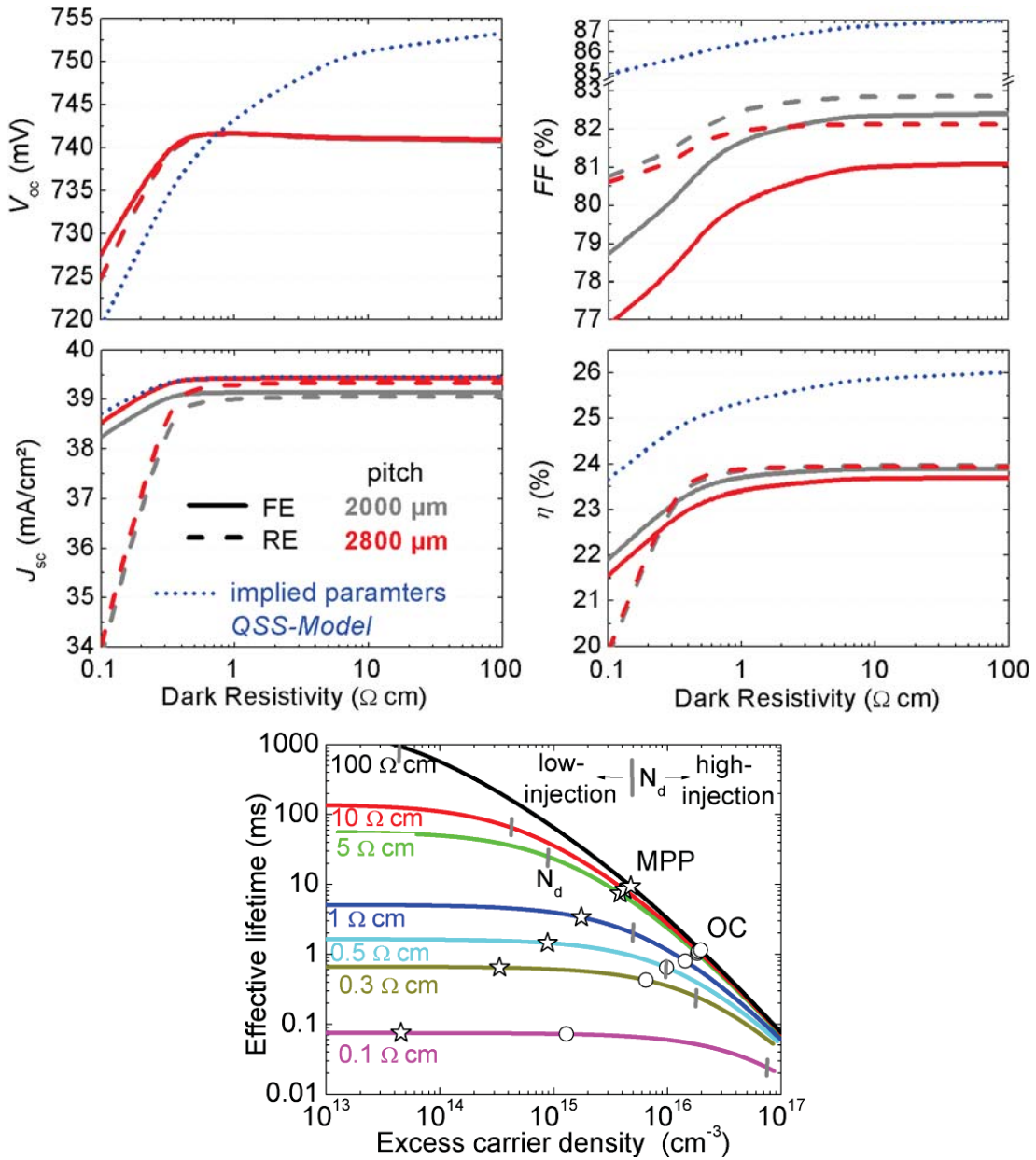


Figure 7.8: Top, cell output parameters for a variation of the absorber dark resistivity for FE (solid lines) and RE cells (dashed lines) featuring an R_{sheet} of 105 Ω /sq and a pitch of either 2 mm (grey) or 2.8 mm (red). The blue dotted line corresponds to the absorber bulk recombination limited cell output parameters (QSS-Model). Bottom, the corresponding injection-level dependent Auger recombination limited c-Si bulk lifetime (QSS-Model). N_d (short vertical grey lines) denotes the absorber’s donor doping density, stars and circles indicate the MPP and OC conditions.

the fact that the field-effect passivation by the high/low junction is lower the higher the absorber doping is [263].

Coming back to the lateral transport within the absorber, the 2D simulation reveal that for none of the devices a drop in FF with increasing dark resistive is observed. Thus, the higher FF of the

RE cells (dashed lines) and hence the more efficient lateral transport in the absorber are maintained even for a very low absorber doping.

Such a pronounced decoupling between the absorber dark resistivity and the FF for lowly doped absorbers should be a unique feature of both side contacted SHJ cells and not be observed for high efficiency homojunction and all back contacted cells. The latter two are characterized by a 2D or 3D design and are suffering from a significant drop in FF with increasing absorber dark resistivity attributed to the much longer transport paths within the absorber (e.g. [264], [265]). In addition, the higher overall device recombination of homojunction cells makes the conductivity modulation less efficient.

Based on the results above, it follows that another advantage of the SHJ cell design is that it is less sensitive to the absorber doping. For the commonly applied n-type material this allows for a higher yield of the ingots which, due to the high segregation coefficient of phosphor, are characterized by a strong variation of the doping along the growth direction. For p-type material such a low sensitivity of the cell concept to the absorber resistivity would allow the application of lowly doped absorbers which are less prone to the efficiency limiting c-Si bulk defect recombination caused by light induced degradation [265].

For RE SHJ cells, a lower absorber doping is not expected to have a detrimental influence on the transport related FF losses. Accordingly, without taking effects like defect recombination into account, a dark resistivity above $1 \Omega \text{ cm}$ should be chosen to avoid operation in the low-injection Auger regime. These results highlight that well designed SHJ cells might function as pIn like devices for which the type and concentration of absorber doping is of less concern.

Illumination dependent performance

In this subsection the low light performance and the performance at low concentrations for FE and RE cells are compared. The main question is whether or not the lower excess carrier density within the absorber for lower illumination has a negative influence on the lateral transport. For the front either an ITO from the simulations above or an IO:H was assumed. The latter is characterized by a higher mobility and comparable optical properties (mainly defined by n_e) which results in a reduced R_{sheet} as can be seen in the inset of Figure 7.9. To concentrate on the 2D effects a lumped series resistance, representing the contribution from the metal grid electrode, is omitted here. Consequently, the 2D transport is defined by the cell design (FE or RE) and R_{sheet} of the TCO, the pitch is set to 2 mm.

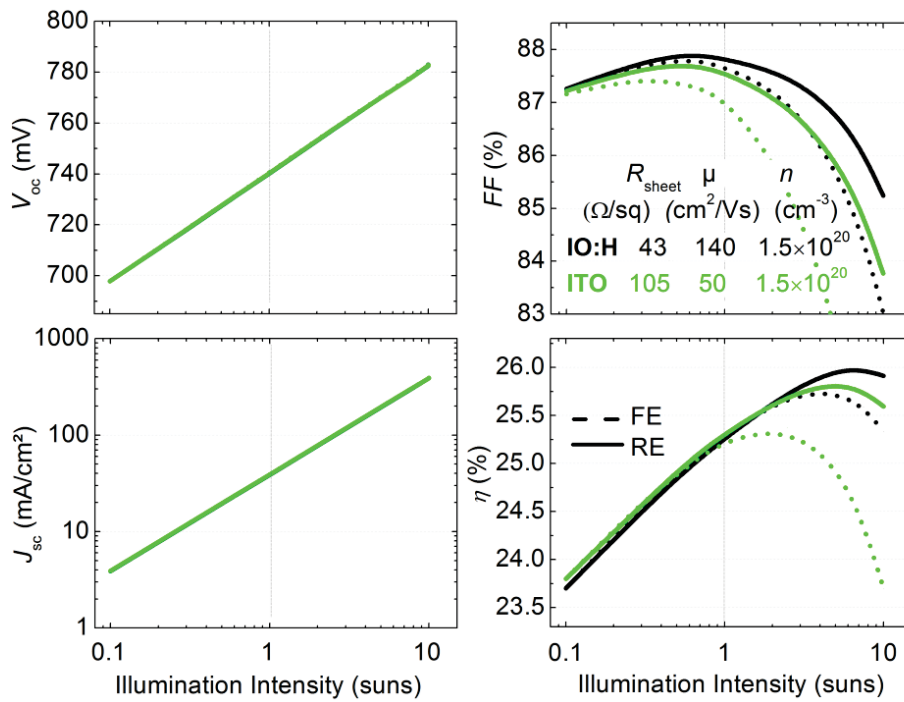


Figure 7.9: Cell output parameters as a function of the illumination intensity. The pitch is 2 mm for both the IO:H(black) and the lightly doped ITO (green). A lumped series resistance is not considered. Optical and electrical data for IO:H adapted from [97].

The V_{oc} and J_{sc} in Figure 7.9 show the expected behavior, i.e. a logarithmic and linear increase with the illumination intensity [266], [267], respectively. The FF first increases with illumination and then tails off rapidly. This behavior is dominated by the 2D carrier collection, i.e. its contribution to the series resistance. With increasing illumination the current density and thus the contribution of the series resistance to the FF loss increases. More precisely, the power losses linked to the series resistance are proportional to the square of the J_{sc} . It follows that the efficiency is determined by the increased of J_{sc} and V_{oc} which is competing with a reduction of the FF . The more efficient 2D transport of the RE design leads to higher FF 's even for illumination intensities below 1 sun. Hence, a reduced low light performance is not expected for the RE cell. The additional lateral transport path of the RE cell is beneficial especially at high illumination intensities and lowers the dependence on R_{sheet} . The most interesting feature in Figure 7.9 is that the RE cell with ITO shows an efficiency characteristic which is comparable to the one for the high mobility IO:H having a much lower R_{sheet} .

It should be noted that SHJ devices fulfill some important prerequisites which makes them appealing candidate for low concentration photovoltaic (LCPV) and thus to bringing down the cost of PV [268], [269], i.e. the high 1-sun efficiencies, the superior temperature coefficient, promising approaches to reduce the series resistance contribution from the metal electrode (Cu

plating, multi-busbar design), the 1D carrier transport at the rear and the efficient conductivity modulation.

On the basis of this simulations, it can be concluded that for operation in the field, i.e. for illumination intensities below 1 sun no negative influence on the energy yield is expected for the RE design as compared to the conventional FE design. For low concentration photovoltaic (LCPV) on the other hand, the RE design brings the clear advantage of cutting down the contribution of the 2D carrier transport to the FF loss which strongly increase with illumination and current density.

Less restrictions on the TCO mobility: IO:H, ITO and AZO

In this paragraph three different front side TCOs featuring different motilities are investigated regarding their ability to balance the optical and electrical losses at the front side. In Figure 7.10 the simulated cell output parameters as a function of the pitch of the grid electrode for a high, two medium and a low μ TCO are compared.

In general, the V_{oc} is hardly affected and the J_{sc} increases by about 2 mA/cm^2 with increasing pitch. The FF is defined by the R_{sheet} of the TCO and whether a RE or FE design is applied. For a high μ TCO (IO:H, black) excellent optical and electrical properties can be combined [97]. The high μ allows for a low free carrier density without compromising on R_{sheet} . Thus, a high J_{sc} is maintained and the very low R_{sheet} of $43 \text{ } \Omega/\text{sq}$ allows for an efficient 2D transport even for a FE device. The highest FF is reached with this TCO and the drop of the FF with increasing pitch is lower as compared to the other TCOs which are featuring a higher R_{sheet} . For such a low R_{sheet} the gain in efficiency is negligible for the RE design for one sun applications. However, a wider maximum of the efficiency is observed as for a higher pitch the transport via the absorber becomes more efficient assisting the lateral carrier collection at the front. It is shown experimentally in Ref [239] that the application of the RE design can be beneficial even for a high μ TCO (IWO, $\mu > 80 \text{ cm}^2/\text{Vs}$ [270]).

In general, the optimum R_{sheet} of a TCO will be shifted to higher values with decreasing mobility. To maintaining a certain conductivity, a lower mobility cannot be compensated by the corresponding increase of the free carrier density without generating significant optical losses [119]. Hence, it is clear that the RE design will be more beneficial for such low μ TCOs as it tolerates a higher R_{sheet} . For the medium μ TCOs (ITO, green and blue) and the low μ TCO (AZO, red) a significant increase in FF and efficiency is observed for the application of the RE design. It

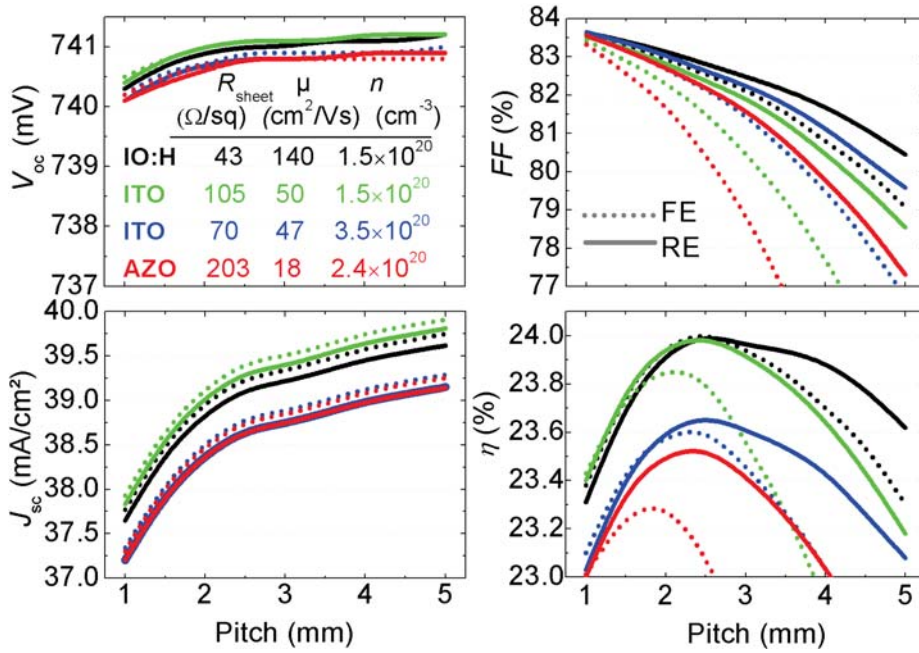


Figure 7.10: Simulated cell output parameters as a function of the pitch for FE and RE devices and three different front side TCOs. Optical and electrical data for ITO and AZO are from in-house layers and for IO:H adapted from [97].

is noteworthy that for the lowly doped ITO (green) the efficiency can be improved to the level of the high μ TCO despite its much lower mobility. For the indium free AZO the efficiency is increased by about 0.25% absolute and as the maximum is shifted to higher pitches the reduced amount of fingers will also lower the metal consumption.

To sum up, just like for the application of a high mobility TCO, the RE design lowers the constraints on the TCO and the grid electrode to balance the optical and electrical losses. This should be of economic importance as it facilitates the application of indium free front side TCOs with lower motilities. The application of wider pitches and less fingers can lower the metal consumption and the related costs.

7.3 Solar cell results: Front vs. rear emitter

7.3.1 Experimental details

For the experimental verification of the additional lateral absorber conductivity and the higher FF potential of the rear emitter (RE) design, $2 \times 2 \text{ cm}^2$ monofacial solar cells featuring either the conventional FE design or a RE design with a variable pitch and two different R_{sheet} of the front side TCO were produced. We fabricated the devices on double side shiny etched, $200 \mu\text{m}$ thick, $4.3\text{-}5.8 \Omega \text{ cm}$, (100) oriented, n-type float-zone silicon wafers. The applied TCO consists of a medium- μ TCO, namely tin doped In_2O_3 (ITO), and was deposited by reactive dc magnetron sputtering from a high density $\text{In}_2\text{O}_3\text{:SnO}_2$ target featuring a 90/10 wt% ratio at a set temperature of 100°C and 2 mTorr. The TCO doping and therefore the manipulation of the electrical and optical TCO properties of the $\sim 70 \text{ nm}$ thin films was carried out via adapting the oxygen flow ratio $OC = \text{O}_2 / (\text{O}_2 + \text{Ar})$ during the sputtering process [186]. At the rear a TCO is omitted and an Ag single layer is deposited by thermal evaporation. The front side metal grid electrode (thermally evaporated Cr/Pd/Ag) features a variable pitch of 800, 1430, 2000 and $2860 \mu\text{m}$ and was structured by photolithography and lift-off technique. To prevent additional FF losses introduced by an increasing power loss in the fingers in the case of a higher pitch and the decreasing amount of fingers, the metallization fraction and hence the total cross section of the fingers was kept constant for all pitches. This means that the individual finger width is not constant and is increasing with increasing pitch. The electrical TCO bulk properties were determined by R_{sheet} measurements using a four-point-probe setup for ITO layers deposited on glass and the transfer length method on solar cells, both in the dark.

7.3.2 Results

Four-point probe: Parallel / series connection of TCO and absorber

Qualitatively, the improved 2D carrier collection by the RE cells design is easily explained by the results from four-point probe measurements. Four-point probe measurements are a common method to determine the sheet resistance of a certain layer [252]. To ensure that the measurement probes only the lateral conductivity of the layer / stack of interest an insulating substrate is applied or a depletion region insulates the layer from the conductive substrate underneath. In the case of an SHJ structure the TCO is representing the conductive layer and the c-Si absorber the conductive substrate as it is illustrated in Figure 7.11. The Schottky contact formed between the TCO and the doped SiTF and the induced p/n or high/low junction define to

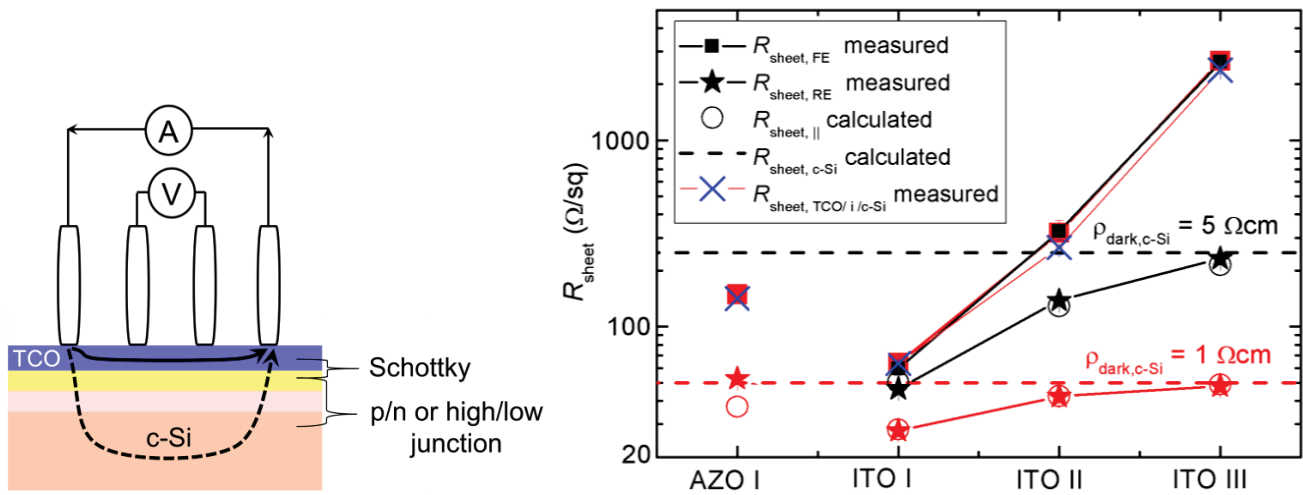


Figure 7.11: Left, schematics of the parallel connection between the TCO and the absorber and the four-point probe. Right, results from four-point probe measurements on the front side of FE and RE structure. More details in the text. Lines for the three different ITO are guide to the eye.

which extend the TCO and the absorber are electrically coupled. The induced p/n junction insulates the TCO from the absorber which means that the measured R_{sheet} corresponds to that of the TCO (FE design). For a high/low junction such an insulating depletion region is not induced into the absorber which allows for the parallel connection of the TCO and the absorber (RE design). The presence of a pronounced Schottky barrier is expected to impede the vertical transport and thus the coupling between the TCO and the absorber for such a parallel connection. Figure 7.11 shows the R_{sheet} measured at the front side of unmetallized RE ($R_{sheet, RE}$) and FE cells ($R_{sheet, FE}$) for a moderately doped AZO and a highly, moderately and very lowly doped ITO. The dashed lines are representing $R_{sheet, c-Si}$ which follows from the dark resistivity of the absorber ($\rho_{dark, c-Si}$) and its thickness (d) ($R_{sheet} = \rho/d$). The stars are representing $R_{sheet, ||} = 1/((1/R_{sheet, FE}) + (1/R_{sheet, c-Si}))$ which describes the sheet resistance expected for a parallel connection of the TCO and the absorber. The measurements for the ITO samples have been performed on n-type absorbers featuring a dark resistivity of 1 Ωcm (red symbols) and 5 Ωcm (black symbols), for AZO on 1 Ωcm material only. The blue crosses correspond to values where a doped a-Si:H is omitted and the Schottky barrier between the TCO and the undoped a-Si:H as well as the corresponding induced junction define the coupling to the absorber.

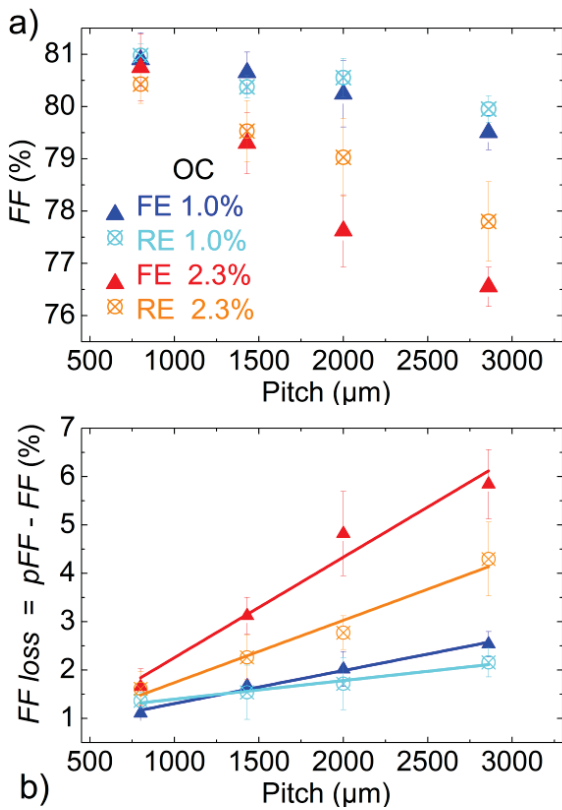
Looking at the three ITOs the measured values can be well described by the parallel and series connection of the RE and FE, respectively. $R_{sheet, FE}$ is increasing as it is expected from the selected deposition parameters of the TCO and is in good agreement with the values measured on glass

(not shown). In addition, $R_{\text{sheet,FE}}$ is independent of the absorber dark resistivity. Both facts show that for this configuration the measured R_{sheet} is representing the lateral conductivity of the TCO only. For the RE structures the measured R_{sheet} follows the behavior expected from a parallel connection. $R_{\text{sheet,RE}}$ is approaching $R_{\text{sheet,c-Si}}$ with increasing resistivity of the TCO (which is $R_{\text{sheet,FE}}$) and for the ITO samples the calculated $R_{\text{sheet||}}$ matches the measured $R_{\text{sheet,RE}}$ very well. For AZO the measured R_{sheet} for the RE configuration is above the expected value. This is most likely explained by the Schottky contact which is more pronounced for AZO than for the ITO samples preventing an efficient vertical transport in the absorber. For the samples where a doped a-Si:H is omitted the characteristics follows that of the FE. This is explained by the effective work function of the TCOs which are expected to be close to midgap of the c-Si absorber [171]. The corresponding Schottky barrier penetrates into the absorber resulting in a depleted or even slightly inverted absorber region which is blocking the current from the TCO into the absorber similar to the induced p/n junction of the FE. It also should be noted that the observed experimental behavior for the induced junction is similar to the measurement of R_{sheet} of diffused or implanted p/n and high/low homojunctions [260].

Regarding the results above it should be considered that similar to J-V dark measurements applied to extract the series resistance of solar cells the current flow in the device under operation and under illumination is in the opposed direction and that the current paths are different as well [258]. However, the results illustrate that for having a high/low junction underneath the TCO an additional transport via the absorber facilitates the lateral carrier transport. This means that for MPP conditions the voltage drop caused by the lateral transport is lower which reduces the ohmic and non-generation losses at the front side. The interplay between the TCO conductivity and the pitch under operation conditions are investigated in the following for finished solar cells.

Fill factor of solar cells

Figure 7.12 collects the measured FF in dependence of the pitch of the front side metal grid electrode for FE and RE cells featuring either a highly conductive ITO ($OC = 1\%$) or lowly conductive ITO ($OC = 2.3\%$) at the front. For the interpretation of the series resistance related FF loss (ohmic and non-generation losses) we plot the difference between the FF determined by $J-V$ measurements and the pFF determined by Suns- V_{oc} measurements. The fact that in the case of the narrowest pitch of $800 \mu\text{m}$ a comparable FF loss of only $\sim 1.5\%$ is observed for the four



	OC (%)	$R_{sheet, glass}$ (Ω/sq)	$R_{sheet, TLM}$ (Ω/sq)	$pFF-FF$ (%)	FF loss (%/mm)
FE	1.0	70	77	2.0	0.7
RE			51	1.7	0.4
FE	2.3	340	495	4.8	2.1
RE			152	2.8	1.3

Figure 7.12: (a) Measured FF dependence on the pitch for FE and RE devices featuring a front ITO with 1.0% and 2.3% OC, respectively.

(b) The corresponding FF reduction in respect to the pFF and a linear fit to the data.

(c) R_{sheet} measured on glass and cell level for the two ITOs, the corresponding series resistance and non-generation loss related FF loss for a pitch of 2000 μm and the slope of the linear fit for the pFF-FF data from b).

different configurations (Table) indicates that we managed to obtain comparable (and good) contact properties for the front side Cr / ITO and ITO / doped a-Si:H contacts and the doped a-Si:H / Ag contact at the rear, regardless of the a-Si:H doping type and the ITO doping. A series resistance of about 0.3 Ωcm^2 can be derived from this FF loss [271]. For all four configurations, average FFs of above 80% are reached. Looking at the evolution of the FF loss with increasing pitch it can clearly be seen that the RE devices are outperforming their FE counterparts. This effect is more pronounced for the less conductive front side TCO (OC = 2.3%). However, as can be seen in the Table, even for the highly conductive ITO, a gain in FF of 0.3 %_{abs} is observed for a pitch of 2000 μm . For the less conductive front side TCO, the gain amounts to 2.0 %_{abs}, thereby clearly demonstrating the additional lateral current path of RE devices. This behavior is reflecting the findings from above of the parallel connection between the TCO and the absorber for the RE design. Accordingly, the RE design can improve the FF by lowering the 2D transport related losses. This however is only true if the 2D transport is limiting the FF of the corresponding FE design. Thus, for a very low R_{sheet} and/or a small pitch the lateral transport is not further improved by the RE design.

For a further quantification of the 2D carrier transport related losses, the slope of the linear fit of the ohmic and non-generation related FF losses from the lower graph in Figure 7.12 is shown

in the Table in Figure 7.12. Again, it can be seen that for both front side TCO conductivities, the FF loss associated with the lateral carrier collection is less pronounced for RE devices, as indicated by the much smaller slope. Another indication for the existence of an additional lateral current path can be drawn from the comparison of the R_{sheet} measured on glass ($R_{\text{sheet, glass}}$) and on cell level ($R_{\text{sheet, TLM}}$) in the Table in Figure 7.12. It can be seen that $R_{\text{sheet, TLM}}$ of the RE devices is significantly lower compared to $R_{\text{sheet, TLM}}$ of the FE devices for a given $R_{\text{sheet, glass}}$. This difference is higher for the lowly doped ITO (OC = 2.3%). As explained in the previous section this stems from the fact that for the $R_{\text{sheet, glass}}$ and $R_{\text{sheet, TLM}}$ samples of the FE devices the injected current during measurements is confined within the TCO as (i) an insulating glass substrate was used or (ii) the blocking p/n junction prevents the parallel connection with the absorber. For the RE devices on the other hand, the current can pass the high/low junction forming an additional lateral current path via the absorber. Consequently, a lower effective R_{sheet} is measured for the RE devices. For the dark resistivity of $5 \Omega \text{ cm}$ and the thickness of $200 \mu\text{m}$ lead to an absorber sheet resistance of R_{absorber} of $250 \Omega/\text{sq}$. The calculated $R_{\text{sheet} \parallel}$ then amounts to 55 and $144 \Omega/\text{sq}$ for the highly and lowly doped ITO, respectively. This values are in accordance to the $R_{\text{sheet, TLM}}$ of 51 and $152 \Omega/\text{sq}$ measured at the corresponding RE devices.

Concerning future work, experiments on textured cells are required to investigate the shift of the lateral transport from the front side TCO into the absorber at non-planar surfaces. Furthermore, the potential advantages of the RE design featuring other TCO materials, including high- μ and low- μ TCOs have to be investigated. Additionally, the potential advantages in terms of 1D effects of having the n-type SHJ instead of the p-SHJ at the illuminated front needs to be analyzed. This configuration should offer additional advantages as the optimization of the front SHJ [119] might be less challenging as one can benefit from intrinsic superior material properties of the n-SiTFs in its amorphous and crystalline phase, i.e. excellent surface passivation, higher doping efficiency and lower parasitic absorption [272]. Additionally, contact formation to the n-type TCOs might be less challenging when the n-type SHJ is situated at the front side. As the optimization of the p-type SHJ is not dictated by the parasitic absorption within the SiTFs anymore [119] optimization of the p-type SHJ can be focused on carrier recombination, carrier transport and the contact formation to the TCO.

7.4 Chapter Summary

In this chapter a novel approach was presented which facilitates balancing the contradictory requirements on excess carrier generation and the lateral transport at the front side of monofacial SHJ cells. A detailed comparison between the classical both-side contacted SHJ cell design, i.e. an n-type absorber having the emitter located the front side (front emitter) and cells having the emitter at the rear side (rear emitter) was carried out.

The influence of the optical and electrical properties of the front side TCO and the pitch of the front side metal grid electrode on the performance of SHJ cells was investigated in detail by two-dimensional numerical device simulations for ITO, IO:H and AZO as front side TCO. By simply flipping the p/n junction of SHJ cells from the front to the rear fewer restrictions for the choice of the front side TCO and the design of the front side metal grid electrode are observed. With the high/low junction at the front the power losses caused by the 2D carrier transport can be reduced as the lateral conductivity of the absorber is utilized opening up an additional transport path. The trade-off between optical and electrical bulk properties of the front side TCO is less pronounced which translates into lower demands either on the pitch, the TCO mobility or free carrier density. A reduced free carrier density or an increased pitch allow for a higher J_{SC} without compromising on the FF (or vice versa) and thus can result in an increased efficiency. In contrast the use of indium free TCOs with a lower mobility is expected to be of economic interest. Furthermore, it is shown by simulations that for high efficiency devices higher requirements on the absorber quality in terms of defect recombination and doping levels are not expected for the RE design. With respect to the absorber doping level, a similar low-light performance and an improved performance for operation under moderate concentration were also shown. The existence and relevance of the additional lateral transport path via the absorber was experimentally proven for ITO as front side TCO.

Further experimental investigations are required to fully evaluate the advantages of the SHJ rear emitter cell design over the conventional front emitter design including investigations of low mobility indium free TCOs and the potential of the RE design to lower the 1D losses of SHJ cells. The cell architecture developed in this chapter is the basis for the efficiency of 22.8% on hybrid cells achieved in this thesis (see chapter 6.3.4).

8 Summary and Outlook

8.1 Summary

Recombination at the unpassivated metal / semiconductor contact is the decisive disadvantage of homojunction solar cells. Sophisticated device designs are needed for loss mitigation and are essential for high efficiencies. A more elegant strategy is the application of passivating and carrier selective contacts. They combine a passivating buffer layer and a suitable contact layer on top in one layer system. The buffer passivates the surface of the c-Si surface and thus enables a high density of excess holes and electrons. The selective extraction of these excess holes and electron from the absorber into the respective external device terminals is the fundamental function of the contact layers. The most prominent example for a very efficient passivated contact system is the a-Si:H / c-Si silicon heterojunction which shares many similarities with the induced junctions based on the Semiconductor-Insulator-Semiconductor (SIS) and Metal-Insulator-Semiconductor (MIS) systems. It consists of an a-Si:H(i) layer as the passivating buffer layer and a doped a-Si:H layer which is capped with an TCO as the contact layers. However, even this system has not yet reached the scientific and technological maturity as standard diffused homojunction cells. The lack of knowledge regarding important operation principles and adequate characterization approaches triggered this work. Besides a thorough understanding, several aspects of device optimization and characterization were addressed experimentally and via simulation with *AFORS-HET* and *Sentaurus Device*. Suitable characterization approaches, novel contact materials and novel cell designs were successfully established.

Simulations revealed that as a unique feature, **non-optimized contact schemes** may provide sufficient c-Si surface passivation and hence a high implied voltage, but fail to maintain this voltage in the contact region. For such conditions the **external terminal voltage is significantly lower than the internal voltage** in the absorber (For simplicity this effect is called non-ideal voltage “extraction”). This highlighted the need for adequate characterization and optimization taking non-classical losses into account which are not predicted by the standard p/n-junction theory (only minority carrier recombination and ohmic losses). Such a non-ideal voltage extraction is observed if low-injection conditions in the contact region are not maintained during operation. A sufficiently high **doping**, a properly **induced junction** and the avoidance of **Schottky barriers** were essential to prevent such peculiarities of the external cell characteristic resulting in FF and V_{oc} losses. Analyzing the **illumination level dependence of the V_{oc}** by *Suns-*

V_{oc} measurements was introduced in this work as an effective and easy method for the identification of such losses already in the early stage of contact optimization.

The upper limit of the internal voltage (implied voltage, iV_{oc}) imposed by the injection level dependent **c-Si passivation** by the a-Si:H buffer was investigated by a novel approach. Corona charging was used to investigate the chemical and field-effect passivation. It was highlighted that excellent surface passivation is reflected rather in a high implied fill factor (iFF) than in a high iV_{oc} . While surface passivation is in many cases sufficient high such that the iV_{oc} is already relatively close to the intrinsic limit imposed by the c-Si bulk recombination. This is not the case for the maximum-power-point (MPP) conditions and hence the iV_{MPP} for which recombination at the c-Si surface is still representing the dominant contribution. This imposes **significant FF losses compared to the intrinsic limit** of about 89% which is quantified by the fact that the pFF of our cells is hardly exceeding 83%. Hence, much higher FFs and efficiencies can be achieved if the recombination losses at the a-Si:H / c-Si is reduced considerably.

With respect to extraction of this implied voltage at the external terminals, different contact schemes were investigated. An **a-Si:H(p) doping variation** was performed as a showcase for analyzing the contact properties regarding a **non-ideal voltage extraction**. For insufficient doping such a non-ideal behavior was clearly observed. Without any doping, when the **parasitic Schottky** behavior dominates, the external V_{oc} was limited to about 400 mV resulting a voltage loss of about 300 mV in the contact region. For sufficient doping the external voltage reached the limit imposed by the iV_{oc} of about 730 mV, meaning that voltage extraction was ideal. It could be shown that a voltage loss in the contact region manifested itself by an ideality factor of the $Suns-V_{oc}$ curve which drops below the one predicted by the standard p/n junction theory. A clear correlation between this slope and the corresponding FF and V_{oc} losses was observed. Another indicator for non-ideal voltage extraction was the temperature dependence of the FF and the V_{oc} . With respect to the FF, in the ideal case the temperature dependence was dominated by the pFF showing a linear reduction with increasing temperature caused by the increase of recombination. For insufficient doping, unsuited work functions or other parameters hampering the excess carrier extraction the slope of this linear FF reduction was reduced and for poor contacts even a non-linear behavior was observed. This was explained by the fact that thermally active transport path resulted in a reduction of the transport related fill factor losses while these are rather temperature-independent in the ideal case.

Beyond doped amorphous silicon, several contact materials like metals, different TCO films and materials adopted from organic electronics were investigated in detail. **Pure metal films** were not suited to form carrier selective contacts. Besides a pronounced Fermi-level pinning, more fundamental limitations resulted from the deterioration of the chemical c-Si passivation already at moderate annealing temperatures, poor adhesion and poor optical properties in terms of rear side reflection. However, Ag was used to replace the ITO electrode at the rear a-Si:H(p) emitter of **hybrid SHJ cells**, a concept which was established in the course of this thesis. An **efficiency of 22.8 %** ($V_{oc} = 705$ mV, $J_{sc} 39.9$ mA/cm², FF 81.2%) could be achieved with this approach.

A **doping variation of ITO films** on test structures showed that the work function at the a-Si:H(i) / TCO interface could be changed in the desired manner. The work function was increased for lower doping which was expected to be beneficial / detrimental for the hole / electron contact of the standard SHJ featuring doped a-Si:H in contact to ITO. However, this was not reflected by the solar cell results as a similar influence for the hole and electron contact was observed. This was pointing out that aspects other than work function matching need to be taken into account with respect junction engineering.

Regarding, the **materials adopted from organic electronics** (caesium carbonate, lithium fluoride, PEDOT:PSS, titanium dioxide, ITO, molybdenum oxide and tungsten oxide), no material was found so far which was capable of forming an electron selective contact. However, promising results were obtained for the hole selective contact on test structures with PEDOT:PSS, molybdenum oxide (MoO_x) and tungsten oxide (WO_x) as the external V_{oc} was about 700 mV. Surface photo voltage measurements revealed the **high work function of MoO_x and WO_x** and the p/n-junction induced in the absorber. More detailed investigations for both high work function metal oxides proved their general applicability to either form a direct hole contact, by replacing the p-type a-Si:H, or to assist the hole collection for the standard silicon heterojunction, if sandwiched between the a-Si:H(p) and ITO or AZO. With MoO_x the **efficiency** of planar test solar cells, before annealing, could be **significantly improved compared to the reference** (~18.7 % vs. ~17.6 %) as both optical and electric properties were improved when the a-Si:H(p) was replaced. For WO_x as an additional contact layer, presumably by an **improved work function matching**, the parasitic Schottky contact between ITO and a-Si:H(p) of the standard SHJ structure could be improved. This was quantified by a significant FF gain compared to the reference (~81.1 % vs. ~79.6 %). Finally, for an **a-Si:H less hole contact**, with WO_x direct on c-Si an **efficiency comparable to the reference** was observed (~17.6 % vs. ~17.5 %). This simple

structure might be an appealing approach to replace the Al-BSF of the standard homojunction cell. With these very encouraging results it could be demonstrated that novel contact material adopted from other fields of electronic devices are interesting candidates for future silicon solar devices.

Finally, the **ohmic and non-generation losses caused by the lateral transport at the front side** of the standard SHJ were addressed. A simple yet successful approach to facilitate this optimization problem based on utilizing the lateral conductivity of the absorber by **flipping the p/n junction from the front to the rear** was presented. Lower constraints on the TCO and grid electrode to provide the lateral transport were presented which makes the design trade-off between optical and electrical properties less pronounced. This **“rear emitter” design** has already been adopted by different companies and institutes and has proven to be beneficial in terms of efficiency. This makes it very likely to become the standard cell design, i.e. to replace the “front emitter” design.

The investigation performed in this thesis led to a better understanding of the fundamental loss mechanisms in heterojunction solar cells. With this improved understanding it was possible to increase the efficiency of heterojunction solar cells up to 22.8% at Fraunhofer ISE, to introduce suitable characterization approaches and new contact materials which are promising candidates for a new generation of carrier-selective contacts for silicon wafer based solar cells.

8.2 Outlook

Regarding future work, a more comprehensive understanding is needed which also means that more heterojunction specific effects have to be taken into account. Examples are the hetero-barriers in the conduction and valence band, additional transport path, e.g. multi-step tunneling into the band gap states of the adjacent materials, interface dipoles and the non-metal-like behavior of lowly doped materials (e.g. the depletion of metal oxides). Accordingly, each layer should be described by its actual properties and should not be approximated, e.g. by a metal which reduces the actual contact layer properties solely to its work function. This means a simulation setup is needed which for example describes the ITO/MoO_x/buffer/c-Si contact by a structure which consists of two wide gap n-type semiconductors, the buffer, and the absorber. In general, it is of great importance to characterize the actual microscopic contact and material properties on device relevant structures and their modification during subsequent processing. Combined with adequate device simulations this should allow for a more holistic understanding of such rather novel contact schemes thereby providing guidelines for an efficient junction engineering.

Alternative buffer layers need to be investigated to test their influence on the selectivity and to overcome the moderate temperature stability of the a-Si:H buffer. The search for alternative contact materials needs to be extended to other materials used for e.g. organic electronics [224]. This includes other high and low work function metal oxides [222] and dipole layers [273]. The latter have proven to modify the effective interface work function for organic semiconductors and it is interesting to check to which extent such or other intentionally implemented dipoles can be used to modify the interface of the inorganic semiconductors or dielectric buffer layers used here.

The applicability of such novel contact materials to the so called tunneling oxide passivated contact scheme (TOPCon) [274] or related poly silicon based contacts should be investigated. This applies in particular to the hole-selective and p-type contact which suffers from inferior surface passivation compared to its n-type counterpart. The application of such materials might lower the demands on the applicable doping which in turn might lower the doping induced defect recombination of minority carriers.

Another important aspect is to check if such contact materials deposited by soft deposition techniques (e.g. thermal evaporation, ALD) allow to shield the sputter damage caused by the subsequent ITO deposition from the buffer / absorber interface which adversely affects the

minority carrier recombination. An elegant approach for the rear side would be to replace the ITO/metal back reflector by a thick metal oxide/metal stack. Another aspect that needs to be looked at is the temperature stability of such materials and their compatibility with the subsequent process. This applies for the “low temperature” approach followed in this thesis and the “high temperature” steps used for homojunction, TOPCon and poly Si based contact systems.

Regarding minority carrier recombination more attention must be paid to the limitation of the FF by the latter. Much potential to increase the efficiency lies in increasing the pseudo FF which calls for a more profound understanding of the chemical and field-effect passivation by the contact scheme and its modification by the different process steps.

The benefits of the rear emitter structure should be investigated for the TOPCon and related structure as well. Besides the improved lateral carrier transport this should allow for more degrees of freedom for the optimization of the unilluminated p-type contact which optimization is typically more challenging compare to the n-type contact. Hence, optimization can be focused on the electrical rather than optical contact properties.

9 References

- [1] A. Goodrich, P. Hacke, Q. Wang, B. Sopori, R. Margolis, T. L. James, and M. Woodhouse, "A wafer-based monocrystalline silicon photovoltaics road map: Utilizing known technology improvement opportunities for further reductions in manufacturing costs", *Sol Energ Mat Sol C*, vol. 114, p. 110-135, 2013.
- [2] D. M. Powell, M. T. Winkler, H. J. Choi, C. B. Simmons, D. B. Needleman, and T. Buonassisi, "Crystalline silicon photovoltaics: a cost analysis framework for determining technology pathways to reach baseload electricity costs", *Energy & Environmental Science*, vol. 5, p. 5874-5883, 2012.
- [3] S. De Wolf, A. Descoedres, Z. C. Holman, and C. Ballif, "High-efficiency Silicon Heterojunction Solar Cells: A Review", *green*, vol. 2, p. 7-24, 2012.
- [4] M. Taguchi, A. Yano, S. Tohoda, K. Matsuyama, Y. Nakamura, T. Nishiwaki, K. Fujita, and E. Maruyama, "24.7% Record Efficiency HIT Solar Cell on Thin Silicon Wafer", *Photovoltaics, IEEE Journal of*, p. 1-4, 2013.
- [5] D. A. J.L. Hernández, D. Schroos, N. Valckx, N. Menou, T. Uto, M. Hino, M. Kanematsu, H. Kawasaki, R. Mishima, K. Nakano, H. Uzu, T. Terashita, K. Yoshikawa, T. Kuchiyama, M. Hiraishi, N. Nakanishi, M. Yoshimi, K. Yamamoto "High Efficiency Copper Electroplated Heterojunction Solar Cells and Modules – The Path towards 25% Cell Efficiency," in *28th EU PVSEC*. Paris, 2013.
- [6] A. Richter, M. Hermle, and S. W. Glunz, "Reassessment of the Limiting Efficiency for Crystalline Silicon Solar Cells", *Photovoltaics, IEEE Journal of*, vol. 3, p. 1184-1191, 2013.
- [7] F. Feldmann, M. Bivour, C. Reichel, H. Steinkemper, M. Hermle, and S. W. Glunz, "Tunnel oxide passivated contacts as an alternative to partial rear contacts", *Sol Energ Mat Sol C*, vol. 131, p. 46-50, 2014.
- [8] U. Römer, R. Peibst, T. Ohrdes, B. Lim, J. Krügener, E. Bugiel, T. Wietler, and R. Brendel, "Recombination behavior and contact resistance of n+ and p+ poly-crystalline Si/monocrystalline Si junctions", *Sol Energ Mat Sol C*, 2014.
- [9] P. Würfel, *Physics of Solar Cells - From principles to new concepts*. Weinheim: Wiley-Vch Verlag GmbH & Co KgaA, 2005.
- [10] M. A. Green, *Solar cells: operating principles, technology and system applications*. Kensington: The University of New South Wales, 1998.

- [11] R. M. Swanson and R. A. Sinton, "High-efficiency silicon solar cells," in *Advances in solar energy*, vol. 6, K. W. Böer, Ed. New York: Plenum Press, 1990, p. 427-84.
- [12] A. Goetzberger, J. Knobloch, and B. Voss, *Crystalline silicon solar cells*. Chichester, UK: John Wiley & Sons Ltd, 1998.
- [13] C. Honsberg and S. Bowden, "PV EDUCATION, <http://pveducation.org/pvcdrom>."
- [14] A. L. Fahrenbruch and R. H. Bube, *Fundamentals of solar cells*. New York: Academic Press, 1983.
- [15] W. G. J. H. M. van Sark, L. Korte, and F. Roca, *Physics and technology of amorphous-crystalline heterostructure silicon solar cells*: Springer Verlag, Heidelberg, Germany, 2012.
- [16] Y. Kwark, "SIPOS heterojunction contacts to silicon," Ph.D. thesis, Stanford Univ., 1985.
- [17] M. W. M. van Cleef, "Amorphous-crystalline silicon heterostructures and solar cells," Utrecht University, 1998.
- [18] L. Korte, "Die elektronische Struktur des amorph-kristallinen Silizium-Heterostruktur-Kontakts," *PhDT*, Philipps-Universität Marburg, 2006.
- [19] S. Olibet, "Properties of interfaces in amorphous / crystalline silicon heterojunctions," *Dissertation*, Université de Neuchâtel, 2009.
- [20] T. F. Schulze, "Structural, electronic and transport properties of amorphous/crystalline silicon heterojunctions," Universitätsbibliothek, 2011.
- [21] C. Leendertz, "Effizienzlimitierende Rekombinationsprozesse in amorph/kristallinen und polykristallinen Siliziumsolarzellen," Universitätsbibliothek, 2011.
- [22] D. Pysch, "ASSEMBLY AND ANALYSIS OF ALTERNATIVE EMITTER SYSTEMS FOR HIGH EFFICIENT SILICON SOLAR CELLS," 2011.
- [23] R. Varache, "Development, characterization and modeling of interfaces for high efficiency silicon heterojunction solar cells. ," 2012.
- [24] S. M. De Nicolas, "a-Si: H/c-Si heterojunction solar cells: back side assessment and improvement," Université Paris Sud-Paris XI, 2012.
- [25] B. Demareux, "Passivating contacts for homojunction solar cells using a-Si: H/c-Si hetero-interfaces," ÉCOLE POLYTECHNIQUE FÉDÉRALE DE LAUSANNE, 2014.
- [26] S. M. Sze, *Physics of semiconductor devices*, 2nd ed. New York: John Wiley & Sons, Inc., 1981.
- [27] A. Richter, *PhD*, 2013.

- [28] A. Richter, S. W. Glunz, F. Werner, J. Schmidt, and A. Cuevas, "Improved quantitative description of Auger recombination in crystalline silicon", *Physical Review B*, vol. 86, p. 165202, 2012.
- [29] W. Shockley and W. T. J. Read, "Statistics of the recombinations of holes and electrons", *Physical Review*, vol. 87, p. 835-42, 1952.
- [30] R. N. Hall, "Electron-hole recombination in germanium", *Physical Review*, vol. 87, p. 387, 1952.
- [31] W. D. Eades and R. M. Swanson, "Calculation of surface generation and recombination velocities at the Si-SiO₂ interface", *J. Appl. Phys.*, vol. 58, p. 4267-76, 1985.
- [32] R. B. M. Girisch, R. P. Mertens, and R. F. De Keersmaecker, "Determination of Si-SiO₂ interface recombination parameters using a gate-controlled point-junction diode under illumination", *IEEE Trans. Electron Devices*, vol. 35, p. 203-22, 1988.
- [33] A. G. Aberle, S. Glunz, and W. Warta, "Impact of illumination level and oxide parameters on Shockley-Read-Hall recombination at the Si-SiO₂ interface", *Journal of Applied Physics*, vol. 71, p. 4422-31, 1992.
- [34] S. Steingrube, D. S. Steingrube, R. Brendel, and P. P. Altermatt, "Comprehensive model for interface recombination at a-Si:H/c-Si interfaces based on amphoteric defects", *physica status solidi (c)*, vol. 7, p. 276-279, 2010.
- [35] W. Ruppel and P. Würfel, "Upper limit for the conversion of solar energy", *Electron Devices, IEEE Transactions on*, vol. 27, p. 877-882, 1980.
- [36] J. Greulich, H. Höffler, U. Würfel, and S. Rein, "Numerical power balance and free energy loss analysis for solar cells including optical, thermodynamic, and electrical aspects", *Journal of Applied Physics*, vol. 114, p. -, 2013.
- [37] S. M. Sze, *Semiconductor devices, Physics and Technology.*, 2nd ed. New York, NY, USA: John Wiley & Sons Inc., 2002.
- [38] B. Fischer, "Loss analysis of crystalline silicon solar cells using photoconductance and quantum efficiency measurements," *Dissertation*, Universität Konstanz, 2003.
- [39] U. Würfel, A. Cuevas, and P. Würfel, "Charge Carrier Separation in Solar Cells", *Photovoltaics, IEEE Journal of*, vol. PP, p. 1-9, 2014.
- [40] W. Shockley, "The theory of p-n junctions in semiconductors and p-n junction transistors", *Bell System Tech. J.*, vol. 28, p. 435-489, 1949.

- [41] R. L. Y. Sah, R. N. Noyce, and W. Shockley, "Carrier Generation and Recombination in P-N Junctions and P-N Junction Characteristics", *Proceedings of the IRE*, vol. 45, p. 1228-1243, 1957.
- [42] F. A. Lindholm, J. G. Fossum, and E. L. Burgess, "Application of the superposition principle to solar-cell analysis", *Electron Devices, IEEE Transactions on*, vol. 26, p. 165-171, 1979.
- [43] S. J. Robinson, A. G. Aberle, and M. A. Green, "Departures from the principle of superposition in silicon solar cells", *Journal of Applied Physics*, vol. 76, p. 7920-7930, 1994.
- [44] K. R. McIntosh, "Lumps, humps and bumps: Three detrimental effects in the current-voltage curve of silicon solar cells," *Dissertation*, University of New South Wales, 2001.
- [45] F. Feldmann, 2015.
- [46] R. Singh, M. A. Green, and K. Rajkanan, "Review of conductor-insulator-semiconductor (CIS) solar cells", *Solar Cells*, vol. 3, p. 95-148, 1981.
- [47] W. Shockley, US Patent 2 569 347, 1951.
- [48] H. Kroemer, "Theory of a Wide-Gap Emitter for Transistors", *Proceedings of the IRE*, vol. 45, p. 1535-1537, 1957.
- [49] H. Kroemer, "Heterostructure bipolar transistors and integrated circuits", *Proceedings of the IEEE*, vol. 70, p. 13-25, 1982.
- [50] E. Yablonovitch, T. Gmitter, R. M. Swanson, and Y. H. Kwark, "A 720 mV open circuit voltage SiO_x:c-Si:SiO_x double heterostructure solar cell", *Applied Physics Letters*, vol. 47, p. 1211-1213, 1985.
- [51] T. Matsushita, N. Oh-uchi, H. Hayashi, and H. Yamoto, "A silicon heterojunction transistor", *Applied Physics Letters*, vol. 35, p. 549-550, 1979.
- [52] F. Feldmann, M. Bivour, C. Reichel, M. Hermle, and S. W. Glunz, "Passivated rear contacts for high-efficiency n-type Si solar cells providing high interface passivation quality and excellent transport characteristics", *Sol Energ Mat Sol C*, 2013.
- [53] T. D. R. Brendel, R. Gogolin, H. Hannebauer, N.-P. Harder, J. Hensen, S. Kajari-Schröder, R. Peibst, J.H. Petermann, U. Römer, J. Schmidt, H. Schulte-Huxel, V. Steckenreiter "Recent Progress and Options for Future Crystalline Silicon Solar Cells", in *28th European Photovoltaic Solar Energy Conference and Exhibition*, Paris, 2013.
- [54] I. R. C. Post, P. Ashburn, and G. R. Wolstenholme, "Polysilicon emitters for bipolar transistors: a review and re-evaluation of theory and experiment", *IEEE Transactions on Electron Devices*, vol. 39, p. 1717-31, 1992.

- [55] N. G. Tarr, "A polysilicon emitter solar cell", *IEEE Electron Device Letters*, vol. 6, p. 655-8, 1985.
- [56] F. A. Lindholm, A. Neugroschel, M. Arienzo, and P. A. Iles, "Heavily doped polysilicon-contact solar cells", *IEEE Electron Device Letters*, vol. 6, p. 363-5, 1985.
- [57] J.-Y. Gan and R. Swanson, "Polysilicon emitters for silicon concentrator solar cells", in *Photovoltaic Specialists Conference, 1990., Conference Record of the Twenty First IEEE*, 1990.
- [58] M. Green, F. King, and J. Shewchun, "Minority carrier MIS tunnel diodes and their application to electron-and photo-voltaic energy conversion—I. Theory", *Solid-State Electronics*, vol. 17, p. 551-561, 1974.
- [59] J. Shewchun, M. Green, and F. King, "Minority carrier MIS tunnel diodes and their application to electron-and photo-voltaic energy conversion—II. Experiment", *Solid-State Electronics*, vol. 17, p. 563-572, 1974.
- [60] J. Shewchun, D. Burk, and M. B. Spitzer, "MIS and SIS solar cells", *Electron Devices, IEEE Transactions on*, vol. 27, p. 705-716, 1980.
- [61] M. A. Green and J. Shewchun, "Minority carrier effects upon the small signal and steady-state properties of Schottky diodes", *Solid-State Electronics*, vol. 16, p. 1141-1150, 1973.
- [62] R. B. Godfrey and M. A. Green, "655 mV open-circuit voltage, 17.6% efficient silicon MIS solar cells", *Applied Physics Letters*, vol. 34, p. 790-793, 1979.
- [63] A. W. Blakers, M. A. Green, S. Jiquan, E. M. Keller, S. R. Wenham, R. B. Godfrey, T. Szpitalak, and M. R. Willison, "18-percent efficient terrestrial silicon solar cells", *Electron Device Letters, IEEE*, vol. 5, p. 12-13, 1984.
- [64] J. Shewchun, R. Singh, and M. A. Green, "Theory of metal-insulator-semiconductor solar cells", *Journal of Applied Physics*, vol. 48, p. 765-70, 1977.
- [65] Y.-C. Yeo, T.-J. King, and C. Hu, "Metal-dielectric band alignment and its implications for metal gate complementary metal-oxide-semiconductor technology", *Journal of Applied Physics*, vol. 92, p. 7266, 2002.
- [66] J. Robertson, "Band offsets, Schottky barrier heights, and their effects on electronic devices", *Journal of Vacuum Science & Technology A: Vacuum, Surfaces, and Films*, vol. 31, p. 050821-050821-18, 2013.
- [67] R. T. Tung, "The physics and chemistry of the Schottky barrier height", *Applied Physics Reviews*, vol. 1, p. -, 2014.

- [68] J. F. J.-B. Heng, B. Kong, Y. Chae, W. Wang, Z. Xie, A. Reddy, K. Lam, C. Bietel, Z. Xu "Commercialization of Tunnel Oxide Junction Based Cell and Module with Efficiency and Good Reliability", in *28th European Photovoltaic Solar Energy Conference and Exhibition*, Paris, 2013.
- [69] A. W. Blakers and M. A. Green, "678mV open-circuit voltage silicon solar cells", *Applied Physics Letters*, vol. 39, p. 483-485, 1981.
- [70] J. Bullock, D. Yan, and A. Cuevas, "Passivation of aluminium-n+ silicon contacts for solar cells by ultrathin Al₂O₃ and SiO₂ dielectric layers", *physica status solidi (RRL) – Rapid Research Letters*, p. n/a-n/a, 2013.
- [71] S. Avasthi, S. Lee, Y.-L. Loo, and J. C. Sturm, "Role of Majority and Minority Carrier Barriers Silicon/Organic Hybrid Heterojunction Solar Cells", *Advanced Materials*, vol. 23, p. 5762-5766, 2011.
- [72] Y. Zhang, F. Zu, S.-T. Lee, L. Liao, N. Zhao, and B. Sun, "Heterojunction with Organic Thin Layers on Silicon for Record Efficiency Hybrid Solar Cells", *Advanced Energy Materials*, p. n/a-n/a, 2013.
- [73] J. Schmidt, V. Titova, and D. Zielke, "Organic-silicon heterojunction solar cells: Open-circuit voltage potential and stability", *Applied Physics Letters*, vol. 103, p. -, 2013.
- [74] H. Wagner, T. Ohrdes, A. Dastgheib-Shirazi, B. Puthen-Veetil, D. König, and P. P. Altermatt, "A numerical simulation study of gallium-phosphide/silicon heterojunction passivated emitter and rear solar cells", *Journal of Applied Physics*, vol. 115, p. -, 2014.
- [75] T. Sawada, N. Terada, S. Tsuge, T. Baba, T. Takahama, K. Wakisaka, S. Tsuda, and S. Nakano, "High-efficiency a-Si/c-Si heterojunction solar cell", in *Proceedings of the 1st World Conference on Photovoltaic Energy Conversion* Hawaii, USA, 1994.
- [76] M. Tanaka, M. Taguchi, T. Matsuyama, T. Sawada, S. Tsuda, S. Nakano, H. Hanafusa, and Y. Kuwano, "Development of new a-Si / c-Si heterojunction solar cells: ACJ-HIT (Artificially constructed junction-heterojunction with intrinsic thin-layer)", *Japanese Journal of Applied Physics*, vol. 31, p. 3518-22, 1992.
- [77] W. Fuhs, K. Niemann, and J. Stuke, "Heterojunctions of Amorphous Silicon and Silicon Single Crystals", *AIP Conference Proceedings*, vol. 20, p. 345-350, 1974.
- [78] M. Tanaka, M. Taguchi, T. Takahama, T. Sawada, S. Kuroda, T. Matsuyama, S. Tsuda, A. Takeoka, S. Nakano, and H. Hanafusa, "Development of a new heterojunction structure (ACJ-HIT) and its application to polycrystalline silicon solar cells", *Progress in Photovoltaics: Research and Applications*, vol. 1, p. 85-92, 1993.

- [79] M. Taguchi, K. Kawamoto, S. Tsuge, T. Baba, H. Sakata, M. Morizane, K. Uchihashi, N. Nakamura, S. Kiyama, and O. Oota, "HITTM cells—high-efficiency crystalline Si cells with novel structure", *Progress in Photovoltaics: Research and Applications*, vol. 8, p. 503-513, 2000.
- [80] M. Taguchi, A. Yano, S. Tohoda, K. Matsuyama, Y. Nakamura, T. Nishiwaki, K. Fujita, and E. Maruyama, "24.7% record efficiency HIT[®] solar cell on thin silicon wafer", in *Proceedings of the 39th IEEE Photovoltaic Specialists Conference*, Tampa, Florida, USA, 2013.
- [81] M. A. Green, K. Emery, Y. Hishikawa, W. Warta, and E. D. Dunlop, "Solar cell efficiency tables (version 41)", *Progress in Photovoltaics: Research and Applications*, vol. 21, p. 1-11, 2013.
- [82] P. J. Cousins, D. D. Smith, H.-C. Luan, J. Manning, T. D. Dennis, A. Waldhauer, K. E. Wilson, G. Harley, and W. P. Mulligan, "Generation 3: improved performance at lower cost", in *Proceedings of the 35th IEEE Photovoltaic Specialists Conference*, Honolulu, Hawaii USA, 2010.
- [83] J. Zhao, A. Wang, M. A. Green, and F. Ferrazza, "19.8% efficient "honeycomb" textured multicrystalline and 24.4% monocrystalline silicon solar cells", *Applied Physics Letters*, vol. 73, p. 1991-3, 1998.
- [84] W. P. Mulligan, D. H. Rose, M. J. Cudzinovic, D. M. De Ceuster, K. R. McIntosh, D. D. Smith, and R. M. Swanson, "Manufacture of solar cells with 21% efficiency", in *Proc. 19th EC PVSEC*, Paris, France, 2004.
- [85] J. Zhao, A. Wang, and M. A. Green, "24.5% Efficiency silicon PERT cells on MCZ substrates and 24.7% efficiency PERL cells on FZ substrates", *Progress in Photovoltaics: Research and Applications*, vol. 7, p. 471-4, 1999.
- [86] D. D. Smith, P. J. Cousins, A. Masad, *et al.*, "Generation III high efficiency lower cost technology: Transition to full scale manufacturing", in *Proceedings of the 38th IEEE Photovoltaic Specialists Conference*, Austin, Texas, 2012.
- [87] S. Olibet, E. Vallat-Sauvain, L. Fesquet, C. Monachon, A. Hessler-Wyser, J. Damon-Lacoste, S. De Wolf, and C. Ballif, "Properties of interfaces in amorphous/crystalline silicon heterojunctions", *physica status solidi (a)*, vol. 207, p. 651-656, 2010.
- [88] H. Angermann, F. Wünsch, M. Kunst, A. Laades, U. Stürzebecher, E. Conrad, L. Korte, and M. Schmidt, "Effect of wet-chemical substrate pretreatment on electronic interface properties and recombination losses of a -Si:H/c -Si and a -SiNx:H/c -Si hetero-interfaces", *physica status solidi (c)*, vol. 8, p. 879-882, 2011.

- [89] C. Leendertz, N. Mingirulli, T. F. Schulze, J. P. Kleider, B. Rech, and L. Korte, "Discerning passivation mechanisms at a-Si:H/c-Si interfaces by means of photoconductance measurements", *Applied Physics Letters*, vol. 98, p. 202108-1--202108-3, 2011.
- [90] Y. Tawada, M. Kondo, H. Okamoto, and Y. Hamakawa, "Hydrogenated amorphous silicon carbide as a window material for high efficiency a-Si solar cells", *Solar energy materials*, vol. 6, p. 299-315, 1982.
- [91] T. M. Brown, C. Bittencourt, M. Sebastiani, and F. Evangelisti, "Electronic states and band lineups in c-Si (100)/a-Si $1-x$ C_x:H heterojunctions", *Physical Review B*, vol. 55, p. 9904, 1997.
- [92] J. Temmler, "Boron Doped a-SiC:H Front Layers for Silicon Heterojunction Cells", in *28th EU PVSEC*, 2014.
- [93] A. Klein, C. Körber, A. Wachau, F. Säuberlich, Y. Gassenbauer, S. P. Harvey, D. E. Proffit, and T. O. Mason, "Transparent Conducting Oxides for Photovoltaics: Manipulation of Fermi Level, Work Function and Energy Band Alignment", *Materials*, vol. 3, p. 4892-4914, 2010.
- [94] M. Bivour, S. Schröer, and M. Hermle, "Numerical Analysis of Electrical TCO / a-Si:H(p) Contact Properties for Silicon Heterojunction Solar Cells", *Energy Procedia*, vol. 38, p. 658-669, 2013.
- [95] W. Jackson, R. Nemanich, M. Thompson, and B. Wacker, "Schottky barriers on phosphorus-doped hydrogenated amorphous silicon: The effects of tunneling", *Physical Review B*, vol. 33, p. 6936-6945, 1986.
- [96] A. Kanevce and W. K. Metzger, "The role of amorphous silicon and tunneling in heterojunction with intrinsic thin layer (HIT) solar cells", *Journal of Applied Physics*, vol. 105, p. 094507-1--094507-7, 2009.
- [97] T. Koida, H. Fujiwara, and M. Kondo, "Reduction of Optical Loss in Hydrogenated Amorphous Silicon/Crystalline Silicon Heterojunction Solar Cells by High-Mobility Hydrogen-Doped In₂O₃ Transparent Conductive Oxide", *Applied Physics Express*, vol. 1, p. 041501, 2008.
- [98] L. Barraud, Z. C. Holman, N. Badel, P. Reiss, A. Descoedres, C. Battaglia, S. De Wolf, and C. Ballif, "Hydrogen-doped indium oxide/indium tin oxide bilayers for high-efficiency silicon heterojunction solar cells", *Sol Energy Mat Sol C*, vol. 115, p. 151-156, 2013.
- [99] R. Stangl, C. Leendertz, and J. Haschke, "Numerical simulation of solar cells and solar cell characterization methods: the open-source on demand program AFORS-HET", *Solar Energy (RD Rugescu, ed.)*, INTECH, Croatia, p. 319-352, 2010.

- [100] S. Schröder, "2-Dimensionale Simulation von amorph / kristallinen Silicium-Hetero-Solarzellen " *Diploma Thesis*, Albert-Ludwigs-Universität Freiburg im Breisgau, 2013.
- [101] W. Kern, *Handbook of semiconductor wafer cleaning technology*. Park Ridge, New Jersey: Noyes, 1993.
- [102] J. Temmler, "Analyse der Dotierung und Legierung einer a-Si:H Schicht zur Anwendung in Silizium-Heterosolarzellen," *Master Thesis*, University Potsdam, 2015.
- [103] R. A. Sinton and A. Cuevas, "A quasi-steady-state open-circuit voltage method for solar cell characterization", in *Proceedings of the 16th European Photovoltaic Solar Energy Conference*, Glasgow, UK, 2000.
- [104] R. A. Sinton and A. Cuevas, "Contactless determination of current-voltage characteristics and minority-carrier lifetimes in semiconductors from quasi-steady-state photoconductance data", *Appl. Phys. Lett.*, vol. 69, p. 2510-2, 1996.
- [105] M. A. Green, "Solar Cell Fill Factors: General Graph and Empirical Expression", *Solid State Electronics*, vol. 24, p. 788-789, 1981.
- [106] B. Michl, D. Impera, M. Bivour, W. Warta, and M. C. Schubert, "Suns-PLI as a powerful tool for spatially resolved fill factor analysis of solar cells", *Progress in Photovoltaics: Research and Applications*, p. 2293, 2012.
- [107] D. Impera, "Charakterisierung von amorph-kristallinen Silicium-Hetero-Solarzellen mit multikristallinem Absorber," *Diploma Thesis*, Albert-Ludwigs-Universität Freiburg, 2012.
- [108] R. Stangl and C. Leendertz, "General Principles of Solar Cell Simulation and Introduction to AFORS-HET and Modeling an a-Si:H/c-Si Solar Cell with AFORS-HET," in *Physics and Technology of Amorphous-Crystalline Heterostructure Silicon Solar Cells*, vol. 0, *Engineering Materials*, W. J. H. M. Sark, L. Korte, and F. Roca, Eds.: Springer Berlin Heidelberg, 2011, p. 445-482.
- [109] M. Reusch, "Analyse von Füllfaktor limitierenden Mechanismen von Silizium-Heterosolarzellen," *Master Thesis*, Albert-Ludwigs-Universität Freiburg im Breisgau, 2013.
- [110] M. Rüdiger and I. Fraunhofer, *Analysis and Simulation of Crystalline Silicon Solar Cells*: Fraunhofer Verlag, 2014.
- [111] M. Bivour, M. Reusch, F. Feldmann, M. Hermle, and S. Glunz, "Requirements for Carrier Selective Silicon Heterojunctions", in *24th Workshop on Crystalline Silicon Solar Cells & Modules: Materials and Processes*, Breckenridge, Colorado, 2014.
- [112] T. Fellmeth, F. Clement, and D. Biro, "Analytical Modeling of Industrial-Related Silicon Solar Cells", *Photovoltaics, IEEE Journal of*, vol. PP, p. 1-10, 2013.

- [113] D. Zielke, J. H. Petermann, F. Werner, B. Veith, R. Brendel, and J. Schmidt, "Contact passivation in silicon solar cells using atomic-layer-deposited aluminum oxide layers", *physica status solidi (RRL) – Rapid Research Letters*, vol. 5, p. 298-300, 2011.
- [114] J. Bullock, A. Cuevas, C. Samundsett, D. Yan, J. McKeon, and Y. Wan, "Simple silicon solar cells featuring an a-Si:H enhanced rear MIS contact", *Sol Energ Mat Sol C*, vol. 138, p. 22-25, 2015.
- [115] K. T. K.C. Fong, K.R. McIntosh, A.W. Blakers, E. Franklin, S.Z. Ngwe, A. Fell, "Optimisation of N+ Diffusion and Contact Size of IBC Solar Cells", in *28th EUPVSEC*, Paris, 2013.
- [116] R. R. King, R. A. Sinton, and R. M. Swanson, "Studies of diffused phosphorus emitters: saturation current, surface recombination velocity, and quantum efficiency", *Electron Devices, IEEE Transactions on*, vol. 37, p. 365-371, 1990.
- [117] S. Sterk, S. W. Glunz, J. Knobloch, and W. Wettling, "High efficiency (>22%) Si-solar cells with optimized emitter", in *Proceedings of the 1st World Conference on Photovoltaic Energy Conversion*, Hawaii, USA, 1994.
- [118] M. Rudiger, J. Greulich, A. Richter, and M. Hermle, "Parameterization of Free Carrier Absorption in Highly Doped Silicon for Solar Cells", *Electron Devices, IEEE Transactions on*, vol. 60, p. 2156-2163, 2013.
- [119] Z. C. Holman, A. Descoeurdes, L. Barraud, F. Z. Fernandez, J. P. Seif, S. De Wolf, and C. Ballif, "Current Losses at the Front of Silicon Heterojunction Solar Cells", *Photovoltaics, IEEE Journal of*, vol. 2, p. 7-15, 2012.
- [120] T. Koida, H. Fujiwara, and M. Kondo, "High-mobility hydrogen-doped In₂O₃In₂O₃ transparent conductive oxide for a-Si:H/c-Si heterojunction solar cells", *Sol Energ Mat Sol C*, vol. 93, p. 851-854, 2009.
- [121] J. Bullock, A. Cuevas, D. Yan, B. Demareux, A. Hessler-Wyser, and S. De Wolf, "Amorphous silicon enhanced metal-insulator-semiconductor contacts for silicon solar cells", *Journal of Applied Physics*, vol. 116, p. -, 2014.
- [122] R. M. Swanson, "Approaching the 29% limit efficiency of silicon solar cells", in *Proceedings of the 31st IEEE Photovoltaic Specialists Conference*, Orlando, USA, 2005.
- [123] M. A. Shibib, F. A. Lindholm, and F. Therez, "Heavily doped transparent-emitter regions in junction solar cells, diodes, and transistors", *Electron Devices, IEEE Transactions on*, vol. 26, p. 959-965, 1979.
- [124] J. del Alamo, J. van Meerbergen, F. D'Hoore, and J. Nijs, "High-low junctions for solar cell applications", *Solid-State Electronics*, vol. 24, p. 533-538, 1981.

- [125] R. Varache, J. P. Kleider, M. E. Gueunier-Farret, and L. Korte, "Silicon heterojunction solar cells: Optimization of emitter and contact properties from analytical calculation and numerical simulation", *Materials Science and Engineering: B*, vol. 178, p. 593-598, 2013.
- [126] R. Rößler, C. Leendertz, L. Korte, N. Mingirulli, and B. Rech, "Impact of the transparent conductive oxide work function on injection-dependent a-Si:H/c-Si band bending and solar cell parameters", *Journal of Applied Physics*, vol. 113, p. -, 2013.
- [127] J. K. Arch, F. A. Rubinelli, J.-Y. Hou, and S. J. Fonash, "Computer analysis of the role of p-layer quality, thickness, transport mechanisms, and contact barrier height in the performance of hydrogenated amorphous silicon p-i-n solar cells", *Journal of Applied Physics*, vol. 69, p. 7057-7066, 1991.
- [128] A. Cuevas and Y. Di, "Misconceptions and Misnomers in Solar Cells", *Photovoltaics, IEEE Journal of*, vol. 3, p. 916-923, 2013.
- [129] S. De Wolf, C. Ballif, and M. Kondo, "Kinetics of a-Si:H bulk defect and a-Si:H/c-Si interface-state reduction", *Physical Review B*, vol. 85, 2012.
- [130] R. S. Crandall, E. Iwaniczko, J. V. Li, and M. R. Page, "A comprehensive study of hole collection in heterojunction solar cells", *Journal of Applied Physics*, vol. 112, p. 093713, 2012.
- [131] B. V. Roedern and G. H. Bauer, "Material Requirements for Buffer Layers Used to Obtain Solar Cells with High Open Circuit Voltages", *MRS Online Proceedings Library*, vol. 557, p. null-null, 1999.
- [132] J. A. del Alamo and R. M. Swanson, "The physics and modeling of heavily doped emitters", *Electron Devices, IEEE Transactions on*, vol. 31, p. 1878-1888, 1984.
- [133] A. Wagenpfahl, D. Rauh, M. Binder, C. Deibel, and V. Dyakonov, "S-shaped current-voltage characteristics of organic solar devices", *Physical Review B*, vol. 82, p. 115306, 2010.
- [134] W. Tress, K. Leo, and M. Riede, "Optimum mobility, contact properties, and open-circuit voltage of organic solar cells: A drift-diffusion simulation study", *Physical Review B*, vol. 85, p. 155201, 2012.
- [135] E. L. Ratcliff, A. Garcia, S. A. Paniagua, S. R. Cowan, A. J. Giordano, D. S. Ginley, S. R. Marder, J. J. Berry, and D. C. Olson, "Investigating the Influence of Interfacial Contact Properties on Open Circuit Voltages in Organic Photovoltaic Performance: Work Function Versus Selectivity", *Advanced Energy Materials*, vol. 3, p. 647-656, 2013.

- [136] M. Pietsch, S. Jäckle, and S. Christiansen, "Interface investigation of planar hybrid n-Si/PEDOT: PSS solar cells with open circuit voltages up to 645 mV and efficiencies of 12.6%", *Applied Physics A*, p. 1-5, 2014.
- [137] M. Reusch, M. Bivour, M. Hermle, and S. W. Glunz, "Fill Factor Limitation of Silicon Heterojunction Solar Cells by Junction Recombination", *Energy Procedia*, p. article in press, 2013.
- [138] S. W. Glunz, D. Biro, S. Rein, and W. Warta, "Field-effect passivation of the SiO₂-Si interface", *Journal of Applied Physics*, vol. 86, p. 683-91, 1999.
- [139] M. Wilson, J. Lagowski, L. Jastrzebski, A. Savtchouk, and V. Faifer, "COCOS (corona oxide characterization of semiconductor) non-contact metrology for gate dielectrics", *AIP Conference Proceedings*, vol. 550, p. 220-225, 2001.
- [140] J. Schmidt, F. Werner, B. Veith, D. Zielke, S. Steingrube, P. P. Altermatt, S. Gatz, T. Dullweber, and R. Brendel, "Advances in the surface passivation of silicon solar cells", in *International Conference on Materials for Advanced Technologies*, 2011.
- [141] G. Dingemans and W. M. M. Kessels, "Status and prospects of Al₂O₃-based surface passivation schemes for silicon solar cells", *Journal of Vacuum Science & Technology A*, vol. 30, p. 040802, 2012.
- [142] F. Lin, B. Hoex, Y. H. Koh, J. Lin, and A. G. Aberle, "Low-temperature surface passivation of moderately doped crystalline silicon by atomic-layer-deposited hafnium oxide films", *ECS Journal of Solid State Science and Technology*, vol. 2, p. N11-N14, 2013.
- [143] A. Descoeur, Z. C. Holman, L. Barraud, S. Morel, S. De Wolf, and C. Ballif, "> 21% Efficient Silicon Heterojunction Solar Cells on n- and p-Type Wafers Compared", *IEEE Journal of Photovoltaics*, vol. 3, p. 83-89, 2013.
- [144] A. G. Aberle, S. J. Robinson, A. Wang, J. Zhao, S. R. Wenham, and M. A. Green, "High-efficiency silicon solar cells: Full factor limitations and non-ideal diode behaviour due to voltage-dependent rear surface recombination velocity", *Progress in Photovoltaics: Research and Applications*, vol. 1, p. 133-143, 1993.
- [145] C. Leendertz, R. Stangl, T. F. Schulze, M. Schmidt, and L. Korte, "A recombination model for a-Si:H/c-Si heterostructures", *physica status solidi (c)*, p. NA-NA, 2010.
- [146] S. Steingrube, R. Brendel, and P. P. Altermatt, "Limits to model amphoteric defect recombination via SRH statistics", *Physica Status Solidi A*, vol. 209, p. 390-400, 2012.
- [147] S. Olibet, E. Vallat-Sauvain, and C. Ballif, "Model for a-Si:H/c-Si interface recombination based on the amphoteric nature of silicon dangling bonds", *Physical Review B*, vol. 76, 2007.

- [148] M. Garin, U. Rau, W. Brendle, I. Martin, and R. Alcubilla, "Characterization of a-Si:H/c-Si interfaces by effective-lifetime measurements", *Journal of Applied Physics*, vol. 98, p. 093711-9, 2005.
- [149] M. L. Green, E. P. Gusev, R. Degraeve, and E. L. Garfunkel, "Ultrathin (<4 nm) SiO₂ and Si-O-N gate dielectric layers for silicon microelectronics: Understanding the processing, structure, and physical and electrical limits", *Journal of Applied Physics*, vol. 90, p. 2057, 2001.
- [150] T. F. Schulze, C. Leendertz, N. Mingirulli, L. Korte, and B. Rech, "Impact of Fermi-level dependent defect equilibration on Voc of amorphous/crystalline silicon heterojunction solar cells", *Energy Procedia*, vol. 8, p. 282-287, 2011.
- [151] S. De Wolf and M. Kondo, "Nature of doped a-Si:H/c-Si interface recombination", *Journal of Applied Physics*, vol. 105, p. 103707-1--103707-7, 2009.
- [152] S. Y. Y. Herasimenka, C. B. Honsberg, S. G. Bowden, C. Tracy, D. Vasileska, Z. Holman, and R. Sinton, "Large Area Ultrapassivated Silicon Solar Cells Using Heterojunction Carrier Collectors," Arizona State University, 2013.
- [153] S. De Wolf and G. Beaucarne, "Surface passivation properties of boron-doped plasma-enhanced chemical vapor deposited hydrogenated amorphous silicon films on p-type crystalline Si substrates", *Applied Physics Letters*, vol. 88, p. 022104, 2006.
- [154] S. C. Deane, M. J. Powell, J. R. Hughes, I. D. French, and W. I. Milne, "Thermal bias annealing evidence for the defect pool in amorphous silicon thin-film transistors", *Applied Physics Letters*, vol. 57, p. 1416, 1990.
- [155] M. Powell and S. Deane, "Improved defect-pool model for charged defects in amorphous silicon", *Physical Review B*, vol. 48, p. 10815-10827, 1993.
- [156] D. Biro, "Passivierte Siliciumoberflächen - Herstellung und Charakterisierung," *Diplomarbeit*, Universität Karlsruhe, 1997.
- [157] G. Dingemans, "Nanolayer surface passivation schemes for silicon solar cells," *Dissertation*, Technische Universiteit Eindhoven, 2011.
- [158] H. Fujiwara and M. Kondo, "Effects of a-Si:H layer thicknesses on the performance of a-Si:H/c-Si heterojunction solar cells", *Journal of Applied Physics*, vol. 101, p. 054516-1--054516-9, 2007.
- [159] T. Desrues, P. J. Ribeyron, A. Vandeneynde, A. S. Ozanne, F. Souche, D. Muñoz, C. Denis, D. Diouf, and J. P. Kleider, "B-doped a-Si:H contact improvement on silicon heterojunction solar cells and interdigitated back contact structure", *physica status solidi (c)*, vol. 7, p. 1011-1015, 2010.

- [160] M. R. Page, E. Iwaniczko, Y. Q. Xu, L. Roybal, F. Hasoon, Q. Wang, and R. S. Crandall, "Amorphous/crystalline silicon heterojunction solar cells with varying i-layer thickness", *Thin Solid Films*, vol. 519, p. 4527-4530, 2011.
- [161] A. Descoeurdes, Z. C. Holman, L. Barraud, S. Morel, S. De Wolf, and C. Ballif, ">21% Efficient Silicon Heterojunction Solar Cells on n- and p-Type Wafers Compared", *IEEE Journal of Photovoltaics*, vol. 3, p. 83-89, 2013.
- [162] P. J. Cousins, D. H. Neuhaus, and J. E. Cotter, "Experimental verification of the effect of depletion-region modulation on photoconductance lifetime measurements", *J. Appl. Phys.*, vol. 95, p. 1854-8, 2004.
- [163] M. Kessler, T. Ohrdes, P. P. Altermatt, and R. Brendel, "The effect of sample edge recombination on the averaged injection-dependent carrier lifetime in silicon", *Journal of Applied Physics*, vol. 111, p. 054508, 2012.
- [164] B. Veith, T. Ohrdes, F. Werner, R. Brendel, P. P. Altermatt, N.-P. Harder, and J. Schmidt, "Injection dependence of the effective lifetime of n-type Si passivated by Al₂O₃: An edge effect?", *Sol Energ Mat Sol C*, vol. 120, Part A, p. 436-440, 2014.
- [165] S. W. Glunz, A. B. Sproul, W. Warta, and W. Wettling, "Injection-level-dependent recombination velocities at the Si-SiO₂ interface for various dopant concentrations", *J. Appl. Phys.*, vol. 75, p. 1611-5, 1994.
- [166] P. Saint-Cast, Y.-H. Heo, E. Billot, P. Olwal, M. Hofmann, J. Rentsch, S. W. Glunz, and R. Preu, "Variation of the layer thickness to study the electrical property of PECVD Al₂O₃ / c-Si interface", *Energy Procedia*, vol. 8, p. 642-647, 2011.
- [167] F. Werner, A. Cosceev, and J. Schmidt, "Interface recombination parameters of atomic-layer-deposited Al₂O₃ on crystalline silicon", *Journal of Applied Physics*, vol. 111, p. -, 2012.
- [168] Synopsis, Zurich, Switzerland, *Sentaurus Device Manual*, (www.synopsis.com), 2012.
- [169] M. Bivour, M. Reusch, S. Schroer, F. Feldmann, J. Temmler, H. Steinkemper, and M. Hermle, "Doped Layer Optimization for Silicon Heterojunctions by Injection-Level Dependent Open-Circuit Voltage Measurements", *IEEE Journal of Photovoltaics*, p. 566-574, 2014.
- [170] M. Bivour, M. Reusch, S. Schröer, F. Feldmann, J. Temmler, and M. Hermle, "Analysis of a-Si:H Doping by Suns-Voc Measurements for Silicon Heterojunctions," in *28th EU PVSEC*. Paris, 2013, p. 1639 - 1644.
- [171] M. Bivour, C. Reichel, M. Hermle, and S. W. Glunz, "Improving the a-Si:H(p) rear emitter contact of n-type silicon solar cells", *Sol Energ Mat Sol C*, vol. 106, p. 11-16, 2012.

- [172] M. Bivour, C. Meinhardt, D. Pysch, C. Reichel, K. Ritzau, M. Hermle, and S. W. Glunz, "n-type silicon solar cells with amorphous/crystalline silicon heterojunction rear emitter", in *Photovoltaic Specialists Conference (PVSC), 35th IEEE*, 2010.
- [173] R. Lachaume, W. Favre, P. Scheiblin, X. Garros, N. Nguyen, J. Coignus, D. Munoz, and G. Reimbold, "Influence of a-Si:H/ITO Interface Properties on Performance of Heterojunction Solar Cells", *Energy Procedia*, vol. 38, p. 770-776, 2013.
- [174] S. M. d. Nicolás, D. Muñoz, A. S. Ozanne, N. Nguyen, and P. J. Ribeyron, "Optimisation of doped amorphous silicon layers applied to heterojunction solar cells", *Energy Procedia*, vol. 8, p. 226-231, 2011.
- [175] M. W. M. van Cleef, F. A. Rubinelli, J. D. Ouwens, and R. E. I. Schropp, "Amorphous-crystalline heterojunction silicon solar cells with an a-SiC:H window layer", in *Proceedings of the 13th European Photovoltaic Solar Energy Conference Nice, France*, 1995.
- [176] L. Korte, E. Conrad, H. Angermann, R. Stangl, and M. Schmidt, "Advances in a-Si:H/c-Si heterojunction solar cell fabrication and characterization", *Sol Energ Mat Sol C*, vol. 93, p. 905-910, 2009.
- [177] D. Pysch, C. Meinhard, N.-P. Harder, M. Hermle, and S. W. Glunz, "Analysis and optimization approach for the doped amorphous layers of silicon heterojunction solar cells", *Journal of Applied Physics*, vol. 110, p. 094516-1--094516-8, 2011.
- [178] A. Janotta, R. Janssen, M. Schmidt, T. Graf, M. Stutzmann, L. Görgens, A. Bergmaier, G. Dollinger, C. Hammerl, S. Schreiber, and B. Stritzker, "Doping and its efficiency in a-SiO_x:H", *Physical Review B*, vol. 69, p. 115206-1--115206-16, 2004.
- [179] Y. Tawada, K. Tsuge, M. Kondo, H. Okamoto, and Y. Hamakawa, "Properties and structure of a-SiC:H for high-efficiency a-Si solar cell", *Journal of Applied Physics*, vol. 53, p. 5273-5281, 1982.
- [180] D. Muñoz, T. Desrues, A.-S. Ozanne, *et al.*, "Key aspects on development of high efficiency heterojunction and IBC heterojunction solar cells: towards 22% efficiency on industrial size", in *Proceedings of the 27th EUPVSEC, Frankfurt, Germany*, 2012.
- [181] P. Roca i Cabarrocas, "Plasma enhanced chemical vapor deposition of amorphous, polymorphous and microcrystalline silicon films", *Journal of Non-Crystalline Solids*, vol. 266, p. 31-37, 2000.
- [182] H. Wernerus, "Entwicklung dünner mikrokristalliner Siliciumschichten für Heterojunction-Solarzellen," *Master Thesis*, Karlsruhe Institute of Technology, 2013.

- [183] M. H. Brodsky, F. Evangelisti, R. Fischer, R. W. Johnson, W. Reuter, and I. Solomon, "Thickness-dependent conductivity and photoconductivity of hydrogenated amorphous silicon", *Solar Cells*, vol. 2, p. 401-406, 1980.
- [184] M. Izzi and L. S. M. Tucci, P. Mangiapane, M. Della Noce, I. Usatii, E. Esposito, L. V. Mercaldo P. Delli Veneri, "Doped SiO_x emitter layer in amorphous/crystalline silicon heterojunction solar cell", *Applied Physics A*, p. 1-8, 2013.
- [185] L. Korte and M. Schmidt, "Investigation of gap states in phosphorous-doped ultra-thin a-Si:H by near-UV photoelectron spectroscopy", *Journal of Non-Crystalline Solids*, vol. 354, p. 2138-2143, 2008.
- [186] Y. Sato, R. Tokumaru, E. Nishimura, P.-k. Song, Y. Shigesato, K. Utsumi, and H. Iigusa, "Structural, electrical, and optical properties of transparent conductive In₂O₃-SnO₂ films", *Journal of Vacuum Science & Technology A: Vacuum, Surfaces, and Films*, vol. 23, p. 1167-1172, 2005.
- [187] T. J. Marks, J. G. C. Veinot, J. Cui, H. Yan, A. Wang, N. L. Edleman, J. Ni, Q. Huang, P. Lee, and N. R. Armstrong, "Progress in high work function TCO OLED anode alternatives and OLED nanopixelation", *Synthetic Metals*, vol. 127, p. 29-35, 2002.
- [188] S. Chen, J. R. Manders, S.-W. Tsang, and F. So, "Metal oxides for interface engineering in polymer solar cells", *Journal of Materials Chemistry*, vol. 22, p. 24202-24212, 2012.
- [189] S. W. Glunz, J. Nekarda, H. Mäkel, and A. Cuevas, "Analyzing back contacts of silicon solar cells by suns-voc-measurements at high illumination densities", in *Proceedings of the 22nd European Photovoltaic Solar Energy Conference* Milan, Italy, 2007.
- [190] M. Page, E. Iwaniczko, Y. Xu, L. Roybal, R. Bauer, H.-C. Yuan, Q. Wang, and D. Meier, "Photoconductive Decay Lifetime and Suns-Voc Diagnostics of Efficient Heterojunction Solar Cells", in *Photovoltaic Specialists Conference (PVSC), 2008 33rd IEEE* San Diego, 2008.
- [191] U. Das, S. Hegedus, Z. Lulu, J. Appel, J. Rand, and R. Birkmire, "Investigation of hetero-interface and junction properties in silicon heterojunction solar cells", in *Photovoltaic Specialists Conference (PVSC), 2010 35th IEEE*, 2010.
- [192] J. Appel, Z. Lulu, U. Das, S. Hegedus, S. Mudigonda, R. Birkmire, and J. Rand, "Effect of junction interface modification of silicon heterojunction solar cells", in *Photovoltaic Specialists Conference (PVSC), 2010 35th IEEE*, 2010.
- [193] K. Heilig, "Determination of surface properties by means of large signal photovoltage pulses and the influence of trapping", *Surface Science*, vol. 44, p. 421-437, 1974.

- [194] M. Reusch, M. Bivour, M. Hermle, and S. W. Glunz, "Fill Factor Limitation of Silicon Heterojunction Solar Cells by Junction Recombination", *Energy Procedia*, vol. 38, p. 297-304, 2013.
- [195] W. Favre, J. Coignus, N. Nguyen, R. Lachaume, R. Cabal, and D. Muñoz, "Influence of the transparent conductive oxide layer deposition step on electrical properties of silicon heterojunction solar cells", *Applied Physics Letters*, vol. 102, p. 181118-1--181118-4, 2013.
- [196] M. A. Green, "General temperature dependence of solar cell performance and implications for device modelling", *Progress in Photovoltaics: Research and Applications*, vol. 11, p. 333-340, 2003.
- [197] W. E. Spear and P. G. Le Comber, "Substitutional doping of amorphous silicon", *Solid State Communications*, vol. 17, p. 1193-6, 1975.
- [198] H. Wernerus, M. Bivour, L. Kroely, M. Hermle, and W. Wolke, "Characterization of ultra-thin $\mu\text{-Si:H}$ films for silicon heterojunction solar cells", *Energy Procedia*, vol. 55, p. 310-9, 2014.
- [199] K.-U. Ritzau, M. Bivour, S. Schröer, H. Steinkemper, P. Reinecke, F. Wagner, and M. Hermle, "TCO work function related transport losses at the a-Si:H/TCO-contact in SHJ solar cells", *Sol Energ Mat Sol C*, vol. 131, p. 9-13, 2014.
- [200] F. Feldmann, K.-U. Ritzau, M. Bivour, A. Moldovan, S. Modi, J. Temmler, M. Hermle, and S. W. Glunz, "High and Low Work Function Materials for Passivated Contacts", in *Energy Procedia 5th International Conference on Silicon Photovoltaics, SiliconPV 2015*, Konstanz, Germany, 2015.
- [201] K.-U. Ritzau, "Transportphänomene in amorph-kristallinen Silicium-Hetero-Solarzellen," 2015.
- [202] B. n. d. Demaurex, S. De Wolf, A. Descoedres, Z. Charles Holman, and C. Ballif, "Damage at hydrogenated amorphous/crystalline silicon interfaces by indium tin oxide overlayer sputtering", *Applied Physics Letters*, vol. 101, p. 171604-1--171604-4, 2012.
- [203] Y. Sato, T. Ashida, N. Oka, and Y. Shigesato, "Carrier Density Dependence of Optical Band Gap and Work Function in Sn-Doped In₂O₃Films", *Applied Physics Express*, vol. 3, p. 061101, 2010.
- [204] S. Muranaka, Y. Bando, and T. Takada, "Influence of substrate temperature and film thickness on the structure of reactively evaporated In₂O₃ films", *Thin Solid Films*, vol. 151, p. 355-364, 1987.

- [205] C. H. Yi, Y. Shigesato, I. Yasui, and S. Takaki, "Microstructure of Low-Resistivity Tin-Doped Indium Oxide Films Deposited at 150~200° C", *Japanese Journal of Applied Physics*, vol. 34, p. L244, 1995.
- [206] M. V. Hohmann, P. Ágoston, A. Wachau, T. J. M. Bayer, J. Brötz, K. Albe, and A. Klein, "Orientation dependent ionization potential of In₂O₃ : a natural source for inhomogeneous barrier formation at electrode interfaces in organic electronics", *Journal of Physics: Condensed Matter*, vol. 23, p. 334203, 2011.
- [207] J. Mitchell, "A model for low temperature interface passivation between amorphous and crystalline silicon", *Journal of Applied Physics*, vol. 114, p. -, 2013.
- [208] M. D. McCluskey, M. C. Tarun, and S. T. Teklemichael, "Hydrogen in oxide semiconductors", *Journal of Materials Research*, vol. 27, p. 2190-2198, 2012.
- [209] J. Kim, A. Abou-Kandil, K. Fogel, H. Hovel, and D. K. Sadana, "The Role of High Work-Function Metallic Nanodots on the Performance of a-Si:H Solar Cells: Offering Ohmic Contact to Light Trapping", *ACS Nano*, vol. 4, p. 7331-7336, 2010.
- [210] F.-J. Haug, R. Biron, G. Kratzer, F. Leresche, J. Besuchet, C. Ballif, M. Dissel, S. Kretschmer, W. Soppe, P. Lippens, and K. Leitner, "Improvement of the open circuit voltage by modifying the transparent indium-tin oxide front electrode in amorphous n-i-p solar cells", *Progress in Photovoltaics: Research and Applications*, vol. 20, p. 727-734, 2012.
- [211] L. J. Park H, Lee Y], Kim H, Jung J, Hussain SQ, Park J, Shin C, Kim S, Ahn S, Yil J., "Inserted Layer of AZO Thin Film with High Work Function Between Transparent Conductive Oxide and *p*-Layer and Its Solar Cell Application", *Journal of Nanoscience and Nanotechnology*, vol. 13, p. 7116-7118, 2013.
- [212] Y. Gassenbauer and A. Klein, "Electronic and chemical properties of tin-doped indium oxide (ITO) surfaces and ITO/ZnPc interfaces studied in-situ by photoelectron spectroscopy", *The Journal of Physical Chemistry B*, vol. 110, p. 4793-4801, 2006.
- [213] W. M. Haynes and D. R. Lide, *CRC handbook of chemistry and physics : a ready-reference book of chemical and physical data*. Boca Raton, Fla.: CRC Press, 2011.
- [214] C. R. Wronski, D. E. Carlson, and R. E. Daniel, "Schottky-barrier characteristics of metal-amorphous-silicon diodes", *Applied Physics Letters*, vol. 29, p. 602-605, 1976.
- [215] F.-J. Haug, T. Söderström, O. Cubero, V. Terrazzoni-Daudrix, and C. Ballif, "Plasmonic absorption in textured silver back reflectors of thin film solar cells", *Journal of Applied Physics*, vol. 104, p. -, 2008.

- [216] Z. C. Holman, M. Filipič, A. Descoeurdes, S. De Wolf, F. Smole, M. Topič, and C. Ballif, "Infrared light management in high-efficiency silicon heterojunction and rear-passivated solar cells", *Journal of Applied Physics*, vol. 113, p. 013107, 2013.
- [217] R. Brendel, "Sunrays: A versatile ray tracing program for the photovoltaic community", in *Proceedings of the 12th European Photovoltaic Solar Energy Conference*, Amsterdam, The Netherlands, 1994.
- [218] M. Bivour, M. Rüdiger, C. Reichel, K.-U. Ritzau, M. Hermle, and S. W. Glunz, "Analysis of the Diffused Front Surface Field of n-type Silicon Solar Cells with a-Si/c-Si Heterojunction Rear Emitter", *Energy Procedia*, vol. 8, p. 185-192, 2011.
- [219] M. Tucci and G. de Cesare, "17% efficiency heterostructure solar cell based on p-type crystalline silicon", *Journal of Non-Crystalline Solids*, vol. 338-340, p. 663-667, 2004.
- [220] M. Bivour, J. Temmler, H. Steinkemper, and M. Hermle, "Molybdenum and Tungsten Oxide: High Work Function Wide Band Gap Contact Materials for Hole Selective Contacts of Silicon Solar Cells", *Sol Energ Mat Sol C*, p. 34-41, 2015.
- [221] M. Bivour, J. Temmler, H. Steinkemper, and M. Hermle, "Alternative Contact Materials for Induced Junction Silicon Solar Cells", *Sol Energ Mat Sol C*, in preparation for submission
- [222] M. T. Greiner and Z.-H. Lu, "Thin-film metal oxides in organic semiconductor devices: their electronic structures, work functions and interfaces", *NPG Asia Mater*, vol. 5, p. e55, 2013.
- [223] J. Meyer, S. Hamwi, M. Kröger, W. Kowalsky, T. Riedl, and A. Kahn, "Transition Metal Oxides for Organic Electronics: Energetics, Device Physics and Applications", *Advanced Materials*, vol. 24, p. 5408-5427, 2012.
- [224] L.-M. Chen, Z. Xu, Z. Hong, and Y. Yang, "Interface investigation and engineering - achieving high performance polymer photovoltaic devices", *Journal of Materials Chemistry*, vol. 20, p. 2575-2598, 2010.
- [225] G. Li, C.-W. Chu, V. Shrotriya, J. Huang, and Y. Yang, "Efficient inverted polymer solar cells", *Applied Physics Letters*, vol. 88, p. -, 2006.
- [226] S. Avasthi, W. E. McClain, G. Man, A. Kahn, J. Schwartz, and J. C. Sturm, "Hole-blocking titanium-oxide/silicon heterojunction and its application to photovoltaics", *Applied Physics Letters*, vol. 102, p. 203901, 2013.
- [227] X. Yin, C. Battaglia, Y. Lin, K. Chen, M. Hettick, M. Zheng, C.-Y. Chen, D. Kiriya, and A. Javey, "19.2% Efficient InP Heterojunction Solar Cell with Electron-Selective TiO₂ Contact", *ACS photonics*, vol. 1, p. 1245-1250, 2014.

- [228] S.-I. Na, G. Wang, S.-S. Kim, T.-W. Kim, S.-H. Oh, B.-K. Yu, T. Lee, and D.-Y. Kim, "Evolution of nanomorphology and anisotropic conductivity in solvent-modified PEDOT:PSS films for polymeric anodes of polymer solar cells", *Journal of Materials Chemistry*, vol. 19, p. 9045-9053, 2009.
- [229] Y. Ji-Hwan, K. Sang Jung, H. Yunho, and L. Koeng Su, "Doping-Free Intrinsic Amorphous Silicon Thin-Film Solar Cell Having a Simple Structure of Glass/SnO₂/MoO₃/i-a-Si/LiF/Al", *Electron Device Letters, IEEE*, vol. 35, p. 96-98, 2014.
- [230] D. Zielke, A. Pazidis, F. Werner, and J. Schmidt, "Organic-silicon heterojunction solar cells on n-type silicon wafers: The BackPEDOT concept", *Sol Energ Mat Sol C*, 2014
- [231] C. Battaglia, S. M. de Nicolás, S. De Wolf, X. Yin, M. Zheng, C. Ballif, and A. Javey, "Silicon heterojunction solar cell with passivated hole selective MoO_x contact", *Applied Physics Letters*, vol. 104, p. -, 2014.
- [232] J. Bullock, A. Cuevas, T. Allen, and C. Battaglia, "Molybdenum oxide MoO_x: A versatile hole contact for silicon solar cells", *Applied Physics Letters*, vol. 105, p. -, 2014.
- [233] M. Liebhaber, M. Mews, T. F. Schulze, L. Korte, B. Rech, and K. Lips, "Valence band offset in heterojunctions between crystalline silicon and amorphous silicon (sub)oxides (a-SiO_x:H, 0 < x < 2)", *Applied Physics Letters*, vol. 106, p. -, 2015.
- [234] A. Cuevas, "Modelling silicon characterisation", *Energy Procedia*, vol. 8, p. 94-99, <http://sun.anu.edu.au/modelling>, 2011.
- [235] M. Bivour, S. Schröer, M. Hermle, and S. W. Glunz, "Silicon Heterojunction Rear Emitter Solar Cells: Less Restrictions on the Optoelectrical Properties of Front Side TCOs", *Sol Energ Mat Sol C*, vol. 122, p. 120-129, 2013.
- [236] M. Bivour, H. Steinkemper, J. Jeurink, S. Schröer, and M. Hermle, "Rear emitter silicon heterojunction solar cells: fewer restrictions on the optoelectrical properties of front side TCOs", *Energy Procedia*, vol. 55, p. 229-234, 2014.
- [237] S. Schröer, M. Bivour, J. Schön, M. Hermle, and S. W. Glunz, "Reduction of absorption losses and efficiency gains by investigating amorphous/crystalline SHJ rear emitter solar cells", in *Proceedings of the 27th European Photovoltaic Solar Energy Conference and Exhibition*, Frankfurt, Germany, 2012.
- [238] F. Wunsch, G. Citarella, O. Abdallah, and M. Kunst, "An inverted a-Si:H/c-Si hetero-junction for solar energy conversion", *Journal of Non-Crystalline Solids*, vol. 352, p. 1962-1966, 2006.

- [239] E. Kobayashi, N. Nakamura, K. Hashimoto, and Y. Watabe, "Rear-emitter Silicon Heterojunction Solar Cells with Efficiencies Above 22%", in *28th European Photovoltaic Solar Energy Conference and Exhibition*, Paris, 2013.
- [240] K. Meyer, C. Schmiga, R. Jesswein, M. Dupke, J. Lossen, H. J. Krokoszinski, M. Hermle, and S. W. Glunz, "All screen-printed industrial n-type Czochralski silicon solar cells with aluminium rear emitter and selective front surface field", in *Photovoltaic Specialists Conference (PVSC) 35th IEEE*, 2010.
- [241] M. Balestrieri, D. Pysch, J. P. Becker, M. Hermle, W. Warta, and S. W. Glunz, "Characterization and optimization of indium tin oxide films for heterojunction solar cells", *Sol Energ Mat Sol C*, vol. 95, p. 2390-2399, 2011.
- [242] X. M. Dai, M. A. Green, and S. R. Wenham, "High efficiency n-silicon solar cells using rear junction structures", in *Conference Record of the Twenty Third IEEE*, 1993.
- [243] M. Rüdiger, C. Schmiga, M. Rauer, M. Hermle, and S. W. Glunz, "Efficiency Potential of n-Type Silicon Solar Cells With Aluminum-Doped Rear p+ Emitter", *IEEE Transactions on Electron Devices*, vol. 59, p. 1295-1303, 2012.
- [244] A. W. J. Zhao, M. Leonhardt, S. Burkhardt, J. Krause, "N-TYPE MONO CRYSTALLINE INGOT CHARACTERIZATION FOR SILICON HETEROJUNCTION TECHNOLOGY IN ROTH&RAU'S PILOT LINE", in *28th EU PVSEC*, Amsterdam, 2014.
- [245] J. Schmidt, A. Cuevas, S. Rein, and S. W. Glunz, "Impact of light-induced recombination centres on the current-voltage characteristic of czochralski silicon solar cells", *Progress in Photovoltaics: Research and Applications*, vol. 9, p. 249-255, 2001.
- [246] B. Michl, M. Rüdiger, J. A. Giesecke, M. Hermle, W. Warta, and M. C. Schubert, "Efficiency limiting bulk recombination in multicrystalline silicon solar cells", *Sol Energ Mat Sol C*, vol. 98, p. 441-447, 2012.
- [247] D. Impera, M. Bivour, B. Michl, M. C. Schubert, and M. Hermle, "Characterization of silicon heterojunctions on multicrystalline absorbers using injection-dependent photoluminescence imaging", *Energy Procedia*, vol. 27, p. 280-6, 2012.
- [248] A. G. Aberle, M. A. Green, and G. Heiser, "Two-dimensional minority carrier flow in high-efficiency silicon solar cells at short-circuit, open-circuit and maximum power point operating conditions", *Sol Energ Mat Sol C*, vol. 34, p. 149-60, 1994.

- [249] M. Filipič, Z. C. Holman, F. Smole, S. De Wolf, C. Ballif, and M. Topič, "Analysis of lateral transport through the inversion layer in amorphous silicon/crystalline silicon heterojunction solar cells", *Journal of Applied Physics*, vol. 114, p. -, 2013.
- [250] T. Fellmeth, A. Born, A. Kimmerle, F. Clement, D. Biro, and R. Preu, "Recombination at Metal-Emitter Interfaces of Front Contact Technologies for Highly Efficient Silicon Solar Cells", *Energy Procedia*, vol. 8, p. 115-121, 2011.
- [251] A. W. Blakers, J. Zhao, A. Wang, A. M. Milne, X. Dai, and M. A. Green, "23% efficient silicon solar cell", in *Proceedings of the 9th European Photovoltaic Solar Energy Conference*, Freiburg, Germany, 1989.
- [252] D. K. Schroder, *Semiconductor material and device characterization*, 3rd ed. Hoboken, New Jersey, USA: John Wiley & Sons, 2006.
- [253] J. Zhao, A. Wang, P. P. Altermatt, S. R. Wenham, and M. A. Green, "24% efficient per1 silicon solar cell: Recent improvements in high efficiency silicon cell research", *Sol Energ Mat Sol C*, vol. 41, p. 87-99, 1996.
- [254] J. L. Hernández, K. Yoshikawa, A. Feltrin, *et al.*, "High Efficiency Silver-Free Heterojunction Silicon Solar Cell", *Japanese Journal of Applied Physics*, vol. 51, p. 10NA04, 2012.
- [255] T. Soederstroem, P. Papet, J. Escare, A. Faes, and M. Despeisse, "Smart heterojunction solar modules," in *NPV Workshop*, 2013.
- [256] M. Steltenpool, J. Rutten, A. Tavakoliyaraki, H. de Groot, G. van der Hofstad, W. Vugts, A. J. M. van Erven, and G. Rajeswaran, "High efficient commercial grade crystalline silicon solar cells with thin film amorphouse silicon passivation", in *Proceedings of the 27th EUPVSEC, Frankfurt, Germany*, 2012.
- [257] J. E. Mahan and G. M. Smirnov, "A new perspective on distributed series resistance effects in photovoltaic devices", in *IEEE 14th Photovoltaic Specialists Conf*, 1980.
- [258] P. P. Altermatt, G. Heiser, A. G. Aberle, A. Wang, J. Zhao, S. J. Robinson, S. Bowden, and M. A. Green, "Spatially resolved analysis and minimization of resistive losses in high-efficiency Si solar cells", *Progress in Photovoltaics: Research and Applications*, vol. 4, p. 399-414, 1996.
- [259] M. Cid and J. M. Ruiz, "Study of injection effects on BSF silicon solar cells", *Electron Devices, IEEE Transactions on*, vol. 36, p. 507-513, 1989.
- [260] F. Book, T. Wiedenmann, G. Schubert, H. Plagwitz, and G. Hahn, "Influence of the Front Surface Passivation Quality on Large Area n-Type Silicon Solar Cells with Al-Alloyed Rear Emitter", *Energy Procedia*, vol. 8, p. 487-492, 2011.

- [261] F. Granek, M. Hermle, D. M. Huljić, O. Schultz-Wittmann, and S. W. Glunz, "Enhanced lateral current transport via the front N+diffused layer of n-type high-efficiency back-junction back-contact silicon solar cells", *Progress in Photovoltaics: Research and Applications*, vol. 17, p. 47-56, 2009.
- [262] R. J. Schwartz, M. S. Lundstrom, and R. Nasby, "The degradation of high-intensity BSF solar-cell fill factors due to a loss of base conductivity modulation", *Electron Devices, IEEE Transactions on*, vol. 28, p. 264-269, 1981.
- [263] M. Hermle, F. Granek, O. Schultz, and S. W. Glunz, "Analyzing the effects of front-surface fields on back-junction silicon solar cells using the charge-collection probability and the reciprocity theorem", *Journal of Applied Physics*, vol. 103, p. 054507, 2008.
- [264] A. Wolf, D. Biro, J.-F. Nékarda, S. Stumpp, A. Kimmerle, S. Mack, and R. Preu, "Comprehensive analytical model for locally contacted rear surface passivated solar cells", *Journal of Applied Physics*, vol. 108, p. 1-13, 2010.
- [265] M. Rüdiger and M. Hermle, "Numerical analysis of locally contacted rear surface passivated silicon solar cells", *Japanese Journal of Applied Physics*, vol. 51, p. 10NA07, 2012.
- [266] M. M. Bunea, K. W. Johnston, C. M. Bonner, P. Cousins, D. D. Smith, D. H. Rose, W. P. Mulligan, and R. M. Swanson, "Simulation and characterization of high efficiency back contact cells for low-concentration photovoltaics", in *Photovoltaic Specialists Conference (PVSC), 2010 35th IEEE*, 2010.
- [267] T. Fellmeth, M. Ebert, R. Efinger, I. Hädrich, F. Clement, D. Biro, P. Noriega, S. Caparros, and H. Castano, "Industrially Feasible All-Purpose Metal-Wrap-Through Concentrator Solar Cells", in *Proceedings of the 40th IEEE Photovoltaic Specialists Conference*, Denver, USA, 2014.
- [268] S. Kurtz, *Opportunities and challenges for development of a mature concentrating photovoltaic power industry*: National Renewable Energy Laboratory, 2009.
- [269] R. M. Swanson, "The promise of concentrators", *Progress in Photovoltaics: Research and Applications*, vol. 8, p. 93-111, 2000.
- [270] E. Kobayashi, N. Nakamura, and Y. Watabe, "Reduction of Optical and Electrical Losses in Silicon Heterojunction Solar Cells by Hydrogenated Tungstendoped In₂O₃", in *Proceedings of the 27th EUPVSEC, Frankfurt, Germany*, 2012.
- [271] D. Pysch, A. Mette, and S. W. Glunz, "A review and comparison of different methods to determine the series resistance of solar cells", *Solar Energy Materials & Solar Cells*, vol. 91, p. 1698-706, 2007.

[272] S. De Wolf and M. Kondo, "Surface Passivation Properties of Stacked Doped PECVD a-Si:H Layers for Hetero-Structure c-Si Solar Cells", in *Photovoltaic Energy Conversion, Conference Record of the 2006 IEEE 4th World Conference on*, 2006.

[273] I. H. Campbell, J. D. Kress, R. L. Martin, D. L. Smith, N. N. Barashkov, and J. P. Ferraris, "Controlling charge injection in organic electronic devices using self-assembled monolayers", *Applied Physics Letters*, vol. 71, p. 3528-3530, 1997.

[274] F. Feldmann, M. Simon, M. Bivour, C. Reichel, M. Hermle, and S. W. Glunz, "Efficient carrier-selective p- and n-contacts for Si solar cells", *Sol. Ener. Mater. Sol. Cells*, vol. 131, p. 100-4, 2014.

[275] K.-U. Ritzau, "Herstellung, Analyse und Optimierung einer Silicium-Hetero-Solarzelle mit multikristallinem Absorber," *Diploma Thesis*, Eberhard Karls Universität Tübingen, 2010.

10 Publications

Journal Paper

Author

M. Bivour, C. Reichel, M. Hermle, and S. W. Glunz, "Improving the a-Si:H(p) rear emitter contact of n-type silicon solar cells," *Solar Energy Materials and Solar Cells*, vol. 106, pp. 11-16, 2012.

M. Bivour, "Silicon Heterojunction Rear Emitter Solar Cells: Less Restrictions on the Optoelectrical Properties of Front Side TCOs," *Solar Energy Materials and Solar Cells*, vol. 122, pp. 120–129, 2013.

M. Bivour, M. Reusch, S. Schroer, F. Feldmann, J. Temmler, H. Steinkemper, and M. Hermle, "Doped layer optimization for silicon heterojunctions by injection-level-dependent open-circuit voltage measurements," *IEEE Journal of Photovoltaics*, vol. 4, pp. 566-74, 2014.

M. Bivour, J. Temmler, H. Steinkemper, and M. Hermle, "Molybdenum and Tungsten Oxide: High Work Function Wide Band Gap Contact Materials for Hole Selective Contacts of Silicon Solar Cells," *Solar Energy Materials and Solar Cells*, vol. 142, pp. 34-41, 2015

M. Bivour, J. Temmler, H. Steinkemper, and M. Hermle, "Vanadium Oxide: A High Work Function Wide Band Gap Contact Materials for Hole Selective Contacts of Silicon Solar Cells," *in preparation for submission*

M. Bivour, J. Temmler, and M. Hermle, "Alternative Contact Materials for Induced Junction Silicon Solar Cells," *in preparation for submission*

M. Bivour, S. Schröer, K. Ritzau, and M. Hermle, "An ITO doping variation as an attempt to modify the parasitic Schottky contact in silicon heterojunction solar cells," *in preparation for submission*

Co-author

C. Reichel, **M. Bivour**, F. Granek, M. Hermle, and S. W. Glunz, "Improved diffusion profiles in back-contacted back-junction Si solar cells with an overcompensated boron-doped emitter," *physica status solidi (a)*, vol. 208, pp. 2871-83, 2011.

D. Pysch, **M. Bivour**, M. Hermle, and S. W. Glunz "Amorphous silicon carbide heterojunction solar cell on p-type substrates," *Thin Solid Films*, vol. 519, pp. 2550-4, 2011.

F. Feldmann, **M. Bivour**, C. Reichel, M. Hermle, and S. W. Glunz, "Passivated rear contacts for high-efficiency n-type Si solar cells providing high interface passivation quality and excellent transport characteristics," *Solar Energy Materials and Solar Cells*, vol. 120, pp. 270-4, 2014.

F. Feldmann, **M. Bivour**, C. Reichel, H. Steinkemper, M. Hermle, and S. W. Glunz, "Tunnel oxide passivated contacts as an alternative to partial rear contacts," *Solar Energy Materials and Solar Cells*, vol. 131, pp. 46-50, 2014.

K.-U. Ritzau, **M. Bivour**, S. Schröer, H. Steinkemper, P. Reinecke, F. Wagner, and M. Hermle, "TCO work function related transport losses at the a-Si:H/TCO-contact in SHJ solar cells," *Solar Energy Materials and Solar Cells*, vol. 131, pp. 9-13, 2014.

B. Michl, D. Impera, **M. Bivour**, W. Warta, and M. C. Schubert, "Suns-PLI as a powerful tool for spatially resolved fill factor analysis of solar cells," *Progress in Photovoltaics: Research and Applications*, pp. 2293, 2012.

P. Löper, D. Stüwe, M. Künle, **M. Bivour**, C. Reichel, R. Neubauer, M. Schnabel, M. Hermle, O. Eibl, S. Janz, M. Zacharias, and S. W. Glunz, "A membrane device for substrate-free photovoltaic characterization of quantum dot based p-i-n solar cells," *Advanced Materials*, vol. 24, pp. 3124-9, 2012.

F. Feldmann, M. Simon, **M. Bivour**, C. Reichel, M. Hermle, and S. W. Glunz, "Efficient carrier-selective p- and n-contacts for Si solar cells," *Solar Energy Materials and Solar Cells*, vol. 131, pp. 100-4, 2014.

F. Feldmann, M. Simon, **M. Bivour**, C. Reichel, M. Hermle, and S. W. Glunz, "Carrier-selective contacts for Si solar cells," *Applied Physics Letters*, vol. 104, pp. 181105, 2014.

K.-U. Ritzau, T. Behrendt, D. Palaferri, **M. Bivour**, and M. Hermle, "Hydrogen doping of ITO due to thermal treatment of hetero-junction solar cells," *Thin Solid Films*, 2015 - submitted.

H. Steinkemper, F. Feldmann, **M. Bivour**, and M. Hermle, "Numerical Simulation of Carrier-Selective Electron Contacts Featuring Tunnel Oxides," *IEEE Journal of Photovoltaics*, 2015 – in press.

Conference Paper

Author

M. Bivour, C. Meinhardt, D. Pysch, C. Reichel, K. U. Ritzau, M. Hermle, and S. W. Glunz, "n-type silicon solar cells with amorphous / crystalline silicon heterojunction rear emitter," presented at Proceedings of the 35th IEEE Photovoltaic Specialists Conference, Honolulu, Hawaii, USA, 2010.

M. Bivour, M. Rüdiger, C. Reichel, K.-U. Ritzau, M. Hermle, and S. W. Glunz "Analysis of the diffused front surface field of n-type silicon solar cells with a-Si/c-Si heterojunction rear emitter,"

presented at Proceedings of the 1st International Conference on Silicon Photovoltaics, Freiburg, Germany, pp. 185-92, 2011.

M. Bivour, S. Schröer, and M. Hermle, "Numerical Analysis of Electrical TCO / a-Si:H(p) Contact Properties for Silicon Heterojunction Solar Cells," *Energy Procedia*, vol. 38, pp. 658-69, 2013.

M. Bivour, H. Steinkemper, J. Jeurink, S. Schröer, and M. Hermle, "Rear emitter silicon heterojunction solar cells: Fewer restrictions on the optoelectrical properties of front side TCOs," *Energy Procedia*, vol. 55, pp. 229-34, 2014.

M. Bivour, M. Reusch, F. Feldmann, M. Hermle, and S. Glunz, "Requirements for Carrier Selective Silicon Heterojunctions," presented at 24th Workshop on Crystalline Silicon Solar Cells & Modules: Materials and Processes, Breckenridge, Colorado, 2014.

Co-author

D. Pysch, **M. Bivour**, K. Zimmermann, C. Schetter, M. Hermle, and S. W. Glunz "Comprehensive study of different PECVD-deposition methods for deposition of thin intrinsic amorphous silicon for heterojunction solar cells," presented at Proceedings of the 24th European Photovoltaic Solar Energy Conference, Hamburg, Germany, pp. 1580-5, 2009.

D. Pysch, C. Meinhardt, K.-U. Ritzau, **M. Bivour**, K. Zimmermann, C. Schetter, M. Hermle, and S. W. Glunz, "Comparison of intrinsic amorphous silicon buffer layers for silicon heterojunction," presented at Proceedings of the 35th IEEE Photovoltaic Specialists Conference, Honolulu, Hawaii, USA, pp. in print, 2010.

C. Meinhardt, D. Pysch, **M. Bivour**, K. Zimmermann, C. Schetter, M. Hermle, and S. W. Glunz "Optimization and analysis of deposition processes of amorphous silicon for silicon heterojunction solar cells," presented at Proceedings of the 25th European Photovoltaic Solar Energy Conference and Exhibition, Valencia, Spain, pp. 1810-5, 2010.

S. W. Glunz, J. Benick, D. Biro, **M. Bivour**, M. Hermle, D. Pysch, M. Rauer, C. Reichel, A. Richter, M. Rüdiger, C. Schmiga, D. Suwito, A. Wolf, and R. Preu, "n-type silicon - enabling efficiencies > 20% in industrial production," presented at Proceedings of the 35th IEEE Photovoltaic Specialists Conference, Honolulu, Hawaii, USA, 2010.

D. Impera, **M. Bivour**, B. Michl, M. C. Schubert, and M. Hermle, "Characterization of silicon heterojunctions on multicrystalline absorbers using injection-dependent photoluminescence imaging," *Energy Procedia*, vol. 27, pp. 280-6, 2012.

R. Müller, P. Löper, D. Hiller, S. Gutsch, R. Keding, C. Reichel, **M. Bivour**, M. Hermle, S. Janz, J. C. Goldschmidt, M. Zacharias, and S. W. Glunz "Calculation of the quasi fermi-level splitting in an ideal superlattice of silicon nanocrystals," presented at Proceedings of the 26th European Photovoltaic Solar Energy Conference and Exhibition, Hamburg, Germany, pp. 465-9, 2011.

S. Schröer, **M. Bivour**, J. Schön, M. Hermle, and S. W. Glunz, "Reduction of absorption losses and efficiency gains by investigating amorphous/crystalline SHJ rear emitter solar cells," presented at Proceedings of the 27th European Photovoltaic Solar Energy Conference and Exhibition, Frankfurt, Germany, pp. 759-62, 2012.

F. Feldmann, **M. Bivour**, C. Reichel, M. Hermle, and G. S. W., "A passivated rear contact for high-efficiency n-type silicon solar cells enabling high VocS and FF>82%," presented at Proceedings of the 28th European Photovoltaic Solar Energy Conference and Exhibition, Paris, France, pp. 988-92, 2013.

B. Michl, J. Benick, A. Richter, **M. Bivour**, J. Yong, R. Steeman, M. C. Schubert, and S. W. Glunz, "Excellent average diffusion lengths of 600 μm of n-type multicrystalline silicon wafers after the full solar cell process including boron diffusion," Energy Procedia, vol. 33, pp. 41-9, 2013.

M. Reusch, **M. Bivour**, M. Hermle, and S. W. Glunz, "Fill Factor Limitation of Silicon Heterojunction Solar Cells by Junction Recombination," Energy Procedia, vol. 38, pp. 297-304, 2013.

H. Wernerus, **M. Bivour**, L. Kroely, M. Hermle, and W. Wolke, "Characterization of ultra-thin $\mu\text{-Si:H}$ films for silicon heterojunction solar cells," Energy Procedia, vol. 55, pp. 310-9, 2014.

F. Feldmann, **M. Bivour**, C. Reichel, M. Hermle, S.W. Glunz, "Efficient carrier-selective contacts using SIS structures," *4th SiliconPV*, s-Hertogenboch, Netherlands, 2014.

F. Feldmann, A. Moldovan, **M. Bivour**, R. Müller, C. Reichel, M. Hermle, S.W. Glunz, "Tunnel oxide passivated carrier-selective contacts," *40th IEEE Photovoltaic Specialists Conference*, Denver, USA, 2014.

J. Temmler, **M. Bivour**, H. Steinkemper, and M. Hermle, "Boron doped a-SiC:H front layers for silicon heterojunction cells," presented at Proceedings of the 29th European Photovoltaic Solar Energy Conference and Exhibition, Amsterdam, The Netherlands, pp. 481-3, 2014.

F. Feldmann, K.-U. Ritzau, **M. Bivour**, A. Moldovan, S. Modi, J. Temmler, M. Hermle, and S. W. Glunz, "High and Low Work Function Materials for Passivated Contacts," presented at Energy Procedia 5th International Conference on Silicon Photovoltaics, SiliconPV 2015, Konstanz, Germany, 2015.

Presentations Author

Oral

"Potential of Silicon Heterojunction Solar Cells with Multicrystalline Absorber", 1th NPV Workshop, 2011

"Silizium Heterojunction auf multikristallinen Absorbern", Silicon Forrest Workshop, 2011

"Improving the a-Si:H(p) rear emitter contact of n-type silicon solar cells", 2nd International Conference on Silicon Photovoltaics, SiliconPV, 2012

"Numerical Analysis of Electrical TCO / a-Si:H(p) Contact Properties for Silicon Heterojunction Solar Cells," 3rd International Conference on Silicon Photovoltaics, SiliconPV, 2013

"Rear emitter silicon heterojunction solar cells: Fewer restrictions on the optoelectrical properties of front side TCOs," 4th International Conference on Silicon Photovoltaics, SiliconPV, 2014

"Alternative Contact Materials for Induced Junction Silicon Solar Cells", 5th International Conference on Silicon Photovoltaics, SiliconPV, 2015

"Requirements for Carrier Selective Silicon Heterojunctions," 24th Workshop on Crystalline Silicon Solar Cells & Modules: Materials and Processes, Breckenridge, Colorado, 2014

Poster/Visual

"n-type Silicon Solar Cells with Amorphouse/Crystalline Silicon Heterojunction Rear Emitter", 35th IEEE Photovoltaic Specialists Conference (PVSC), 2010

"Analysis of the diffused front surface field of n-type silicon solar cells with a-Si/c-Si heterojunction rear emitter", 1th International Conference on Silicon Photovoltaics, SiliconPV, 2011

"Influence of Interfacial ITO Doping on a-Si:H(p) / ITO(n) Contact Properties for Silicon Heterojunction Solar Cells", 27th EU PVSEC, 2012

"Analysis of a-Si:H Doping by Suns-Voc Measurements for Silicon Heterojunctions", 28th EU PVSEC, 2013

"Influence of Interfacial ITO Doping on the Fill Factor of n- and p-Type Silicon Heterojunction Solar Cells", 4th International Conference on Silicon Photovoltaics, SiliconPV, 2014

Patents

M. Hermle, **M. Bivour**, C. Reichel, *Method for manufacturing a single-sided contact solar cell*, DE 10 2009 040 670 A1

Supervised bachelor, master and diploma theses

K.-U. Ritzau, "Herstellung, Analyse und Optimierung einer Silicium-Hetero-Solarzelle mit multikristallinem Absorber," Eberhard Karls Universität Tübingen, 2010.

D. Impera, "Charakterisierung von amorph-kristallinen Silicium-Hetero-Solarzellen mit multikristallinem Absorber," Albert-Ludwigs-Universität Freiburg, 2012. (co-supervised)

M. Reusch, "Analyse von Füllfaktor limitierenden Mechanismen von Silizium-Heterosolarzellen," Albert-Ludwigs-Universität Freiburg im Breisgau, 2013.

S. Schröder, "2-Dimensionale Simulation von amorph / kristallinen Silicium-Hetero-Solarzellen ": Albert-Ludwigs-Universität Freiburg im Breisgau, 2013.

H. Wernerus, "Entwicklung dünner mikrokristalliner Siliciumschichten für Heterojunction-Solarzellen," Karlsruhe Institute of Technology, 2013.

J. Temmler, "Analyse der Dotierung und Legierung einer a-Si:H Schicht zur Anwendung in Silizium-Heterosolarzellen," University Potsdam, 2015.

11 Acknowledgements

I wish to express deepest gratitude to Prof. Eicke R. Weber and Prof. Leonhard Reindl for the supervision of my PhD thesis and for their uncomplicated manner.

I would like to thank Prof. Stefan Glunz and Dr. Martin Hermle for the opportunity to do my PhD at the Fraunhofer ISE. I am very grateful for sharing their knowledge on solar cells with me and the proofreading. The congenial manner in which Stefan Glunz is leading the department needs to be mentioned here as well.

I am indebted to many people who contributed by preparing samples, performing measurements, providing assistance in analysis or simulations and having stimulating discussions.

I am very grateful to my colleague Frank Feldmann for the very pleasant cooperation. This was certainly the base for interesting experimental results and a pleasant working atmosphere. Christina Reichel and Christian Schmiga are gratefully acknowledged for their indispensable support especially in the early stage of the thesis. Just like my office mates Bernhard Michel, Michael Rauer, Marc Rüdiger and Ralph Müller, they provided a pleasant atmosphere and stimulating discussions. Frank and Christian R., I really enjoyed the spare time we spent cycling, skiing, climbing, etc..

I am also very grateful for the collaboration with my colleagues Heiko Steinkemper, Laurent Kroely, Kurt-Ulrich Ritzau, Armin Richter, Bernd Steinhauser,

I'd like to acknowledge the excellent work done by my bachelor, master and diploma students Jan Temmler [102], Markus Reusch [109], Sebastian Schroer [100], Holger Wernerus [182], Davide Impera [107], Kurt-Ulrich Ritzau [275] and Florian Zähringer. The supervision of their work was a great experience for me and they contributed their part to the content and quality of this work. This is also true for the collaboration with Raphael Müller. Many thanks !

I also acknowledge the inspiring discussions with many researchers at conferences or workshops.

I would also like to thank the people without whom no research would be possible, the technicians. Karin Zimmermann, Elisabeth Schäffer, Felix Schätzle, Antonio Leimenstoll, Nadine Weber, Sonja Seitz, Christian Schetter, Harald Steidl, Clemens Veith, Ines Druschke, Nicolas König. I thank the Reiner Lemoine Foundation for financial support during the first part of the thesis.

Finally, I would like to express my deepest thanks to my girlfriend Nicole for her unflinching support, to my daughter Paula and my son Fritz just for existing

Increasing the solar cell efficiency by applying advanced cell architectures is one route for crystalline silicon wafer based PV to achieve significant cost reduction. An elegant strategy to overcome the limiting losses of the currently dominating solar cell designs based on diffused homojunctions is the application of passivating and carrier selective contacts. They combine passivating buffer layers and suitable contact layers in an one dimensional thin films stack.

The lack of knowledge regarding important operation principles and adequate characterization approaches for such novel contacts triggered this work. Besides a thorough understanding, several aspects of device optimization and characterization were addressed experimentally and via numerical simulation. Suitable characterization approaches, novel contact materials and novel cell designs were successfully established.



ISBN 978-3-8396-1166-1

